

**How organs organise their ontogeny:  
Modelling feedback between polarity,  
growth and geometry during Arabidopsis  
leaf development**

**Erika E. Kuchen**

Thesis submitted for the Degree of Doctor of Philosophy

University of East Anglia  
John Innes Centre

September 2011

©This copy of the thesis has been supplied on condition that anyone who consults it is understood to recognise that its copyright rests with the author and that no quotation from the thesis, nor any information derived therefrom, may be published without the author's prior, written consent.



# Abstract

Appendages of animals and plants develop from small buds into a wide variety of shapes. This development is coordinated by underlying systems of growth patterning and organisation. While many genes involved in shape development have been uncovered, it is still largely unclear how patterns of gene expression establish these systems. Growth and polarity may act and interact in a number of ways, whilst being constraint by physical components, thus making shape development a highly complex problem. Here, time lapse imaging of the *Arabidopsis* leaf was applied to generate a description of the early stages of leaf growth. Using this data, computational models were generated to investigate the spatiotemporal coordination of growth and polarity in the leaf. The dynamics of growth could be captured by a model in which growth rate patterns are established early in development and maintained locally during growth. Based on observed dynamics of growth orientations and model outputs, polarity systems in the leaf are likely to locally deform with the tissue geometry, rather than retain their initial conformation. With these assumptions, the model generated the observed spatiotemporal growth dynamics and overall shapes of leaves in two and three dimensions. Small modifications allowed the model to account for leaf excision results and the 3D shape of leaves of the *Arabidopsis jaw-D* mutant. The model was applied to study the formation of serrations along the leaf margins. Serrations generated by a mechanism, involving local polarity field reorganisation combined with local growth rate modifications, showed the best match to observed leaf serrations. All these results indicate that a close interaction between growth and polarity is vital for correct leaf development throughout the period analysed. The model also accounted for the leaf shapes of related species, indicating that an evolutionarily conserved mechanism underlies leaf shape development.

# Contents

<b>List of Figures</b>	<b>9</b>
<b>Acknowledgments</b>	<b>12</b>
<b>1 Introduction</b>	<b>14</b>
1.1 Leaf Morphology and Development . . . . .	16
1.1.1 Leaf Shape Regulation . . . . .	18
1.2 Growth . . . . .	19
1.2.1 Plant Cell Expansion . . . . .	20
1.2.2 Growth Coordination . . . . .	21
1.2.2.1 Morphogens . . . . .	21
1.2.2.2 Mechanical Signals . . . . .	23
1.2.3 Growth Maintenance . . . . .	24
1.3 Polarity and Anisotropy . . . . .	25
1.3.1 Cells and Anisotropy . . . . .	26
1.3.2 Establishment of Tissue Growth Orientation . . . . .	27
1.3.2.1 Morphogens . . . . .	27
1.3.2.2 Cell-Cell Communication . . . . .	27
1.3.2.3 Stress-Based Organisation . . . . .	28
1.3.3 Regulation of Tissue Orientation . . . . .	29
1.3.4 Leaf Polarity . . . . .	30
1.3.4.1 Proximodistal Axis . . . . .	30
1.3.4.2 Ad/abaxial Axis . . . . .	31
1.3.4.3 Mediolateral Axis . . . . .	32
1.3.4.4 Leaf Axes Interactions . . . . .	32
1.3.4.5 Leaf Polarity Maintenance . . . . .	33
1.4 Leaf Shape, Growth and Polarity . . . . .	34
1.5 Modelling Development . . . . .	35
1.5.1 Modelling Tissues . . . . .	35
1.6 This Work . . . . .	37
<b>2 Leaf Growth and Polarity</b>	<b>39</b>
2.1 Introduction . . . . .	39
2.1.1 Model Validation . . . . .	40
2.2 Results . . . . .	41
2.2.1 Leaf Growth Dynamics . . . . .	41

2.2.1.1	Ecotype Comparison . . . . .	44
2.2.2	Measuring Local Growth . . . . .	45
2.2.2.1	Tracking Leaf Growth . . . . .	46
2.2.2.2	Growth Tensors . . . . .	47
2.2.2.3	Growth Parameters . . . . .	49
2.2.2.4	Period of Tracking . . . . .	50
2.2.2.5	Areal Growth Rates . . . . .	52
2.2.3	Growth along the Midline . . . . .	54
2.2.3.1	Midline Growth Parameter Extraction . . . . .	54
2.2.3.2	Midline Growth Results . . . . .	55
2.2.4	Modelling Midline Growth . . . . .	57
2.2.4.1	Propagating Inhibitor Model . . . . .	58
2.2.4.2	Fixed Models . . . . .	61
2.2.4.3	Midline Models and Age . . . . .	65
2.2.5	Growing Polarised Tissue Framework . . . . .	69
2.2.5.1	Specified and Resultant Growth . . . . .	69
2.2.6	Generating a 2D Leaf Model . . . . .	72
2.2.7	Leaf Growth Anisotropy . . . . .	74
2.2.8	Polarity Systems . . . . .	75
2.2.9	Non-Deforming Polarity Model . . . . .	78
2.2.9.1	Lamina Extension at Later Stages . . . . .	80
2.2.9.2	Principal Orientations of Growth . . . . .	82
2.2.10	Deforming Polarity . . . . .	84
2.2.11	Organiser-Based Polarity Systems . . . . .	85
2.2.12	Organiser-Based Polarity Models . . . . .	88
2.2.12.1	Fixed Organiser-Based Polarity Model . . . . .	88
2.2.12.2	Dynamic Organiser-Based Polarity Model . . . . .	90
2.2.12.3	Organiser Positioning . . . . .	92
2.2.13	Testing the Model . . . . .	96
2.2.13.1	Clonal Analysis . . . . .	96
2.2.13.2	Leaf Surgery . . . . .	100
2.2.14	Morphospace . . . . .	110
2.3	Discussion . . . . .	114
2.3.1	Polarity Systems . . . . .	114
2.3.1.1	Polarity and Auxin . . . . .	116
2.3.2	Growth Coordination . . . . .	116
2.3.2.1	Midline Profiles . . . . .	117
2.3.2.2	Early or Continuous Patterning . . . . .	118
2.3.2.3	Beyond the Period Studied . . . . .	121
2.3.3	Growth Factors to Genes . . . . .	122
2.3.3.1	PROX and LAMINA (LAM) . . . . .	122
2.3.3.2	LATE . . . . .	125
2.3.3.3	MIDVEIN (MID) . . . . .	125
2.3.3.4	RIM . . . . .	126

2.3.4	Morphospace . . . . .	126
2.3.5	Future . . . . .	126
<b>3</b>	<b>Leaf Serrations</b>	<b>128</b>
3.1	Introduction . . . . .	128
3.1.1	Serration Genetics . . . . .	129
3.1.2	Proposed Serration Mechanisms . . . . .	130
3.1.3	Generating Serrations . . . . .	131
3.2	Results . . . . .	132
3.2.1	Serration Development . . . . .	132
3.2.2	Organiser-Based Polarity Fields . . . . .	134
3.2.2.1	Polarity Field Examples . . . . .	134
3.2.2.2	Organiser-Based Leaf Models . . . . .	137
3.2.3	Mechanisms of Serration Development . . . . .	137
3.2.3.1	Higher Growth Rates at the Serrations . . . . .	137
3.2.3.2	Serrations through Polarity Field Modifications . . . . .	142
3.2.3.3	Serrations through Growth and Polarity . . . . .	147
3.2.3.4	Serrations through Multiple Organisers . . . . .	150
3.2.4	Serration Maintenance . . . . .	151
3.2.5	Clonal Analysis of Serrated Leaves . . . . .	153
3.2.5.1	Virtual Clonal Analysis . . . . .	153
3.2.5.2	Experimental Clonal Analysis . . . . .	154
3.2.5.3	Comparison . . . . .	155
3.3	Discussion . . . . .	157
3.3.1	Serrations in Leaf 1 . . . . .	157
3.3.2	Model Evaluations . . . . .	158
3.3.3	Maintenance . . . . .	160
3.3.4	Clones and Future Work . . . . .	160
3.3.5	Auxin, CUC2 and Future Work . . . . .	161
3.4	Overview of Serration Models . . . . .	162
<b>4</b>	<b>3D Leaf Growth</b>	<b>164</b>
4.1	Introduction . . . . .	164
4.1.1	3D Leaf Shapes . . . . .	164
4.1.2	Leaf Buckling . . . . .	165
4.1.2.1	TCP Genes . . . . .	166
4.1.2.2	Mechanisms Underlying the <i>jaw</i> -D Phenotype . . . . .	167
4.2	Results . . . . .	167
4.2.1	3D Growth Tensor . . . . .	168
4.2.2	3D Growth in the <i>Gftbox</i> . . . . .	169
4.2.3	Bending . . . . .	169
4.2.4	Canvas Thickness . . . . .	170
4.2.5	Leaf Thickness . . . . .	171
4.2.5.1	Initial Leaf and Canvas Shape . . . . .	173
4.2.6	3D Leaf Model . . . . .	173

4.2.6.1	Reducing Canvas Thickness . . . . .	174
4.2.6.2	Differential Surface Growth . . . . .	176
4.2.7	Modelling Mutants . . . . .	177
4.2.7.1	<i>jaw</i> -D Leaf Shapes . . . . .	178
4.2.7.2	Measuring <i>jaw</i> -D Leaf Growth . . . . .	179
4.2.7.3	<i>jaw</i> -D Models . . . . .	182
4.2.7.4	Buckling . . . . .	186
4.2.7.5	Serrations . . . . .	188
4.3	Discussion . . . . .	191
4.3.1	3D Wild-type Model . . . . .	191
4.3.1.1	Future . . . . .	191
4.3.2	<i>jaw</i> -D Leaves . . . . .	192
4.3.2.1	<i>jaw</i> -D Serrations . . . . .	193
<b>5</b>	<b>General Discussion</b>	<b>195</b>
5.1	Validity of Computational Methods . . . . .	195
5.1.1	Factors . . . . .	196
5.2	Growth Coordination . . . . .	196
5.2.1	Proximodistal Gradient of Growth . . . . .	196
5.2.2	Establishment of Growth Patterns: Early or Re-patterning	197
5.2.2.1	Growth Deceleration . . . . .	199
5.3	Organising Systems . . . . .	200
5.3.1	Maintenance . . . . .	200
5.3.2	Deformation or Re-orientation . . . . .	200
5.4	Rotation, Polarity and Growth . . . . .	202
5.5	Modelling Loop . . . . .	202
5.6	Outlook . . . . .	204
<b>6</b>	<b>Materials and Methods</b>	<b>207</b>
6.1	General Methods . . . . .	207
6.1.1	Standard Growth Conditions . . . . .	207
6.2	Data Acquisition and Processing . . . . .	207
6.2.1	Arabidopsis Leaf Growth Curves . . . . .	207
6.2.1.1	Ecotype Landsberg <i>erecta</i> . . . . .	207
6.2.1.2	Ecotype Columbia . . . . .	208
6.2.1.3	Curve Fitting . . . . .	208
6.2.1.4	Calculating Leaf Initiation . . . . .	209
6.2.2	Time Lapse Imaging . . . . .	209
6.2.2.1	Tracking . . . . .	209
6.2.2.2	Tracking Image Analysis . . . . .	209
6.2.2.3	Tracking Growth Calculations . . . . .	210
6.2.3	Clonal Analysis . . . . .	211
6.2.3.1	Generating <i>Arabidopsis</i> Clones . . . . .	211
6.2.3.2	Generating <i>Antirrhinum</i> Clones . . . . .	212
6.2.3.3	Analysing Clonal Data . . . . .	212

6.2.3.4	Cell Outline Extraction . . . . .	213
6.2.4	Leaf Excisions . . . . .	213
6.2.4.1	Tracking Straight Cut Leaves . . . . .	214
6.2.5	Leaf Serration Measurements . . . . .	214
6.2.6	Optical Projection Tomography . . . . .	215
6.2.6.1	Leaf Thickness Measurements . . . . .	215
6.2.7	<i>jaw</i> -D Crosses . . . . .	215
6.2.8	Imaging Leaves with Fluorescent Constructs . . . . .	216
6.3	Computational Modelling . . . . .	216
6.3.1	The Canvas . . . . .	216
6.3.2	Factors . . . . .	217
6.3.3	Model Output Times . . . . .	218
6.3.4	1D Models . . . . .	218
6.3.5	2D Models . . . . .	219
6.3.5.1	Simulation Details . . . . .	220
6.3.5.2	2D Leaf Model Parameters . . . . .	220
6.3.5.3	2D Example Models . . . . .	222
	<b>List of Abbreviations</b>	<b>224</b>
	<b>Bibliography</b>	<b>226</b>

# List of Figures

1.1	Leaf Axes . . . . .	18
1.2	Scale and Orientation . . . . .	26
1.3	Polarity Theories . . . . .	30
2.1	Measuring Leaf Dimensions . . . . .	41
2.2	<i>Arabidopsis</i> Leaf Growth Curves . . . . .	43
2.3	<i>Arabidopsis</i> Ecotype Comparison . . . . .	44
2.4	Calculating Velocities . . . . .	46
2.5	Point Placement in <i>Point Tracker</i> . . . . .	47
2.6	Point Velocities . . . . .	48
2.7	Defining Regions in <i>Point Tracker</i> . . . . .	49
2.8	2D Growth Parameters . . . . .	50
2.9	Tracking Validation . . . . .	51
2.10	Tracked Areal Growth Rates . . . . .	53
2.11	Midline Growth Rates . . . . .	55
2.12	Lamina Midline Growth Rate Profiles . . . . .	56
2.13	1D Model Canvas . . . . .	58
2.14	Propagating Inhibitor Midline Model Starting Conditions . . . . .	59
2.15	Inhibition Function . . . . .	60
2.16	Propagating Inhibitor Midline Model . . . . .	61
2.17	Propagating Inhibitor Midline Model . . . . .	62
2.18	Growth and Patterning Feedback . . . . .	63
2.19	Growth Promotion Dynamics . . . . .	64
2.20	Fixed Activator Midline Model . . . . .	65
2.21	Growth Deceleration Dynamics . . . . .	67
2.22	Fixed Activator and Age . . . . .	67
2.23	Propagating Inhibitor Model and Age . . . . .	68
2.24	Specified and Resultant Growth Parameters . . . . .	70
2.25	Specified and Resultant Growth Rates . . . . .	71
2.26	Starting Canvas . . . . .	73
2.27	Model Extension to 2D . . . . .	74
2.28	Leaf Growth Anisotropy . . . . .	75
2.29	Polarity Systems: Non-Deforming or Deforming . . . . .	77
2.30	Leaf Model with Growth and Polarity . . . . .	79
2.31	Lateral Growth Model . . . . .	80

2.32	Broad Lamina Model . . . . .	81
2.33	Non-deforming and Deforming Models . . . . .	83
2.34	Principal Orientations of Growth . . . . .	85
2.35	Organiser-Based Polarity Systems . . . . .	86
2.36	Fixed Organiser-Based Polarity . . . . .	87
2.37	Leaf and Model Anisotropy . . . . .	90
2.38	Dynamic Organiser-Based Polarity . . . . .	91
2.39	Organiser Positioning . . . . .	94
2.40	Midline Organiser Positioning . . . . .	95
2.41	Model Test by Clonal Analysis . . . . .	97
2.42	Margin Clones . . . . .	99
2.43	Modelled Distal Excision . . . . .	101
2.44	Leaf Distal Excision . . . . .	102
2.45	Cut Edge Inhibition Model . . . . .	105
2.46	Canvas Deformations . . . . .	106
2.47	Diagonal Excision . . . . .	107
2.48	Side Incision . . . . .	109
2.49	Parameter Space . . . . .	112
2.50	Morphospace . . . . .	113
2.51	PIN1 Expression . . . . .	117
2.52	Modelled Growth Dynamics . . . . .	121
2.53	DR5 Expression . . . . .	122
3.1	Serrations in Leaf 1 . . . . .	133
3.2	Polarity Organiser Types . . . . .	135
3.3	Leaf Polarity Organisers . . . . .	136
3.4	Inhibition Release Model . . . . .	139
3.5	Increased Growth Models . . . . .	141
3.6	Reduced Sinus Growth Model . . . . .	143
3.7	Source Model . . . . .	144
3.8	Sink Models . . . . .	145
3.9	Sink Models and Principal Growth Orientations . . . . .	147
3.10	Growth and Polarity Combination Models . . . . .	149
3.11	Multiple Organiser Models . . . . .	151
3.12	Serration Size Measured and Modelled . . . . .	152
3.13	Clonal Analysis of Serrations . . . . .	156
4.1	3D Leaf Development . . . . .	165
4.2	Axes of Growth in 3D . . . . .	169
4.3	Canvas Growth Rates . . . . .	169
4.4	Canvas Surface Properties . . . . .	170
4.5	Canvas Thickness . . . . .	171
4.6	Leaf Thickness . . . . .	172
4.7	Initial 3D leaf and canvas shape . . . . .	172
4.8	2D Leaf Model in 3D . . . . .	174

4.9	Thickness Investigations . . . . .	175
4.10	Differential Surface Growth . . . . .	176
4.11	<i>jaw</i> -D Leaf Soil Grown . . . . .	178
4.12	Wild-type and <i>jaw</i> -D Leaf Shapes . . . . .	179
4.13	CyclinB1;1 Expression in Young Leaves . . . . .	180
4.14	CyclinB1;1 Expression in Older Leaves . . . . .	181
4.15	Increased Margin Growth Model . . . . .	184
4.16	Failed Arrest Model . . . . .	185
4.17	Canvas Buckling . . . . .	186
4.18	Canvas Thickness and Buckling . . . . .	187
4.20	DR5 Expression in <i>jaw</i> -D Leaf 3 . . . . .	190
4.19	DR5 Expression . . . . .	190

# Oompa Loompa of Science

Thanks to everyone,  
who has supported me on my journey to become an Oompa Loompa of Science!

Thanks to all those,  
who enriched this thesis with their experimental data, millennium-proof image analysis software or vast math-comp expertise: Samantha Fox, Karen Lee, Sandra Bensmihen, Sascha Duttke, Grant Calder, Richard Kennaway, Pierre Barbier de Reuille, Scott Grandison, Paul Southam, Sarah Robinson and Andrew Bangham. Also thanks to everyone who equipped me with media, soil and other useful things, in particular Cindy Cooper and Lesley Phillips.

Thanks to Enrico Coen,  
the thinker, for introducing me to all your theories on development and evolution. Thanks for all the help during my PhD and your supportive attitude (on the whole).

Special thanks to Sam,  
without you this thesis would only be half complete. Thanks for the past years of brilliant collaboration and happy hours of paper writing. Also thanks for your microscopy support, one day I'll reach your level.

Thanks to Richard,  
for making the *GFTbox* and always knowing how to fix it.

Thanks to Pierre,  
for helping me grow my understanding of tensors. Bazinga!

Thanks to Susana Sauret-Güeto,  
for all the *excellent* discussions about life and leaves. And for helping me experimenting. Also, thanks to Katie Abley for joining our discussions more

recently.

Thanks to Karen Lee,  
for making all images in 3D and also for rhyming with OPT, making my thesis poetry.

Thanks to Andrew,  
for helping me model much faster by using the cluster (allowing me to submit on time).

Thanks to the *Antirrhinum* crew,  
who initially helped me get started in the lab, in particular, Xianzhong Feng.

Thanks to my supervisory committee,  
Richard Morris and Michael Lenhard, for good suggestions and filled in forms.

Thanks to Jo Dicks,  
for helping me perform my PhD at JIC, which so far I haven't regretted.

Thanks to my examiners, Verônica Grieneisen and Jan Traas,  
for all the helpful suggestions during my viva. Hopefully you find them implemented.

Danke an Maria, Herby und Robbie,  
für all die Unterstützung/ Ablenkung und die stetige Besorgnis um meine Gesundheit. Ich hab noch genug Creme!

Einen riesen Dank an unser neustes Familienmitglied, Naveed.  
You have been a Wunderstar in cooking, cleaning, baking, making me lunch, shopping, going for walks and generally tolerating my stressed disposition! It would have all been a lot less fun without you.

Thanks to everyone,  
who *critically* read parts of my thesis; Rico, Wiebke Apel, Katie, Karen, Susana, Des Bradley and Katharina Schiessl (and to everyone else who offered!). Also thanks to everyone, who increased my entertainment levels or even biological know-how during my PhD, in particular those people who I should (but forgot to) have mentioned above.

Finally, a big thanks to the sun and clouds,  
which provided (mostly) such a miserable summer that staying indoors was easy.

# Chapter 1

## Introduction

Appendages of animals and plants display a wide variety of shapes, from limbs, tails and wings in animals to leaves and flowers in plants. Despite this diversity, appendages develop from morphologically very similar small buds made up of a collection of cells. From these buds, species specific morphogenic events then create the diversity of final appendage shapes observed. For instance, the *Antirrhinum* flower develops from symmetrical buds into a complex 3D shape with dorsoventral asymmetry, through a complex process involving tissue folding (Green et al., 2010).

During their characteristic shape development, appendages undergo a huge increase in scale associated with an increase in cell size and numbers. For instance, plant cells increase by about 10-1000 fold in volume (Geitmann and Ortega, 2009; Pyke et al., 1991; Roeder et al., 2010; Veytsman and Cosgrove, 1998), which in *Arabidopsis* is associated with a leaf organ size increase of about 1000 fold at maturation (Pyke et al., 1991). During *Drosophila* wing development cell numbers increase from about 50 to 50,000 cells (Hufnagel et al., 2007; Milan et al., 1996).

Appendage-specific developmental dynamics are generated by underlying systems of growth organisation. In addition, developmental processes are associated with physical and physiological limitations (Bonner, 2006). To understand shape development, it is therefore necessary to study growth and the polarity of growth under the influence of these constraints.

Growth and polarity are promoted and coordinated by genetic activities.

While a vast amount of research has identified many genes involved in developmental processes, relatively little is known about how these genes interact, and even less about how they contribute to shape development.

To study how gene expression patterns contribute to patterns of growth, we need qualitative and quantitative data on the spatiotemporal expression patterns of each gene. Generating gene expression maps is not easy given the large number of developmental genes (Efroni et al., 2008; Horiguchi et al., 2006a; Street et al., 2008) and redundancies in gene activities and genetic pathways (Gonzalez et al., 2010). Thus, on the whole accurate spatiotemporal expression data is still lacking.

To really understand how leaf growth patterns are established and maintained, a description of leaf growth is needed, with which the respective contributions of individual genes to growth patterns can be evaluated. Appendage growth has been studied using a number of methods such as time lapse imaging (Aigouy et al., 2010; Gros et al., 2010; Harder et al., 2009; Richards and Kavanagh, 1942; Schmundt et al., 1998; Wolf et al., 1986), fate map studies (Vargesson et al., 1997) and clonal analysis (Baena-Lopez et al., 2005; Dubatolova and Omelyanchuk, 2004; Green et al., 2010; Rolland-Lagan et al., 2003), which allow growth rates and the polarity of growth to be quantified. For instance, time lapse imaging has been used to identify differences in growth dynamics between wild-type and malformed leaves of *Vitis vinifera* (Wolf et al., 1986). In addition to the patterning of growth rates, it is unclear in what way the orientation of growth is organised within the tissue and to what extent polarity is necessary to generate observed shapes.

A major problem with linking gene activities to shape development is the complexity generated by the interaction of many developmental components. For instance, it is difficult to predict how gene-mediated promotion or inhibition of growth in certain regions may influence shape. This problem can be bridged by computational modelling, where tissue dynamics are simulated to reveal the consequences of experimental observations on shape development.

In this work, growth of the *Arabidopsis thaliana* leaf 1 was studied to

understand how growth rate patterning may lead to shape development and how growth processes interact with growth organising systems. Since these processes need to be viewed in the context of physical tissue properties, computational modelling was used to explore the effects of inhomogeneous growth on tissue shape.

## 1.1 Leaf Morphology and Development

Previous studies of leaf growth showed that leaves develop from part of the shoot apical meristem (SAM), which divides periclinally (out of the plane) to form the initial leaf bud primordium (Kessler and Sinha, 2004). Subsequent developmental events differ between different species. However, regardless of their complexity, most leaves develop with roughly left-right symmetry (Semiarti et al., 2001). Unlike the plant root and shoot, leaf development is determinate in that leaves reach a final size (Beemster et al., 2003; Donnelly et al., 1999; Horiguchi et al., 2006a; Pyke et al., 1991).

Leaves are three-dimensional structures consisting of several cell layers. The *Arabidopsis thaliana* leaf consists of about six distinct cell layers, with two outer epidermal layers, termed adaxial and abaxial epidermis, and internal mesophyll layers comprising the palisade mesophyll and the spongy mesophyll. Cell division takes place almost exclusively anticlinally (within the layer; Esau 1965).

Thus, the leaf can be described by its three orthogonal axes (Fig. 1.1). The longest of the three axes is termed the proximodistal axis and runs from the base to the tip of the leaf. The mediolateral axis runs from the leaf mid-vein laterally to the margins. The ad/abaxial (dorsoventral) axis is oriented from the top to the bottom leaf surface.

The main axes of growth are the proximodistal and mediolateral axes (Avery, 1933; Pyke et al., 1991). However, leaf thickness continues to increase after the leaf blade has ceased to expand, due to the continued expansion of the palisade mesophyll cells (Pyke et al., 1991).

In the past, several studies explored the growth processes that underlie leaf

shape changes in a variety of plant species. This showed that the overall leaf area of *Arabidopsis thaliana* initially increases rapidly (Dhondt et al., 2010; Kheibarshekan Asl et al., 2011; Pyke et al., 1991). Growth rates then decelerate as the leaf approaches its final size, which leaf 1 reaches within about 18 days after initiation under a range of standard growth conditions.

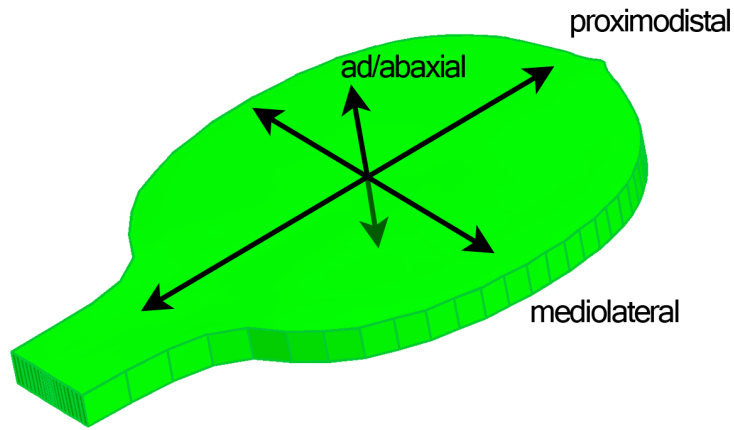
More spatially detailed patterns of growth have been generated by time lapse imaging. Leaf growth of various species has been tracked at the very early primordium stage (Kwiatkowska and Dumais, 2003) or at late stages of development, when the basic leaf shape has already been established (Avery, 1933; Erickson, 1966; Schmundt et al., 1998; Wolf et al., 1986). Tracking primordium outgrowth from the SAM of *Anagallis arvensis* L. revealed that the initially high areal growth rates in the primordium are relatively isotropic (equal in all directions; Kwiatkowska and Dumais 2003). Growth then becomes anisotropic with higher rates along the proximodistal axis of the new leaf primordium. A study of tobacco leaf development by Avery (1933) also showed strong anisotropic growth patterns in the leaf blade with preferential growth in length compared to width at early stages. Tracking leaves of a range of plant species at late stages of development revealed a gradient of growth rates across the leaf, with highest levels at the base and lower levels at the tip (Avery, 1933; Erickson, 1966; Schmundt et al., 1998; Wolf et al., 1986).

Studies on the timing (Donnelly et al., 1999; Pyke et al., 1991) and direction (Kuwabara and Nagata, 2006) of cell division demonstrate that cells proliferate throughout the leaf at early stages and cell proliferation then arrests with a clear proximodistal gradient. First, cells at the distal tip arrest division. Division then arrests in progressively more proximal regions until most cells throughout the leaf have stopped dividing.

Cell division dynamics have also been inferred from clonal analysis. Clonal patterns in cotton and tobacco leaves showed a higher growth and division rate at the leaf base compared to the tip (Dolan and Poethig, 1998; Poethig and Sussex, 1985).

After division arrest, cells expand in size by several fold (Veylder et al., 2002). Therefore, leaf development is often classified into a cell division and a

**Figure 1.1**  
The three orthogonal axes of the leaf: the proximodistal axis, mediolateral axis and ad/abaxial axis.



cell expansion phase.

### 1.1.1 Leaf Shape Regulation

The development of leaf shape and size is controlled by the action of many developmental genes, which has been well described in several reviews (Hake and Micol, 2003; Johnson and Lenhard, 2011; Micol, 2009; Tsukaya, 2006). In particular, a number of large scale phenotypic studies on leaf shape have revealed the complexity of leaf development (Horiguchi et al., 2006b; Pérez-Pérez et al., 2009, 2011). In general, developmental genes either control the cell division or expansion dynamics during development and influence leaf morphology to varying degrees. Several gene mutations alter leaf size and shape within the plane of the leaf blade, while other mutations have dramatic effects on the three-dimensional leaf shape. Although it is useful to know the genes involved in leaf development, it is equally important to identify how these genes interact with one another, with hormones and with environmental conditions (Gudesblat and Russinova, 2011; Tsukaya, 2005). Interaction maps are becoming increasingly more detailed and start to reveal the complexity of leaf development (Gonzalez et al., 2010).

In this work, leaf shape development is largely studied at the organ scale, with a more abstract notion of genes. However, the effects on leaf shape development of two gene families are analysed more closely, as mutations in some of these gene family members provide interesting phenotypes to study the control and maintenance of growth and polarity in leaf margin and overall 3D shape development. One of these families are the *CUP-SHAPED COTYLEDON*

(*CUC*) genes, which belong to the *NAC* family of transcription factors and are essential for serrated leaf margins (Hasson et al., 2011; Nikovics et al., 2006). Mutations in *CUC* genes result in leaves with smooth margins. However, the mode of action of *CUC* in either growth or polarity, or both, is still unclear. The other family of interest here is the *TCP* family of transcription factors. This family is named after three of its members *TEOSINTE BRANCHED 1*, *CYLOIDEA* and *PROLIFERATING CELL FACTORS* (Cubas et al., 1999). Mutations in several of these genes leads to dramatically disturbed three-dimensional leaf structures. In this work, the shape of the *jaw-D* mutant is studied. In this mutant several *TCP* family members are downregulated by the constitutive expression of miR319a (Palatnik et al., 2003). This downregulation results in leaves with highly buckled and serrated margins, probably due to continued cell proliferation at the margins (Efroni et al., 2008; Nath et al., 2003; Palatnik et al., 2003). A more detailed description of these genes and their functions is given in the respective chapters (chapter 3 for *CUCs* and chapter 4 for *TCPs*).

While more and more genes are being uncovered, little is still known about how these genes affect growth rates or polarity. Often mutant gene activity is classified as controlling either cell division or cell expansion according to the overall leaf size and number and size of cells in the leaf, rather than by generating more detailed growth rate information. To understand shape development, it is necessary to understand the mechanisms underlying growth and polarity control and coordination.

## 1.2 Growth

Since changes in shape are determined by growth, it is important to understand how growth patterns are established and maintained during development. Growth is a change in size, such as change in the size of cells making up a tissue. Many studies also define growth as a change in cell number through cell division or cell death (apoptosis; Kheibarshekan Asl et al. 2011; Lecuit and Le Goff 2007; Raff et al. 1998). Apoptosis is not prominent in plants and is largely limited to animal tissues, where it is a means of eliminating less fit

or deleterious cells (Greenberg, 1996; Moreno et al., 2002).

In leaves, cell number is often used as an indicator of growth, since mutations in developmental genes that lead to a change in leaf area are often associated with a change in cell number. For instance, reduced cell numbers in mutants of genes such as *SHORTROOT* (Dhondt et al., 2010), *ARGOS* (Hu et al., 2003), *DA1* (Li et al., 2008) and *BIG BROTHER* (Disch et al., 2006) result in smaller leaves.

However, measuring organ size by cell number is difficult in situations where cell area may vary. The *Arabidopsis* sepal, for instance, consist of a seemingly random distribution of large, long cells and small cells (Roeder et al., 2010). In the leaf, the size of cells at division varies during development and for different leaf regions (Kheibarshekan Asl et al., 2011). In addition, there are several examples where differences in cell number are not correlated with a change in the shape or size of the appendage (reviewed by Day and Lawrence, 2000). For instance, in salamanders and newts, differences in cell size due to different ploidy levels are balanced by a change in cell number, so that the final organisms have a normal (diploid) size with varying cell numbers (Frankhauser, 1945). Experimentally altered cell numbers in the posterior compartment of the *Drosophila* wing disc are also compensated for by cell size (Neufeld et al., 1998). In plants, reductions in cell proliferation due to a mutation of *cdc2* in tobacco, or *AINTEGUMENTA* in *Arabidopsis*, also have little effect on the overall leaf size due to larger cells (Hemerly et al., 1995; Mizukami and Fischer, 2000). Therefore, inferring organ growth from cell numbers may be misleading.

Thus, in this study, cell division is regarded as a way to partition a tissue (Fleming, 2003; Green, 1976), while growth is defined as a change in size.

### 1.2.1 Plant Cell Expansion

Plants cells expand through extending their stiff cell walls in a slow irreversible process, which has been outlined by several reviews (Cosgrove, 2005; Hamant and Traas, 2010; Ingber, 2005; Veytsman and Cosgrove, 1998). Plant cell walls are made up of cellulose microfibrils, which are embedded in a complex polysaccharide matrix by non-covalent interactions. The matrix polysac-

carbohydrates are made up of hemicellulose, pectins as well as structural proteins. Cell wall extension is driven by the uptake of water, vacuolation, into the cell by osmosis. Water uptake increases the turgor pressure inside the cell, which stretches the wall polymers and thereby creates stresses on the wall. The wall stresses constitute the energy necessary for wall loosening. During wall loosening the matrix polysaccharides and cellulose microfibrils network is modified, such as through scissions of stress-bearing crosslinks. For instance, a group of wall proteins, called expansins, break up the non-covalent bonds between microfibrils and the wall matrix. Wall loosening allows the cell wall components to shift and slide relative to each other, reducing wall stresses. The relaxation of wall stresses, in turn, enables cells to take up more water and expand.

In the long run, cell wall weakening during extension is prevented by the synthesis and integration of new wall material into the cell wall. However, expansion and synthesis are not necessarily coupled processes. Thus, factors that control the loosening of the cell wall interactions determine the growth rate of a cell (Hamant et al., 2010).

## **1.2.2 Growth Coordination**

A tissue can grow uniformly, which means that regions across the tissue all grow at the same rate, or non-uniformly, indicating regional differences in growth rates. In the leaf, the clear proximodistal gradient in growth rates at later stages of growth noted in several studies suggests that growth is non-uniform but coordinated (Avery, 1933; Erickson, 1966; Schmundt et al., 1998; Wolf et al., 1986). To coordinate growth rates, cells must be able to communicate with each other or at least receive and interpret supplied information. There is evidence for growth coordination via signalling factors (morphogens) and mechanical signals.

### **1.2.2.1 Morphogens**

Morphogens are mobile substances that dictate the development of a tissue in a concentration dependent manner (Day and Lawrence, 2000; Teleman et al., 2001; Turing, 1952). In animals, there are many examples where mor-

morphogen threshold concentrations activate different downstream genes (Gurdon and Bourillot, 2001; Lawrence and Struhl, 1996; Nellen et al., 1996). However, although in many cases these morphogens are required for appendage growth, downstream genes appear to function as patterning rather than growth factors. Therefore, the role of morphogens in growth rate control is often less clear (Affolter and Basler, 2007; Wolpert, 2011). For instance, in *Drosophila* the morphogen Decapentaplegic (Dpp) forms a gradient across the wing disc, and activates genes such as *brinker*, *optomotor-blind* and *spalt major*, which are involved in vein patterning in the wing (reviewed by Affolter and Basler, 2007). In the absence of Dpp, wing growth is highly reduced. However, the importance of the Dpp gradient formation in growth control is unclear, since Dpp seems to promote growth uniformly across the tissue (Affolter and Basler, 2007; Schwank and Basler, 2010; Schwank et al., 2011).

In plants, there are some examples where genes regulate tissue development non-autonomously, such as *KLUH* (*KLU*; Anastasiou et al. 2007; Eriksson et al. 2010) and *ANGUSTIFOLIA3* (*AN3*; Kawade et al. 2010). *KLU* is produced along the margins of petals, but can control the duration of the cell proliferation phase throughout the whole inflorescence (Eriksson et al., 2010). However, both *KLU* and *AN3* (Bai et al., 2010) are immobile and little is known about the mechanism underlying their non-autonomous activities.

Other mobile messengers include plant hormones, the most important ones for development being auxin, gibberellin, cytokinin and brassinosteroid (reviewed by Gudesblat and Russinova, 2011; Johnson and Lenhard, 2011; Teale et al., 2006; Wolters and Jürgens, 2009). Modifications in their receptors, transporters, biosynthesis or downstream genes have a clear effect on leaf shape and size (Hay et al., 2002; Nakaya et al., 2002; Rashotte et al., 2006). However, there is still little knowledge of how the different hormones are distributed across the leaf and how their distribution and concentration affects leaf growth (Gudesblat and Russinova, 2011). Auxin is required at high concentrations for leaf primordium initiation at the site of primordium outgrowth (Benková et al., 2003; Heisler et al., 2005; Reinhardt et al., 2000). It is thought that auxin modifies the pH of the cell wall and thereby facilitates wall-loosening by expansins leading to an increase in growth rates (reviewed by Cosgrove,

2005).

#### 1.2.2.1.1 Morphogen Propagation

A variety of molecular compounds may act as morphogens, such as steroids and peptides (Matsubayashi and Sakagami, 2006), which may propagate by a variety of modes through a tissue. The simplest means of propagation is by diffusion. For instance, Bicoid and Fibroblast Growth Factor 8 diffuse through the *Drosophila* and zebrafish embryo, respectively (Gregor et al., 2005; Yu et al., 2009). In other methods of transport, morphogens are internalised into the cells, such as by repeated cycles of endocytosis and exocytosis, transfer in lipoprotein particles and directed transport (reviewed by Kornberg and Guha, 2007). Dpp propagates by endocytosis and exocytosis through the *Drosophila* wing (Kicheva et al., 2007) and auxin is largely transported via AUXIN RESISTANCE 1 (AUX1) import and PINFORMED (PIN) efflux carriers from cell to cell.

However, the mode of transport of most morphogens is not well understood due to the difficulties in morphogen gradient visualisation (Affolter and Basler, 2007; Cadigan, 2002). Therefore, computational modelling is increasingly used to test expected morphogen distributions under hypothesised modes of transport. For instance, it is thought that the concentration gradient of auxin is a result of directed transport by the polarly distributed auxin efflux carriers PIN1 (Gälweiler et al., 1998; Sauer et al., 2006) and that PIN1 localisation is determined by the concentration of auxin in neighbouring cells (Friml and Palme, 2002; Sauer et al., 2006). Incorporating these interactions into computational models correctly predicted observed auxin distributions (Jönsson et al., 2006; Smith et al., 2006).

#### 1.2.2.2 Mechanical Signals

In plant tissues, as well as most animal tissues such as the *Drosophila* wing (Shraiman, 2005), cells are connected or adhere to each other. Differences in growth dynamics between tissue regions may therefore result in compression or tension of some regions compared to others. It has been proposed that cells

respond to these stresses, the forces per unit area acting on cells, and adjust their growth accordingly.

While actual growth rates are seldom measured in experiments that investigate the impact of external forces on development, stress clearly affects cell division dynamics. For instance, in a vertebrate tissue culture study, where cells were arranged on a square monolayer, cell proliferation in the middle of the layer was undetectable, whereas high cell proliferation rates were measured at the edges, where cell density mediated external stresses were lower (Nelson et al., 2005). In addition, cell division patterns in the *Drosophila* wing could be successfully modelled by a combination of morphogen induced proliferation through Dpp and stress-induced proliferation arrest (Hufnagel et al., 2007; Shraiman, 2005). Thus, stress may be able to coordinate growth across tissue regions. The connectedness of cells should allow stresses to travel quickly through the tissue.

### 1.2.3 Growth Maintenance

Apart from deciphering the spatial mechanisms of growth coordination in shape development, it is also important to look at the temporal regulation. During growth appendages undergo an enormous increase in scale. For instance, under *in vitro* growth conditions, the *Arabidopsis* leaf 1 increases about 1000 fold in size (Pyke et al., 1991). It is possible that growth interactions are established at an early age and are maintained throughout development. Alternatively, the patterns of growth rate distribution may change during development.

In chick limb bud development, proximodistal identity is established early on as demonstrated by fate map studies (Dudley et al., 2002). By implanting beads, that had been incubated in different concentrations of the morphogen activin, into animal caps, Gurdon et al. (1995) were able to show that cells can respond to an increase in morphogen concentration but not a decrease. This suggests that early morphogen supply would be sufficient to determine growth patterning, which could then be maintained locally throughout development (Gurdon and Bourillot, 2001). In cases where growth patterns are established through a morphogen gradient, it may be advantageous to set up

the gradient early in development when the scale of the tissue is still relatively small. Morphogen gradients may be disturbed by fluctuations of environmental factors, genetic variability and stochastic differences (Jaeger et al., 2008). These fluctuations will have an even greater effect in regions distant from the morphogen source. Therefore, gradients will be more robust and precise early in development, when the distance between the source and the tissue regions are relatively short (Schwank and Basler, 2010).

However, recent studies have shown that continuous signalling of some morphogens is required for correct development, suggesting that growth patterns are not always fixed at an early age. For instance, blocking signalling of Sonic Hedgehog (Shh), which is essential for development of the ventral neural tube in chick embryos, causes cells to revert to express low Shh concentration downstream genes (Dessaud et al., 2010). Similarly, in the *Drosophila* wing, Dpp signalling is required throughout wing disc development (Affolter and Basler, 2007).

In the *Arabidopsis* leaf, transcription maps show that leaf development can be classified into different stages according to the leaf gene expression profile (Efroni et al., 2008). Changes in gene expression patterns suggest that growth patterns may change as well.

### 1.3 Polarity and Anisotropy

While the rate of growth, which determines the increase in scale (Fig. 1.2B), is under control in each cell, the orientation of this growth may also need to be controlled to generate an organ with three axes of different sizes (Fig. 1.2C). It is unclear how a preferential orientation of growth is established and coordinated during development. In principle it is possible that the differently sized organ axes are generated through a complex distribution of isotropic non-uniform growth rates. However, it is often simpler to explain observed organ shape based on anisotropic growth. To grow preferentially in one orientation, cells need to sense their orientation with respect to the overall tissue and grow accordingly. For instance, most leaves primarily grow along their proximodistal and mediolateral axes.

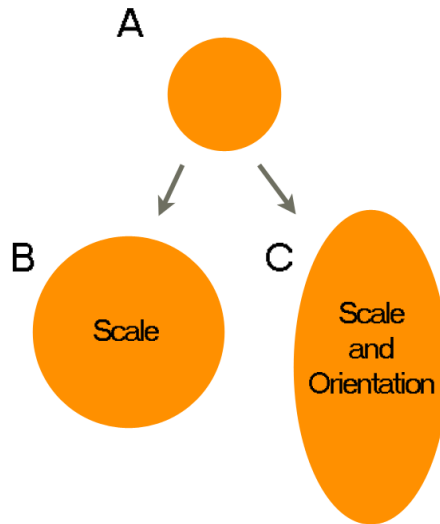


**Figure 1.2** Scale and orientation. **A**, during growth an initial circle, **B**, increases in scale, but may also, **C**, grow primarily along a particular orientation.

### 1.3.1 Cells and Anisotropy

On the cellular level, anisotropic growth may be generated by localised loosening of the cell wall, instead of loosening walls uniformly (reviewed by Baskin, 2005; Hamant and Traas, 2010). Cell wall loosening is required for wall expansion and therefore cell growth (reviewed by Cosgrove, 2005).

The stiffness of the cell wall depends on the cellulose microfibril interactions strengthening it (Baskin, 2005). It has been observed, that microfibrils orientations tend to align in a spiral conformation forming a ring around the cell. This means that growth is easiest, and observed to be maximal, perpendicular to the microfibril orientations, where the cell wall is weakest (Baskin, 2005; Geitmann and Ortega, 2009; Lloyd and Chan, 2004). Microfibril orientations are thought to be guided by cortical microtubules, which also form ordered arrays (reviewed by Baskin, 2005; Traas and Hamant, 2009). Correct microtubule arrangements are essential for anisotropic growth, as cells with depolymerised microtubules grow isotropically (Hamant et al., 2008). However, the relative importance of microfibrils and microtubules in anisotropy determination is still unclear, as microtubule disruption by pharmacological agents or mutations leads to isotropic growth, while microfibril arrangements are maintained (reviewed by Geitmann and Ortega, 2009).

### 1.3.2 Establishment of Tissue Growth Orientation

For coordinated growth in multicellular systems, internal cell anisotropy, arising from microtubule and microfibril arrangements, need to be somehow aligned. The mechanisms that have been proposed and observed for this tissue organisation are similar to those proposed above for the coordination of growth rates (1.2.2 Growth Coordination) and involve morphogens, direct cell-cell communication and stress-based mechanisms.

#### 1.3.2.1 Morphogens

Cells are thought to be able to detect the direction of a morphogen gradient by the morphogen concentration differences along or within their body (Goodrich and Strutt, 2011; Wolpert, 1969). Eukaryotic cells are likely to be sufficiently large, compared to the size of morphogen molecules, to be able to measure these concentration differences (Hu et al., 2010).

In plants, microtubule arrangements can be altered by plant hormones such as auxin, gibberellins and abscisic acid (Baluska et al., 1993; Ishida and Katsumi, 1992; Zandomeni and Schopfer, 1993). Transport of several hormones such as auxin, cytokinin and abscisic acid is directional within the root and shoot (Friml and Palme, 2002; Haberer and Kieber, 2002; Sauter et al., 2001). Disturbance of auxin transport often results in thicker organs, such as thicker roots and leaves (Benková et al., 2003; Borghi et al., 2007; Reinhardt et al., 2000), suggesting that the tissue organisation is disturbed. Inhibition of auxin transport by chemical agents results in increased cell division at the site of the incipient lateral root primordium without a clear primordium outgrowth (Benková et al., 2003), indicating a loss of polarity.

#### 1.3.2.2 Cell-Cell Communication

Assuming that cells can detect the polarities of their neighbours at cell interfaces and orientate their polarity accordingly, a polarity cue from as little as one cell could polarise a whole tissue (Meinhardt, 2007). Polarity genes in many vertebrate and invertebrate tissues interact at cell membranes to create an aligned polarity field, termed planar cell polarity (PCP; Goodrich and Strutt 2011). In the *Drosophila* wing, for example, transmembrane protein

members of the core polarity pathway become confined to opposite poles of the cell, where they interact with members of neighbouring cells of the opposite polarity. In this way cell polarities can become aligned across regions of the wing. It is possible that morphogens such as Dpp and Wnt help to align the PCP across the whole wing (Goodrich and Strutt, 2011).

### 1.3.2.3 Stress-Based Organisation

It is thought that microfibril and microtubule conformations align parallel to the orientation of the highest amount of stress, allowing the cell to better resist these stresses (Hamant et al., 2008). Thus, stress fields may provide a means to align cell orientations across a tissue.

In plants, the predicted stress field around the SAM correlates with the orientations of microtubules (Hamant et al., 2008). In addition, it has been shown that changes in the main orientation of stress through SAM compression result in ectopic leaf outgrowth (Pien et al., 2001). In the *Drosophila* wing, polarity orientations shift to align with the proximodistal wing axis after the pupal stage due to the anisotropic tension created by the contraction of the hinge region of the wing (Aigouy et al., 2010). This tension changes the patterns of cell flow, shear and rotation. In a tissue culture experiment, HeLa cells were shown to orient their cell division axes according to external forces (They et al., 2005).

For a stress-based system, the extent of alignment across a tissue depends largely on the tissue topology. For instance, stress-patterns and microtubule orientations differ regionally across the SAM according to the complex SAM geometry (Hamant et al., 2008).

It is possible that different alignment mechanisms act together to orientate the whole tissue. For instance, it appears that in the *Drosophila* wing, global alignment is a result of cell-cell communication, morphogen signalling and long-distance force transmission (Aigouy et al., 2010; Mammoto and Ingber, 2010).

A difference between the mechanisms of organisation discussed is the type

of information provided. In a stress-based system, the stress field provides cells with *orientation*, which can be denoted by  $\longleftrightarrow$ . In systems with a morphogen gradient or cell-cell communication, cells are provided with different information at their two ends. Thus, in addition to orientation these systems also provide *direction*, which can be denoted by  $\rightarrow$ .

### 1.3.3 Regulation of Tissue Orientation

It has been discussed how cell orientations can be aligned across a tissue. However, there are different ways in which this alignment can be coordinated during development.

It is generally thought that appendage growth is guided by orthogonal organising systems, where axes intersect at right angles (Niehrs, 2010) and in two-dimensions determine the orientation of maximum growth (along one axis of the system) and minimum growth (along the second axis). This is supported by the arrangement of microtubules, which result in an axis of major (perpendicular to the microtubule alignment) and minor growth (parallel to the microtubule alignment; Baskin 2005; Traas and Hamant 2009).

However, it is unclear if orientations of orthogonal organising systems are maintained with tissue deformations resulting from growth (Fig. 1.3A). For instance, assuming that early on in development cells have a proximodistal orientation (Fig. 1.3B), this orientation could either be maintained irrespective of changes in tissue geometry (Fig. 1.3C) or reorientate during development. If the field reorientates, it is possible that this is simply a result of changes in the tissue geometry, which deforms the polarity field (Fig. 1.3D). In this case, polarity fields may be established early in development, after which cells become unresponsive to further polarity signals. Alternatively, cells may remain responsive to repolarisation signals, which may act during development (Fig. 1.3E).

Thus, there are a number of different ways in which the growth orientations of an organ may be organised over time. In the *Drosophila* wing PCP orientations deform locally with the tissue (Aigouy et al., 2010), while clonal analysis in the *Antirrhinum* petal revealed a maintenance of the orientation of growth throughout development (Rolland-Lagan et al., 2003).

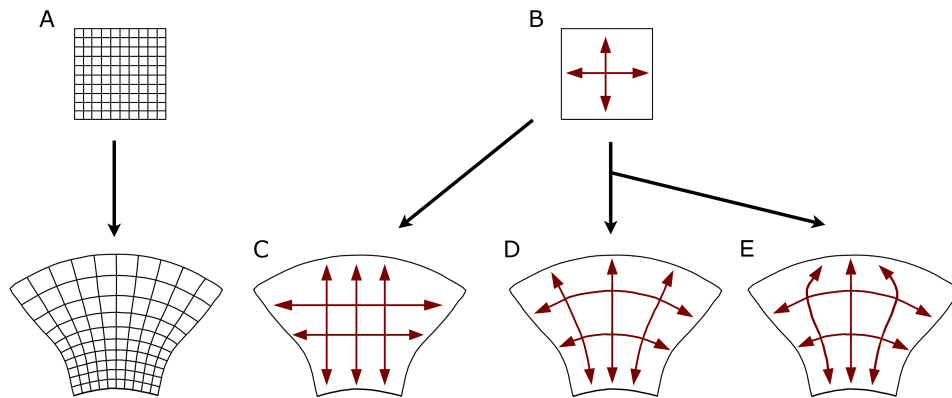


**Figure 1.3** **A**, an initial square is deformed by non-uniform anisotropic growth rates. **B**, initially the underlying polarity system is orthogonal to the geometry of the square. During growth these orientations can either **C**, be maintained, **D**, deform with the geometry of the canvas or **E**, reorientate according to new organising signals.

### 1.3.4 Leaf Polarity

The establishment of the three axes of leaf growth are still poorly understood and it is therefore unclear how leaf growth is organised based on the possible tissue organisation mechanisms discussed above.

#### 1.3.4.1 Proximodistal Axis

Several pieces of evidence suggest that the leaf primordium is polarised during or shortly after initiation. For instance, leaf primordium growth is anisotropic almost from initiation (Kwiatkowska and Dumais, 2003). In addition, the auxin efflux carriers PIN1 are located at the distal membranes of cells of the young primordium (Reinhardt et al., 2000; Scarpella et al., 2006), indicating that cells have a notion of polarity from a young leaf age. Recently it has been shown that cell files alter their growth orientation to grow towards sites of new PIN1-guided auxin maxima at the leaf margins (Kawamura et al., 2010). However, it is not clear if the distribution of auxin and PINs establishes a polarity field or whether these are merely indicators of an underlying polarity field. It has been suggested that PIN1 localisation is determined by the auxin concentration in neighbouring cells (Friml and Palme, 2002; Jönsson et al., 2006; Sauer et al., 2006; Smith et al., 2006) and that auxin guides microtubule

patterns (Zandomeni and Schopfer, 1993). In addition, PIN1 localisations in the meristem correlate with the stress field, suggesting that mechanical signals may provide orientation information (Hamant et al., 2008). If auxin or PINs are involved in the establishment of leaf polarity, they are likely to coordinate proximodistal polarity, based on the distribution of PIN1 in the primordium (Scarpella et al., 2006).

#### 1.3.4.2 Ad/abaxial Axis

In addition to the proximodistal axis, the ad/abaxial axis, which is oriented from the top to the bottom leaf surface, is determined early on. There is a wealth of genetic evidence in *Arabidopsis*, which shows that the ad/abaxial axis is specified by the polar expression of two main gene families that antagonise each other. The class III homeodomain leucine zipper (HD-ZIP III) family members are located adaxially, while *KANADI* (*KAN*) family members are expressed abaxially. Leaves that are partially disconnected from the SAM by an incision at the early primordium stage are abaxialised (Reinhardt et al., 2005). This suggests that the default state of the primordium is abaxial and that adaxial identity emanates from the SAM (Reinhardt et al., 2005). Performing the same surgical experiment after primordium initiation has no effect on ad/abaxial patterning. Thus, ad/abaxial identity appears to be established early on and must be self-maintainable in the absence of the meristem (Snow and Snow, 1959).

The establishment of ad/abaxial identity is generally referred to as polarity. However, while the distribution of ad/abaxial patterns could be viewed as a polar distribution, it differs from the definition of polarity described here, where polarity confers orientation rather than identity with two tissue poles.

It is not clear to what extent these ad/abaxial polarity factors have a graded distribution, according to which cells could orientate their growth. The *HD-ZIP III* gene *PHABULOSA* (*PHB*) has a graded distribution in the plant embryo (McConnell et al., 2001). It has been proposed that a meristem-derived signal activates *PHB* in the early primordium (McConnell et al., 2001). Regions closer to the SAM would receive a higher concentration of this signal

and therefore produce PHB at a higher rate. Positive feedback of PHB on its own production then maintains a high signal of PHB on the adaxial surface as well as a graded distribution as regions grow away from the SAM (McConnell et al., 2001). However, the validity of this hypothesis has not been tested, yet.

Thus, while a large number of studies have revealed the processes involved in patterning along the ad/abaxial axis, little is known about how these factors coordinate growth.

#### **1.3.4.3 Mediolateral Axis**

Ad/abaxial identity is also important in the formation of the mediolateral axis. Up or downregulation of either *HD-ZIP III* or *KAN* genes results in leaves with largely adaxial or abaxial identity (Eshed et al., 2001; McConnell et al., 2001). In the most extreme cases, identity loss results in needle-like radial leaves (Eshed et al., 2001, 2004; McConnell and Barton, 1998; Waites and Hudson, 1995). These observations lead Waites and Hudson (1995) to propose that the juxtaposition of adaxial and abaxial identity is necessary for growth along the mediolateral axis. This theory is supported by the observed ectopic outgrowths in mutants where patches expressing adaxial identity genes are expressed on the abaxial epidermis (Eshed et al., 2001).

Although ad/abaxial polarity seems to be largely established by HD-ZIP III and KAN, it appears that abaxial expression of the *YABBY* (*YAB*) transcription factor family is necessary for growth of the mediolateral axis (Eshed et al., 2004). *YABs* are downstream of *KAN*. They are immobile, but have non-autonomous short-range effects (Goldshmidt et al., 2008).

#### **1.3.4.4 Leaf Axes Interactions**

The effect of disruption of ad/abaxial identity on growth along the mediolateral axis clearly shows that growth coordination of the leaf axes is linked. In addition, severe ad/abaxial defects also disturb the proximodistal axis (Waites et al., 1998).

There are several studies that showed a link between auxin and ad/abaxial identity. For instance, disruption of polar auxin transport results in thicker

leaves with disturbed abaxial identity (Borghi et al., 2007; Reinhardt et al., 2000). The AUXIN RESPONSE FACTOR family of transcription factors is known to promote *YAB* expression (Kidner and Timmermans, 2007; Pekker et al., 2005), while KANs regulate several genes involved in auxin metabolism and response (Wu et al., 2008). In addition, the auxin importer AUX1 is specifically localised on the abaxial epidermis of the leaf primordium (Reinhardt et al., 2003).

In principal, since the proximodistal and ad/abaxial axes are orthogonal to each other, the specification of these two axes is sufficient to uniquely establish growth along three axes (Shraiman, 2005).

#### 1.3.4.5 Leaf Polarity Maintenance

The three axes of leaf growth not only have to be established but also maintained during development. The maintenance of an auxin maximum at the leaf tip throughout development suggests that the proximodistal axis is specified throughout growth (Aloni et al., 2003). After leaf initiation, this maximum is at least partially maintained by auxin synthesis at the tip mediated through *YUCCA* genes (Zhao, 2008).

Ad/abaxial polarity may be maintained by the mutual antagonism between the adaxial HD-ZIPs III and abaxial KANs. In addition, adaxial expression of *HD-ZIP III* genes is thought to remain high on the adaxial side by the positive feedback of PHB on its own production (McConnell et al., 2001). Moreover, HD-ZIP III are negatively regulated by miR165 and miR166 on the abaxial side (Bao et al., 2004).

How these genetic interactions lead to the establishment and maintenance of polarity is still unknown. The observation that leaf microtubule arrangements switch from a mostly mediolateral orientation to a proximodistal orientation during growth (Sainsbury et al., 2008), suggests that growth orientations change during development.

## 1.4 Leaf Shape, Growth and Polarity

Possible mechanisms of growth and polarity coordination have been discussed. The relative importance of these two processes in leaf morphogenesis is, however, unclear. For instance, during the early stages of leaf primordium development, growth is highly anisotropic (Kwiatkowska and Dumais, 2003), while at later stages leaves are thought to grow more isotropically (Baskin, 2005; Boudaoud, 2010).

It is possible that these interactions within the plane of the leaf are sufficient to generate the 3D leaf shape. 3D bending might be facilitated by the preferential growth parallel to the leaf plane, rather than perpendicular to it, which causes the leaf to become thinner relative to its surface area with time (Pyke et al., 1991). These changes in dimensions are likely to affect the bending properties of the leaf (Hufnagel et al., 2007). Alternatively, the 3D shape might be controlled more actively by, for instance, differential growth rates on the two surfaces. There are many genes that are expressed on either the adaxial or abaxial surface of the leaf (Kidner and Timmermans, 2007), suggesting that growth patterns on the two surfaces might differ.

Apart from the development of the overall leaf shape, there are other morphogenetic events that contribute to leaf development. For instance, simple leaves like those of *Arabidopsis* develop serrations along their proximal margins. Experimental studies suggest that both growth (Bilsborough et al., 2011; Blein et al., 2008; Larue et al., 2009; Nikovics et al., 2006) and polarity (Bilsborough et al., 2011; Kawamura et al., 2010) are involved in the establishment of these serrations. Since serrations develop a few days after leaf initiation, their development indicates that growth or polarity patterns are not fully established at leaf initiation. Although a number of genes are known to affect margin serrations, the mechanisms underlying serration formation are still unknown.

To explore leaf shape development, we need a way to test how gene expression can change shape in the context of physical constraints.

## 1.5 Modelling Development

It is clear that shape development is highly complex, involving coordination of growth and polarity on a range of scales, such as across a whole tissue and within single cells. Biochemical factors are likely to play a major role in the control of shape development, whilst being constrained by physical factors. It is also possible that physical factors are involved more directly in growth and polarity coordination.

With such complexity it is difficult to decipher the core mechanisms underlying a given developmental process. In addition, with an increasing knowledge of developmental dynamics, mathematical formulations of growth are becoming more complex, involving non-linear equations, which cannot be solved analytically. Therefore, computational modelling is increasingly employed to test whether hypothesised or experimentally measured interactions can account for developmental observations. Even when the genetic and physical factors of a developmental process are known, the expected outcome as a result of factor interactions is often non-intuitive. For instance, computational studies have shown that higher growth rates at the margins of a tissue compared to the centre can lead to tissue buckling, similar to the phenotype observed for many flowers and leaves (Liang and Mahadevan, 2009, 2011). Measurements of the growth rates of lily petals revealed a higher growth rate at the margins compared to the centre (Liang and Mahadevan, 2011). Thus, models can show how particular growth patterns may deform a tissue. Alternatively, by starting with a particular geometry, it can be shown how shape may feed back on patterning. For instance, computational analysis of lateral root formation has shown that root primordia are more likely to form at sites, where the main root is curved (Laskowski et al., 2008).

### 1.5.1 Modelling Tissues

With an increasing recognition for the need of computational analysis in biology, the number of computational tools adapted to understand questions on various scales is also increasing (reviewed by Kumar and Bentley, 2003). In general, computational limitations restrict the extent to which these scales

can be combined into unified models.

In models of tissue dynamics, tissues are either treated as discrete or continuous systems. In discrete systems, the tissue is regarded as a collection of discrete entities, which in models of biological tissues generally represent cells. In continuous systems, in contrast, the tissue is treated as a continuum. For computational purposes this continuum is discretised into smaller regions for which ordinary differential equations can be formulated and solved mathematically (Brodland, 1994; Zienkiewicz, 1983). Biologically, modelling the tissue as a mechanical continuum assumes that there are few cell rearrangements, which is generally a valid hypothesis in plant growth and to some extent in animal growth (Greenberg, 1996; Hufnagel et al., 2007).

These two types of model are each adapted for different purposes. To model biological cell behaviours, such as cell division, cell differentiation or cell rearrangements, discrete systems are more appropriate. For example, a discrete model is suitable for modelling morphogenesis of the slime mould *Dictyostelium discoideum*, which involves cell rearrangements to form clusters with cells of similar identity (Marée et al., 1999). In addition, discrete systems are suitable when dealing with subcellular processes and situations where the realistic cell shapes are important. For instance, in models of planar cell polarity, coupled cells directly communicate at their membranes. This requires cells to express polarity genes in their correctly oriented and shaped membranes (Aigouy et al., 2010; Amonlirdviman et al., 2005; Axelrod and Tomlin, 2011). Similarly, auxin transport involves the polar distribution of PIN proteins at the cell membranes (Friml and Palme, 2002). Thus, models of auxin transport are generally discrete (Grieneisen et al., 2007; Jönsson et al., 2006; Smith et al., 2006; Stoma et al., 2008; Wabnik et al., 2010). However, realistic auxin patterns have also been generated by a continuous implementation (Newell et al., 2008).

In general, continuous formalisms are adapted for modelling biological systems on the tissue scale. For instance, the finite element method (FEM) is a continuous formalism and has been used to model tissue dynamics in a wide

variety of biological systems such as invagination in the *Drosophila* embryo (Conte et al., 2008) or *Antirrhinum* flower development (Green et al., 2010). But it is also possible to model growth of single cells, such as growth of pollen tubes in plants (Bolduc et al., 2006; Fayant et al., 2010).

The difference between these two approaches is not always apparent, as continuous systems may be discretised into cell-like structures. For instance, in mass-spring models, the continuous system is divided by point masses that are linked by springs. Mass-spring models of biological tissues generally use the point masses to represent cell junctions or points on a cell wall, while springs represent cell walls (De Boer et al., 1992; Rudge and Haseloff, 2005).

The choice of model formalism used also depends on the tissue properties to be investigated. While mass-spring models are mainly limited to two-dimensional sheets (Kennaway et al., 2011; Traas and Hamant, 2009), FEM treats tissues as solids with a non-negligible thickness and is therefore more appropriate for modelling volumes.

## 1.6 This Work

The vast number of partially redundant developmental genes and pathways (Gonzalez et al., 2010; Horiguchi et al., 2006a) and the difficulty to study the effect of genetic perturbations (Barkoulas et al., 2007; Gonzalez et al., 2010) demonstrate the need for a simplified system to understand leaf development. Therefore, in this work, combinatorial models of growth and polarity factors are presented with the aim to elucidate leaf shape development based on experimentally measured growth dynamics and in the context of physical constraints.

To really understand how leaf growth and polarity patterns are established and maintained, a description of leaf growth is needed. While leaf growth studies have either concentrated on leaf primordium outgrowth from the SAM (Kwiatkowska and Dumais, 2003) or on leaf growth at late stages (Avery, 1933; Erickson, 1966; Schmundt et al., 1998; Wolf et al., 1986), a description of leaf growth during the period in which the characteristic leaf shape is established is still lacking.

In the past, growth rate and orientation have been measured by time lapse imaging (Richards and Kavanagh, 1942; Schmundt et al., 1998; Wolf et al., 1986) and clonal analysis (Green et al., 2010; Rolland-Lagan et al., 2003). Here, time lapse imaging was used to measure growth rates and growth orientations of the *Arabidopsis thaliana* rosette leaf 1 during the early stages of leaf development. In addition, leaf growth orientations were visualised using clonal analysis.

Computational models of leaf growth were generated using a recently developed framework, termed the Growing Polarised Tissue (GPT) framework (Kennaway et al., 2011). A central idea of this framework is the ability to study the effects of growth and polarity on tissue deformation independently. Computationally this framework has been implemented in a toolbox, called *GFTbox*, in MATLAB and is based on FEM. In this implementation, the tissue is treated as a continuum. This approach has been chosen, as it allows organ deformations to be studied on a tissue scale without having to consider the vast increase in cell numbers during development.

This work aims at understanding the general mechanisms underlying observed shape and size changes during development by identifying the minimum components necessary to generate observed leaf shapes. Using this toolbox, it will be shown how growth and polarity dynamics, together with mechanical constraints resulting from growth of a connected tissue, affect the generation of the 2D and 3D leaf geometry. In addition, the processes underlying changes in the leaf margin structure, such as serration development and margin buckling will be investigated.

## Chapter 2

# Leaf Growth and Polarity

### 2.1 Introduction

Despite their versatile shapes, appendages develop from morphologically similar small buds made up of few cells. From these buds, the distinct shape of different appendages develops through interacting systems of growth and polarity. How these systems are controlled is, however, unclear.

For instance, it is possible that growth patterns, specified by genetic activities, are established early in development and determine organ growth patterns throughout development. Alternatively, organ shape might underlie changes in growth patterns at each developmental stage.

Apart from the correct distribution of growth rates, organ development is likely to be guided by orthogonal polarity systems, which allow for anisotropic growth. It is possible that early established organising systems maintain their initial conformation throughout growth, irrespective of changes in tissue geometry, or that directions reorientate during development. Similar to growth rate patterning, organising systems may act early in development after which the tissue becomes unresponsive to further reorganisation signals. In such cases, directions may still deform with the tissue geometry. Alternatively, the polarity field may remain responsive to polarity reorganisation signals, which may act during development, and to changes in tissue geometry.

A previous study of petal growth in *Antirrhinum* has revealed that growth directions retain their proximodistal orientations throughout growth (Rolland-Lagan et al., 2003). Similarly, schematic representations have assumed that

leaf growth directions are independent from tissue geometry (Fleming, 2003; Tsuge et al., 1996). However, relatively little experimental and theoretical work has been conducted on this problem.

Here, development of *Arabidopsis* leaf 1 was studied to explore how these systems of growth and polarity are controlled in the leaf and interact to generate the shapes observed. The dynamics of growth were quantified by time lapse imaging. Leaf 1 is the first leaf to emerge from the *Arabidopsis* seedling and was therefore easily trackable. Time lapse imaging was performed over a period in which the young primordium-like leaf transforms into a shape close to its final characteristic leaf shape. The observed dynamics were used to generate a computational model of leaf development.

Although leaves are three-dimensional structures, they mainly grow along two axes (the proximodistal and mediolateral axes). To understand the mechanisms that drive the characteristic (flattened) leaf shapes, first leaf growth was studied in two-dimensions.

### 2.1.1 Model Validation

The ability of the leaf models generated here to correctly account for leaf development was tested by clonal analysis and leaf surgery.

An interesting growth phenomenon is the ability of appendages to regenerate after injury. For instance, amphibians such as salamanders show a great potential to regenerate their limbs at any stage during their life and development (reviewed by Yokoyama, 2008). Regeneration has also been observed in many other vertebrate and invertebrate systems (reviewed by Poss, 2010). Recently, it has been reported that leaves are able to regenerate after the distal half of the leaf is removed at early stages (Sena et al., 2009; Sugimoto et al., 2011). An accurate leaf model should therefore be able to replicate these regeneration results.

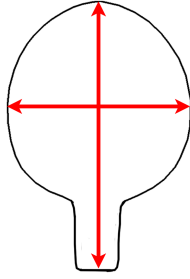


**Figure 2.1**  
Leaf dimensions were measured along the longest axes of the leaf (red arrows).

## 2.2 Results

### 2.2.1 Leaf Growth Dynamics

To investigate how the *Arabidopsis* leaf shape develops, it was first necessary to describe the timing and patterns of these shape changes. These descriptions also served as a reference for the computational leaf models.

Since the rate of growth and development differs slightly between different plants grown under the same conditions, the temporal changes in leaf dimensions were measured based on a number of leaves.

The overall length and width of leaf 1 (metamer 2) of *Arabidopsis thaliana* ecotype Landsberg *erecta* (*Ler*) was measured and analysed by Samantha Fox. Leaves from about 10 plants per day were removed from the plants, flattened and measured. Leaf length was measured across the longest axis of the leaf, from the petiole base to the distal tip (Fig. 2.1). Leaf width was measured across the widest point of the lamina (Fig. 2.1). Leaf dimensions,  $y$ , were recorded on a daily basis and a logistic curve was fitted to the data (Fig. 2.2A):

$$y = \frac{-A}{1 + e^{(t-t_m)k}} + A, \quad (2.1)$$

where  $A$  is final leaf size,  $t$  is time,  $t_m$  the time of inflection where half of the growth has occurred and  $k$  is the early exponential growth rate. This function was fitted to the datasets using least-squares minimisation (tool written by Pierre Barbier de Reuille) and then manually adjusted, as leaf dimensions during the younger stages, studied further in this work, were overestimated by the fitted curve (Fig. 2.2A). The best fitting parameter values for leaf length were  $A = 9.5 \text{ mm}$ ,  $t_m = 310 \text{ h}$  and  $k = 0.021 \text{ h}^{-1}$  and for leaf width  $A = 6 \text{ mm}$ ,  $t_m = 306 \text{ h}$  and  $k = 0.020 \text{ h}^{-1}$ . The times  $t$  and  $t_m$  were mea-

sured in hours after stratification. A better notion of the leaf age was gained by classifying leaves according to their age after initiation. The time of leaf initiation was calculated from the fitted curve, where it was assumed that the leaf primordium consists of two cells at initiation, which corresponds to an initial width of  $y \approx 0.02 \text{ mm}$ . Extrapolating the fitted logistic curve back to this primordium size revealed the time of initiation of leaf 1 to be 21  $h$  after stratification (Fig. 2.2A, inset). Therefore,  $t_m$  was adjusted to  $t_m = 289$  hours after leaf initiation for leaf length and  $t_m = 285 \text{ h}$  for leaf width. Both correspond to a leaf age of about 12 days after initiation (Fig. 2.2B).

Plotting the same data on a log scale revealed that leaf dimensions increased exponentially up to about day 6, after which growth slowed down (Fig. 2.2B, inset).

These measurements were compared to observed leaf shapes (Fig. 2.2B, green shapes). The smallest and largest leaf shapes present example leaves, whereas the three intermediate leaf outlines are average leaf shapes. Average leaf shapes were calculated by manually segmenting the leaf outlines of 10 to 25 leaves for each developmental phase. Equally spaced points were placed around the segmented leaf outlines from which the average leaf outline was calculated by Samantha Fox using a toolbox developed by Andrew Hanna (*Sector Analysis Toolbox*).

During the early periods of growth, the leaf developed from a young dome-shaped leaf to a more elongated leaf with a short petiole. After day 6, the lamina broadened so that around day 9 the leaf shape was close to the final one, but smaller. The leaf then mainly increased in size, in particular at the petiole, while the lamina roughly maintained its shape.

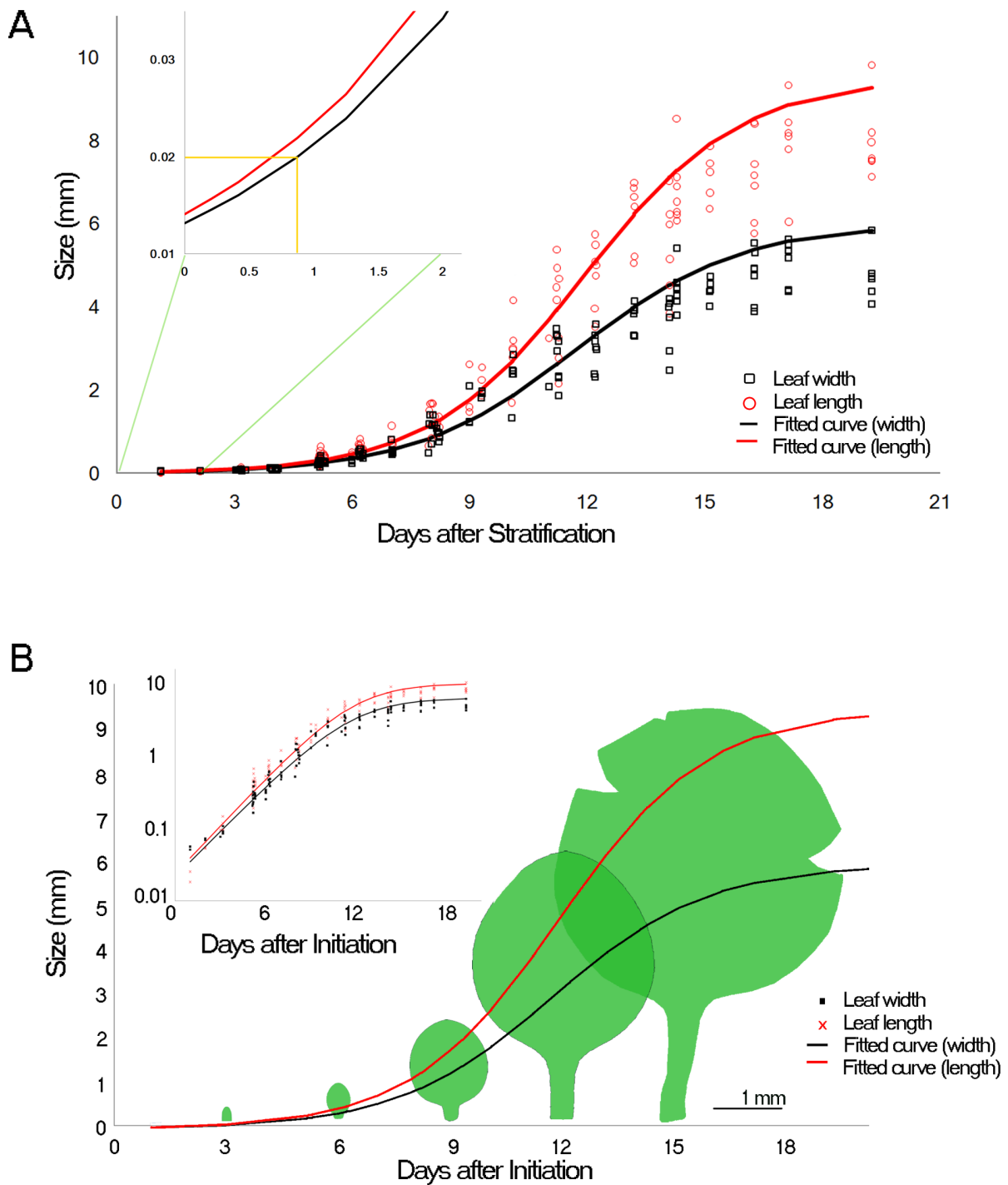


**Figure 2.2** Growth of *Arabidopsis thaliana* ecotype *Ler* leaf 1. **A**, leaf length and width at different days after stratification (data points). Logistic curves were fitted to the data (lines). Inset shows the logistic function extrapolated backwards to determine the time of leaf initiation at a leaf width of 0.02 mm (yellow lines). **B**, the same logistic curves fitted to leaf length and width as in **A** and plotted over days after initiation (lines). Example leaf shapes at different developmental stages (green shapes). Inset shows the same curves (lines) and the measured leaf length and width data (points) on a log scale. Scale bar 1 mm for green leaf outlines.

### 2.2.1.1 Ecotype Comparison

The above growth curves (Fig. 2.2) describe growth of the *Arabidopsis* ecotype Landsberg *erecta*, which was used for the growth studies presented in this work. Since gene expression constructs presented here were in the Columbia (Col-0) ecotype, growth of Col-0 leaves was also measured by Samantha Fox and myself. Col-0 width was compared to that of *Ler* (Fig. 2.3) and the same logistic equation (Eqn. 2.1) was fitted to the Col-0 data with,  $A = 5.3 \text{ mm}$ ,  $t_m = 242 \text{ h}$  (about 10 days after initiation) and  $k = 0.023 \text{ h}^{-1}$ . Thus, Col-0 leaf width increases slightly faster than that of *Ler*, but growth decelerates earlier as well, so that the final leaf width of Col-0 is slightly smaller than that of *Ler*.

The growth analyses allowed leaves to be classified according to their width. This meant that for all further growth analyses leaves could be chosen that had a comparable width, which corresponded to the expected width at their age. In addition it has been shown here that different *Arabidopsis* ecotypes may differ in their growth dynamics, which has to be taken into account when comparing leaves from different ecotypes.

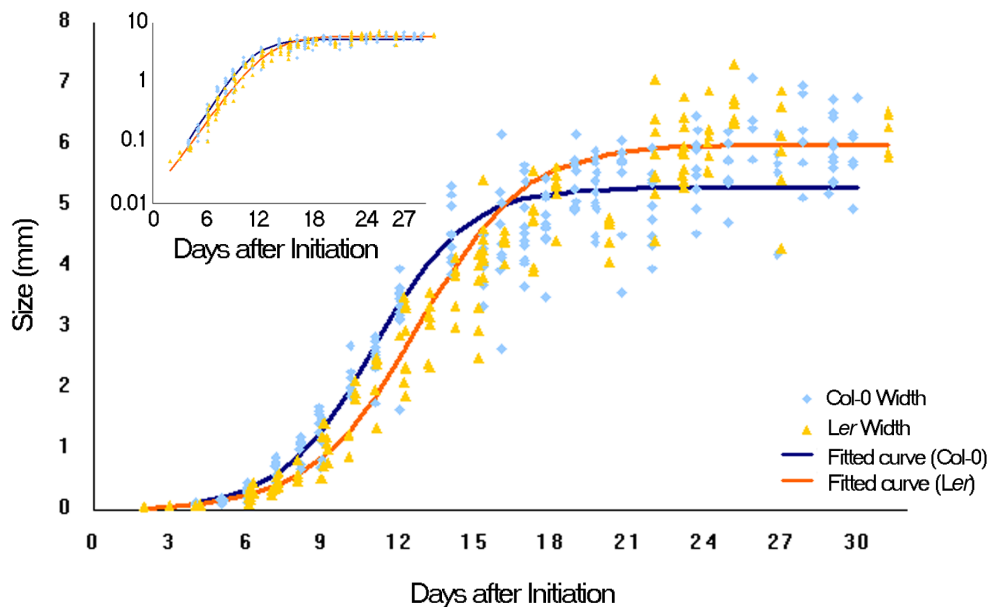


**Figure 2.3** Leaf width of *Arabidopsis thaliana* ecotypes *Ler* and Col-0 (points) with the fitted logistic curves (lines) over days after initiation. Inset the same data and curves shown on a log scale.

## 2.2.2 Measuring Local Growth

The growth analyses above describe leaf growth as a change in overall dimensions and thereby limit the problem to one-dimension. However, overall geometrical changes may not be an accurate description of growth when the underlying growth dynamics are non-uniform and therefore differ between regions (Richards and Kavanagh, 1942). A better description of dimension changes is gained by subdividing a one-dimensional structure into smaller segments based on identifiable marker points (Fig. 2.4A, orange and blue points). Growth along the dimension can then be calculated by the displacement of these markers over space with respect to time (Fig. 2.4). Displacement per unit time is the velocity,  $V$ . The velocity of a point is described as:

$$V = \frac{x_{t+\delta t} - x_t}{\delta t}, \quad (2.2)$$

where  $x$  is position of the point,  $t$  is time and  $\delta t$  is the time interval. Since the displacement of a point in a structure is not only determined by the point's own velocity but also the velocity of neighbouring points, velocity is generally calculated relative to a point of reference (Hejnowicz and Romberger, 1984). Once the velocity of each point is known, a change in the length of each segment,  $L$ , which lies between a set of neighbouring points (Fig. 2.4, green and purple bars), can be calculated by the difference in velocities of the two points:

$$\frac{dL}{dt} = V_{i+1} - V_i, \quad (2.3)$$

where  $i$  refers to a point.

This discretisation of space along an axis increases the accuracy with which growth can be measured. However, on the multidimensional leaf, points may not be displaced strictly along one dimension. A more accurate description of leaf growth would therefore involve discretising the whole leaf surface into smaller regions and measuring growth of each region separately. As above regions can be discretised by marker points that surround it. In the past, local leaf growth rates have been measured by the displacement of anatomical markers such as vein junctions (Erickson, 1966; Wolf et al., 1986) and artifi-

cial markers such as ink dots (Avery, 1933; Granier and Tardieu, 1999; Koehl et al., 2008; Peters and Bernstein, 1997) over time. Measuring growth by the displacement of points assumes that the only process displacing markers is due to growth (Hejnowicz and Romberger, 1984). This is generally a valid assumption in plants and in particular the leaf epidermis, where cell divisions are anticlinal and cell rearrangements are limited.

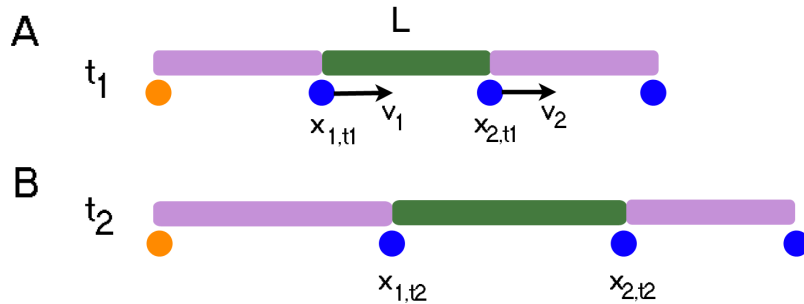


**Figure 2.4** Growth of a one-dimensional structure measured by the velocity,  $V$ , of marker points (orange and blue). The position of points at **A**,  $t_1$  and **B**,  $t_2$ . Velocity is defined as the displacement in space,  $(x_{t_2} - x_{t_1})$ , over a time unit,  $(t_2 - t_1)$ . Velocities were measured by aligning the structure at a position at the two time points (orange point). Placed points divide the structure into segments of size  $L$  (green and purple bars).

### 2.2.2.1 Tracking Leaf Growth

Spatial discretisation was employed in this work to obtain local leaf growth information. Plants were grown in a tracking chamber, which was placed under a confocal microscope and leaves were imaged at regular intervals by Samantha Fox and myself. Analysis of the tracking data was carried out by Samantha Fox. Growth was measured by the displacement of cell junctions, which were visualised in plants that constitutively express GFP or YFP in their plasma membranes (Fig. 2.5). This allowed leaf growth to be studied from an earlier age than would have been possible with external markers such as ink dots (Gor et al., 2006). The displacement of each cell junction over a given time interval was measured by manually placing points at the corresponding positions on confocal images showing the leaf at the beginning and end of the time interval studied (Fig. 2.5). Points were placed using software called *Point Tracker* written by Pierre Barbier de Reuille. This software was also used for the

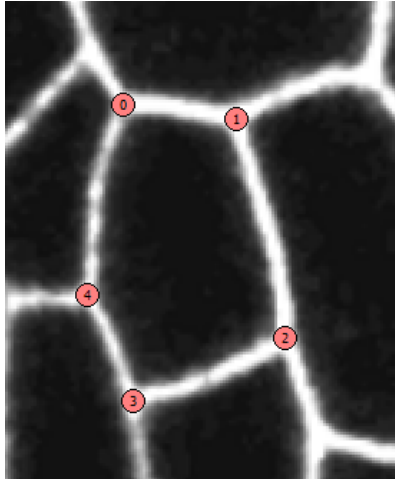


**Figure 2.5** Confocal image of a small region on a leaf. Cells express *pAR169* (YFP) in their plasma membranes. Cell junctions were marked using *Point Tracker* (red points). Image by Samantha Fox.

growth calculations.

Similar to previous studies (Avery, 1933; Erickson, 1966; Schmundt et al., 1998; Wolf et al., 1986), leaf growth was measured based on the epidermis only. The *Arabidopsis* leaf is made up of several cell layers, which, based on their their different properties (Pyke et al., 1991), are likely to also differ in their growth rates. However, to maintain the integrity of the tissue, layer expansions must be roughly similar. Thus, for simplicity, the abaxial epidermal layer was measured only.

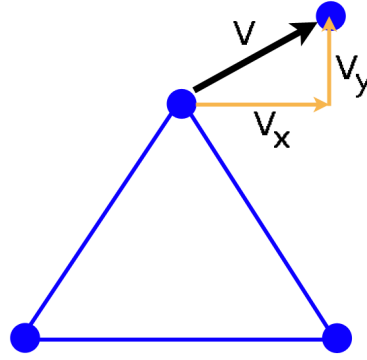
### 2.2.2.2 Growth Tensors

Above it was shown how growth of one-dimensional segments can be described by the velocities of marker points along one axis. In two-dimensions, these points define patches, which are deformed by point displacements. Thus, the deformation of the patch can be described by the change in velocity of the points (Feynman et al., 1965; Hejnowicz and Romberger, 1984; Silk and Erickson, 1979). The velocity of each point can be divided into the velocity components in the direction of the axes of reference  $V_x$  along the  $x$ -axis and  $V_y$  along the  $y$ -axis (Fig. 2.6). Then the rate of change of the velocities along the axis is expressed as:

$$\frac{\partial V_x}{\partial x} = V_{xx} \quad \frac{\partial V_x}{\partial y} = V_{xy} \quad \frac{\partial V_y}{\partial x} = V_{yx} \quad \frac{\partial V_y}{\partial y} = V_{yy},$$

where  $V_x$  and  $V_y$  are the velocity components in the direction of the  $x$  and  $y$ -axis, respectively. For double subscripts, the first subscript defines the axis

**Figure 2.6** Points in a small region are displaced at a velocity,  $V$  (black arrow), which has a component along the  $x$ -axis,  $V_x$ , and along the  $y$ -axis,  $V_y$  (yellow arrows).



of the velocity component and the second subscript the axis of reference.

Thus, in two-dimensions the deformation of a very small region of a tissue over a small time interval is fully described by these 4 partial derivatives ( $V_{xx}, V_{xy}, V_{yx}, V_{yy}$ ), which give the gradient of the velocity field and represent the growth tensor,  $T_{growth}$ :

$$T_{growth} = \begin{bmatrix} V_{xx} & V_{yx} \\ V_{xy} & V_{yy} \end{bmatrix}$$

In a tissue, such a growth tensor is associated with every infinitesimally small region, creating a growth tensor field. Here, the Cartesian coordinate system with  $xy$ -axes was used as a reference to calculate the growth tensor field. In principle, however, any set of orthogonal axes or coordinate system can be used (Feynman et al., 1965).

### 2.2.2.2.1 Estimating Growth Tensors

In practice, the ability of a calculated growth tensor to correctly describe the deformations of a tissue region depends largely on the spatiotemporal resolution chosen to calculate the tensor. In fact, the growth tensor is only accurate if the assumption holds true that growth within the region described is homogeneous. In general this means that the region has to be infinitesimally small.

A growth tensor describes the linear transformation of a region over time. Since velocity is a continuous variable that increases exponentially, tissue de-

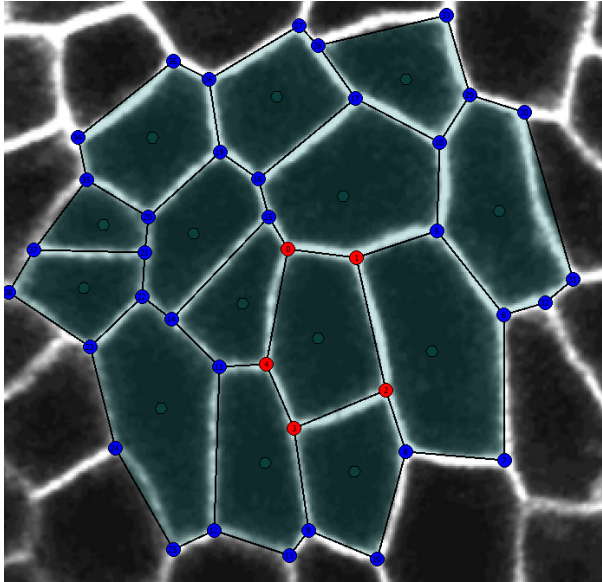


**Figure 2.7** Confocal image of a small region of a leaf. Cells express *pAR169* (YFP) in their plasma membranes. Points were placed on cell junctions and connected by edges to form a mesh using *Point Tracker* (blue and red points). Each cell area is defined by the points on the cell junctions surrounding it (red points) and the edges between these points. Image by Samantha Fox.

formations are not linear in time. Therefore, small time discretisations provide more accuracy.

#### 2.2.2.2.2 Cell Growth Tensors

The *Point Tracker* software, used to calculate the growth tensors, allows placed points to be grouped together and connected by edges, creating a connected irregular mesh (Fig. 2.7). The growth tensor of each cell is calculated as the gradient of the velocity field from the points defining the cell (Fig. 2.7, red points). However, despite their small size, growth within one cell is generally not homogeneous. This means, that it is normally not possible to describe the velocities of the cell-associated points by a single growth tensor. Therefore least-squares minimisation was used to determine the best fitting growth tensor for each cell.

#### 2.2.2.3 Growth Parameters

While the growth tensor fully describes the growth transformation of a small region, it is often desirable to consider certain aspects of this transformation only. These aspects or parameters of growth can be extracted from the growth tensor by singular value decomposition and constitute the growth rates, the main direction of growth and the rotation (Goodall and Green, 1986).

The growth rates define the amount of growth along the major,  $K_{max}$ ,

and minor,  $K_{min}$ , axes of growth of the region (Fig. 2.8A). These axes are always orthogonal to each other. In cases where growth is isotropic, which means that the region grows in all directions equally,  $K_{max}$  and  $K_{min}$  are the same. When growth is anisotropic  $K_{max}$  and  $K_{min}$  differ at an amount, which can be captured by the anisotropy. Here, the relative anisotropy is defined as  $\frac{K_{max}-K_{min}}{K_{max}}$ , however, other definitions of anisotropy can be used (Baskin, 2005). The sum of  $K_{max}$  and  $K_{min}$  is the areal growth rate,  $K_{area}$ .

When growth is anisotropic it is also interesting to know the orientation of the principal axis of growth, i.e. the orientation of  $K_{max}$ . This direction can be quantified as the angle between the axis and the external reference system (Fig. 2.8B).

Finally, even in the absence of growth regions may alter their conformation through rotation. This rotation angle is calculated as the angle between the previous orientation and the final orientation of a region (Fig. 2.8C).

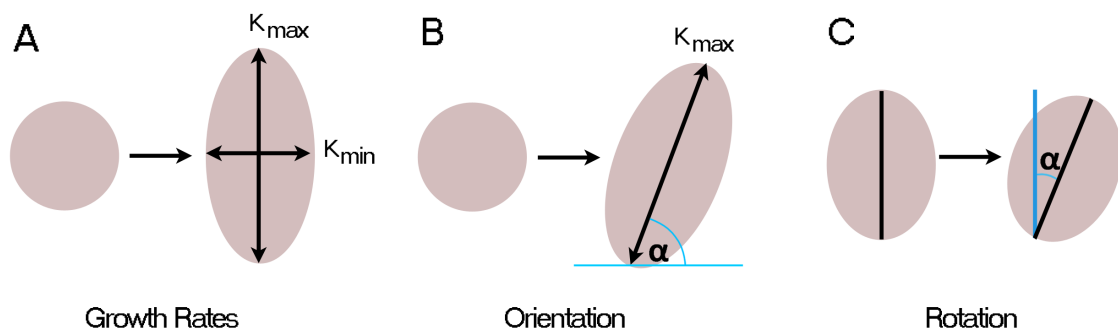


**Figure 2.8** The tensorial description of growth can be decomposed into the parameters of growth. These parameters of multidimensional growth each describe different geometric transformations of a region, here exemplified by a circle and an ellipse. **A**, growth of a region can be described by the growth rates along the major,  $K_{max}$ , and minor,  $K_{min}$ , axes. **B**, the orientation of major growth can be measured as the angle,  $\alpha$ , of the major axis of growth and an external axis. **C**, even without growth regions may alter their conformation through rotation by an angle,  $\alpha$ , relative to their previous orientation.

#### 2.2.2.4 Period of Tracking

The above sections describe the methods used to obtain regional measurements of the leaf growth parameters during periods of leaf development, in which the primordium-like leaf transformed into a shape close to the characteristic leaf shape. The overall growth analysis above (2.2.1 Leaf Growth

Dynamics) revealed that the main leaf lamina shape changes occur early in development within the first 10 days, confirming previous reports (Pyke et al., 1991). Therefore, time lapse imaging was carried out during this early period of development.

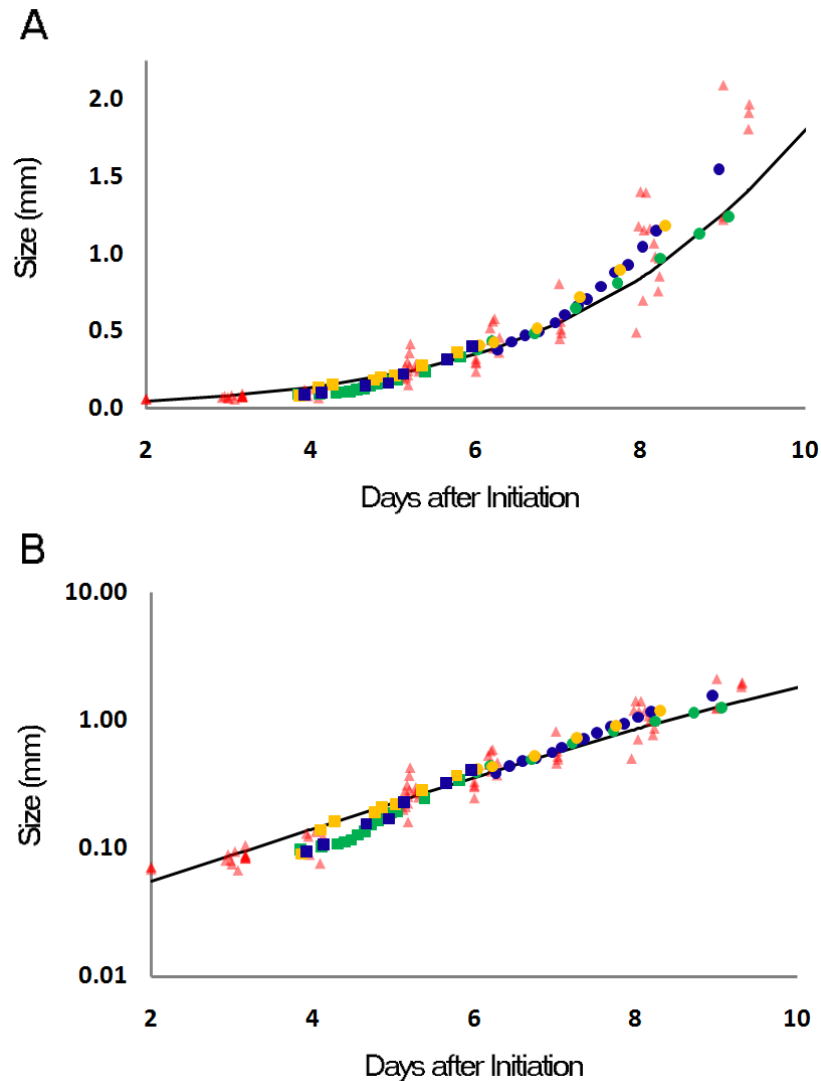


**Figure 2.9** Width comparison of leaves grown under standard growth conditions (pink triangles) and in the growth chamber (other colours). Individual tracked leaves are represented in green, blue and yellow with leaves tracked from day 4 to day 6 (squares) and leaves tracked from day 6 to day 8 (circles). The fitted logistic curve is also shown (black line). Leaf width was compared over the early stages after leaf initiation showing **A**, leaf width in *mm* and **B**, leaf width in *mm* on a log scale. Image by Samantha Fox.

To avoid prolonged plant exposure to the growth conditions in the tracking chamber, time lapse imaging was restricted to 2-3 day periods. Three plants were tracked from day 4 to day 6 and three plants from day 6 to day 9 after

leaf initiation. To allow comparison between tracked leaves, leaves of the right age (in days after initiation) were selected for tracking based on their width. According to the fitted logistic growth curve, leaves should be about  $85 \mu m$  wide at the end of day 3 and  $340 \mu m$  wide at the end of day 6.

Leaves tracked from day 6 to day 9 were initially slightly bigger than expected ( $410 \mu$  instead of  $340 \mu m$ ). They also grew faster than expected and reached a size of  $1.2 mm$  on day 8 (rather than day 9, as expected; Fig. 2.9). This discrepancy is likely to be due to the growth conditions of the tracking chamber, slight underestimations of leaf width by the fitted growth curve at later stages and natural developmental variations (Fig. 2.9; Pérez-Pérez et al. 2002).

The tracking data shown here is therefore based on leaves 4-8 days after leaf initiation, an interval that has received little attention in previous time lapse imaging studies. Previous studies concentrated mainly on either the very early leaf primordium stages (Kwiatkowska and Dumais, 2003) or on later stages, where the leaf was easily accessible but had already developed most of its final shape (Avery, 1933; Erickson, 1966; Schmundt et al., 1998; Wolf et al., 1986).

#### 2.2.2.5 Areal Growth Rates

Areal growth rates were extracted from the growth tensors calculated over  $24 h$  intervals (Fig 2.10). Due to the curvature of the leaf, marginal regions could not be imaged at high enough resolution for growth rates to be calculated accurately. In the method used, 3D  $z$ -stack images were compressed to 2D. Such compression results in loss of information in regions, where the leaf grew out of the plane, such as at the margins. Therefore, leaf growth was only tracked in the central regions, which were roughly parallel to the microscope objective.

During leaf growth the number of cells increases and the leaf blade becomes flatter. Therefore, it was possible to track more cells at later stages than earlier ones. While the number of placed points at the beginning and end of one growth interval had to be the same, it was possible to add additional points at new cell junctions in subsequent intervals. This is indicated

by the red outlines (Fig 2.10A, B and D), which represent the area that was trackable at the beginning of an interval to generate the output at the end of that interval. At later stages, when cell areas were small compared to the area of the leaf, growth was calculated over a small number of cells rather than for each cell individually (Fig. 2.10D and E).

Areal growth rates showed a proximodistal gradient over the leaf at all stages, which decreased distally (Fig. 2.10). These results agreed well with those observed previously for later stages of leaf development (Avery, 1933; Erickson, 1966; Schmudt et al., 1998; Wolf et al., 1986) and by clonal analysis (Dolan and Poethig, 1998; Poethig and Sussex, 1985). Areal growth rates were low in the midvein and higher towards lateral regions. Rates remained high in the proximal lateral regions throughout the period analysed.

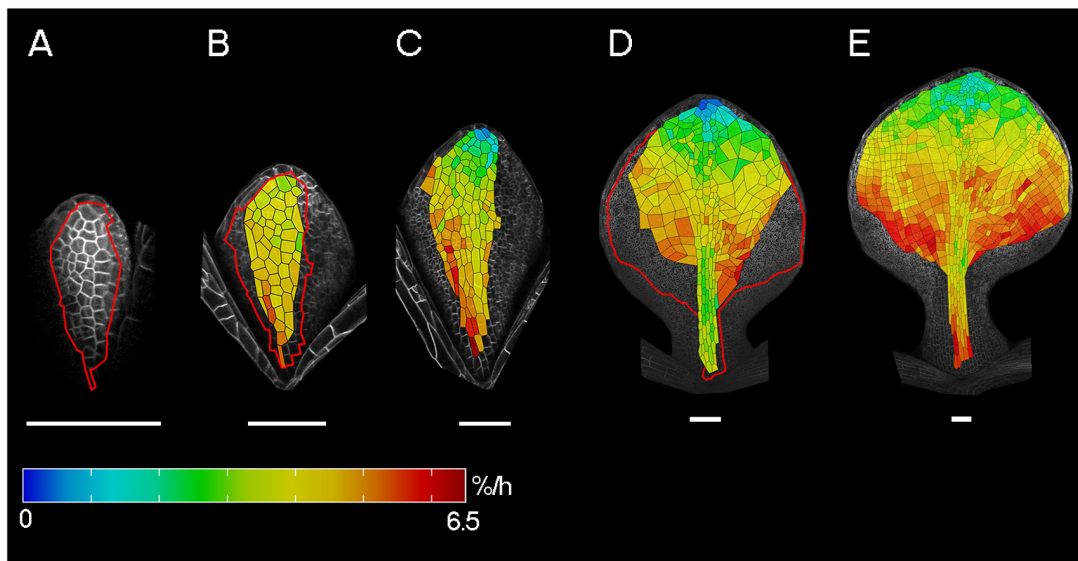


**Figure 2.10** Time lapse imaging of two leaves showing areal growth rates calculated over 24 *h* intervals. **A-C**, leaf tracked from day 4 to day 6 showing **A**, the leaf at the start of time lapse imaging (day 4). The red outline indicates the region that was suitable for growth calculations, displayed on **B**. **B**, the leaf on day 5 showing growth from day 4 to day 5. The red outline indicates the region that was suitable for growth calculations during the subsequent interval displayed on **C**. **C**, the leaf on day 6 with areal growth rates calculated from day 5 to day 6. **D-E**, leaf tracked from day 6 to day 8 showing **D**, the leaf on day 7 with areal growth rates calculated from day 6 (not shown) to day 7. The red outline indicates the region tracked to calculate growth rates over the next interval displayed on **E**. **E**, the leaf on day 8 showing areal growth rates calculated from day 7 to day 8. Image by Samantha Fox. Scale bars 100  $\mu m$ .

### 2.2.3 Growth along the Midline

The measured overall leaf size changes together with more detailed tracking results provided a good description of leaf growth and allowed the main questions of this work to be addressed. Namely, how is leaf growth controlled to yield these patterns and how do these growth patterns generate the leaf shapes observed?

To answer the first of these questions, it is necessary to get a better idea of the shape of the growth profiles. For instance, the coloured heat map of areal growth rates does not readily reveal whether growth rates drop linearly with leaf length or underlie an alternative trend. Therefore, for the same leaves and intervals depicted above the growth rate profiles along the leaf midline were extracted and plotted over leaf length.

#### 2.2.3.1 Midline Growth Parameter Extraction

The leaf midline was defined as the longest leaf axis and was in line with the petiole. Cells in this midline region were selected manually (Fig. 2.11). The tracked cell junction positions, as stored by *Point Tracker*, were used to calculate the areal growth rates as well as growth parallel to the midline and perpendicular to it using several scripts written by Pierre Barbier de Reuille, Sarah Robinson and myself.

In each case the leaf midline axis was defined by two points that lie on the axis (Fig. 2.11A, yellow points and white line). This midline axis together with the centroid position of all midline cells was then rotated to be parallel to the  $y$ -axis. The position of each cell was determined as the distance from the petiole-lamina boundary along the  $y$ -axis. Differences in the position along the  $x$ -axis were small compared to those on the  $y$ -axis and were ignored.

In several instances the leaf midline did not grow perfectly straight (Fig. 2.11B). In these cases the leaf was divided into smaller segments, for each of which the midline axis was determined separately in the same way as above (Fig. 2.11B, yellow points). The sum of all these midline segments presents the total leaf length (Fig. 2.11B, white lines). For each cell or small region, growth rate components parallel,  $K_{ml}$ , and perpendicular,  $K_{lat}$ , to the aligned

midline were extracted from the calculated growth tensor field.

### 2.2.3.2 Midline Growth Results

Due to variability of growth rates in the leaf petiole (most likely an artifact of the growth conditions in the tracking chamber), results are shown for the lamina midline only.

At early stages, areal growth rates,  $K_{area}$ , decreased approximately linearly with distance from the lamina base (Fig. 2.12A i). While growth rates became more uniform in proximal regions, rates declined steeply in distal regions (Fig. 2.12A ii). These trends were maintained, but growth rates in proximal regions decreased relatively uniformly, while central regions maintained high rates (Fig. 2.12A iii). At the end of the developmental period analysed, growth rates in the proximal and central regions became more uniform again, but remained slightly lower at the tip (Fig. 2.12A iv). To gain a clearer picture, areal growth rates were divided into growth rates along the midline axis,  $K_{ml}$  (Fig. 2.12B), and growth rates perpendicular to this axis, the mediolateral axis,  $K_{lat}$  (Fig. 2.12C).

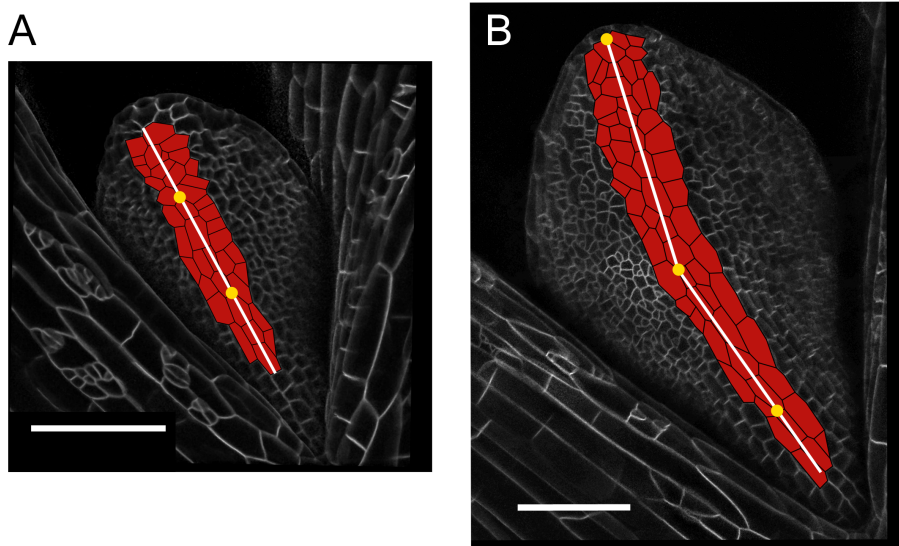


**Figure 2.11** Growth rates along the midline were calculated by selecting tracked cells in the midline region (red). **A**, the midline axis (white line) was identified by two tracked points (yellow points) that lie on it. **B**, in cases where the leaf had no straight midline axis, several axis segments were identified (white lines) by points that lie on them (yellow points). The angles of these axes were used to align the midline with the  $y$ -axis. Scale bars 100  $\mu m$ .

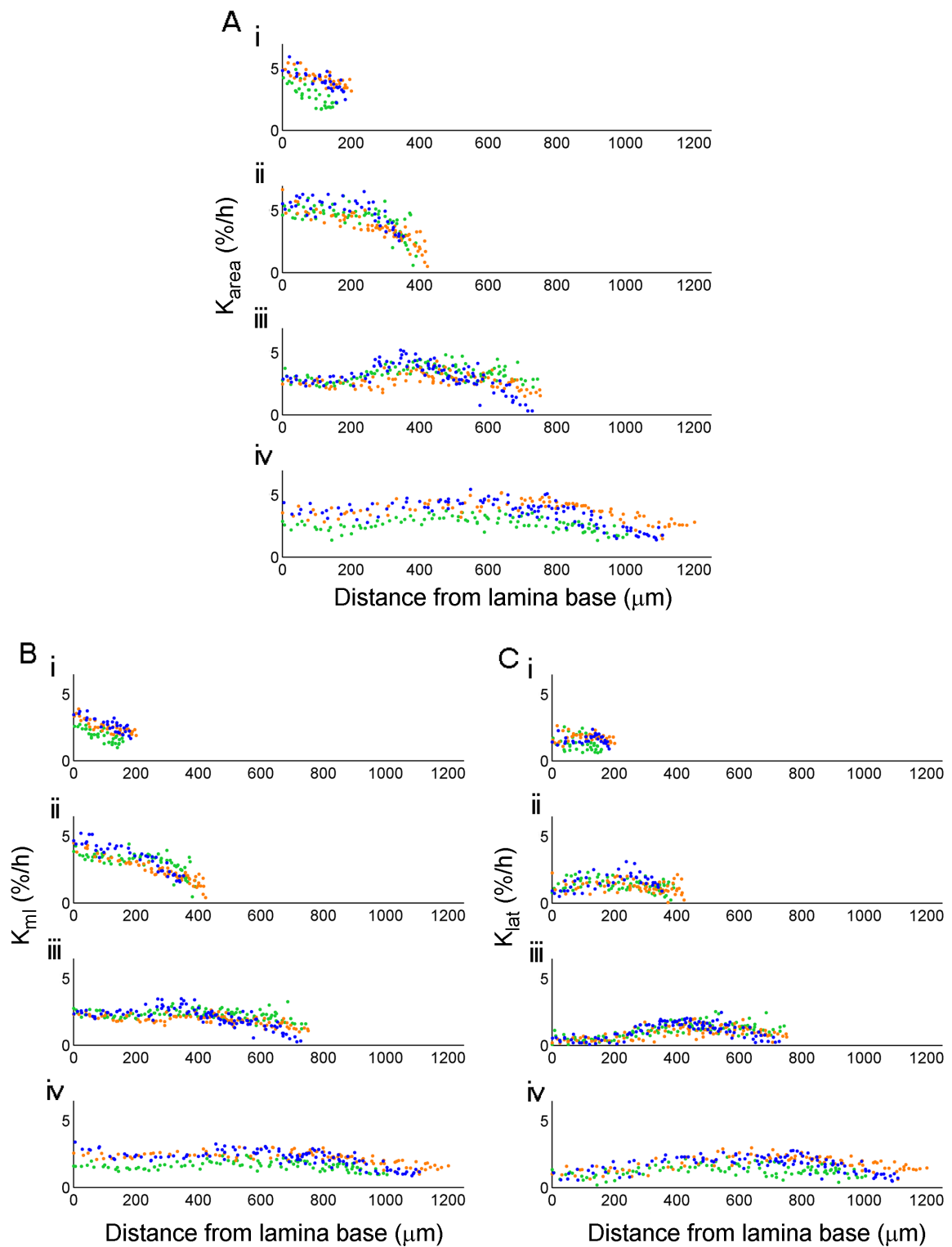


**Figure 2.12** Tracking results for 6 leaves for which growth rates along the lamina midline were calculated over 24  $h$  intervals. Growth was calculated as **A**, areal growth rates ( $K_{area}$ ), **B**, growth rates along the lamina midline ( $K_{ml}$ ) and **C**, growth rates perpendicular to the midline, in the mediolateral direction ( $K_{lat}$ ). Colours represent different leaves. Three leaves were tracked from day 4 to day 6, (i) day 4-5 and (ii) day 5-6. Three other leaves were tracked from day 6 to day 8, (iii) day 6-7 and (iv) day 7-8.

In general growth rates parallel to the midline were higher than those perpendicular to it (compare Fig. 2.12B and C). The higher  $K_{ml}$  compared to  $K_{lat}$  at early stages (Fig. 2.12B i, ii and C i, ii) may account for the elongated leaf shape observed above (Fig. 2.10C). The magnitude of both  $K_{ml}$  and  $K_{lat}$  decreased slightly over time across the leaf.

Similar to  $K_{area}$ ,  $K_{ml}$  decreased approximately linearly with distance at early stages and became more uniform in proximal regions at later stages, but maintained a steeper decline near the tip (Fig. 2.12B). In contrast, growth rates in the mediolateral direction,  $K_{lat}$ , were low at the distal tip at early stages and rapidly dropped in the proximal regions during development, so that highest rates were observed in the central regions of the midline (Fig. 2.12C). Thus, both  $K_{ml}$  and  $K_{lat}$  contribute to the low areal growth rates at the tip, whereas low proximal value of  $K_{area}$  can be attributed to  $K_{lat}$  alone. These low proximal growth rates correlate with the position of the midvein.

The dynamics of  $K_{ml}$  at the tip resembled those observed during cell proliferation arrest in the leaf, where a division arrest front initiates at the tip and progresses towards the leaf base (Donnelly et al., 1999; Sylvester et al., 1990). Interestingly, however, spatial differences in growth rates were evident throughout the organ from the beginning of the growth analysis, while at these early stages cell proliferation arrest appears to be largely confined to the very tip (Donnelly et al., 1999). This highlights the importance of measuring growth directly rather than inferring growth dynamics from cell division patterns (Green, 1976).

#### 2.2.4 Modelling Midline Growth

The more detailed analysis of leaf growth profiles along the midline revealed non-uniform spatiotemporal patterns, which have to be accounted for when wishing to explain leaf growth. Therefore, different hypotheses, that might account for these patterns, were tested using computational modelling.

Growth along the leaf midline was simulated by one-dimensional models in MATLAB. The starting shape of these models comprises a line, here termed the canvas, whose length of 100  $\mu\text{m}$  corresponds to the leaf length 3-4 days

after initiation. The line is made up of multiple segments of equal length,  $L_0$ , joined at vertices (Fig. 2.13), where each line segment grows by:

$$L(t) = L_0 e^{Kt}, \quad (2.4)$$

where  $K$  is the growth rate and  $t$  is time in hours.  $L$  is the new length of the segment after growth. In these models growth is driven by growth factors, which can either propagate, designated by  $\mathbf{s}_{FACTORNAME}$  for signalling, or retain fixed values for segments of the canvas, designated by  $\mathbf{i}_{FACTORNAME}$  for identity. It is assumed that factor levels do not dilute with growth and are uniform within each segment. Parameters values for all 1D models can be found in the Materials and Methods chapter (6.3.4 1D Models).

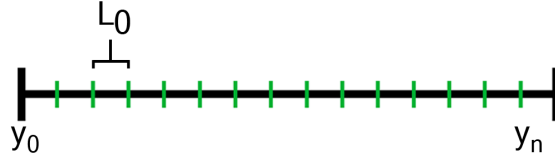


**Figure 2.13** The one-dimensional model starting line, here termed canvas, is discretised into 1000 segments. Fewer segments are shown on the example canvas presented here.  $L_0$  is the initial length of each segment and the starting position of each segment is denoted by  $y$ , where  $y_0$  is the position of the first (proximal) segment and  $y_n$  is the position of the last (distal) segment.

#### 2.2.4.1 Propagating Inhibitor Model

Given that similar to observed cell division arrest patterns (Donnelly et al., 1999)  $K_{ml}$  rates also dropped towards the leaf tip, I first investigated whether the spatiotemporal growth dynamics along the midline could be explained by a similar mechanism. For this purpose,  $K$  was modified by a growth inhibitor,  $\mathbf{s}_{DIST}$ , which is produced at a rate  $b_{dist}$  at the distal end only.  $\mathbf{s}_{DIST}$  production is controlled by the Dirac delta function,  $\delta(y)$ , which in the implementation here, adopts a value of 1 at the most distal segment,  $x_n$ , and a value of zero elsewhere.  $\mathbf{s}_{DIST}$  propagates through the canvas:

$$\frac{\partial \mathbf{s}_{DIST}}{\partial t} = D_{dist} \nabla^2 \mathbf{s}_{DIST} + b_{dist} \delta(y - y_n) - \mu_{dist} \mathbf{s}_{DIST}, \quad (2.5)$$

where  $D_{dist}$  is the diffusion coefficient of  $\mathbf{s}_{DIST}$ ,  $\mu_{dist}$  the decay rate of  $\mathbf{s}_{DIST}$  and  $y$  is the initial position of the beginning of each segment (Fig. 2.13). Growth of the canvas was calculated at fixed time steps of 1  $h$  and the steady state distribution of  $\mathbf{s}_{DIST}$  at each time step was found using a partial differential equation solver in MATLAB.  $\mathbf{s}_{DIST}$  levels were allowed to reach steady state before growth commenced (Fig. 2.14A).

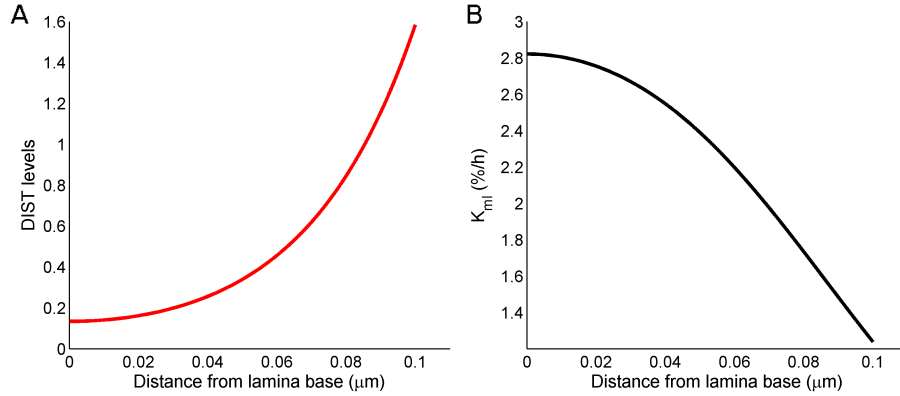


**Figure 2.14** Initial starting conditions of the propagating inhibitor model. **A**, initial steady state distribution of  $\mathbf{s}_{DIST}$ . **B**, initial growth rate along the midline,  $K$ , determined by  $\mathbf{s}_{DIST}$ .

$\mathbf{s}_{DIST}$  inhibits growth by an inhibition function,  $\text{inh}(h_f, \mathbf{x}_F)$ , which has been used throughout this work (Fig. 2.15):

$$\text{inh}(h_f, \mathbf{x}_F) = 1/(1 + h_f \mathbf{x}_F), \quad (2.6)$$

where  $\mathbf{x}_F$  is a growth factor and  $h_f$  the inhibition coefficient of that factor. This function equals 1 when  $\mathbf{x}_F$  is 0 and decreases with increasing levels of  $\mathbf{x}_F$ .

The growth rate  $K$  was defined as:

$$K = pmax \text{inh}(h_{dist}, \mathbf{s}_{DIST}), \quad (2.7)$$

where  $pmax$  is the maximum growth rate of the canvas.  $h_{dist}$  is the amount of inhibition by  $\mathbf{s}_{DIST}$ . This gives an initial distribution of growth rates shown in Figure 2.14B. Modelled growth rates were calculated over the same interval

as those of the tracking data:

$$K_{\delta t} = \ln \frac{L_{t+\delta t}}{L_t} \frac{1}{\delta t}, \quad (2.8)$$

where  $L_t$  and  $L_{t+\delta t}$  are the segment sizes at time  $t$  and  $t + \delta t$ , respectively. Here the time interval  $\delta t$  was 24 h. The parameters of this model were visually fitted to the early tracking data.

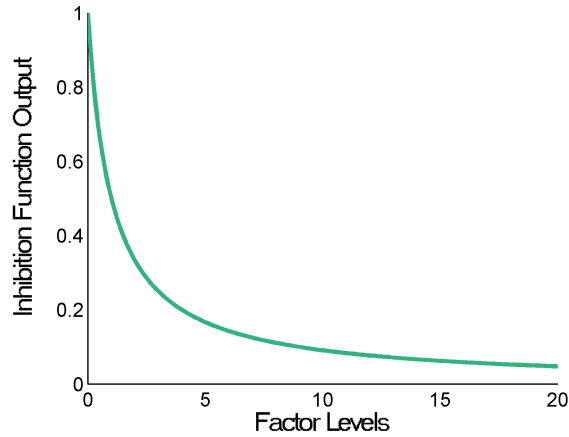


**Figure 2.15** Inhibition function. This function returns the amount of growth inhibition by a factor  $\mathbf{x}_F$ . At low values of  $\mathbf{x}_F$ , the output is close to 1 and inhibition is therefore small. At increasing levels of  $\mathbf{x}_F$  the function output decreases and inhibition increases. In this example  $h_f = 1$ .

The propagating inhibitor model generated growth rate profiles similar to those observed along the lamina midline (Fig. 2.16). The initial gradient became more uniform in proximal regions and declined more steeply towards the tip (Fig. 2.16B). However, at later stages the growth rates in the proximal regions predicted by the model exceeded those observed (Fig. 2.16C and D). The  $\mathbf{s}_{DIST}$  levels in these regions were very low, allowing growth to proceed at a rate specified by  $pm_{ax}$ . Low inhibitor levels are a result of the increased distance between the proximal regions and the inhibitor source at the tip, which did not allow proximal regions to be supplied with  $\mathbf{s}_{DIST}$  at later stages. With continuous inhibitor decay, proximal regions became depleted of  $\mathbf{s}_{DIST}$  levels. This suggest that such a model is not suitable for controlling growth rates throughout the leaf at increasing leaf sizes, unless other growth inhibiting factors are present.

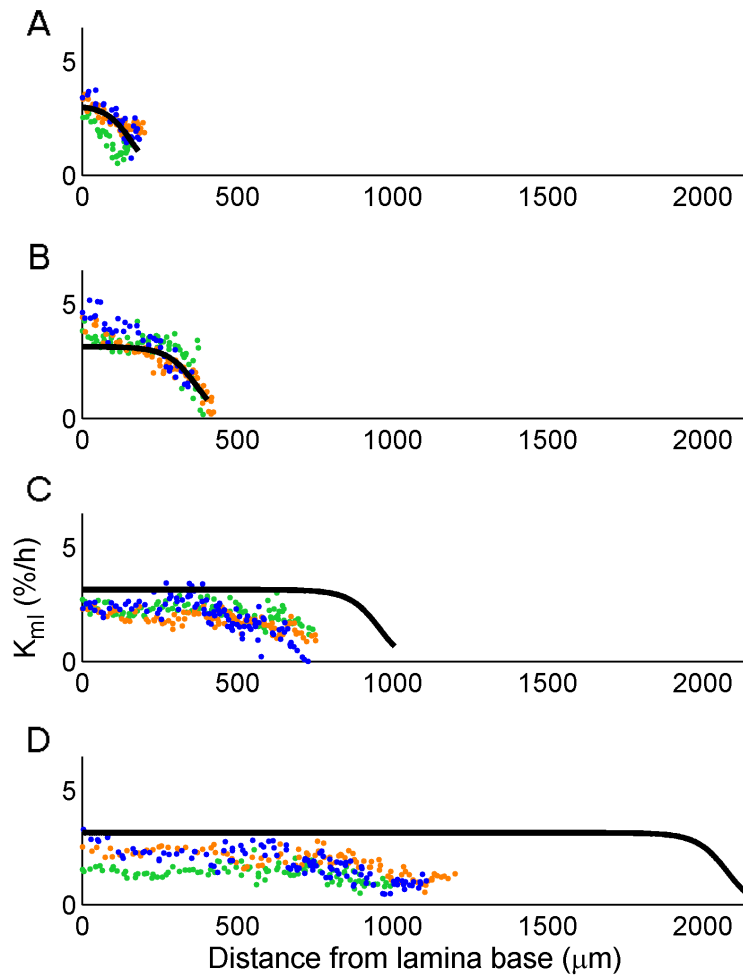


**Figure 2.16** Propagating inhibitor model (black lines) and the tracked growth profiles along the lamina midline ( $K_{ml}$ ) as shown above (data points; Fig. 2.12B). Model  $K$  and  $K_{ml}$  were calculated over 24  $h$  intervals. Colours represent different leaves tracked from day 4-8.

#### 2.2.4.2 Fixed Models

Interestingly, similar results are obtained with a model, in which an initial  $s_{DIST}$  distribution is achieved through diffusion and levels then become fixed to the canvas locally to determine the growth rate of each segment throughout the simulation (Fig. 2.17). Here,  $D_{dist}$  was slightly reduced compared to the above propagating inhibitor model.

The fixed inhibitor model suggests that the changes in the growth rate profile are a result of the initial magnitude of the regional growth rates. As an illustration of this point, consider a factor that has a linear distribution across the canvas initially (Fig. 2.18A). If this factor has no effect on the growth rate and growth is uniform throughout the canvas, this linear profile should

be maintained during development (Fig. 2.18B). Alternatively, if there is an underlying non-uniform growth profile, independent from the factor levels, such as that shown in Figure 2.18C (inset), the profile of the factor is expected to change according to the underlying growth profile (Fig. 2.18C).

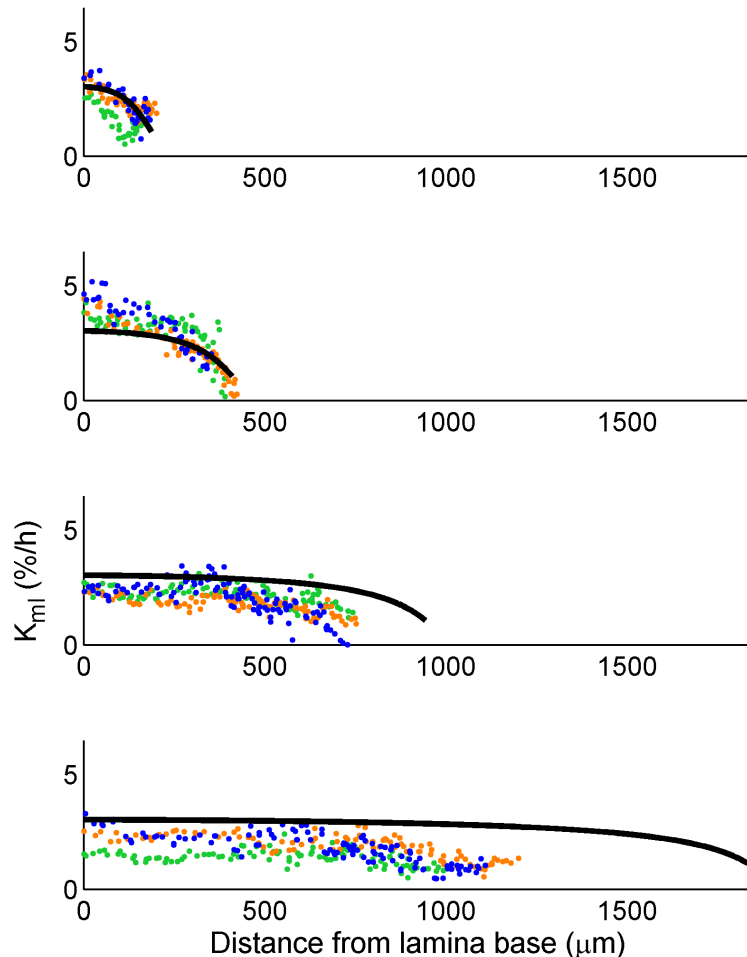


**Figure 2.17** Fixed inhibitor model (black lines) and the tracked growth profiles along the lamina midline ( $K_{ml}$ ) as shown above (data points; Fig. 2.12B). Model  $K$  and  $K_{ml}$  were calculated over 24  $h$  intervals. Colours represent different leaves tracked from day 4-8.

In the example shown here, the high and low end of the factor levels have been stretched over the growing region, while the middle of the canvas did not grow and the factor therefore retains a steep, linear profile in the middle region. Finally, the levels of the factor may directly influence the growth rate. In this case, the initially linear gradient of the factor becomes more shallow in the proximal regions, where growth rates are high. In the distal regions, in contrast, growth rates, specified by the factor, are lower, so that the gradient does not become as shallow. Thus, the distribution of a factor, which influ-

ences the growth rate, is itself changed by the resulting growth, creating a feedback between patterning and growth. This last example also shows that, in principal, an initially linear gradient in growth rates can transform into a curve with a steeply declining distal end, similar to the midline growth profiles observed for the tracking data.

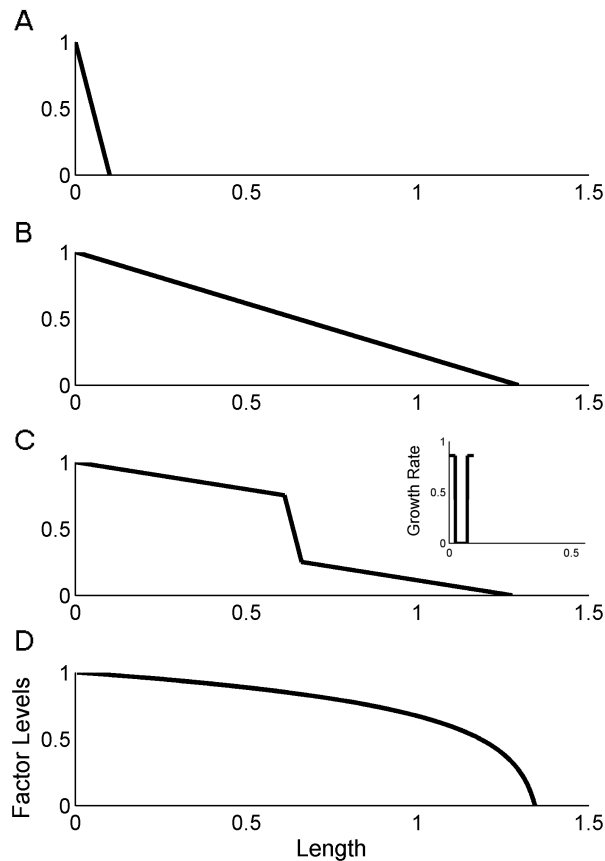


**Figure 2.18** Examples of feedback between patterning and growth. **A**, the distribution profile of a factor with an initially linear gradient across a canvas deforms according to the underlying growth profile. **B**, the factor does not influence the underlying uniform growth rates. **C**, the factor does not influence the underlying non-uniform growth profile (shown in inset). **D**, the factor directly determines the growth rate.

#### 2.2.4.2.1 Fixed Activator Model

To test whether an initially linear gradient, which gets fixed to the canvas after establishment, could account for the observed growth profiles, a growth activator,  $i_{PROX}$ , was created, which was expressed with a linear gradient across the canvas before growth commenced and did not propagate, decay or

dilute (Fig. 2.19):

$$\mathbf{i}_{PROX} = \frac{y_n - y}{\Sigma L_0} (1 - b_{prox}) + b_{prox}, \quad (2.9)$$

where  $\Sigma L_0$  is the initial length of the whole canvas. The initial position of the start of each segment of the canvas is described by  $y$ , where the position of the last segment is denoted  $y_n$ . The basal level of  $\mathbf{i}_{PROX}$  in the canvas is set by  $b_{prox}$ . Using this equation,  $\mathbf{i}_{PROX}$  has a maximum level of 1 in the most proximal segment corresponding to the petiole base and a level of  $b_{prox}$  in the most distal segment. Biologically, a linear morphogen gradient could be established by a morphogen source and sink. Morphogen levels could then get fixed to the tissue at early stages and be maintained locally during growth. Alternatively propagation might continue at low rates.

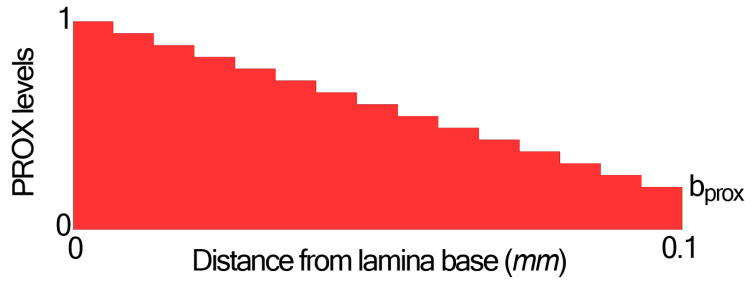


**Figure 2.19** Initial distribution of  $\mathbf{i}_{PROX}$  levels across the 1D canvas. Levels are uniform within each segment and do not change over time.

The canvas was grown according to this initial  $\mathbf{i}_{PROX}$  gradient:

$$K = p_{prox} \mathbf{i}_{PROX}, \quad (2.10)$$

where  $p_{prox}$  is the promotion of growth by  $\mathbf{i}_{PROX}$ . As for the inhibitor models, the model parameters were largely adjusted to the early time points (Fig. 2.20). High growth rates in the proximal regions resulted in extensive proximal elongation, which stretched out the initially steep gradient (Fig. 2.20C and D). At the distal end, in contrast, growth rates were lower and the regions elongated little compared to the proximal regions. Therefore the growth rate gradient at the distal end appeared steep throughout growth.

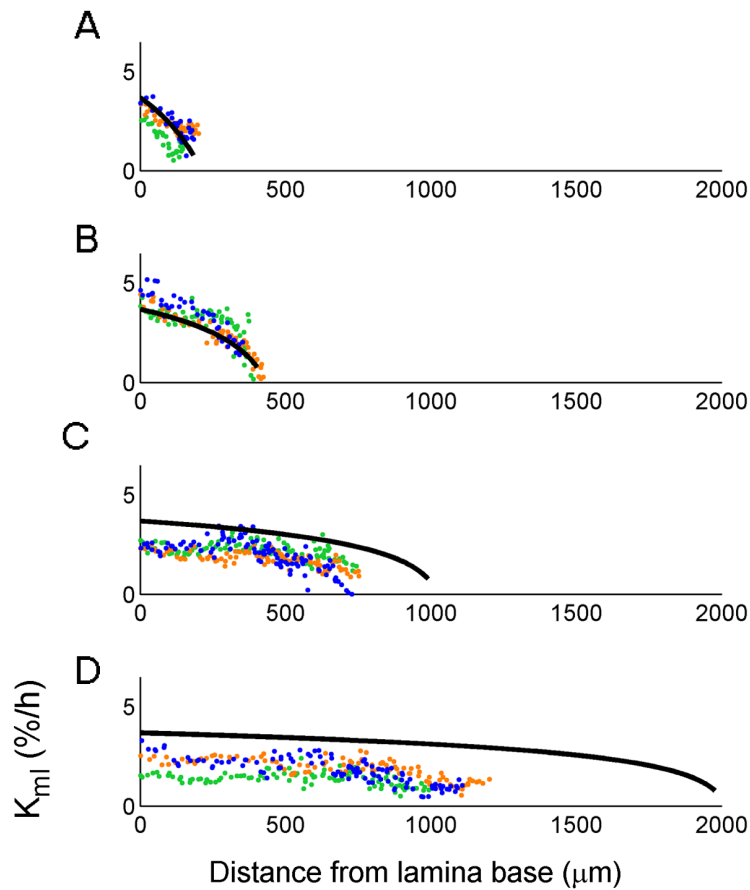


**Figure 2.20** Fixed activator model (black lines) and tracked growth profiles along the midline ( $K_{ml}$ ) as shown above (Fig. 2.12B). Model  $K$  and  $K_{ml}$  were calculated over 24  $h$  intervals. Colours represent different leaves tracked from day 4-8.

Thus, the overall growth profile trends of the tracked leaves could be generated with both a tip-inhibitor model and a fixed-activator model. Given the available tracking data, it was difficult to distinguish between the two models. In both model types, the modelled growth rates exceed those observed at later stages of development.

### 2.2.4.3 Midline Models and Age

The overestimation of leaf length at later stages by the models suggests the need for a mechanism to reduce growth rates over time. For computational speed growth rate reductions with age are initially explored for the fixed activator model.

In the fixed activator model, growth rates may be reduced over time by

letting  $\mathbf{i}_{PROX}$  levels dilute with growth. Thus far, it has been assumed that  $\mathbf{i}_{PROX}$  levels are maintained locally in the canvas throughout growth.

Dilution was added to the model by assuming that  $\mathbf{i}_{PROX}$  levels drop proportionally with the length of each segment. This addition resulted in a drastic reduction in growth rates over the period modelled (Fig. 2.22A). Growth rates dropped considerably at early stages, while observed leaf growth rates remained high initially (Fig. 2.22A ii). Observed reductions in growth rates in the overall leaf size were only evident about 6 days after leaf initiation (Fig. 2.2B). Thus, growth deceleration in the leaf could not simply be explained by  $\mathbf{i}_{PROX}$  dilution.

However, the mode of growth deceleration was difficult to determine, since there was only a small decrease in growth rates during the period analysed by time lapse imaging. Therefore, in accordance with observed overall leaf dynamics, growth rates were reduced uniformly in space and linearly with time after day 6. For this purpose an additional factor,  $\mathbf{i}_{LATE}$ , was added to the model.  $\mathbf{i}_{LATE}$  increases linearly throughout the canvas with a rate determined by  $g_{late}$  after day 6, which corresponds to 148  $h$  in the model (Fig. 2.21):

$$\mathbf{i}_{LATE} = \begin{cases} 0 & \text{for } t < 148 h \\ g_{late} (t - 148 h) & \text{for } t \geq 148 h \end{cases} \quad (2.11)$$

$\mathbf{i}_{LATE}$  inhibits  $K$ :

$$K = p_{prox} \mathbf{i}_{PROX} \cdot \text{inh}(h_{late}, \mathbf{i}_{LATE}), \quad (2.12)$$

where  $p_{prox}$  is the promotion of growth by  $\mathbf{i}_{PROX}$  and  $h_{late}$  is the amount of growth inhibition by  $\mathbf{i}_{LATE}$ . With the addition of  $\mathbf{i}_{LATE}$  growth patterns were more comparable to the spatiotemporal growth dynamics of the midline and correctly predicted leaf length at later stages (Fig. 2.22B).

Applying the same  $\mathbf{i}_{LATE}$  interactions to the propagating inhibitor model with  $\mathbf{s}_{DIST}$  shows that the addition of  $\mathbf{i}_{LATE}$  is also sufficient to adjust the model profiles to the data (Fig. 2.23A).

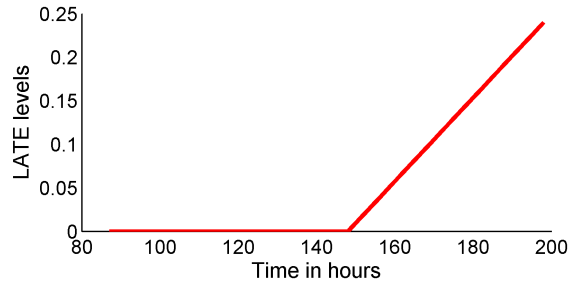


**Figure 2.21** Dynamics of  $i_{LATE}$  with time.

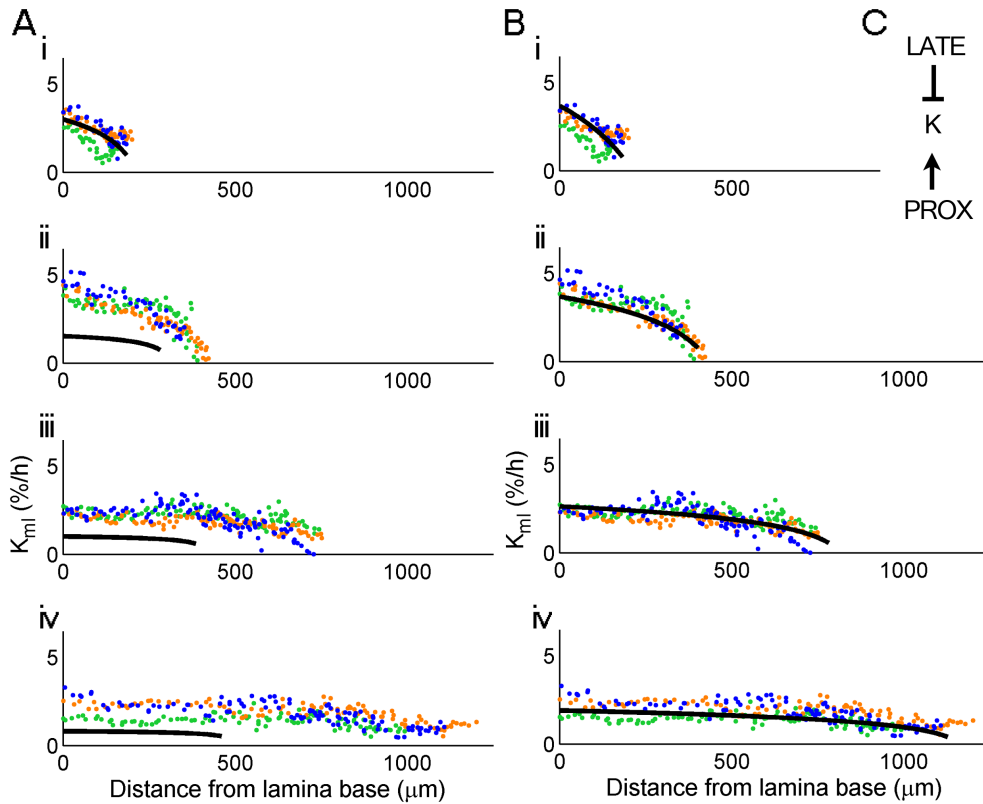


**Figure 2.22** Fixed activator models with growth deceleration. **A-B**, the tracked growth profiles along the midline ( $K_{ml}$ ) as shown above (Fig. 2.12B) with fitted one-dimensional models (lines). Model  $K$  and  $K_{ml}$  were calculated over 24  $h$  intervals. Colours represent different leaves tracked from day 4-8. **A**, fixed activator model with dilution. **B-C**, fixed activator model with  $i_{LATE}$ , which reduces growth rates at later stages (**iii** and **iv**). **C**, growth interaction network.

Growth rates along the leaf lamina midline could therefore be described by a model consisting of only two components,  $i_{PROX}$  and  $i_{LATE}$  (Fig. 2.22C) or  $s_{DIST}$  and  $i_{LATE}$  (Fig. 2.23B). The model assumes that the main growth patterns are established very early on in development. In the propagating inhibitor model, the low diffusion versus decay rate means that  $s_{DIST}$  mainly

acts locally.

During development the gradient in growth rates causes proximal regions to expand extensively compared to distal regions, which grow very little. This suggests that most of the leaf area observed at later stages originates from the initially proximal regions. A high contribution of proximal regions to the final organ shape has also been observed for the *Arabidopsis* sepal (Roeder et al., 2010). The clear spatial gradient in growth rates prior to a visible temporal decline in growth suggests that growth rate patterning and growth deceleration are at least partially uncoupled.

The assumption of early establishment of growth patterns has been tested by leaf surgery, which will be outlined in a later section (2.2.13.2 Leaf Surgery).

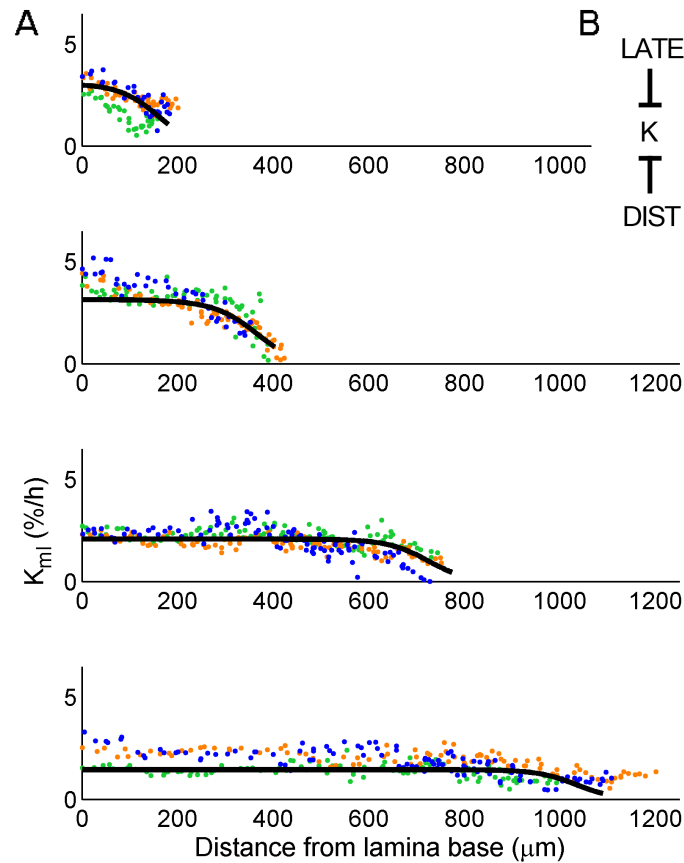


**Figure 2.23** Propagating inhibitor model with growth deceleration. **A**, the tracked growth profiles along the midline ( $K_{ml}$ ) as shown above (Fig. 2.12B) with fitted model (lines), where  $i_{LATE}$  reduces growth rates at later stages. Model  $K$  and  $K_{ml}$  were calculated over 24  $h$  intervals. Colours represent different leaves tracked from day 4-8. **B**, growth interaction network.

## 2.2.5 Growing Polarised Tissue Framework

The 1D models were generated to explore the mechanism underlying the observed growth patterns along the midline. However, to understand leaf shape development, a multidimensional modelling framework is required. Here, 2D leaf shape was modelled using the Growing Polarised Tissue (GPT) framework developed by Kennaway et al. (2011). The GPT framework is based on finite element method and has been implemented in a toolbox, *Gftbox*, in MATLAB. Under this framework a tissue is treated as a continuous sheet, termed the canvas, with two surfaces and a thickness, reflecting the sheet-like structure of many leaves and floral organs. To compute the growth of this sheet, it is discretised into prisms, which together form a continuous canvas. Growth is controlled by factors, which have one value for each vertex of the canvas. Elasticity theory is used to compute the deformations of the canvas at each time step. Since factors are associated with particular regions on the canvas, their expression also expands and gets distorted with growth.

Biologically, the growth properties of a tissue will be controlled by several components such as the material properties of the tissue and gene expression patterns. For simplicity, it is assumed that the material properties are uniform across the canvas. It is also assumed that residual stresses are not retained by the tissue, but are instead discarded after each simulation step.

Treating the leaf as a continuous sheet ignores discreteness at the level of individual cells. However, since in plants, the dynamics of individual cells are heavily constraint by those of their neighbours through the cell walls, leaf tissues could be regarded as continuous tissues. In addition, treating the tissue as a continuum means that leaf shape can be explored on the organ-level without having to account for the large number of cells at later stages.

### 2.2.5.1 Specified and Resultant Growth

Using the *Gftbox*, it is possible to model the deformation of tissue based on given growth interactions. For instance, we can distribute a linear field of areal growth rates across a square canvas and observe how these deform the canvas during growth (Fig. 2.24A). A linear distribution of growth rates was specified using the same equation as for  $i_{PROX}$  in the 1D fixed activator mod-

els (Eqn. 2.9). Growth within each region was isotropic. To visualise local tissue deformations during growth, a square grid was drawn onto the canvas (Fig. 2.24B; Thompson 1917).

With these growth specifications, during growth the horizontal edges of the canvas curved (Fig. 2.24C). Similarly, despite remaining orthogonal locally (i.e. intersecting at right angles), on a global level gridlines splayed out from the canvas base. These gridline deformations indicate rotations of canvas regions relative to each other. This could be confirmed by plotting the measured canvas rotation for each region (Fig. 2.24D). Rotations were not specified as part of the growth interactions and arose by applying the interactions to this continuous canvas, where regions are connected.

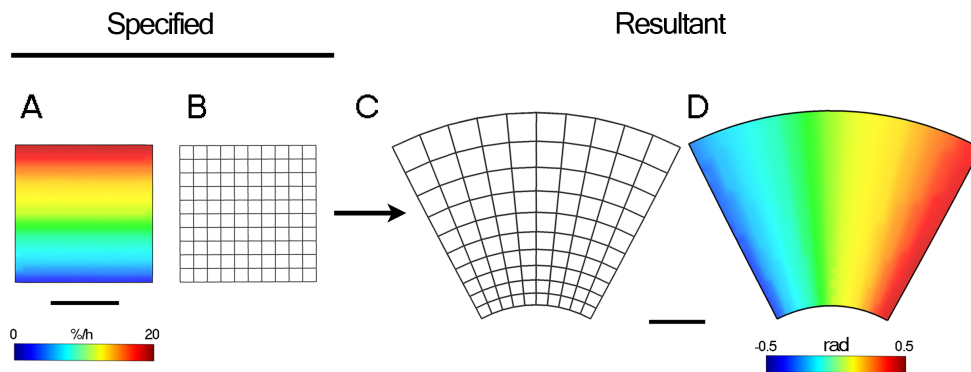


**Figure 2.24** 2D example model with isotropic growth. **A**, specified linear gradient of areal growth rates on initial canvas, **B**, square grid on initial canvas. **C**, resulting canvas shape and grid, **D**, resultant rotation rates in radians after a period of growth. Scale bars 1 *mm*.

This connectedness also affects the other growth parameters. For instance, in a model where isotropic growth rates are specified to decrease towards the middle of the square (Fig. 2.25A), the actual amount according to which the canvas grows differs from this specified rate (compare Fig. 2.25B and 2.25C). In the example shown the canvas is specified not to grow along the middle strip. However, the observed growth rates (as a result of the canvas connect- edness) are slightly higher in the centre of the canvas, while at the central side growth rates are actually negative, due to the force exerted by adjoining regions that have higher growth rates.

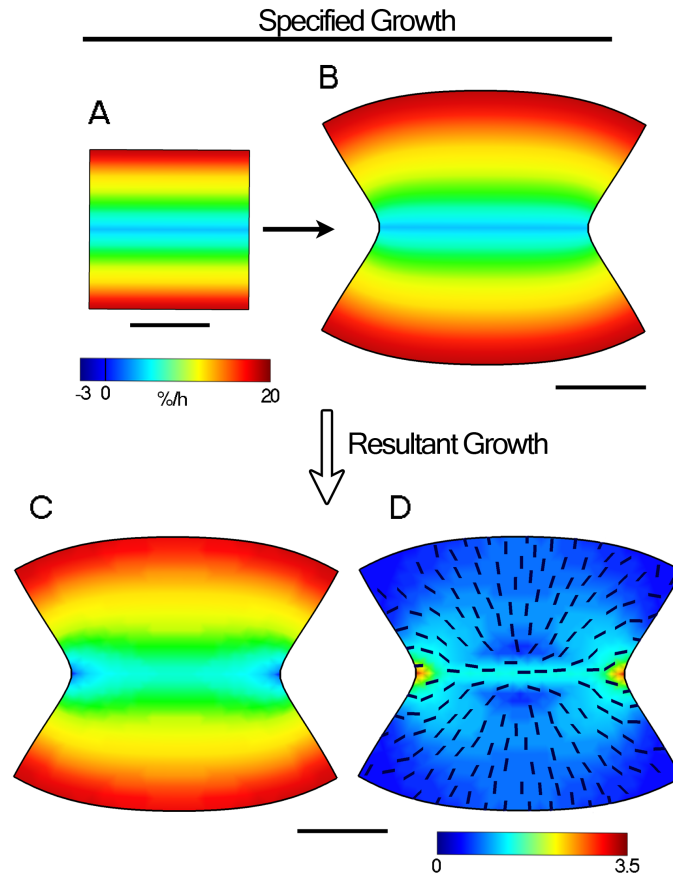


**Figure 2.25** 2D example model with an initial square canvas and isotropic non-uniform growth. **A-C**, specified linear gradient of areal growth rates from the centre showing **A**, specified growth rates on initial canvas, **B**, specified growth rates on resultant canvas after a period of growth, **C**, resultant growth rates and **D**, anisotropy and growth orientation of growth on canvas after a period of growth. Scale bars 1 *mm*.

Although the specified growth should be isotropic, the non-uniform growth rates within the canvas create regions of anisotropic growth with locally aligned orientations of growth (Fig. 2.25D). Anisotropy is highest in the central side regions, where the canvas is compressed. The locally aligned field of growth orientations shows that non-uniform growth rates within a connected tissue may be one way to coordinate growth orientations in a tissue. These simple example show that the connectedness of the canvas means that elements are not necessarily able to grow according to their desired rates, but instead find a compromise between their specified growth rate and that of their neighbours. Thus, it is necessary to distinguish between two types of growth parameters, those that are specified by the system and those that are actually observed. In the case of the *GFTbox* the specified parameters may be set up through the

growth and polarity interactions, while in biological systems these are specified by the action and interaction of genes and other biotic and abiotic factors. Resultant parameters, in contrast, are the observed parameters, which result from the specified growth parameters and neighbourhood constraints. Specified and resultant growth would be the same if each region grew in isolation or there are no growth conflicts, which is rarely the case. A main focus of the modelling work here is to determine the specified properties necessary to generate the resultant leaf shapes and growth characteristics observed.

### 2.2.6 Generating a 2D Leaf Model

To determine the specified growth and polarity necessary to generate the observed leaf shapes, the 1D leaf model was extended to 2D. Time lapse imaging of the leaf during the first half of leaf development showed that there are no cell rearrangements within the epidermal layer or in between the epidermis and the underlying layers, as reported previously (Meyerowitz, 1997). In addition the leaf is a thin structure with the main axes of growth lying within the plane. Therefore, leaf growth was approximated by a 2D model, which aimed at capturing the leaf shape within the plane.

The 2D model starting shape was loosely based on the size and shape of the flattened leaf primordium at the end of day 3 after initiation. At this stage the leaf is about 100  $\mu\text{m}$  in length and 85  $\mu\text{m}$  in width (Fig. 2.26A). Since, at this age the leaf is still relatively dome-shaped, the abaxial side of the young leaf was computationally flattened by Jerome Avondo (Fig. 2.26B). In the *GFtbox* a starting canvas of finite elements was created corresponding to these measurements (Fig. 2.26C). The initial canvas is oriented with regard to the external  $xy$ -coordinate system such that the canvas base is parallel to the  $x$ -axis and the midline parallel to the  $y$ -axis. Growth at the baseline is constrained to be parallel to the  $x$ -axis, reflecting the constraints of the anchored leaf at the stem.

As for the 1D models above, growth is driven by growth factors, which can either propagate ( $\mathbf{s}_{FACTORNAME}$ ) or retain fixed values for each vertex of the tissue ( $\mathbf{i}_{FACTORNAME}$ ). It is assumed that factor levels do not dilute with growth. All parameter values used in the models can be found under Material

and Methods (6.3.5.2 2D Leaf Model Parameters).

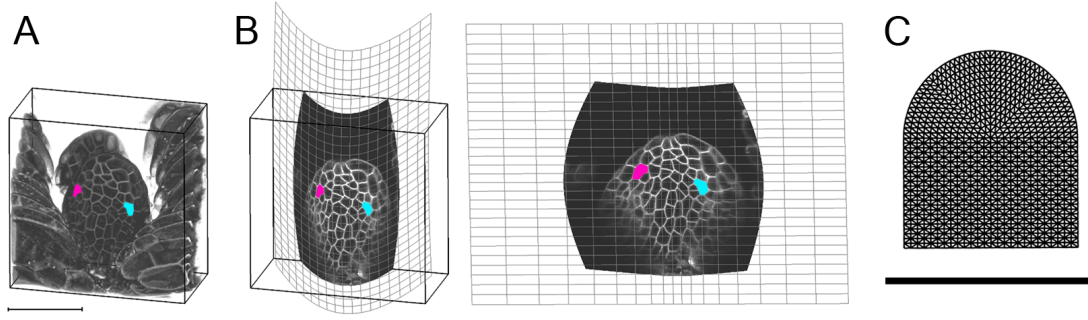


**Figure 2.26** **A**, shape of leaf 1 of *Arabidopsis* 3 days after initiation imaged by Samantha Fox. **B**, the primordium was computationally flattened by Jerome Avondo. Coloured cells indicate cell positions prior to and after the transformation. **C**, the 2D starting canvas made up of a mesh of finite elements. Scale bars **A-B**, 50  $\mu m$  and **C**, 100  $\mu m$ .

As a first attempt the growth factors of the 1D fixed activator model with  $\mathbf{i}_{LATE}$  (Fig. 2.22C, Eqn. 2.12) were mapped onto the canvas:

$$K = p_{prox} \mathbf{i}_{PROX} \cdot \text{inh}(h_{late}, \mathbf{i}_{LATE}),$$

where  $p_{prox}$  presents the promotion of growth by  $\mathbf{i}_{PROX}$  and  $h_{late}$  the amount of inhibition by  $\mathbf{i}_{LATE}$ .  $\mathbf{i}_{PROX}$  is expressed as a linear gradient with the highest level of 1 at the base (Fig. 2.27A). The growth inhibitor  $\mathbf{i}_{LATE}$  is expressed throughout the canvas after 148  $h$  and  $\mathbf{i}_{LATE}$  levels increase with age (Eqn. 2.11, Fig. 2.21). Specified growth of the canvas is isotropic but non-uniform as defined by  $\mathbf{i}_{PROX}$  (Fig. 2.27B).

The initial shape expanded to form a larger lobe with an indented tip and without much resemblance to the *Arabidopsis* leaf shape (Fig. 2.27C). To generate a better matching model shape to that of the leaf an additional identity factor,  $\mathbf{i}_{PET}$ , was introduced.  $\mathbf{i}_{PET}$  inhibits growth in the base regions, where the petiole is normally positioned (Fig. 2.27D-F):

$$K = p_{prox} \mathbf{i}_{prox} \cdot \text{inh}(h_{late}, \mathbf{i}_{late}) \cdot \text{inh}(h_{pet}, \mathbf{i}_{PET}), \quad (2.13)$$

where  $h_{pet}$  is the amount of inhibition by  $\mathbf{i}_{PET}$ . The resultant canvas shape was too wide to compare well to the observed leaf shapes and the petiole failed

to elongate (Fig. 2.27G). In both isotropic models the tip was indented at later stages due to the low growth rates at the tip specified by  $i_{PROX}$  and higher rates in regions proximal to the tip. Thus, leaf growth could not be readily explained by an isotropic growth model.

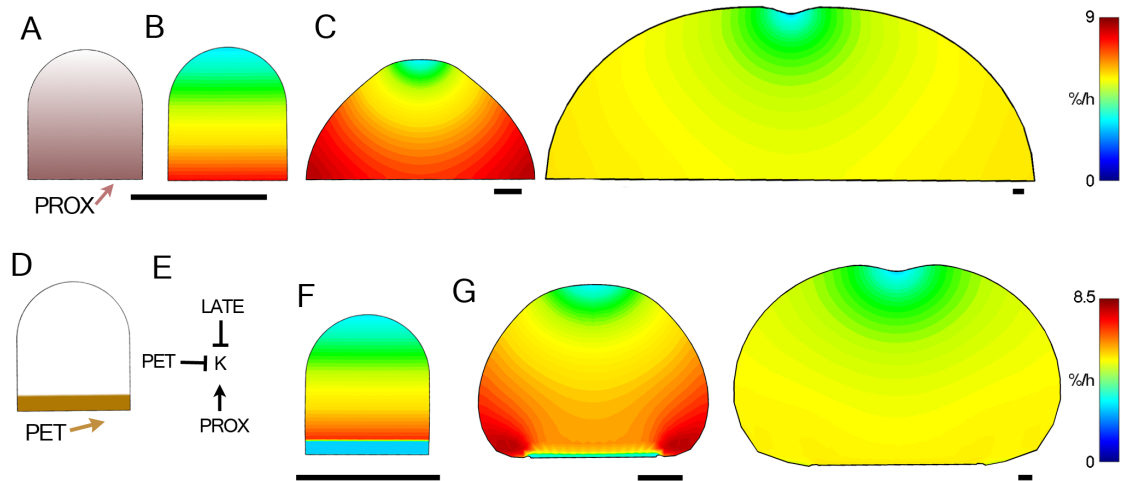


**Figure 2.27** **A**, distribution of  $i_{PROX}$  on the initial 2D canvas. **B-C**, the isotropic 2D model showing **B**, specified areal growth rates on the initial canvas and **C**, resultant growth rates and canvas shapes after 3 and 5 days of growth. **D-G**, the isotropic 2D model with  $i_{PET}$  showing **D**, distribution of  $i_{PET}$  on the initial canvas, **E**, the growth regulatory network with  $i_{PET}$ , **F**, specified areal growth rates on the initial canvas **G**, resultant growth rates and canvas shapes after 3 and 5 days of growth. Scale bars  $100 \mu m$ .

### 2.2.7 Leaf Growth Anisotropy

The extent of anisotropy in the leaf was calculated for small regions across the leaf using the same tracked leaves as above. Anisotropy was calculated as  $\frac{K_{max} - K_{min}}{K_{max}}$ .

Anisotropy was high in the petiole throughout development (Fig. 2.28A). In addition, anisotropy decreased mediolaterally from the midvein outward, in particular at later stages. A decrease in anisotropy with time has also been observed in previous leaf studies (Richards and Kavanagh, 1942). In addition, the principal orientations of growth were computed (Fig. 2.28B). At early stages growth was orientated proximodistally and orientations converged towards the leaf tip (Fig. 2.28B, pink arrow). At intermediate stages orientations become more oblique in the lamina and finally point largely mediolaterally at the last

stage analysed here.

Thus, anisotropy not only varies spatially, but also temporally. Moreover, the direction of growth changes over time. The uniformity of spatial patterns within small regions suggests that these patterns are being coordinated. This coordination can be provided by a polarity system.

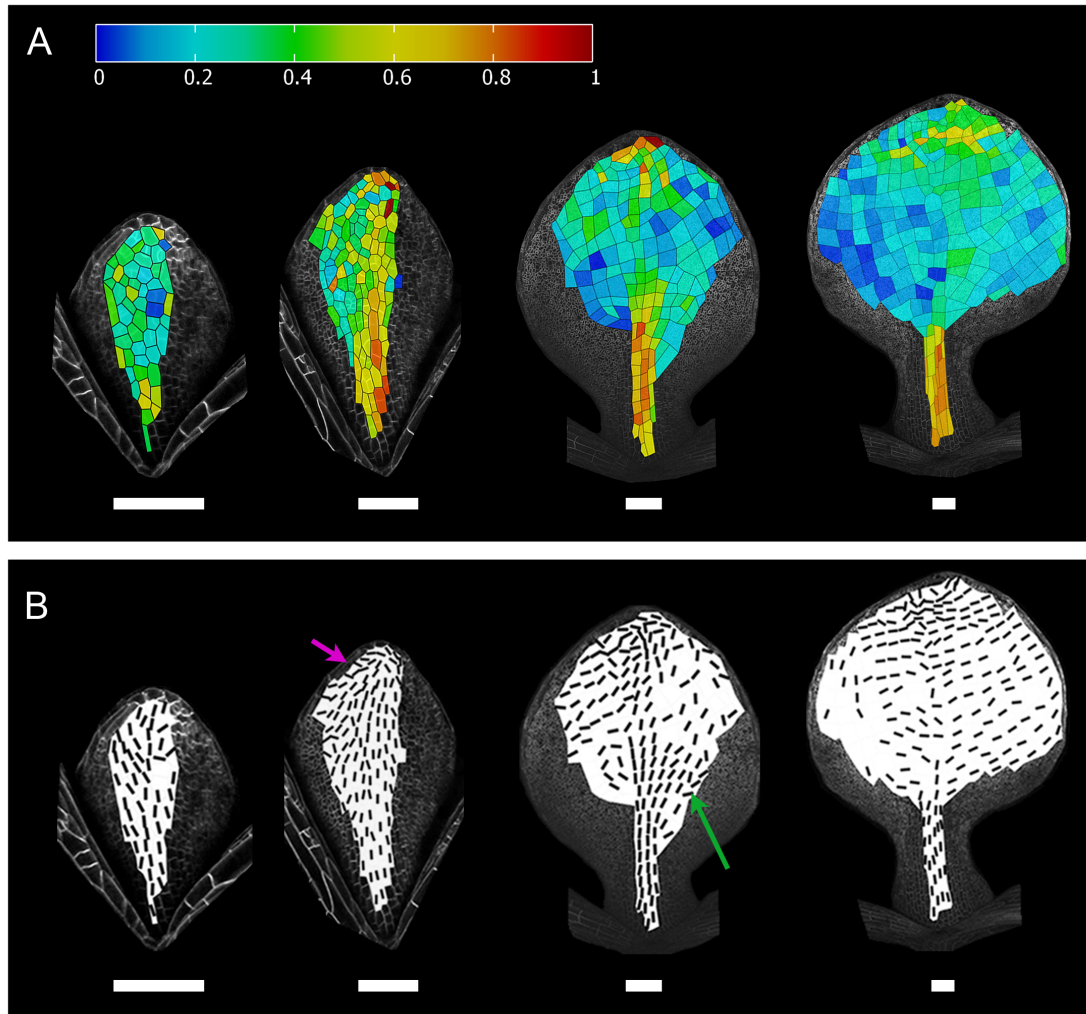


**Figure 2.28** Growth parameters calculated over 24 *h* intervals showing leaves 5-8 days after initiation. **A**, anisotropy and **B**, principal orientations of growth displayed for regions with an anisotropy > 10 %. Image by Samantha Fox. Scale bars 100  $\mu\text{m}$ .

### 2.2.8 Polarity Systems

In the simple example model above (Fig. 2.25) it was shown that non-uniform growth rates within a connected canvas are able to generate a locally aligned field of growth orientations. Thus, mechanical signals are likely to be

able to provide orientation to a tissue. However, the angle of these orientations is highly dependent on the underlying growth field. In contrast, in the GPT-framework growth orientations can also be specified through a polarity factor, independently of the growth field. This distinction allows the effects of growth and polarity on tissue shape to be studied independently.

In principle, there are several ways in which tissue polarity could be coordinated over time. For instance, polarity directions could be maintained throughout growth according to the initial polarity field. In this case, the polarity field is independent from changes in the tissue geometry and therefore non-deforming. In other cases, the polarity field may reorientate during development. Such a change might simply be a result of changes in the geometry of the tissue (deforming polarity system) or result from a re-organisation of tissue polarity during development. Here, the effects of a non-deforming and deforming polarity field on tissue shape have been investigated by introducing polarity systems into the example canvas presented above (2.2.5.1 Specified and Resultant Growth).

A square canvas was oriented parallel to the  $xy$ -axes and grown isotropically. A linear gradient of growth rates was distributed across it (Fig. 2.29A), which transformed the square into a fan-like shape. One way to specify growth directionality to this canvas is through the gradient of a morphogen. Growth rates can then be specified parallel to this gradient,  $K_{par}$ , and perpendicular to it,  $K_{per}$ . In the examples presented here,  $K_{par} = 0\% h^{-1}$  and  $K_{per}$  was specified by the linear gradient of a growth factor, generating growth rates that ranged from 0 to 10  $\% h^{-1}$ .

In the first example, a non-deforming proximodistal polarity field is specified by the gradient of the polarity factor,  $\mathbf{i}_{POLARISER}$  ( $\mathbf{i}_{POL}$ ; Fig. 2.29B). For simplicity, a gradient of  $\mathbf{i}_{POL}$  was imposed onto the system using a similar equation as for the 1D fixed activator models above (Eqn. 2.9), which creates a  $\mathbf{i}_{POL}$  gradient parallel to the  $y$ -axis, that decreases distally:

$$\mathbf{i}_{POL} = \frac{y_n - y}{y_n} b_{pol}, \quad (2.14)$$

where  $y$  is the position of each node along the  $y$ -axis and  $y_n$  describes the  $y$ -axis position of the nodes at the top end of the canvas.  $b_{pol}$  is the highest level of  $\mathbf{i}_{POL}$  in the canvas. In the same way as the linear gradient of growth rates,  $\mathbf{i}_{POL}$  has a linear gradient across the canvas with highest levels ( $b_{pol}$ ) at the base and levels of 0 at the top end.  $\mathbf{i}_{POL}$  levels are defined for each node and interpolated across each finite element.

To generate a non-deforming polarity system, this polarity field was maintained parallel to the  $y$ -axis throughout growth by re-establishing the linear  $\mathbf{i}_{POL}$  gradient at every iteration (Fig. 2.29C). There was thus no feedback between canvas deformations and the polarity field. Retaining directions consistently parallel to the  $y$ -axis resulted in a fan-like geometry with concave sides.

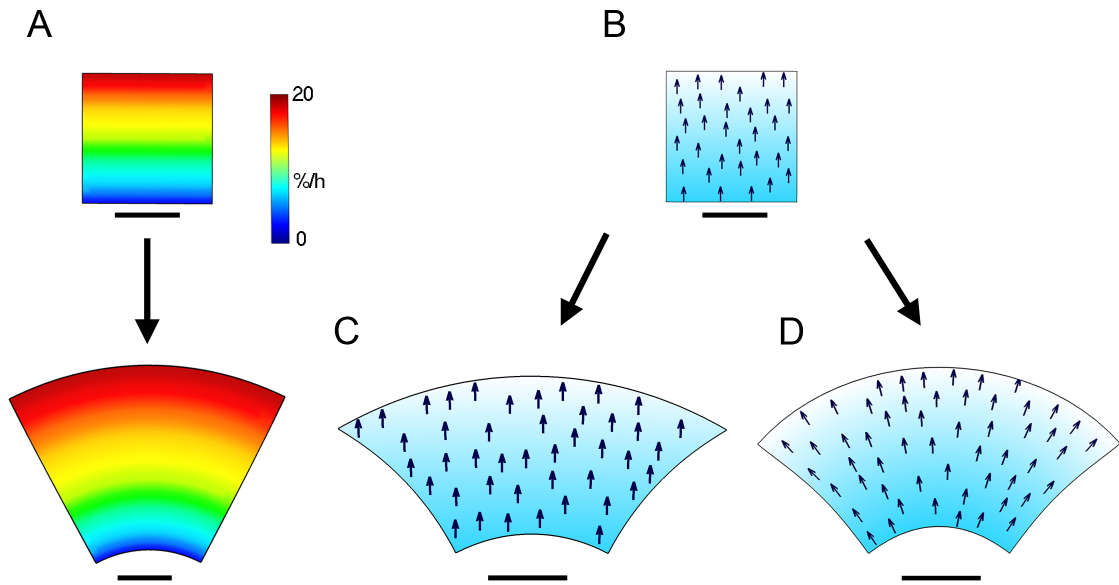


**Figure 2.29** **A**, linear gradient of areal growth rates (colours) with isotropic growth showing the initial canvas and the resultant shape. **B**, an initial polarity field (arrows) based on the linear gradient of  $\mathbf{i}_{POL}$  (blue) **C**, is maintained throughout growth (non-deforming model) or **D**, is deformed with the growing canvas (deforming model). Scale bars 1  $mm$ .

In an alternative (deforming) model, the polarity field was defined by the same  $\mathbf{i}_{POL}$  gradient. However, instead of re-establishing the gradient of  $\mathbf{i}_{POL}$  continuously, the distribution of  $\mathbf{i}_{POL}$  was maintained by each region of the canvas after setup. In this case, the gradient of  $\mathbf{i}_{POL}$ , and therefore the polarity

field, deformed with the geometry of the canvas during growth (Fig. 2.29D). These interactions resulted in an intermediate shape between the isotropic model (Fig. 2.29A) and the non-deforming model (Fig. 2.29C).

Thus, the two models presented here make different assumptions of how growth coordination is maintained during development, generating different resultant shapes. As above, the deformation of the canvas is due to non-uniform growth rates within the connected canvas, which cause the regions of the canvas to rotate relative to each other. In the deforming model the polarity field rotates with the canvas, altering the principal direction of growth and therefore the growth field. In this way, growth and polarity feedback on each other.

### 2.2.9 Non-Deforming Polarity Model

The dynamics of the polarity field during development have been explored in the leaf by applying the two different polarity systems introduced above to the 2D leaf model.

First, a proximodistal polarity field was specified by a linear  $\mathbf{i}_{POL}$  gradient, which was oriented parallel to the canvas midline ( $y$ -axis) and decreased distally (Fig. 2.30A). The orientations of this polarity field were maintained throughout growth by re-establishing the  $\mathbf{i}_{POL}$  gradient at each iteration.

The growth rate  $K$  could now be divided into growth parallel and perpendicular to this gradient,  $K_{par}$  and  $K_{per}$ , respectively. The growth equation that was used to model the growth dynamics parallel to the midline (Eqn. 2.12) was therefore applied to  $K_{par}$  only (Fig. 2.30B):

$$K_{par} = p_{prox} \mathbf{i}_{PROX} \cdot \text{inh}(h_{late}, \mathbf{i}_{LATE}), \quad (2.15)$$

where  $p_{prox}$  is the promotion of growth by  $\mathbf{i}_{PROX}$ , which has a linear gradient across the canvas with highest levels at the base, and  $h_{late}$  is the inhibition of growth by  $\mathbf{i}_{LATE}$ , which is expressed uniformly throughout the canvas after day 6. This model resulted in a needle-like canvas (Fig. 2.30C), demonstrating the need to specify  $K_{per}$  as well.

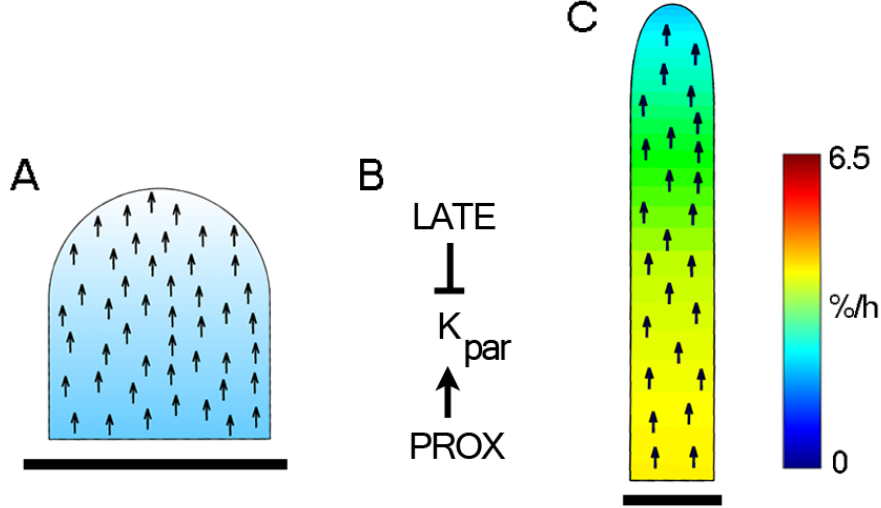


**Figure 2.30** 1D fixed activator model interactions applied to a 2D model with a specified non-deforming polarity system. **A**, initial canvas with non-deforming specified polarity field (arrows) by  $\mathbf{i}_{POL}$  (blue). **B**, growth interaction network. **C**, resultant canvas with areal growth rates calculated over a 24  $h$  interval (colours) and specified polarity field (arrows) shown at a time corresponding to a leaf 6 days after initiation. Scale bars 100  $\mu m$ .

To account for lateral growth, two additional factors,  $\mathbf{i}_{LAMINA}$  ( $\mathbf{i}_{LAM}$ ) and  $\mathbf{i}_{MIDVEIN}$  ( $\mathbf{i}_{MID}$ ), were introduced (Fig.2.31A).  $\mathbf{i}_{LAM}$  promotes  $K_{per}$  and is expressed throughout the canvas, but with reduced levels in the distal regions and the most proximal regions. Thus,  $\mathbf{i}_{LAM}$  replaces the need for  $\mathbf{i}_{PET}$ . The areal growth rates of the tracked leaves were low in the midvein region of the leaves compared to the rates in the lamina (Fig. 2.31C).  $K_{per}$  was therefore inhibited in the midvein regions by  $\mathbf{i}_{MID}$ . Both factors were expressed at maximum levels of 1.  $K_{per}$  was thus defined as:

$$K_{per} = p_{lam} \mathbf{i}_{LAM} \cdot \text{inh}(h_{mid}, \mathbf{i}_{MID}), \quad (2.16)$$

where  $p_{lam}$  is the promotion of  $K_{per}$  by  $\mathbf{i}_{LAM}$  and  $h_{mid}$  the magnitude of inhibition of  $K_{per}$  by  $\mathbf{i}_{MID}$ . The canvas was grown according to these growth interactions (Eqn. 2.15 and 2.16, Fig. 2.31B and E) and with a non-deforming polarity field (Fig. 2.31D). The resultant shapes and growth rates (Fig. 2.31F) compared well to the measurements at early stages (compare Fig. 2.31C i and F i). However, the final canvas shape was too narrow compared to the data (compare Fig. 2.31C ii and F ii). Modelled growth rates dropped at late

stages, whereas growth remained high in the lamina regions of the tracked leaves.

Thus, the model was able to capture leaf growth at early stages, but not later ones, suggesting that further regulatory interactions are necessary to capture growth at later stages.

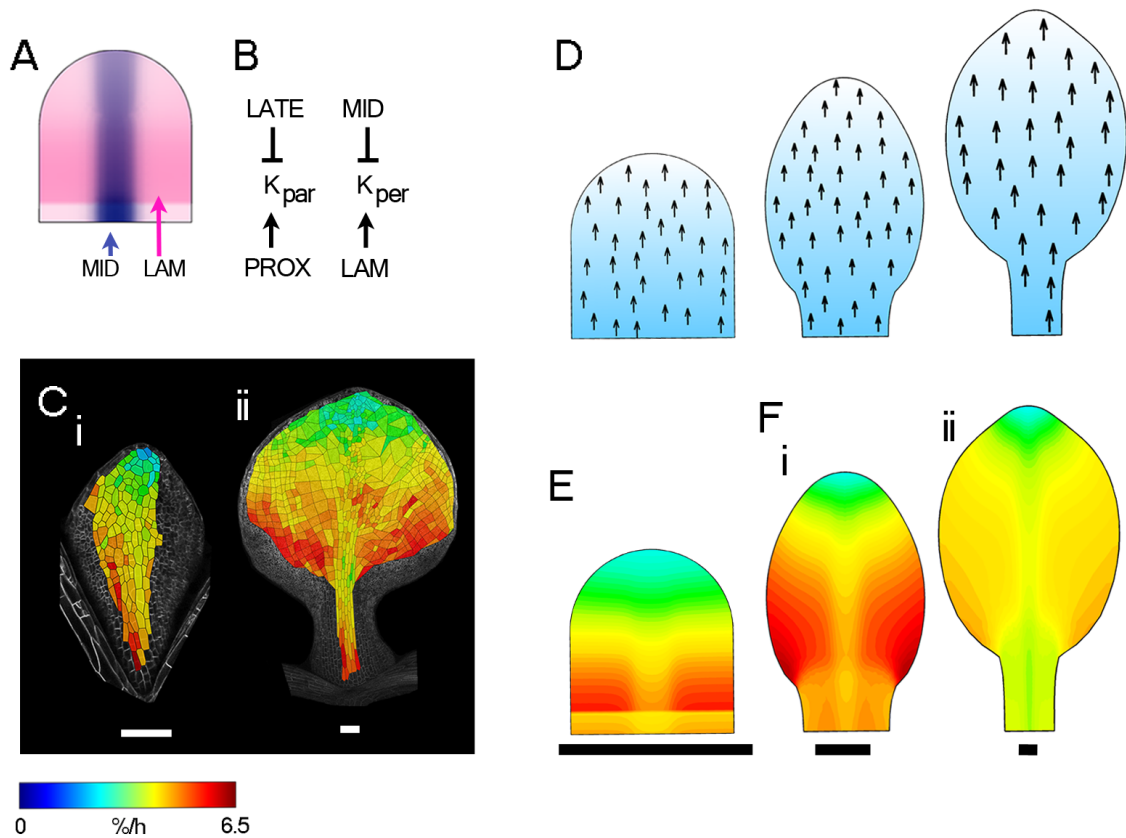


**Figure 2.31** **A**, distribution of  $i_{LAM}$  and  $i_{MID}$  on the initial canvas. **B**, growth regulatory network of the non-deforming model. **C**, observed areal growth rates of leaves (i) 6 and (ii) 8 days after initiation. **D-F**, non-deforming model with **D**, specified polarity (arrows) and  $i_{POL}$  (blue) on the initial and resultant canvasses. **E**, specified areal growth rates on the initial canvas. **F**, resultant canvas shapes and areal growth rates. Canvas sizes are shown at times corresponding to a leaf (i) 6 and (ii) 8 days after initiation. All resultant areal growth rates were calculated over 24 h intervals. Scale bars 100  $\mu m$ .

### 2.2.9.1 Lamina Extension at Later Stages

The high areal growth rates in the lateral regions of the leaf at later stages correlated with a substantial broadening of the lamina (Fig. 2.32A). This suggests that growth in width either increases at later stages or decreases less dramatically than growth in length. Given that areal growth rates remained

roughly constant in the lateral lamina during development, but growth rates along  $K_{par}$  decreased, an increase in  $K_{per}$  would be required to maintain high areal growth rates at later stages.

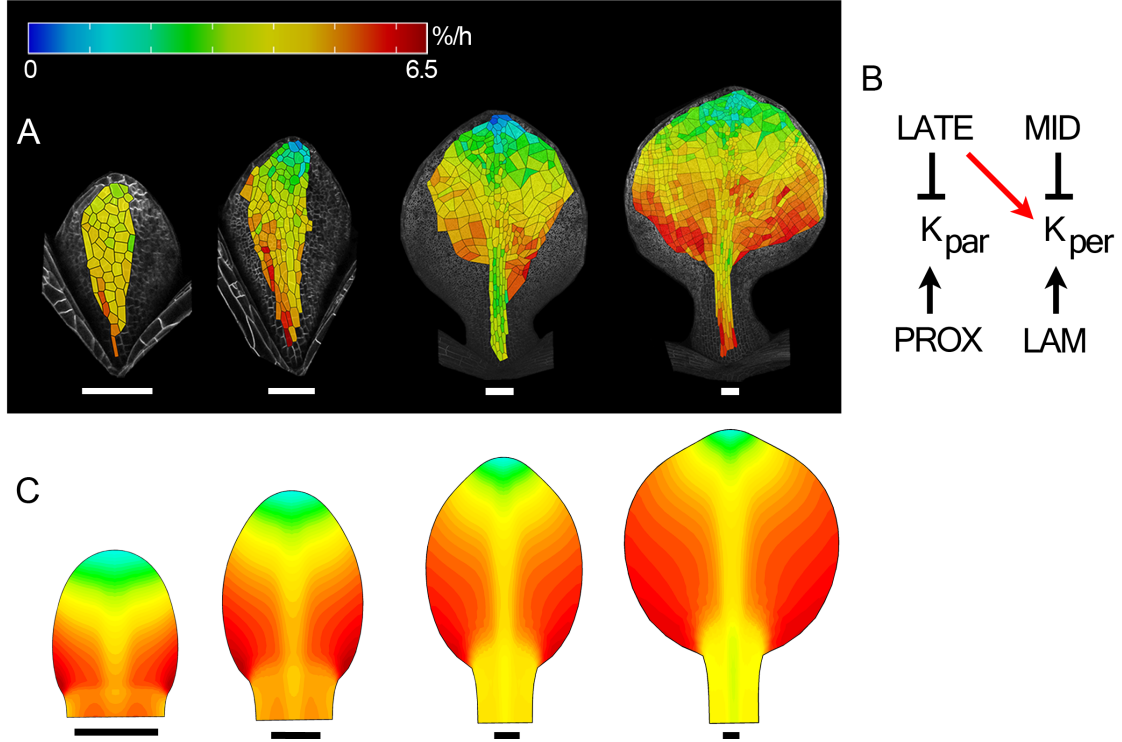


**Figure 2.32** **A**, areal growth rates calculated from time lapse imaging data. **B-C**, non-deforming model with  $\mathbf{i}_{LATE}$  promoting  $K_{per}$  (red arrow in **B**) showing **B**, the growth interaction network and **C**, the resultant canvas shapes and areal growth rates at stages comparable to **A**. All areal growth rates were calculated over 24  $h$  intervals. Scale bars 100  $\mu m$ .

In the model this was incorporated by an additional interaction, where  $\mathbf{i}_{LATE}$  in addition to inhibiting  $K_{par}$ , also promotes  $K_{per}$  (Fig. 2.32B, red arrow). Similar to growth inhibition, growth promotion was specified by a promotion function  $\text{pro}(p_f, \mathbf{x}_f)$ , which promotes growth proportionally to factor levels:

$$\text{pro}(p_f, \mathbf{x}_f) = 1 + p_f \mathbf{x}_f, \quad (2.17)$$

where  $\mathbf{x}_f$  is a factor and  $p_f$  is the promotion coefficient of that factor.

$K_{per}$  was thus defined as:

$$K_{per} = p_{lam} \mathbf{i}_{LAM} \cdot \text{inh}(h_{mid}, \mathbf{i}_{MID}) \cdot \text{pro}(p_{late}, \mathbf{i}_{LATE}), \quad (2.18)$$

where  $p_{lam}$  and  $p_{late}$  are the promotion coefficients of  $K_{per}$  by  $\mathbf{i}_{LAM}$  and  $\mathbf{i}_{LATE}$ , respectively.  $h_{mid}$  is the inhibition of  $K_{per}$  by  $\mathbf{i}_{MID}$ .

This ensured that areal growth rates remained high during the simulation and resulted in laminar outgrowth to generate the characteristic *Arabidopsis* leaf shape (Fig. 2.32C). Thus, this model, consisting of four factors with a non-deforming polarity field, was able to capture the overall growth rate patterns and leaf shape changes during the developmental period studied here.

### 2.2.9.2 Principal Orientations of Growth

Since the factors controlling polarity in the leaf are still elusive, it was not possible to measure polarity directions in the leaf directly and compare them to those generated by the model. However, orientations of principal growth (Fig. 2.33A) can be used as a proxy for an underlying polarity. Therefore, observed principal orientations of growth were compared to those generated by the non-deforming model and those generated by other polarity mechanisms to investigate how growth is coordinated in the leaf.

Similar to the observed orientations, growth orientations of the non-deforming model (Fig. 2.33B i) were principally oriented proximodistally at early stages (Fig. 2.33B ii). During the later stages, the promotion of lateral growth by  $\mathbf{i}_{LATE}$  caused orientations to flip so that growth rates were highest along the mediolateral axis in most of the lamina. In the very proximal lamina, orientations splayed out away from the midvein. Overall, these patterns agreed with those observed in the tracked leaves. However, on closer examination modelled and observed orientations differed in certain regions (Fig. 2.33A and B ii, coloured ellipses). Observed growth orientations converged towards the tip at young stages, whereas model orientations remained largely parallel to the midline (Fig. 2.33A and B ii, pink ellipses). Additionally, at slightly later stages observed orientations in the proximal regions of the leaf splayed out away from the midvein, whereas model orientations did not splay out (Fig. 2.33A and B ii, green ellipses).

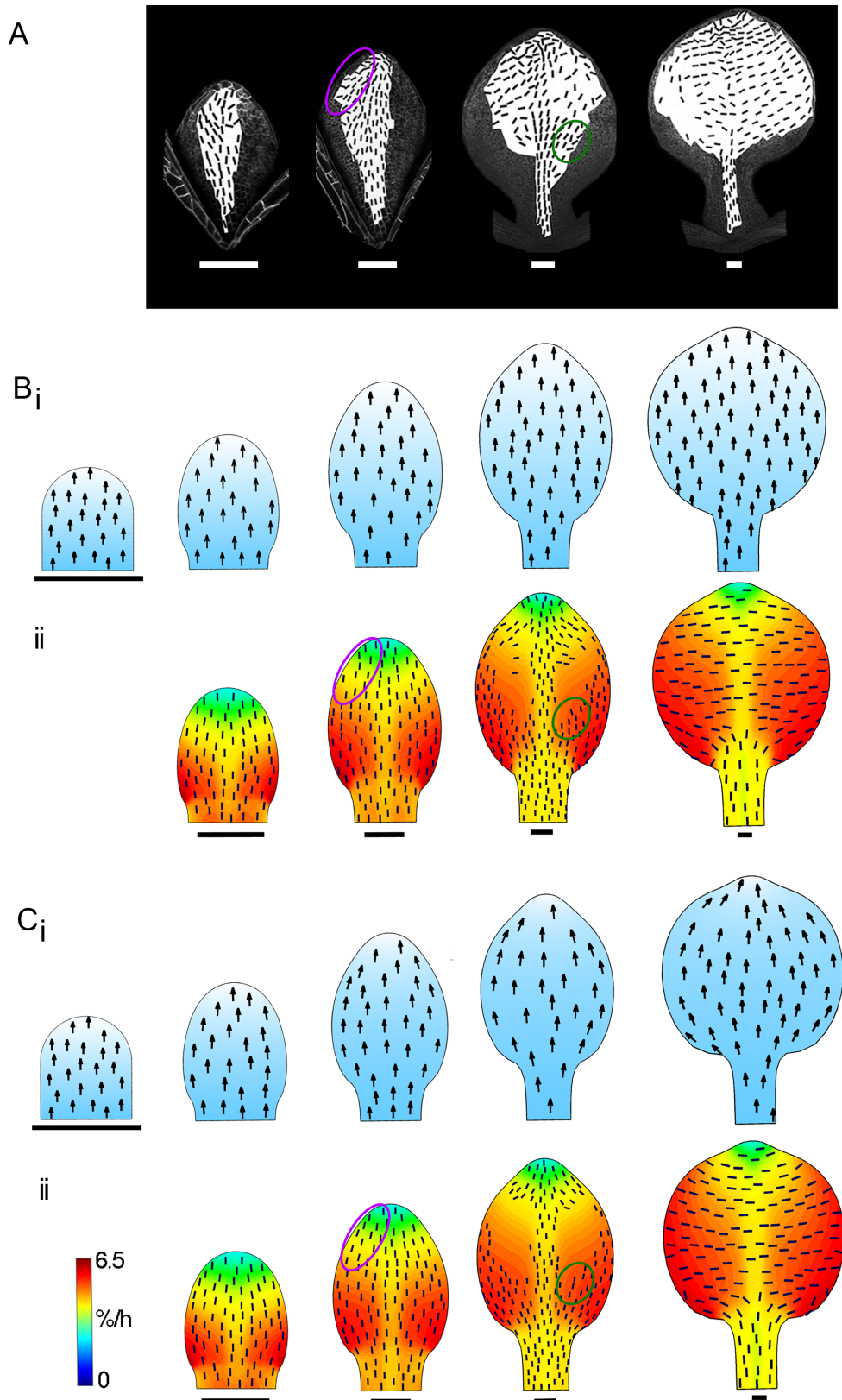


**Figure 2.33** **A**, principal orientations of growth displayed for regions with an anisotropy  $> 10\%$  showing leaves 5-8 days after initiation. **B-C**, model outputs at corresponding stages. **B**, non-deforming model and **C**, deforming model. **(i)** specified polarity field (arrows) according to the  $i_{POL}$  (blue) gradient. **(ii)** resultant canvas shapes, resultant growth rates (colours) and principal orientations of growth (black lines) displayed for regions with an anisotropy  $> 5\%$ . Coloured ellipses emphasise regions of discrepancy between observations and models. All areal growth rates and principal orientations of growth were calculated over 24  $h$  intervals. Scale bars 100  $\mu m$ .

### 2.2.10 Deforming Polarity

It was next tested whether a better match to the observed orientations of growth could be generated by a model in which the polarity field deforms with the canvas. In this deforming model, the polarity field was established as for the non-deforming model by placing a linear gradient of the polarity factor  $i_{POL}$  onto the initial canvas with highest  $i_{POL}$  levels at the base. In contrast to the non-deforming model,  $i_{POL}$  levels were maintained locally across the canvas and deformed with it. The gradient of  $i_{POL}$  determined the polarity field (Fig. 2.33C i).

The resultant canvas shapes and principal orientations of growth were similar to those observed with the non-deforming model. Orientations of the deforming model provided a slightly better match to observed orientations compared to those of the non-deforming model. Although, in the deforming model at early stages, orientations showed some convergence towards the distal tip, orientations were still largely aligned parallel to the midline (Fig. 2.33C ii and Fig. 2.34, pink ellipses). At later stages, however, orientations in the proximal regions splayed out away from the midline similar to those observed (Fig. 2.33A and C ii and Fig. 2.34, green ellipses). The difference in angles between the models and the data was further quantified by determining the overall orientation of growth in the ellipse regions (Tab. 2.1). This quantification was carried out by Richard Kennaway and showed that although the deforming model still did not match the data perfectly, it tends towards the right direction, while the non-deforming model showed almost opposite trends compared to the data (Fig. 2.34).

It thus appears that leaf polarity orientations change with the geometry of the tissue rather than being maintained during growth. The discrepancies between the models and observations in distal regions at early stages suggest that the polarity field of the leaf at stages corresponding to the starting canvas is not linear at the tip, but might already follow the geometry of the leaf.

### Angle of Orientation of Growth (in degrees)

Time	Observed Data	Non-deforming Model	Deforming Model
148 <i>h</i> (purple ellipses)	51.8, 46.2, 22.3	0.7	9.9
180 <i>h</i> (green ellipses)	37.7, 20.2, 64.7	-10.0	0.9

**Table 2.1** Quantification of the angles of the orientations of growth of the data (3 datasets), non-deforming and deforming model at the time points of the presented ellipses.

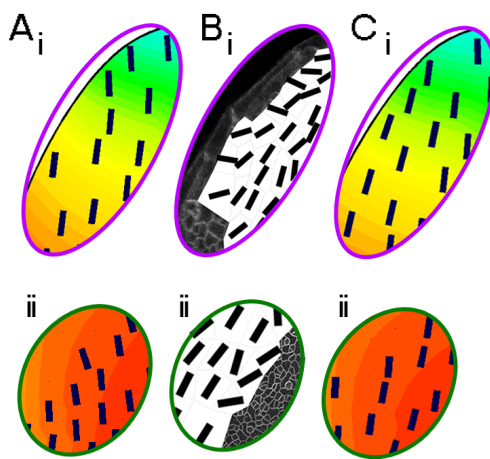


**Figure 2.34** Close up of principal orientations of growth of ellipse regions in Figure 2.33, (i) pink ellipses correspond to leaves 6 days after initiation and (ii) green ellipses to leaves 7 days after initiation. **A**, non-deforming model. **B**, tracking data. **C**, deforming model. Orientations are displayed for regions with an anisotropy  $> 5\%$  (model) or  $> 10\%$  (data). Orientations were calculated over 24 *h* intervals.

#### 2.2.11 Organiser-Based Polarity Systems

The polarity systems explored above deal with the question of how the polarity field might behave during growth. They do not, however, address the question of how a polarity field is established initially, since the polarity factor gradient was simply distributed across the canvas.

More mechanistically, a polarity field could be established by the propagation of a polarity factor. This is exemplified by the same square example canvas used above (2.2.8 Polarity Systems).

The polarity factor  $\mathbf{i}_{POL}$  was allowed to propagate, meriting a name change to  $\mathbf{s}_{POL}$ .  $\mathbf{s}_{POL}$  levels are regulated by a specific region of the tissue, where  $\mathbf{s}_{POL}$  is produced. This region therefore acts as an organiser of polarity. In this work, models with  $\mathbf{s}_{POL}$  propagation and organisers are termed organiser-based models.  $\mathbf{s}_{POL}$  is produced in a region defined by the expression of  $\mathbf{i}_{PROXORG}$  (proximal organiser):

$$\frac{\partial \mathbf{s}_{POL}}{\partial t} = D_{pol} \nabla^2 \mathbf{s}_{POL} - \mu_{pol} \mathbf{s}_{POL} + p_{pol} \mathbf{i}_{PROXORG}, \quad (2.19)$$

where  $D_{pol}$  is the diffusion rate and  $\mu_{pol}$  the decay rate of  $\mathbf{s}_{POL}$  throughout the canvas.  $p_{pol}$  is the production rate of  $\mathbf{s}_{POL}$  by  $\mathbf{i}_{PROXORG}$ .  $\mathbf{i}_{PROXORG}$  is expressed at the base of the canvas (Fig. 2.35B).  $\mathbf{s}_{POL}$  propagation from  $\mathbf{i}_{PROXORG}$  regions creates a polarity field parallel to the  $y$ -axis.  $\mathbf{s}_{POL}$  levels were allowed to establish before growth commenced. As in the examples above, a linear gradient of growth rates was specified across the canvas to promote  $K_{per}$ , while  $K_{par} = 0 \% h^{-1}$  (Fig. 2.35A).

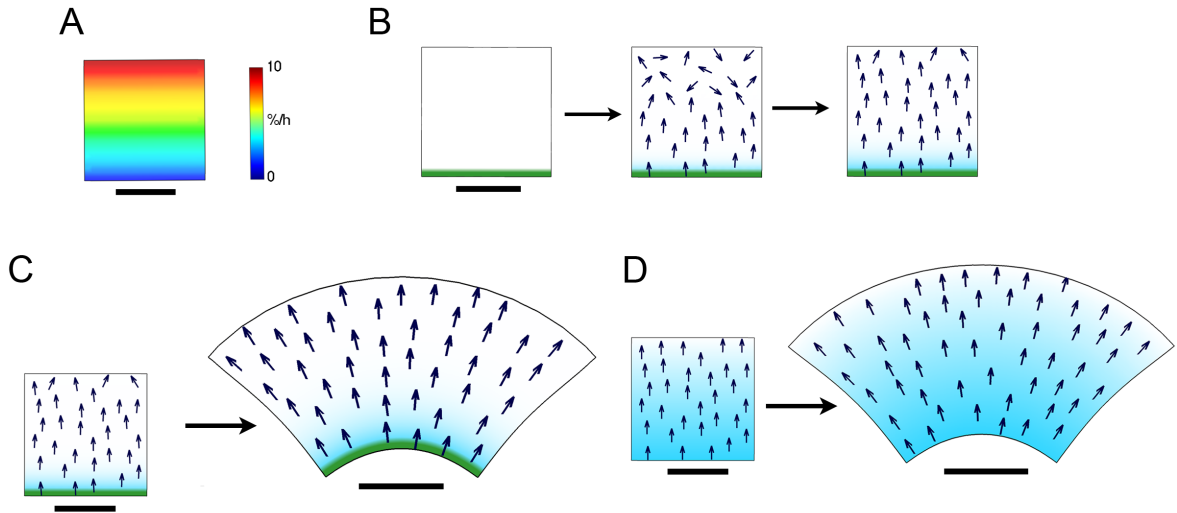


**Figure 2.35** **A**, linear gradient of growth rates specified across the initial canvas. **B**, polarity field (arrows) establishment using an organiser-based mechanism with  $\mathbf{s}_{POL}$  (blue) and  $\mathbf{i}_{PROXORG}$  (green). **C**, organiser-based model with a proximodistal polarity field (arrows) showing the initial canvas and the resultant canvas with  $\mathbf{s}_{POL}$  (blue) and  $\mathbf{i}_{PROXORG}$  (green). **D**, deforming model showing the initial canvas and the resultant canvas with the polarity field (arrows) and  $\mathbf{i}_{POL}$  (blue). Scale bars 1 mm.

Growing the canvas with this polarity field and growth interactions resulted in a canvas shape very similar to that of the deforming model (compare Fig. 2.35C and D). In both cases, the polarity field followed the shape of the canvas. However, unlike above, where a proximodistal gradient was imposed onto the canvas, the polarity field was established through propagation from an organiser.

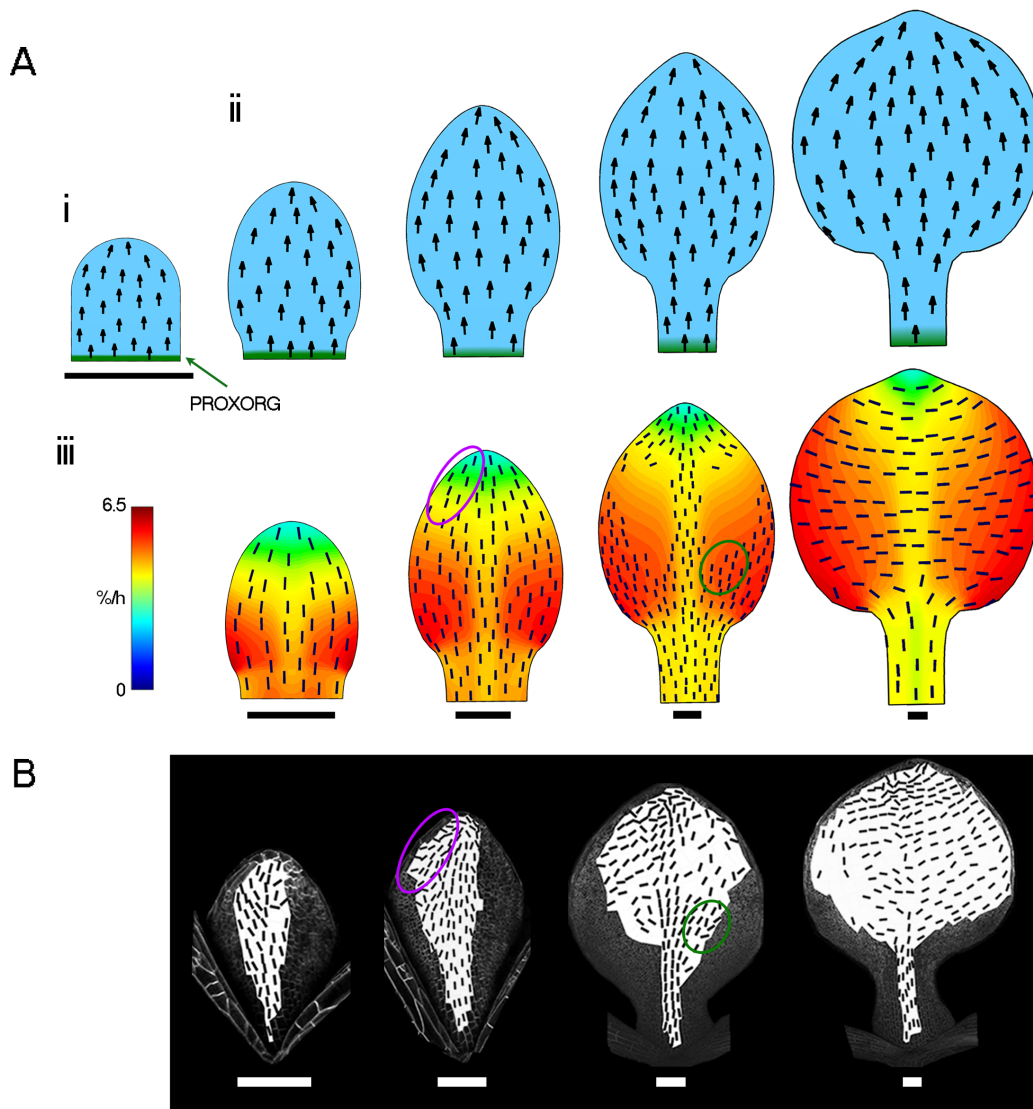


**Figure 2.36** **A**, fixed organiser-based leaf model. **(i)** a polarity field (arrows) is specified by the signalling factor  $SPOL$  (blue) produced by  $i_{PROXORG}$  (green) showing the initial canvas. **(ii)** the polarity field deforms with the geometry of the canvas. **(iii)** resultant canvas shapes with resultant areal growth rates (colours) and principal orientations of growth (black lines) displayed for regions with an anisotropy  $> 5\%$ . Resultant canvas shapes shown at stages corresponding to leaves in **B**. **B**, principal orientations of growth showing leaves 5-8 days after initiation. Principal orientations were displayed for regions with an anisotropy  $> 10\%$ . All growth rates and orientations were calculated over 24  $h$  intervals. Scale bars 100  $\mu m$ .

### 2.2.12 Organiser-Based Polarity Models

The leaf model with a deforming polarity system generated patterns comparable to those observed, indicating that the polarity field of the leaf deforms with the leaf geometry. However, it is unclear whether the polarity field is established early on, then becomes fixed to the tissue and unresponsive to any further polarisation signals (as assumed by the deforming model). Alternatively, it is possible that the tissue remains responsive to re-organisation signals and is able to readjust its polarity field accordingly.

Assuming that tissue polarity is controlled by the gradient of a polarity factor (as above), these options could be tested by allowing the polarity factor to propagate. Polarity factor propagation and production at a source would provide a mechanism of establishing a polarity field. The importance of continued tissue responsiveness to changes in the polarity factor gradient could be tested by either arresting propagating after the polarity field is established or continuing propagation throughout development.

An organiser-based mechanism was applied to establish a polarity field in the leaf model. In the first version of this organiser-based mechanism (fixed),  $\mathbf{s}_{POL}$  propagation was arrested after the polarity field had been established. In the second version (dynamic),  $\mathbf{s}_{POL}$  continued to propagate.

#### 2.2.12.1 Fixed Organiser-Based Polarity Model

An identity factor,  $\mathbf{i}_{PROXORG}$ , is expressed along the base of the canvas with a level of 1. Different from the example models above,  $\mathbf{s}_{POL}$  levels at the source, defined by  $\mathbf{i}_{PROXORG}$ , are maintained constant at a level specified by  $b_{pol}$ .  $\mathbf{s}_{POL}$  levels are specified according to the equation:

$$\frac{\partial \mathbf{s}_{POL}}{\partial t} = D_{pol} \nabla^2 \mathbf{s}_{POL} - \mu_{pol} \mathbf{s}_{POL}, \quad (2.20)$$

where  $D_{pol}$  is the diffusion rate and  $\mu_{pol}$  the decay rate of  $\mathbf{s}_{POL}$  throughout the canvas.  $\mathbf{s}_{POL}$  distribution is allowed to establish during the setup phase for 20  $h$  before growth commenced. Instead of the initial linear polarity field generated by the non-deforming and deforming models, the organiser-based

system generated a curvilinear polarity field (Fig. 2.36A i). This polarity field was parallel to the midline in proximal regions but converged towards the distal tip. The shape of the POL gradient was limited by the geometry of the dome-shaped primordium.

After this polarity field establishment (before growth), the polarity directions were locked to the canvas by setting  $s_{POL}$  diffusion and decay to zero. This model was termed the fixed organiser-based model. Thus, the deforming model and fixed organiser-based model only differed in the orientations of the initial polarity field in the distal half of the canvas. In both cases, the polarity field deformed with the geometry of the canvas (Fig. 2.36A ii).

The resultant canvas shapes and growth orientations were very similar to those of the deforming model (Fig. 2.33C ii and Fig. 2.36A iii). However, at early stages orientations did converge towards the tip as has been observed for the real leaves (Fig. 2.36A iii and B, pink ellipses).

#### 2.2.12.1.1 Model Anisotropy Patterns

Another way to verify the ability of this fixed organiser-based model to account for leaf growth was to compare the anisotropy of the model to that observed. In both cases, the anisotropy was calculated as  $\frac{K_{max}-K_{min}}{K_{max}}$ .

Observed and modelled anisotropy were higher in the petiole region and lower in the lateral regions (Fig. 2.37). In the model, anisotropy decreased during development, but increased again at later stages, probably reflecting the change in the principal orientations of growth. The anisotropy in the real leaf also decreased with time, although an increase in anisotropy at later stages was not evident.

The fixed organiser-based model was able to capture the general dynamics of growth rates, orientations and anisotropy. In this model, the polarity field deformed with the geometry of the canvas. However, it is possible that similar patterns can be obtained by a system in which the tissue continues to respond

to changes in the  $s_{POL}$  gradient, but that this gradient is not reorganised during development.

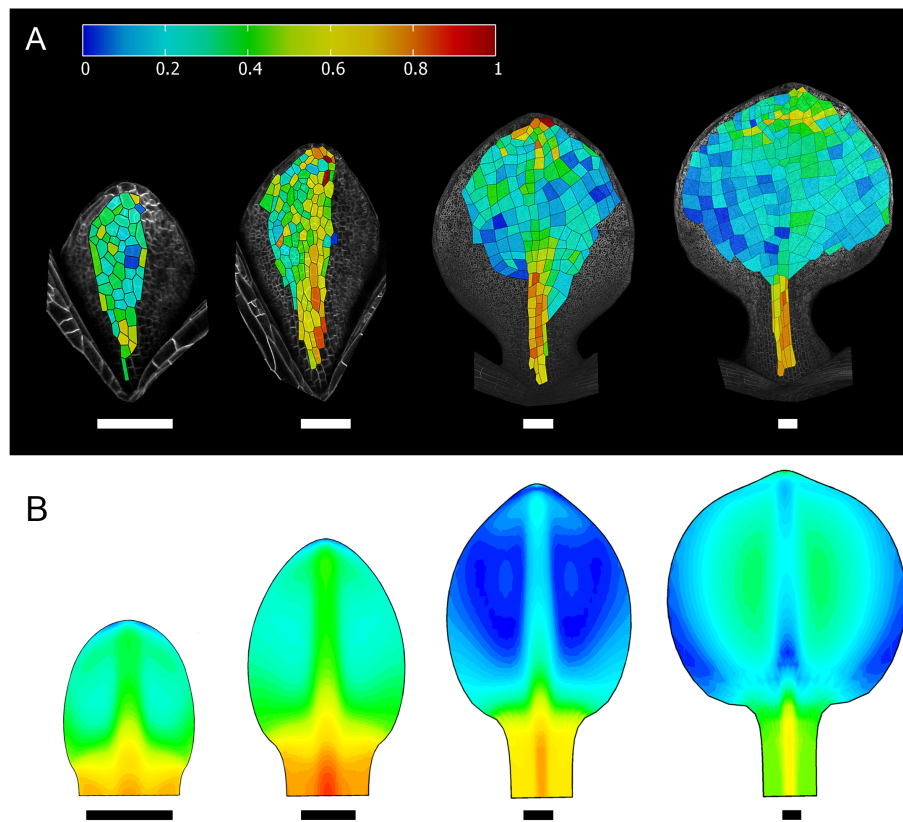


**Figure 2.37** Leaf and model anisotropy. **A**, leaf anisotropy showing leaves 5-8 days after initiation **B**, anisotropy of the fixed organiser-based model shown at comparable times as in **A**. Anisotropy was calculated over 24  $h$  intervals. Scale bars 100  $\mu m$ .

### 2.2.12.2 Dynamic Organiser-Based Polarity Model

The growth patterns generated by an organiser-based system with a fixed polarity field were compared to those generated by a dynamic organiser-based model version, in which the polarity field is continuously aligned according to the gradient of  $s_{POL}$ . In this model,  $s_{POL}$  propagation and decay were maintained throughout the simulation (Fig. 2.38A i).

The resultant canvas shapes, areal growth rates and principal orientations of growth were very similar to those of the fixed organiser-based model (compare Fig. 2.36A iii and Fig. 2.38A ii). However, it is possible that these patterns were so similar to the fixed model, because the propagation rate was so low that there were few local changes in the  $s_{POL}$  gradient during the period modelled.

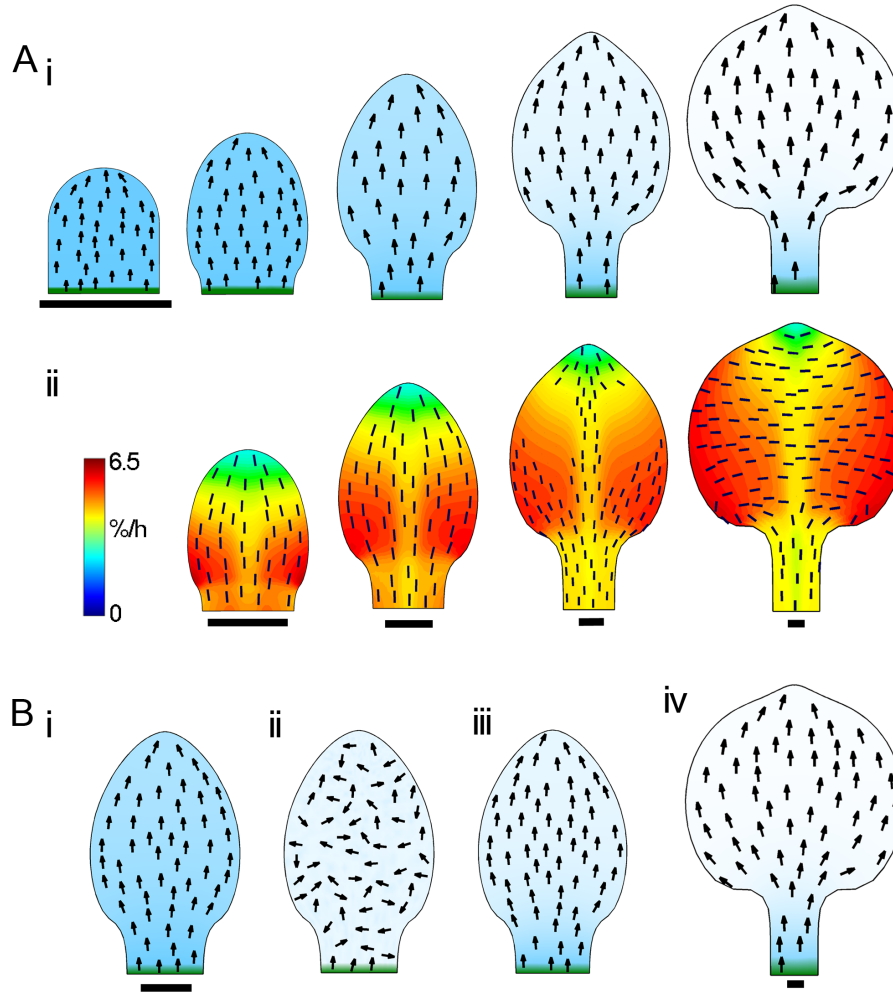


**Figure 2.38** Dynamic organiser-based model with  $s_{POL}$  (blue) diffusion throughout growth and readjusting polarity orientations (arrows) **A(i)**, specified polarity on resultant canvas shapes and **(ii)** resultant areal growth rates with principal orientations of growth (black lines) displayed for regions with an anisotropy  $> 5\%$ . Areal growth rates and orientations were calculated over  $24\ h$  intervals. Canvas shapes are shown at times corresponding to leaves 4-8 days after initiation. **B**, transient reduction and redistribution of  $s_{POL}$  (blue) levels except at  $i_{PROXORG}$  (green) showing the canvas corresponding to a leaf 6 days after initiation with the polarity field (arrows) **(i)** before, **(ii)** just after and **(iii)**  $1\ h$  after  $s_{POL}$  transient removal. **(iv)** final canvas shape with re-established polarity field corresponding to a leaf on day 8. Scale bars  $100\ \mu m$ .

To show that  $s_{POL}$  propagation was sufficient to coordinate polarity throughout the simulation,  $s_{POL}$  levels were reduced by a quarter and randomised throughout the canvas, except in regions expressing  $i_{PROXORG}$ , at  $148\ h$  (day 6; Fig. 2.38B ii). This resulted in an immediate loss of polarity. However, the proximodistal polarity field was quickly re-established ( $< 1\ h$ ) by  $s_{POL}$  diffusion from  $i_{PROXORG}$  according to Equation 2.20 (Fig. 2.38B iii). The final

polarity field was very similar to that of the dynamic organiser-based model without transient removal (compare Fig. 2.38A i and 2.38B iv). Thus, even at continued and high propagation of  $s_{POL}$ , the polarity field deforms with the canvas, as propagation is limited by the geometry of the canvas.

### 2.2.12.3 Organiser Positioning

The importance of the positioning of polarity organisers was investigated by attempting to reproduce the observed principal orientations of growth patterns with models, in which the polarity organiser was repositioned. In the three models presented below, the polarity field remained dynamic throughout the simulation.

#### 2.2.12.3.1 Reversed Polarity Field

First,  $i_{PROXORG}$  was expressed at the tip instead of the base (Fig. 2.39A i). The propagation and decay rates of  $s_{POL}$  were the same as for the organiser-based models above. The overall resultant canvas shapes and the principal orientations of growth compared well to those observed by time lapse imaging (compare Fig. 2.36B and 2.39A ii). There were very slight differences in the principal orientations of growth in the proximal regions between this tip-organiser model and the base-organiser models shown above (Fig. 2.36A ii, Fig. 2.38 A ii and 2.39A ii).

#### 2.2.12.3.2 Rotated Polarity Field

The observed principal orientations of growth at early stages of leaf development suggest that one of the axes of growth follows a proximodistal orientation (Fig. 2.36B). Therefore, in all leaf models above, the underlying polarity field had a proximodistal orientation with the second axis of growth being specified perpendicular to it. However, proximodistal growth orientations could also be established by a polarity field with a mediolateral organisation. In this case, the direction of the polarity field would not reflect the orientations of principal growth at early stages. Instead the orientations are specified along

the axis perpendicular to the polarity. The ability of such a model to generate the correct growth patterns was verified by expressing  $\mathbf{i}_{PROXORG}$  along the midvein of the leaf canvas (midvein-organiser model; Fig. 2.39B i). To account for the shorter axis of leaf width compared to leaf length, the diffusion rate of  $\mathbf{s}_{POL}$ ,  $D_{pol}$ , was reduced to  $2.5 \times 10^{-6} \text{ mm}^2 \text{ h}^{-1}$  (compared to  $0.01 \text{ mm}^2 \text{ h}^{-1}$ ). This generated a polarity field oriented roughly perpendicular to the midvein in the main part of the canvas (Fig. 2.39B i). In distal regions the polarity field splayed out from the midvein. To generate the correct growth patterns the definitions of  $K_{par}$  and  $K_{per}$  were switched compared to those in Equations 2.15 and 2.18, so that  $K_{par}$  was defined by the equation for  $K_{per}$  and vice versa:

$$K_{par} = p_{lam} \mathbf{i}_{LAM} \cdot \text{inh}(h_{mid}, \mathbf{i}_{MID}) \cdot \text{pro}(p_{late}, \mathbf{i}_{LATE}) \quad (2.21)$$

$$K_{per} = p_{prox} \mathbf{i}_{PROX} \cdot \text{inh}(h_{late}, \mathbf{i}_{LATE}), \quad (2.22)$$

where  $p_{lam}$  and  $p_{late}$  are the promotion of  $K_{par}$  by  $\mathbf{i}_{LAM}$  and  $\mathbf{i}_{LATE}$ , respectively. The levels of  $\mathbf{i}_{LAM}$  are high in the proximal lamina regions and low in the very proximal regions of the canvas.  $\mathbf{i}_{LATE}$  is expressed uniformly throughout the canvas and increases linearly after day 6.  $h_{mid}$  is the inhibition of  $K_{par}$  by  $\mathbf{i}_{MID}$ , which is expressed in the central, midline region of the canvas.  $p_{prox}$  is the promotion of  $K_{per}$  by  $\mathbf{i}_{PROX}$ , which has a linear gradient with highest levels at the base, and  $h_{late}$  is the inhibition of  $K_{per}$  by  $\mathbf{i}_{LATE}$ .

Using the same parameters as for the proximodistal polarity field models, the resultant canvas shapes were slightly broader than those of the other organiser-based models. Initially the polarity directions in the proximal regions were oriented parallel to the canvas base. However, during growth orientations deformed with the canvas. This was at least partially due to the low diffusion rate of  $\mathbf{s}_{POL}$  (whilst maintaining the same decay and production rate as in the other models), which resulted in a largely local maintenance of the polarity field at later stages. The resultant growth orientations matched well to those observed for the leaves (Fig. 2.39B ii). However, at the distal end, resultant growth tensors were oriented parallel to the canvas margins resulting in distal canvas tips rounder than those observed.

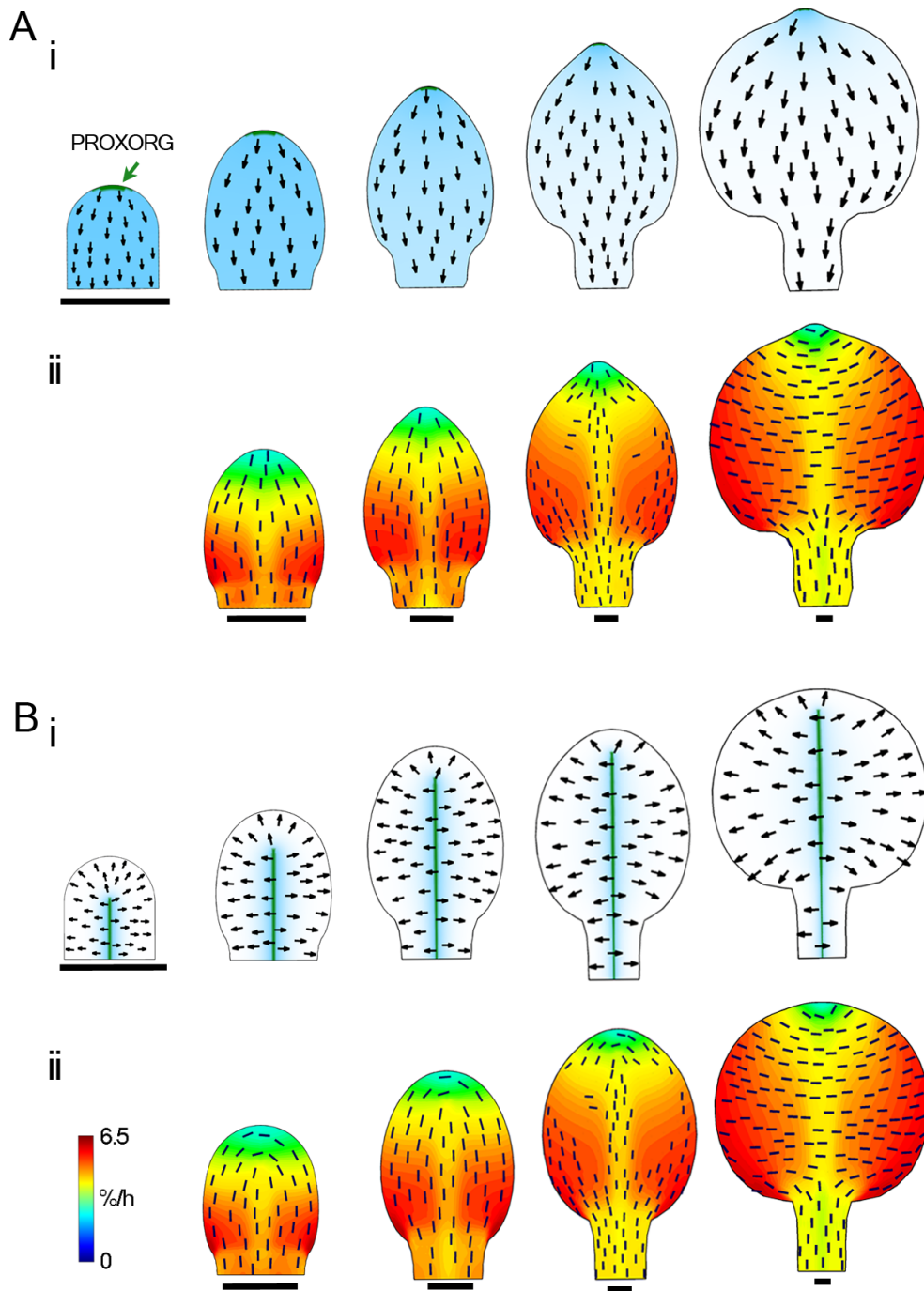


**Figure 2.39** Repositioned polarity organiser models. **A**, tip-organiser model and **B**, midvein-organiser model showing (i) specified polarity field (arrows) with  $s_{POL}$  (blue) and  $i_{PROXORG}$  (green) and (ii) resultant areal growth rates (colours) with principal orientations of growth (black lines) displayed for regions with an anisotropy  $> 5\%$ . Modelled growth rates and principal orientations of growth were calculated over 24  $h$  intervals. Scale bars 100  $\mu m$ .

### 2.2.12.3.3 Organiser-Based Non-Deforming Model

The large influence of canvas geometry on the underlying polarity field raised the question whether it is possible to create a non-deforming polarity field using an organiser-based model at the modelling scale employed here. In the non-deforming model above (2.2.9 Non-Deforming Polarity Model) the polarity field was specified parallel to the midline and re-established at every iteration.

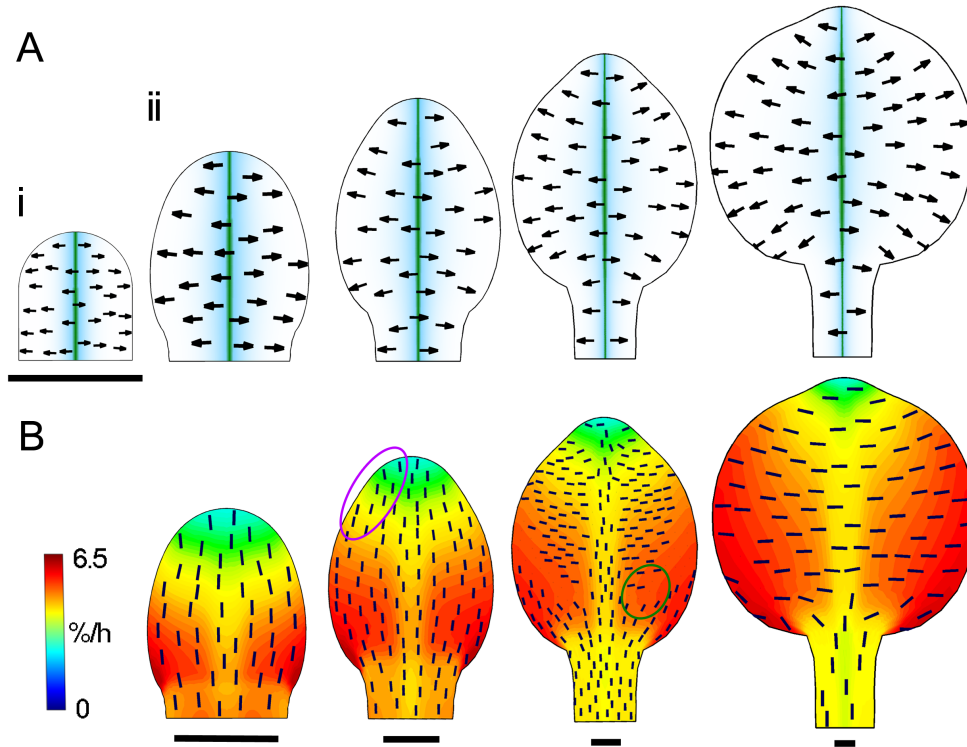


**Figure 2.40** Midline-organiser model showing **A**, polarity field (arrows) with  $s_{POL}$  (blue) and  $i_{PROXORG}$  (green). **B**, resultant areal growth rates (colours) with principal orientations of growth (black lines) displayed for regions with an anisotropy > 5 %. Growth rates and orientations were calculated over 24 h intervals. Scale bars 100  $\mu m$ .

By expressing  $i_{PROXORG}$  along the midline of the canvas it was possible to generate a polarity field perpendicular to the midline (midline-organiser model; Fig. 2.40A i). During early stages of growth this polarity field was roughly maintained parallel to the canvas base, but at later stages also deformed with the canvas shape (Fig. 2.40A ii). The resultant principal orientations of growth showed a similar pattern. At early stages orientations in the distal regions failed to converge towards the leaf tip, similar to the non-deforming model (compare Fig. 2.33B ii and Fig. 2.40B, pink ellipses). At later stages,

however, orientations splayed out away from the midvein as has been observed for the real leaves (compare Fig. 2.36B and 2.40B, green ellipses).

Thus, variations in the position of organisers may yield polarity fields and resultant principal orientations of growth comparable to those observed. However, coordinating growth through proximodistal polarity systems generated slightly better matching principal orientations of growth patterns or canvas shapes and models were substantially less sensitive to the diffusion coefficient of  $s_{POL}$ . The feedback of canvas geometry on polarity makes the maintenance of polarity orientations during growth difficult. This was the case for the mechanisms explored here, where the polarity field was coordinated by one polarity organiser only. However, it is possible that more elaborate combinations of different localisations and types of tissue organisers or more cell-based models could create a non-deforming polarity system, as has been suggested for the *Antirrhinum* petal, where the polarity field is maintained during development (Coen et al., 2004; Green et al., 2010). The results obtained here, suggest that growth orientations are not maintained during development but deform with the geometry of the tissue. However, based on the data available it was not possible to distinguish between models in which the polarity field was either fixed early or dynamically adjusts according to the  $s_{POL}$  gradient.

### 2.2.13 Testing the Model

The ability of the proximodistal organiser-based models to account for leaf growth dynamics was tested by comparing model performance against experimental data from clonal analysis and leaf surgery. The data from these experiments was generated by Samantha Fox, unless indicated otherwise.

#### 2.2.13.1 Clonal Analysis

Clonal analysis provides information on the local growth dynamics of a tissue. As leaves can be removed from the plant and flattened clonal analysis allows growth data for margin regions to be obtained, which are less accessible by time lapse imaging due to the curvature of the leaf.

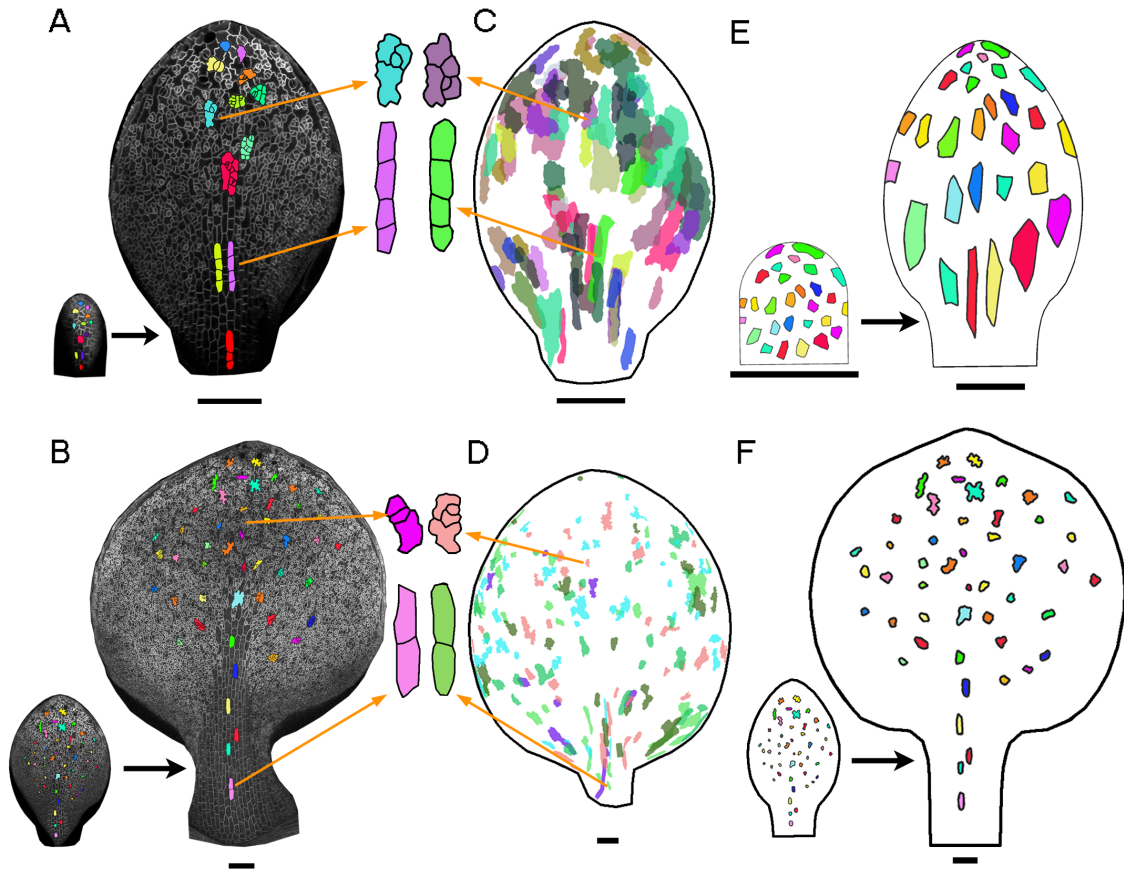


**Figure 2.41** Clonal analysis. **A-B**, tracked leaves with selected cell lineages followed from **A**, day 4 to day 6 and **B**, day 6 to day 8 after leaf initiation. **C-D**, clonal analysis showing mean leaf shapes and warped clones. Colours represent data from individual leaves. Clones were **A**, induced on day 3 and imaged on day 6 and **B**, induced on day 6 and imaged on day 9 after leaf initiation. **E-F**, fixed organiser-based model with cell outlines projected onto the model and grown with it for corresponding developmental periods **E**, day 3 to day 6 and **F**, day 6 to day 8. Scale bars 100  $\mu m$ .

Here, clones were generated using lines carrying a *GFP* heat-shock inducible Cre-Lox line (Gallois et al., 2002). The exposure of plants to a short period of elevated temperatures resulted in GFP expression in random cells across the leaf. During cell division GFP expression is passed on to the daughter cells creating patches of GFP expressing cells. Clone size and orientation reflect the local growth dynamics of the leaf over the period analysed (Rolland-Lagan et al., 2003). Leaves were heat shocked 3 and 6 days after initiation and imaged 6 and 9 days after initiation, respectively. For this analysis, leaves were chosen based on their correct age as well as width, in accordance with the generated growth curve (2.2.1 Leaf Growth Dynamics). These times corresponded

to the developmental age of the leaves subjected to time lapse imaging. Large datasets of leaves with clonal patterns were generated for the individual clonal analysis experiments. The leaf shapes in each dataset were used to calculate the mean leaf shapes on day 6 and 9 after initiation using the *Sector Analysis Toolbox*. For each dataset, observed clonal shapes were then warped to these mean shapes (Fig. 2.41C and D).

Clones generated over a developmental period from day 3 to 6 after leaf initiation were narrow in the petiole and midvein regions (Fig. 2.41C). Clones followed the geometry of the leaf and splayed out away from the midvein in the proximal lamina regions, while converging towards the leaf tip. Similar patterns could be observed for clones generated between day 6 and 9 of leaf development (Fig. 2.41D). Although by that time the rate of cell divisions had slowed down, resulting in small clones consisting of one or few cells only.

These clonal patterns were compared to the time lapse imaging data by following selected cell lineages over the tracking period (Fig. 2.41A and B). Clonal patterns and cell lineages compared well in the trackable central regions of the leaf.

The experimental results were compared to virtual clones generated by the fixed organiser-based model. Although the *GFTbox* implementation does not consider cells directly, it is possible to superimpose a cell layer on top of the canvas. This layer is locked to the canvas and therefore grows and deforms with the underlying growth interactions. The superimposed cell layer was made up of cell outlines of leaves of comparable ages as the clonal and tracking data. For the 3 day old leaf, cell shapes were extracted from the flattened leaf, which had served as a template for the initial canvas (Fig. 2.26B). For the 6 day old leaf, cell shapes were extracted from one of the tracked leaves on day 6 (Fig. 2.41B, small leaf). Cell outlines were extracted by placing a large number of points ( $n \approx 20$ ) around the cell outline using *Point Tracker*. The position of each cell, as stored by *Point Tracker* was loaded into the *GFTbox*. The cell outlines were projected onto the canvas at corresponding times and positions (Fig. 2.41E and F). Overall, the virtual clones generated compared

well to the experimental ones. Clones were narrower in the petiole and mid-vein region and followed the geometry of the canvas. Thus, clonal analysis not only served to support the validity of the model to capture leaf growth but also provided a means of verifying the time lapse imaging data.

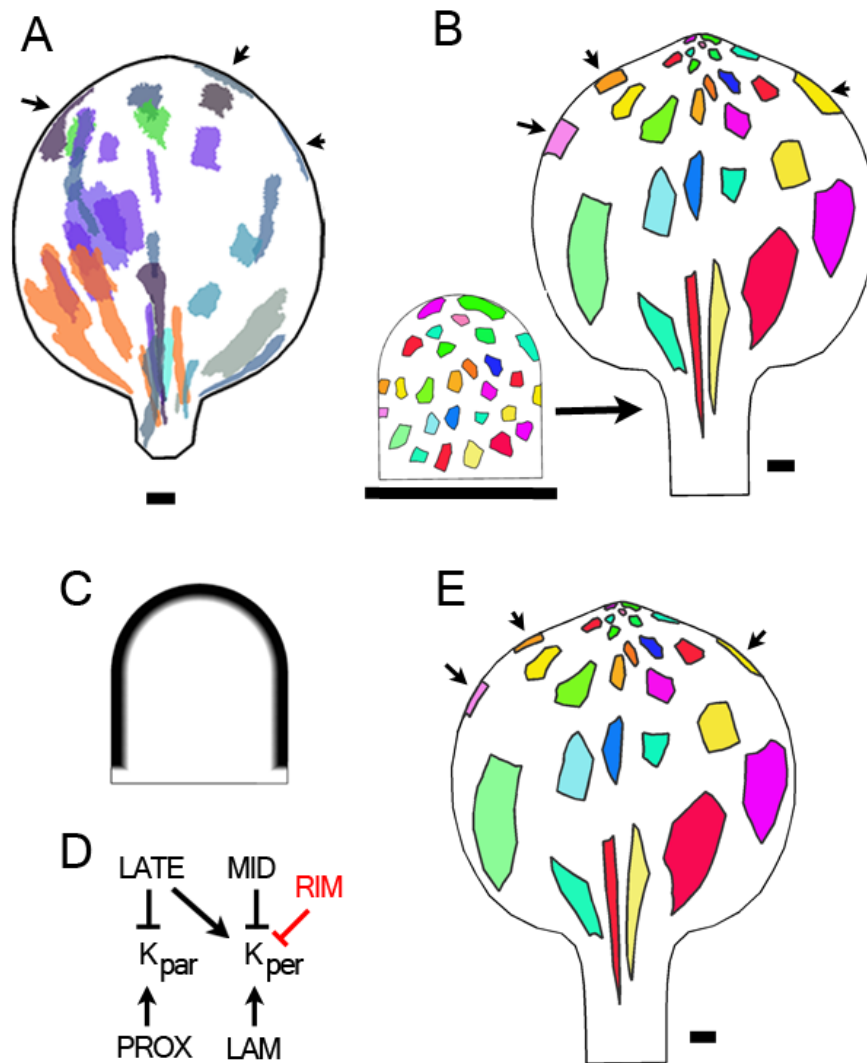


**Figure 2.42** **A**, clonal analysis of leaves heat shocked on day 3 and imaged on day 9 showing calculated mean leaf shape on day 9 with warped clones. Colours represent data from individual leaves. Clones at the leaf margins are narrow (black arrows). **B**, fixed organiser-based model with cell shapes from a 3-day old primordium projected onto the canvas, which was grown for a comparable developmental period as **A**. Modelled margin clones are not narrow (black arrows). **C-E**, margin model with fixed-organiser based polarity system showing **C**, the distribution of  $i_{RIM}$  on the initial canvas, **D**, the growth interaction network and **E**, the resultant canvas shape with superimposed cell shapes grown for the same developmental period as in **B**. Scale bars 100  $\mu m$ .

As a further test, experimental and virtual clones were induced on day 3 after leaf initiation and imaged on day 9 (Fig. 2.42A and B). Observing clones over such a long period of time revealed a clear gradient in clone sizes with bigger proximal and smaller distal clones in both experiments and model. However, experimental clones were clearly narrower along the margins than those predicted by the model (Fig. 2.42A and B, black arrows). Narrow marginal clones have also been observed in tobacco and *Xanthium* leaves (Erickson, 1966; Poethig and Sussex, 1985). Therefore, to generate a more accurate model of leaf development another identity factor,  $\mathbf{i}_{RIM}$ , was introduced along the margins of the canvas (Fig. 2.42C).  $\mathbf{i}_{RIM}$  inhibits  $K_{per}$  along the margins (Fig. 2.42D). The previous equation of  $K_{per}$  (Eqn. 2.18) was modified to:

$$K_{per} = plam \mathbf{i}_{LAM} \cdot \text{inh}(h_{mid}, \mathbf{i}_{MID}) \cdot \text{pro}(plate, \mathbf{i}_{LATE}) \cdot \text{inh}(h_{rim}, \mathbf{i}_{RIM}), \quad (2.23)$$

where  $h_{rim}$  is the inhibition of  $K_{per}$  by  $\mathbf{i}_{RIM}$ .

The resulting model had narrow marginal clones (Fig. 2.42E, black arrows), which better matched the observations. Models with a proximodistal organiser-based polarity field and with  $K_{per}$  restrictions in the margins, were termed margin models and used in all further work.

### 2.2.13.2 Leaf Surgery

One assumption of the leaf model is that the spatial patterns of growth rates are established early in leaf development and deform with the canvas. This assumption has been tested by leaf surgery. If growth patterns are indeed determined early, the excision of parts of the leaf should not have any effect on overall growth patterns. Surgery was performed on the margin model with either fixed or dynamic  $s_{POL}$  propagation. Thereby leaf surgery was also used to try and distinguish between the two organiser-based model versions, fixed and dynamic.

Three different types of cuts were performed on the models and the results compared to cuts repeated experimentally. Canvas and leaf surgery were carried out on leaves 6 days after initiation.

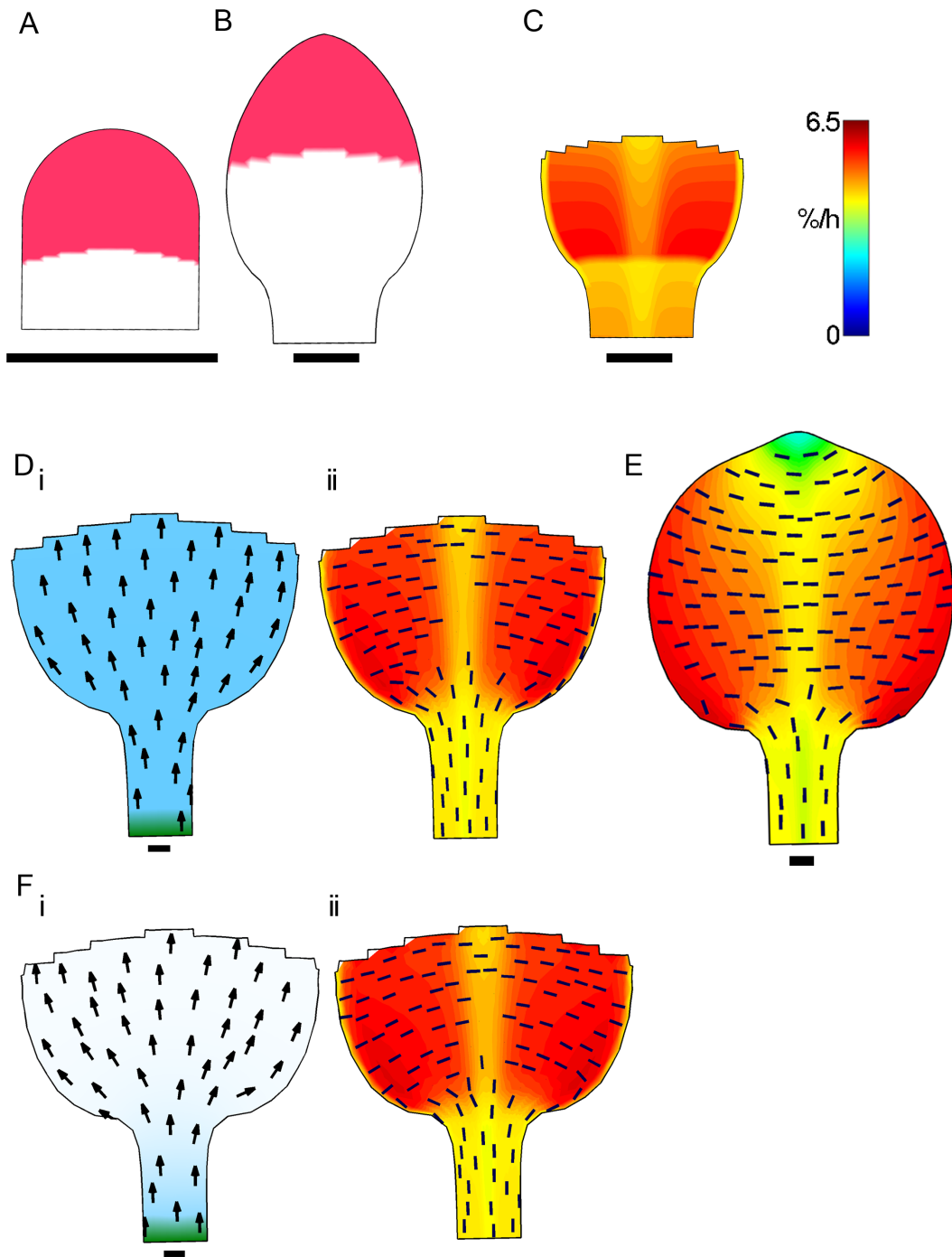


**Figure 2.43** Modelled distal excision **A**, distribution of  $i_{DISTAL}$  on the initial canvas. **B**, distribution of  $i_{DISTAL}$  on the canvas just prior to excision. **C**, remaining canvas half after removal of regions expressing  $i_{DISTAL}$  on day 6 showing specified areal growth rates. **D** and **F**, the remaining canvas grown to a time corresponding to a leaf age of 8 days with **D**, fixed  $s_{POL}$  propagation and **F**, dynamic  $s_{POL}$  propagation. **(i)** polarity field (arrows) with  $s_{POL}$  (blue) and  $i_{PROXORG}$  (green), **(ii)** areal growth rates (colours) and principal orientations of growth (black lines) for regions with an anisotropy  $> 5\%$ . **E**, corresponding uncut canvas with resultant areal growth rates (colours) and principal orientations of growth (black lines) for regions with an anisotropy  $> 5\%$ . All resultant areal growth rates and principal orientations of growth were calculated over 24  $h$  intervals. Scale bars 100  $\mu m$ .

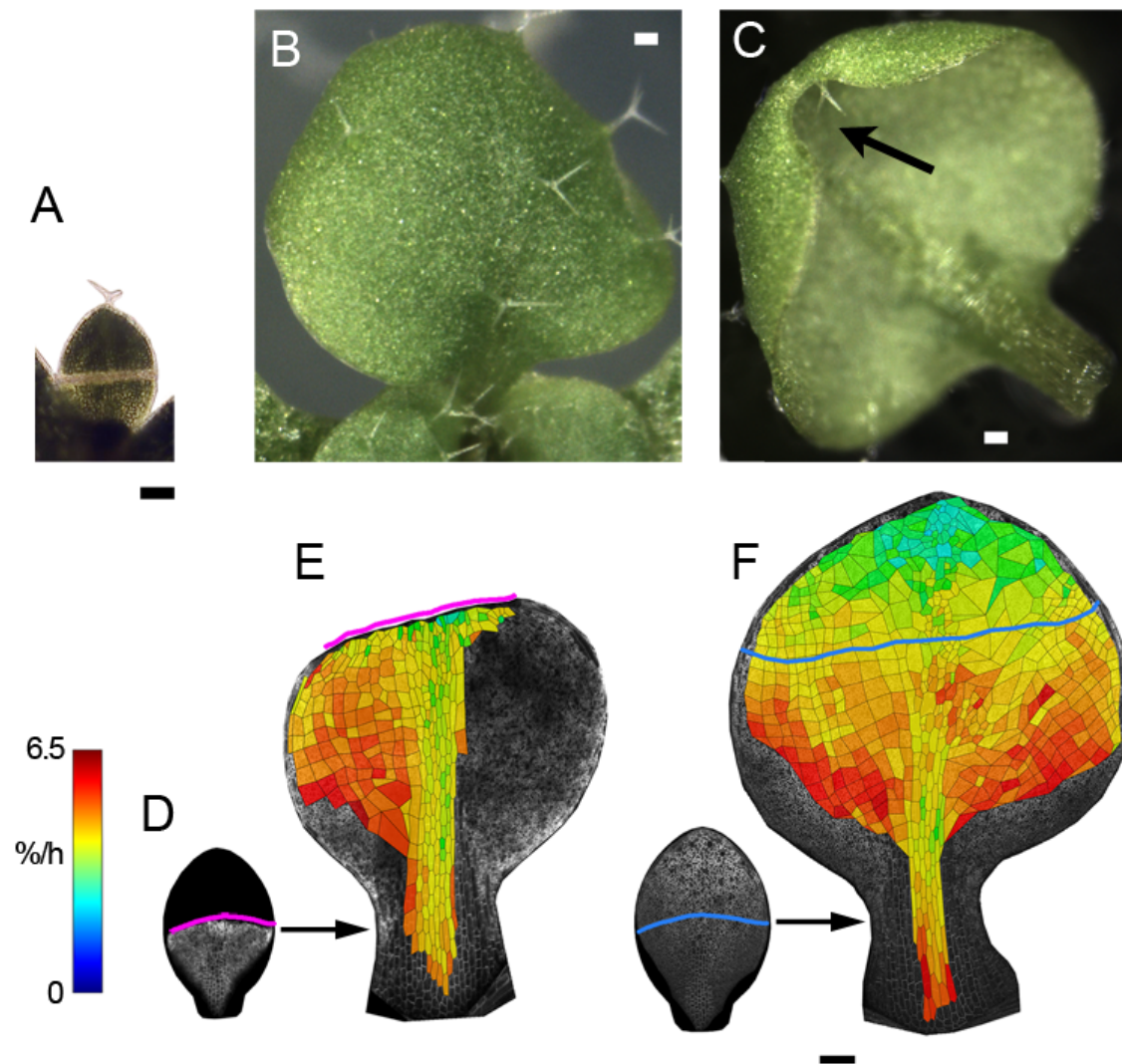


**Figure 2.44** **A**, the distal half of the leaf was excised 6 days after leaf initiation using a laser. **B-C**, cut leaves were grown to day 12 showing **B**, the adaxial side and **C**, the abaxial side. **D**, the distal half of the leaf was excised 6 days after leaf initiation using a laser and leaves were tracked up to **E**, day 9 showing resultant areal growth rates calculated over a 24 *h* interval. The pink line marks the cut edge. **F**, corresponding uncut leaf on day 9 showing resultant areal growth rates calculated over a 24 *h* interval. Position of the cut edge on the uncut leaf is indicated by the blue line. The figure was generated by Samantha Fox. Scale bars 100  $\mu\text{m}$ .

### 2.2.13.2.1 Distal Excision

In the first test, the distal half of the canvas lamina was excised. During model setup the distal part of the canvas was marked by an identity factor,  $i_{DISTAL}$  (Fig. 2.43A). At 148 *h* (end of day 6) half of the canvas lamina expressed  $i_{DISTAL}$  (Fig. 2.43B). These regions were removed from the canvas (Fig. 2.43C) and the remaining canvas was grown for a further 3 days (here

57 h; Fig. 2.43D and F). As expected from the modelled growth interactions, there were no changes in the regional growth rates compared to a corresponding uncut canvas (Fig. 2.43E) in neither the fixed organiser-based model (Fig. 2.43D) nor the dynamic organiser-based model (Fig. 2.43F).

Unfortunately, these results contradicted earlier reports of leaf growth, which claimed that leaves are able to regenerate after distal excision (Sena et al., 2009), thus questioning the validity of the leaf model. Therefore, leaf excision was repeated experimentally to resolve this discrepancy.

#### **2.2.13.2.1.1 Distal Leaf Excision**

In a previous experiment Sena et al. (2009) showed that leaves are able to regenerate following removal of the distal half of the leaf at early developmental stages. Here their experiment was repeated. The distal half of leaves 6 days after initiation was surgically removed using laser ablation (Fig. 2.44A). Leaves were grown for 6 days after excision. The leaf shape after this period appeared normal from above (adaxial view, Fig. 2.44B). However, when turned over, the cut edge was clearly visible (abaxial view, Fig. 2.44C). Measuring the length of the cut edge at cutting and after 6 days of growth showed that the cut edge grew little over this period (measuring 0.3 mm and 0.4 mm, respectively).

To investigate growth of the cut edge more closely, Samantha Fox and I tracked leaves following distal excision. The distal half of the leaf lamina was surgically removed with a laser on day 6 (Fig. 2.44D). The leaf was then tracked for the following 3 days of growth (Fig. 2.44E). The spatial patterns of growth were similar to those of a control uncut leaf (Fig. 2.44F), except at the cut where growth was reduced (Fig. 2.44E, pink line). The cut edge was relatively flat and parallel to the leaf base after this period of growth, rather than curved as after 6 days of growth (Fig. 2.44 C). This might partially be due to growth in the tracking chamber, where leaves are less free to curve.

### 2.2.13.2.1.2 Restricted Cut Edge

The distal excision model above generated a similar sized lamina to the excised real leaf, but with a very wide cut edge. Therefore, according to leaf excision observations, growth along the cut edge was restricted in the model after excision. An additional identity factor,  $\mathbf{i}_{INC}$  (inhibitor induced by cut), was expressed at the cut edge, which reduced the areal growth rates at the cut edge following excision (Fig. 2.45A and B):

$$\begin{aligned}
 K_{par} &= p_{prox} \mathbf{i}_{PROX} \cdot \text{inh}(h_{late}, \mathbf{i}_{LATE}) \cdot \text{inh}(h_{inc}, \mathbf{i}_{INC}) \\
 K_{per} &= p_{lam} \mathbf{i}_{LAM} \cdot \text{inh}(h_{mid}, \mathbf{i}_{MID}) \cdot \text{pro}(p_{late}, \mathbf{i}_{LATE}) \\
 &\quad \cdot \text{inh}(h_{rim}, \mathbf{i}_{RIM}) \cdot \text{inh}(h_{inc}, \mathbf{i}_{INC}), \tag{2.24}
 \end{aligned}$$

where,  $h_{inc}$  is the amount of inhibition by  $\mathbf{i}_{INC}$  of both  $K_{par}$  and  $K_{per}$ . Excision and inhibition at the cut edge were implemented for both the fixed (Fig. 2.45D) and the dynamic (Fig. 2.45E) polarity models. Both models generated resultant leaf shapes that compared well to that observed (Fig. 2.45C). Similar to the real leaf growth orientations, modelled orientations near the cut edge pointed towards the cut (Fig. 2.45D ii and E ii). However, the extent of reorientation was greater in the dynamic model than the fixed model. This difference is a result of the subtle differences in the underlying polarity fields (Fig. 2.45D i and E i). In the case of the fixed model, the polarity field was unaffected by the cut, whereas in the dynamic model, the polarity field readjusted to the new canvas geometry. The more extensive reorientations in growth directions of the dynamic model provided a better match to the observed leaf growth orientations, suggesting that the polarity field is able to readjust to changes in leaf geometry at later stages and therefore not fixed at early stages.

The apparent regeneration of the leaf claimed previously seems to be an artifact resulting from reduced growth at the cut edge (making it more difficult to discern at later stages) combined with growth mainly occurring in the proximal regions of the leaf (Fig. 2.46). Therefore, with a slight modification, the leaf models were able to predict changes in the resultant canvas shapes, areal growth rates and principal orientations of growth following leaf excision.

The model were validated with to two further types of cuts.

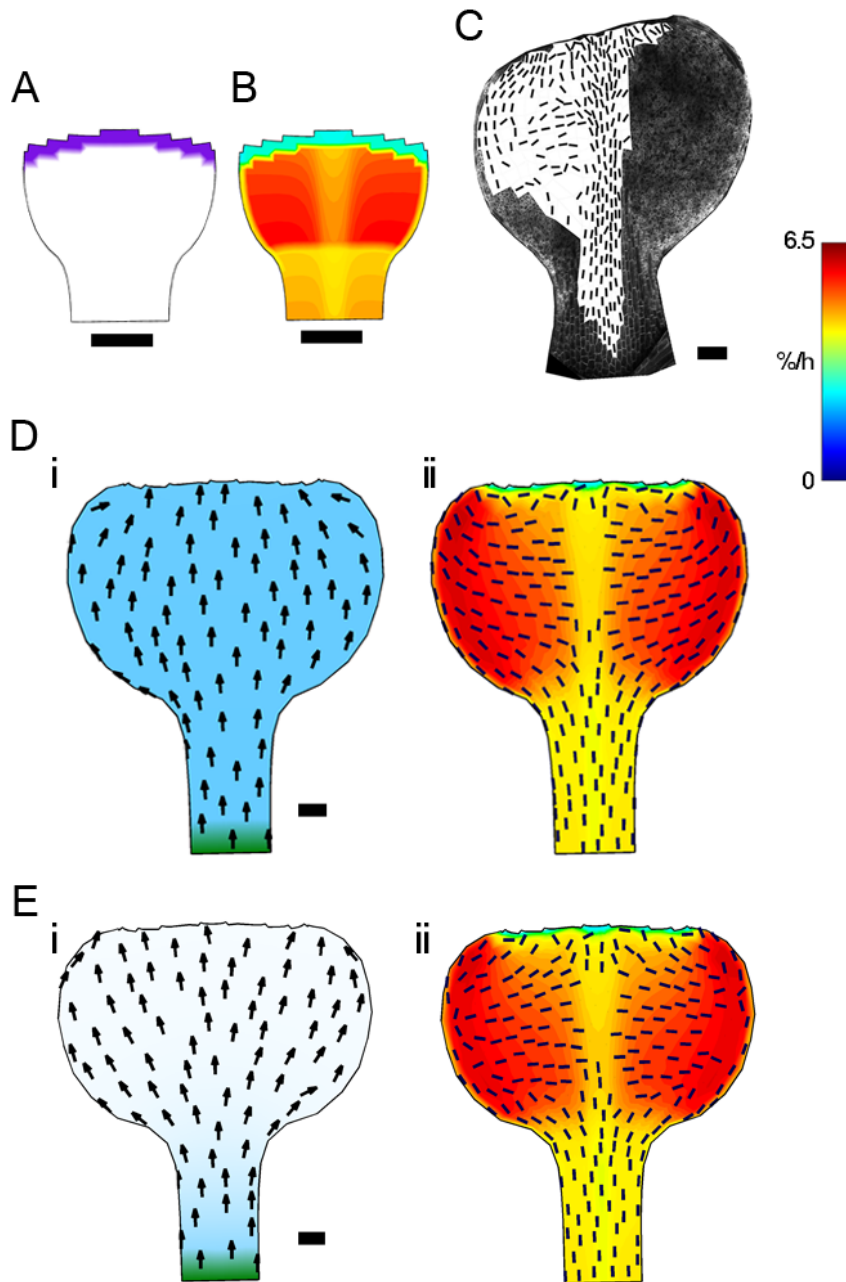


**Figure 2.45** Cut edge inhibition model. **A**, distribution of  $i_{INC}$  just after distal canvas excision on the canvas corresponding to a leaf 6 days after initiation. **B**, specified areal growth rates after excision with growth inhibition at the cut edge by  $i_{INC}$ . **F**, tracked leaf showing resultant principal orientations of growth displayed for regions with an anisotropy  $> 10\%$  on leaf 8 days after initiation. **D-E**, distal excision models with growth restriction at the cut edge showing the canvas corresponding to a leaf 8 days after initiation. **D**, fixed  $s_{POL}$  propagation and **E**, dynamic  $s_{POL}$  propagation. **(i)** specified polarity field (arrows),  $s_{POL}$  (blue) and  $i_{PROXORG}$  (green). **(ii)** resultant areal growth rates (colours) with principal orientations of growth (black lines) displayed for regions with an anisotropy  $> 5\%$ . All resultant growth rates and orientations were calculated over 24  $h$  intervals. Scale bars 100  $\mu m$ .

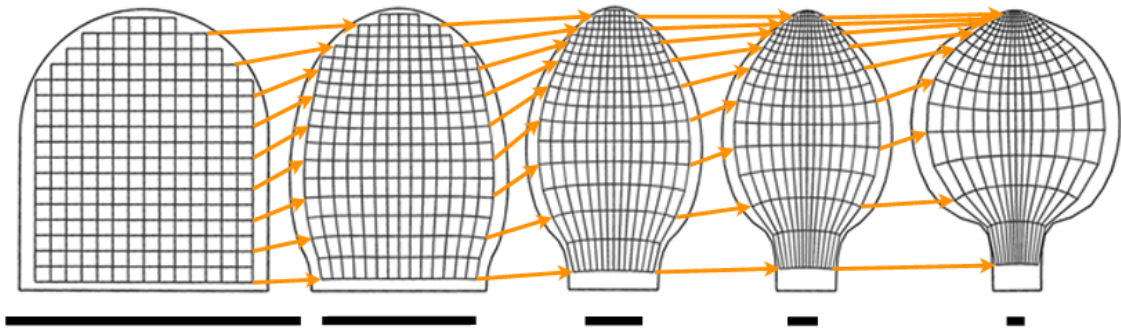


**Figure 2.46** The canvas non-uniformly deforms with growth as demonstrated by a superimposed grid. Scale bars  $100 \mu m$ .

### 2.2.13.2.2 Diagonal Cut

In a further experiment, leaves expressing  $DR5rev::GFP$  were cut diagonally across the leaf lamina 6 days after initiation using a laser (Fig. 2.47A i). After 3 days of growth the cut edge was still clearly visible, but again appeared to have grown very little compared to the rest of the leaf, so that the remaining regions seemed to engulf the cut (Fig. 2.47A ii). The presence of high levels of  $DR5rev::GFP$  at the cut suggests a build up of auxin at the cut edge.

This experiment was repeated computationally by expressing  $i_{DISTAL}$  at  $148 h$  in the distal lamina, diagonally to the midline (Fig. 2.47B). Canvas regions expressing  $i_{DISTAL}$  were then removed and the remaining canvas was grown for a further 3 days (Fig. 2.47C). Without growth restriction at the cut edge, the edge remained wide and straight unlike the real cut leaf (Fig. 2.47C).

Therefore, areal growth rates at the cut edge were again inhibited by  $i_{INC}$  (Eqn. 2.24; Fig. 2.47D and E). The inhibition was slightly stronger than in the distal excision model above. This oblique cut with cut edge inhibition was performed on the two margin model versions with fixed and dynamic  $s_{POL}$  propagation.

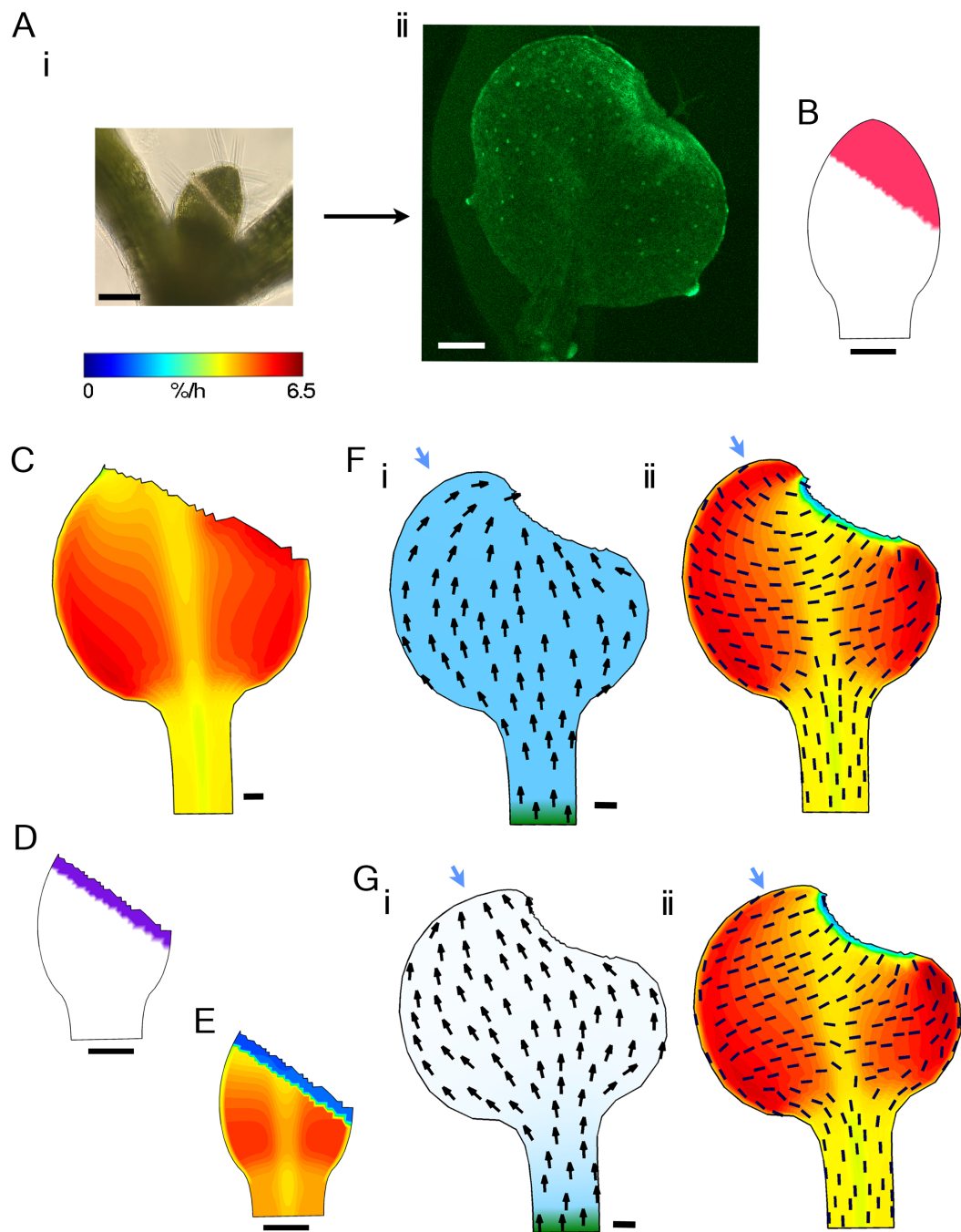


**Figure 2.47** Diagonal excision. **A**, the distal half of the leaf lamina was removed with a diagonal cut using laser ablation showing (i) leaf on day 6 after initiation and (ii) leaf expressing *DR5rev::GFP* (green) 9 days after initiation. **B**, distribution of  $i_{DISTAL}$  on the canvas corresponding to a leaf 6 days after initiation. **C**, margin model with fixed  $s_{POL}$  propagation showing resultant areal growth rates calculated over a 24 h interval. **D**, distribution of  $i_{INC}$  just after excision and **E**, specified areal growth rates. **F**, margin model with fixed  $s_{POL}$  propagation and **G**, margin model with dynamic  $s_{POL}$  propagation. Both models were restricted at the cut edge by  $i_{INC}$  and grown to a developmental age of 8 days showing (i) the polarity field (arrows) with  $s_{POL}$  (blue) and  $i_{PROXORG}$  (green), (ii) areal growth rates calculated over 24 h intervals (colours) and principal orientations of growth (black lines) shown for regions with an anisotropy  $> 5\%$ . Scale bars **A**(i) 150  $\mu m$ , (ii) 200  $\mu m$ , **B-F**, 100  $\mu m$ .

For both versions the overall resultant canvas shapes looked similar to the shape of the excised real leaf (compare Fig. 2.47A ii, F and G). There were small differences in the polarity field of the fixed and dynamic model in the distal parts of the two canvasses, which resulted in slightly different shapes (Fig. 2.47F i and G i, blue arrows). These differences were also visible in the principle orientations of growth at the distal end (Fig. 2.47F ii and G ii, blue arrows). In both versions, principal orientations of growth were pointed towards the cut edge.

Thus, it appears that time lapse imaging of leaves excised diagonally could further resolve if the leaf polarity field is fixed at early stages or remains responsive throughout development. The accumulation of auxin at the cut edge might indicate a reorganisation of the polarity field at the cut edge. However, computationally the observed leaf shape post cutting could be recreated without the assumption of polarity reorganisation.

### 2.2.13.2.3 Side Cut

The final type of cut performed was a small incision in the distal part of the lamina ranging from the margins to the centre of the leaf using laser ablation for leaves 6 days after initiation (Fig. 2.48A i). After 3 days of growth the cut edge was still clearly visible, but appeared to be invaginated by the surrounding tissue (Fig. 2.48A ii). Similar to the diagonal cut, *DR5rev::GFP* expression was high at the cut edge.

This experiment was repeated computationally by incising the canvas along a thin strip from the margin to the midline in the distal region (Fig. 2.48B, black arrow) at a canvas size corresponding to a leaf 6 days after initiation. The canvas was grown for a period corresponding to 3 days, while growth along the cut edge was inhibited by  $i_{INC}$  (Eqn. 2.24, Fig. 2.48C). This small incision was performed on the margin models versions with fixed and dynamic  $s_{POL}$  propagation.

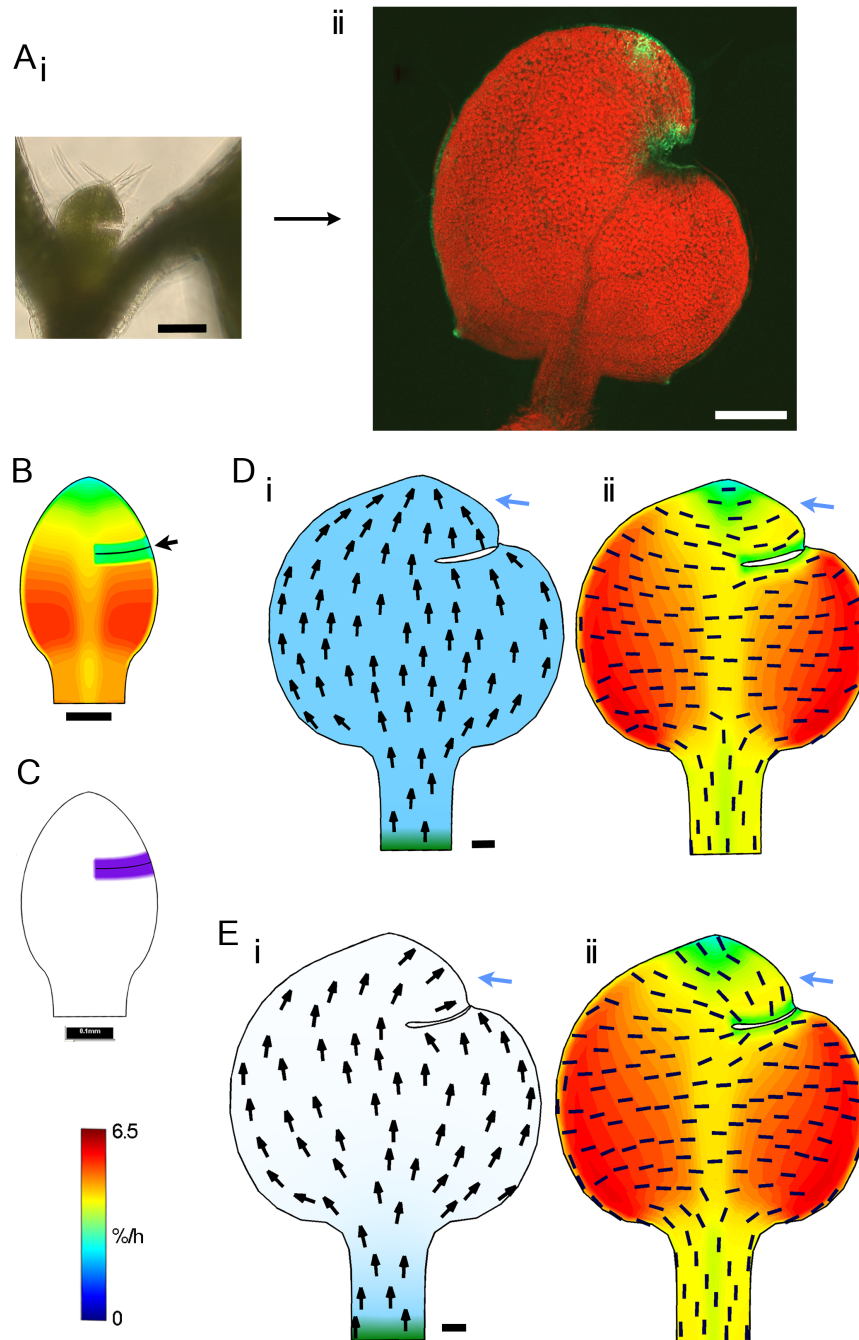


**Figure 2.48** A(i), the distal half of the leaf is removed with a diagonal cut 6 days after initiation. (ii) the same leaf after 3 days of growth on day 9 showing *DR5rev::GFP* (green). B, canvas at time corresponding 6 days after leaf initiation with incision in the distal part of the canvas (black arrow) showing specified areal growth rates (colours). C, distribution of  $i_{INC}$  just after incision. D, margin model with fixed  $s_{POL}$  propagation and E, margin model with dynamic  $s_{POL}$  propagation. Both versions were restricted at the cut edge by  $i_{INC}$  and grown to a developmental age of 8 days showing (i) the polarity field (arrows) with  $s_{POL}$  (blue) and  $i_{PROXORG}$  (green), (ii) areal growth rates calculated over 24 h intervals (colours) and principal orientations of growth (black lines) for regions with an anisotropy > 5 %. Scale bars A(i) 150  $\mu m$ , (ii) 200  $\mu m$ , B-E 100  $\mu m$ .

In both cases, the edge regions seemed to invaginate the cut (Fig. 2.48D and E), similar to the observations. The polarity field in the distal regions was different under the two model versions. For the fixed version orientations maintained their proximodistal alignment, whereas in the dynamic version the distal polarity field diverted to the distal margins above the incision (Fig. 2.48D i and E i, blue arrows). This also affected the orientations of principal growth (Fig. 2.48D ii and E ii, blue arrows). Time lapse imaging is needed to resolve which of these versions better describes the polarity field of the leaf. The expression of *DR5rev::GFP* at the cut edge suggests that the distribution of auxin is affected at the cut edge. Thus, it is possible that the polarity field is re-organised, favouring a dynamic model of polarity organisation.

Similar to the models above, the growth interactions of the margin model gave a good representation of leaf growth with excision. However, the modelled cut edges remained close together, whereas the observed cut edges grew further apart. It is possible that this is largely an artifact of flattening the leaf for imaging.

Time lapse imaging of leaves subjected to surgery showed that growth rates are affected locally at the cut edge rather than being subject to large-scale rearrangements. Incorporating these observations into the leaf model allowed to accurately predict *Arabidopsis* leaf growth under different conditions.

The different types of excision experiments also provided a means to distinguish between a mechanism of early-fixed and dynamic polarity coordination, favouring a dynamic version. However, further time lapse imaging is needed to make definite statements regarding the polarity system employed in the leaf.

#### 2.2.14 Morphospace

The spatiotemporal dynamics at early stages of leaf development could be explained by a model with a small number of parameters (Fig. 2.49A). If the model presented here is indeed of general importance, it should also be able to predict leaf growth patterns of other, related plant species. Therefore the parameter sensitivity of the margin model was tested together with its ability to produce a range of observed leaf shapes.

The robustness of the model to parameter changes was tested by varying each parameter value by 20%. To detect any changes in the growth and polarity fields due to altered parameter values, round circles were induced at the beginning of each simulation, which deformed into ellipses during growth. Variations in most parameter values had a limited effect on the canvas shapes and clone patterns (Fig. 2.49B). Two parameters had a larger effect on leaf shape and size. This included changes in the promotion of  $K_{par}$  by  $\mathbf{i}_{PROX}$  through  $p_{prox}$  (Fig. 2.49B,  $p_{prox}$ ). When  $p_{prox}$  was reduced the leaf had a squat shape, whereas increases in  $p_{prox}$  resulted in a more elongated elliptical leaf shape. Changes in the promotion of  $K_{per}$  by  $\mathbf{i}_{LAM}$  through  $p_{lam}$  had the opposite effect to changes in  $p_{prox}$ . At low values of  $p_{lam}$  the leaf was elliptical and at high values showed a large amount of lateral growth, which resulted in an indented tip. In addition some parameters had a more subtle effect on leaf shape. For instance, changes in  $b_{prox}$ , which controls the minimum levels of  $\mathbf{i}_{PROX}$  at the tip, created a pointy or flat tip (Fig. 2.49B,  $b_{prox}$ ).

Thus, the leaf model was robust to most parameter changes with only small divergences of canvas size and shape. The small differences in the growth dynamics of the *Arabidopsis thaliana* ecotypes *Ler* and *Col-0* (Fig. 2.3) might therefore be a result of small changes in one or more of these parameters.

The integrated model generated here can explain leaf growth during the first half of leaf development. To be biologically relevant, however, it should be able to account for the leaf shapes of related species through small parameter changes. Here, the parameter value of  $b_{prox}$  was varied by 80% and  $p_{lam}$  was varied by 20% (Fig. 2.50A-I). The resulting morphospace included many botanically described leaf shapes, such as obovate (Fig. 2.50A and D), ovate (Fig. 2.50F) and elliptic (Fig. 2.50H and I; Swink and Wilhelm 1994).

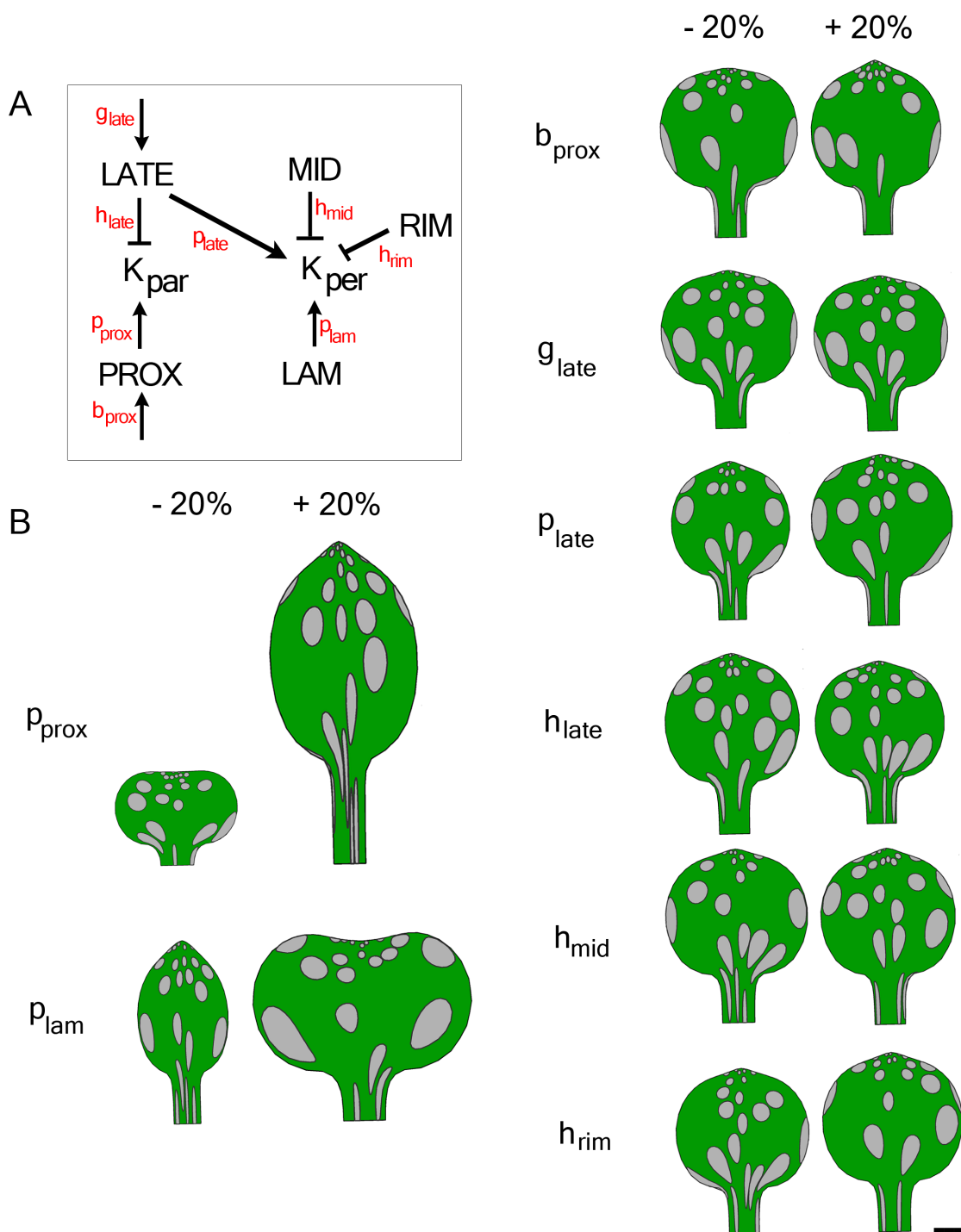


**Figure 2.49** **A**, the growth interaction network with growth factors in black and parameter values in red. **B**, each parameter value is changed by 20% in turn. Scale bar 300  $\mu m$ .

As a further test the predicted clonal patterns were compared to those of a different leaf species, *Antirrhinum*, which has a more elliptical leaf shape (Fig. 2.50J). *Antirrhinum* is amenable to clonal analysis (Rolland-Lagan et al., 2003). Clones were induced at a metamer 4 width of 50-100  $\mu m$ , using a

temperature-sensitive transposon and visualised in the mature metamer 4 by Sandra Bensmihen. The mean leaf shape at maturity was calculated and the clones warped to this shape using the same method as described above for the *Arabidopsis* leaves (2.2.13.1 Clonal Analysis). Leaf shape and clonal patterns were comparable to those generated at low values of  $p_{lam}$  (Fig. 2.50H and I), where large narrow clones diverge outwards from the lamina base and smaller clones converge towards the tip.

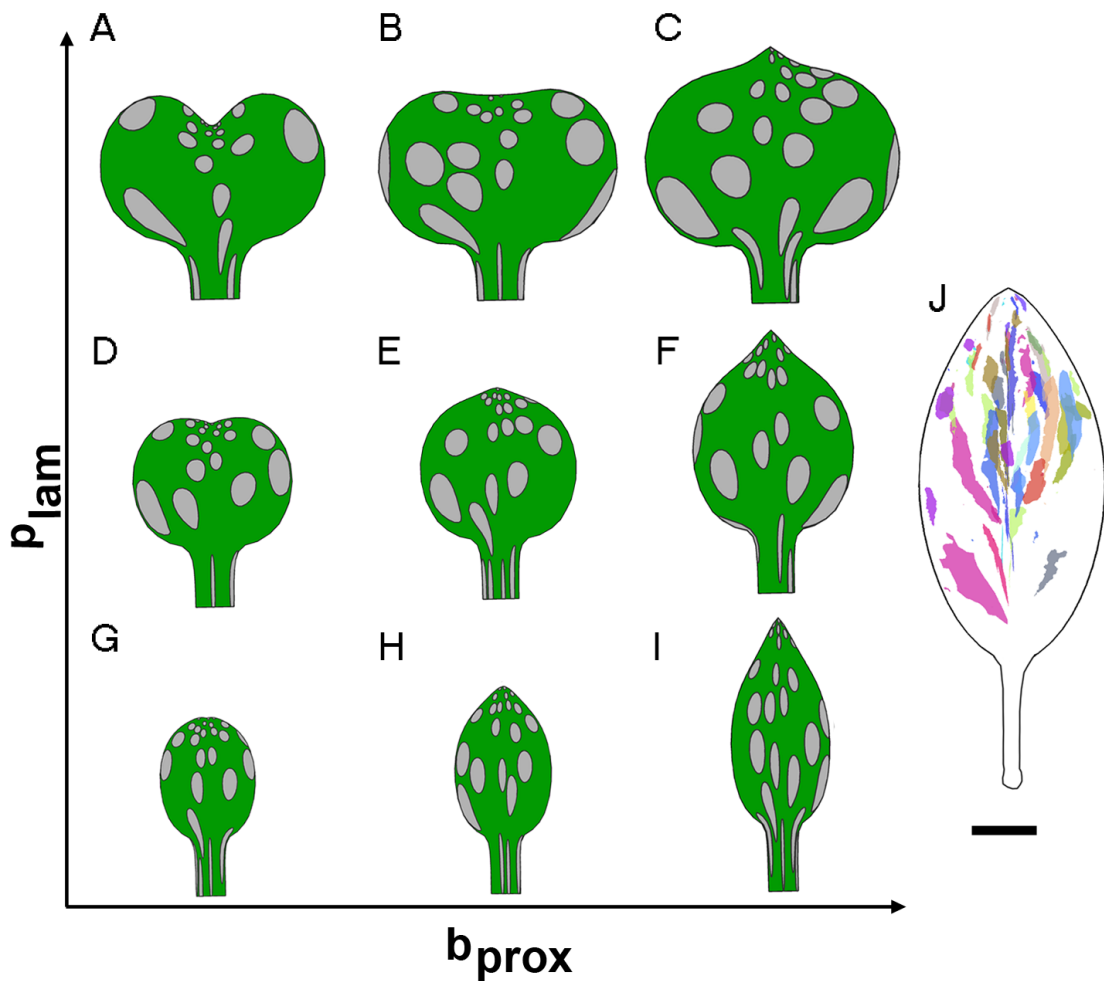


**Figure 2.50** A-I, parameter values of  $b_{prox}$  varied by 80% and  $p_{lam}$  varied by 20%. J, clonal patterns of metamer 4 of *Antirrhinum* showing mean leaf shape with warped clones. Colours present data from different leaves. Scale bar 1 cm.

## 2.3 Discussion

In this chapter, the two main processes underlying organ development, namely growth rate and orientation, were explored. Although, growth rates and polarity were specified independently, it is clear from the resultant growth and polarity fields that both feedback on each other. While the direction of growth is determined by a polarity field, resulting growth rates deform the canvas, which rotates the polarity field. This feedback was evident in models where the polarity field was attached to the canvas at early stages and deformed with it, but also in the dynamic organiser-based models, where the *sPOL* gradient was limited by the canvas geometry. This interaction might explain why several morphogens seem to be involved in specifying both growth and polarity. In the *Drosophila* wing, Dpp signalling is necessary for growth and cell division (Lawrence and Struhl, 1996), but also for polarised cell elongation (Widmann and Dahmann, 2009). Similar double functions have been reported for Fat and Dachous in the *Drosophila* wing (Baena-Lopez et al., 2005).

### 2.3.1 Polarity Systems

The experimental and computational results obtained suggest that leaf growth orientations are not maintained during development but deform with the geometry of the tissue. Polarity orientations that deform during development also seem to underly *Drosophila* wing development (Aigouy et al., 2010) and thus may be a general feature of morphogenesis (Green, 1996).

However, it is possible that a non-deforming model with a different initial polarity field, than the one tested here, would generate patterns more similar to those observed for the leaf. Unfortunately, it was not possible to test the maintenance of polarity orientations under different initial polarity fields due to *GFTbox* implementation limitations. For instance, given the shape of the young leaf, a fairer evaluation of the non-deforming model would have considered an initial curvilinear system that does not deform with growth. However, such a model would also have struggled to reproduce the oblique principal growth orientations observed in proximal leaf regions at later stages. It is, of course, possible, that polarity field orientations are oblique in proximal regions

from the start and do not deform.

Since, tissue geometry limits diffusion, growth orientations may be a result of an underlying polarity system, which, at the two extremes, is specified early and then only deforms with the geometry of the tissue, or a polarity system, which remains responsive to a polarity organiser and readjusts throughout growth. Based on the overall leaf shape, it was not possible to distinguish between these two systems. Observed patterns could be captured by simply assuming that directions deform with the canvas, without the need for polarity reorganisation adjustments. However, changing the canvas geometry by excision revealed that directions appear to adjust to new geometries. Thus, leaf excision data presented here was best accounted for by a model with a dynamic polarity field. Further time lapse imaging of leaves subjected to surgery is necessary to resolve whether the polarity field simply reorientates to the new geometry or whether in addition the polarity field repolarises locally upon surgery, as suggested by other studies (Goodbody and Lloyd, 1990; Hardham, 1982) and changes in the levels of auxin at the cut edge (Sauer et al., 2006; Wabnik et al., 2010).

Different variations of an organiser-based model were explored by positioning the organising centre at the canvas base, tip or centre. All of these models generated similar patterns of principal orientations of growth and were therefore difficult to distinguish based on the data available. In animal systems, growth and polarity organisers are generally positioned at organ compartment boundaries to control dynamics across the rest of the compartment (Umetsu and Dahmann, 2010). For instance, Dpp is produced at the anterior-posterior boundary, which runs across the *Drosophila* wing and divides the wing into two compartments (Lawrence and Struhl, 1996; Nellen et al., 1996). Unlike the wing, simple leaves, like those of *Arabidopsis*, appear less compartmentalised within the plane. Therefore it is more likely that polarity is specified at the organ boundaries, such as the leaf base, rather than in the midvein region. The round tip generated by the midvein-organiser model also indicates that the leaf polarity field is not coordinated from the midvein.

### 2.3.1.1 Polarity and Auxin

The establishment of a polarity field in the organiser-based models was limited by the dome-shaped geometry of the canvas. Organiser-based models generated a curvilinear polarity field in the distal canvas regions with polarity converging towards the tip. Similar convergence towards the leaf primordium tip has been observed for the orientation of PIN1 proteins (Fig. 2.51; Benková et al. 2003; Reinhardt et al. 2003; Scarpella et al. 2006). The PIN-mediated polar transport of auxin through the leaf makes auxin an appealing candidate for the the polarity factor,  $s_{POL}$ . However, the mechanisms determining PIN polarity are still unclear (Stoma et al., 2007; Wabnik et al., 2010). It is possible that auxin itself promotes the polar distribution of PINs. Computational models have shown that auxin gradients in the epidermal layers can form through a self-promoting system, in which PIN proteins are expressed at cell membranes facing neighbouring cells with high auxin concentrations (Jönsson et al., 2006; Smith et al., 2006). Thus, auxin may be the main determinant for polarity. Alternatively, auxin might simply be a read-out of an underlying polarity field. For instance, auxin is thought to be necessary for the establishment of polarity in the early embryo (Grunewald and Friml, 2010). However, recently it has been shown that the initial embryonic polarity is established by the transcription factor WRKY2 and is independence of auxin (Ueda et al., 2011).

If auxin plays a role in the establishment or maintenance of polarity, it is possible that the organising centre predicted here is positioned at the leaf tip or base. At both sites high auxin levels are maintained by the auxin synthesis gene family *YUCCA* (Cheng et al., 2007, 2006). It is therefore possible that there is more than one centre of polarity organisation in the leaf.

### 2.3.2 Growth Coordination

The pattern of growth rates across the leaf had a clear proximodistal distribution throughout the period analysed. These results agreed well with

those observed at later stages of leaf development (Avery, 1933; Erickson, 1966; Schmundt et al., 1998; Wolf et al., 1986) and those generated by clonal analysis (Dolan and Poethig, 1998; Poethig and Sussex, 1985). Moreover, similar proximodistal growth gradients were also observed for macroalgae blades (Koehl et al., 2008).

Spatial differences in growth rates were evident from the beginning of the growth analysis, at which point cell divisions should still be frequent throughout most of the organ (Donnelly et al., 1999). From previous growth studies it appears that this gradient in growth rates is maintained at late stages, when divisions should have ceased (Avery, 1933; Erickson, 1966; Schmundt et al., 1998; Wolf et al., 1986). This highlights the importance of measuring growth directly rather than inferring growth dynamics from cell division patterns (Green, 1976). However, to establish to what extent growth and cell division dynamics are correlated, cell division data would need to be collected from the time lapse imaging data as well.

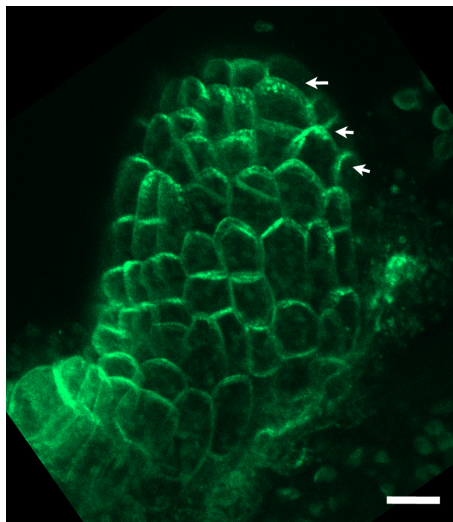


**Figure 2.51** Expression of *PIN1::PIN1-GFP* in a leaf 2 days after initiation. White arrows indicate high concentrations of PIN1 expression at the distal end of cells in the abaxial epidermal layer. Scale bar 10  $\mu\text{m}$ .

### 2.3.2.1 Midline Profiles

The observed growth patterns along the midline could be accounted for by a mechanism in which a propagating inhibitor is produced at the distal end of the leaf. However, there is a fundamental problem with a mechanism based

on a propagating inhibitor from the tip, as the direction of propagation is opposed by growth, which increases the distance between the inhibitor source and the remaining tissue. This is evident in the model, where the proximal regions never received sufficient inhibitor levels.

Cell division arrest dynamics are thought to commence first at the tip and progress towards the leaf base (Donnelly et al., 1999; Sylvester et al., 1990). If such distal inhibitor mechanism is indeed employed in cell division arrest, stringent control of inhibitor levels and growth would be required, potentially explaining the high amount of genetic redundancies in leaf growth control (Gonzalez et al., 2010).

A good match with the observed growth dynamics could be generated by a model, where the linear distribution of growth rates is specified by the growth promoter,  $i_{PROX}$ .  $i_{PROX}$  levels were fixed to the canvas at early stages and locally deformed with the canvas during growth.

The model has not dealt with the question of how the initial  $i_{PROX}$  gradient is established, since this event was assumed to precede the start of the leaf growth analysis. Initial gradient establishment is likely to be mediated by  $i_{PROX}$  propagation. A linear morphogen gradient can be established by  $i_{PROX}$  production at the leaf base and  $i_{PROX}$  decay at the distal end (Wolpert, 1969). How the concentration of  $i_{PROX}$  is then maintained locally and prevented from diluting with cell division during development is, however, unclear. It is possible that early patterns of  $i_{PROX}$  may activate downstream genes, which maintain the growth patterns at later stages.

### **2.3.2.2 Early or Continuous Patterning**

It was assumed that similar to  $i_{PROX}$ , the other growth factors (apart from  $i_{LATE}$ ) are also established early and are maintained locally. This assumption of early establishment of growth rates was tested by leaf surgery. It had previously been claimed that leaves have the ability to regenerate following injury (Sena et al., 2009). The leaf model, on the other hand, is based on growth interactions that are established at early stages and could not be disturbed by surgery. Repeating the experiments by Sena et al. (2009) showed

that in contrast to tissue regeneration, the area at the cut edge grew little. Restricting growth at the cut edge in the model generated a similar leaf shape as was observed for the leaf in this study. It therefore appears that previous reports of regeneration were misinterpretations of leaf growth dynamics. Using the model, it could be shown that this growth restriction together with the underlying distribution of high proximal growth rates was sufficient to account for the apparent wound closure observed. The large contributions of proximal regions to the final organ shape have also been reported for the *Arabidopsis* sepal (Roeder et al., 2010). Thus, the ablation of the distal half of the leaf at early stages has a limited impact on the final shape and size. Interestingly, the situation seems to be reversed in vertebrate limbs, where distal regions contribute considerably more than proximal ones to the final organ shape (Vargesson et al., 1997).

The lack of observed regeneration is in accordance with more recent studies, which show that tissues are less able to regenerate from injury than previously thought. In general, regeneration potential seems to be conferred by a small number of dispersed totipotent cells (Poss, 2010; Sena and Birnbaum, 2010). In plants, callus is derived from few of these undifferentiated cells rather than the whole cell mass (Sugimoto et al., 2011). In salamanders and newts, totipotent cells are dispersed throughout the organism and are able to initiate regeneration upon injury throughout their development, whereas many bird and mammalian appendages show little regeneration potential (Poss, 2010; Yokoyama, 2008).

#### **2.3.2.2.1 Growth Deceleration**

In addition to the early established growth patterns, growth rates were observed to decrease slightly at later stages of development studied by time lapse imaging. In the leaf models generated here, it has been assumed that growth deceleration at later stages along the leaf length is controlled by the immobile growth inhibitor  $\mathbf{i}_{LATE}$ .  $\mathbf{i}_{LATE}$  increases uniformly in space and linearly with time. This mechanism has been implemented, as better evidence for the real mechanism underlying growth deceleration was not available from

the period studied by time lapse imaging. It is possible that growth deceleration is not uniform, but that spatiotemporal differences in arrest across the leaf contribute to the leaf shape at later stages. Further time lapse imaging data is needed to resolve this issue.

### 2.3.2.2.2 Lateral Growth

Despite the observed decrease in proximodistal growth rates, areal growth rates remained high throughout the period analysed. In the models, this was accounted for by an increase in mediolateral growth rates mediated by  $\mathbf{i}_{LATE}$ . This interaction provided a means of increasing growth rates in the lateral regions, which ensured the lateral extension of the lamina at later stages. Unfortunately, due to the curvature of the leaf and therefore limited availability of tracking data for these lateral regions, it was not possible to simplify mediolateral growth to one-dimension and visualise the dynamics better.

The model thus assumes that growth interactions are established early and are maintained during growth, but that there is some re-patterning at later stages of development. While  $\mathbf{i}_{LATE}$  did not affect the spatial patterns of growth rates, it did change the ratio of growth along the two axes of growth,  $K_{par}$  and  $K_{per}$  (Fig. 2.52).

It is possible that instead of a change in growth rates, observed changes in the principal orientations of growth may be due to a reorientation of the polarity field. For instance, instead of maintaining a proximodistal orientation, the polarity field might divert to a mediolateral orientation in the lamina regions at later stages. This option has not been explored here, where models were based on a polarity field coordinated by one organiser only. Reorientations of the polarity field during development, independent from the tissue geometry, may require more than one type of polarity organiser. In addition, changes in the polarity field directions alone would not explain the increase in growth isotropy with time. Thus, the models shown here present a simpler way to capture the observations.

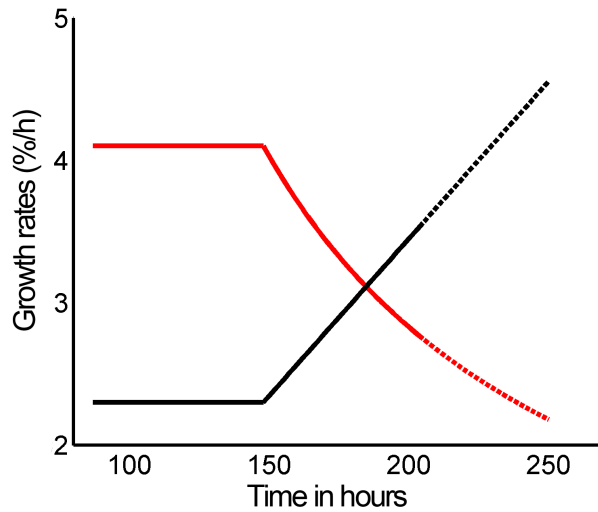


**Figure 2.52** Modelled changes in growth dynamics mediated by  $i_{LATE}$  showing dynamics of  $K_{par}$  (red) and  $K_{per}$  (black). Solid lines show dynamics during the developmental period modelled and dotted lines the predicted changes if the model simulation was continued further in time.

### 2.3.2.3 Beyond the Period Studied

Under the current model interactions, mediolateral growth does not decrease. In fact, while proximodistal growth rates decrease, mediolateral growth rates increase with time (Fig. 2.52). The model is therefore limited to the first half of leaf development, for which time lapse imaging data is available.

For the developmental period analysed here, proximodistal and mediolateral growth was controlled differently. However, after the establishment of a round leaf blade, the leaf shape is roughly maintained for the rest of leaf development. In addition, time lapse imaging showed that growth dynamics become more isotropic and uniform with time, in particular in lateral regions. Interestingly, levels of auxin, which has been discussed as a potential polarity factor, increase in the leaf lamina at later stages of development and appear to be distributed more uniformly throughout the lamina (Fig. 2.53; Aloni et al. 2003). It is therefore possible that growth dynamics in the leaf lamina become isotropic at later stages of development, as suggested by previous studies (Avery, 1933; Baskin, 2005; Boudaoud, 2010; Erickson, 1966). During the period analysed, orientations of growth were largely aligned, suggesting that growth is anisotropic and coordinated. Tracking data beyond the developmental period analysed here is needed to clarify the mediolateral growth dynamics and changes in anisotropy at later stages.

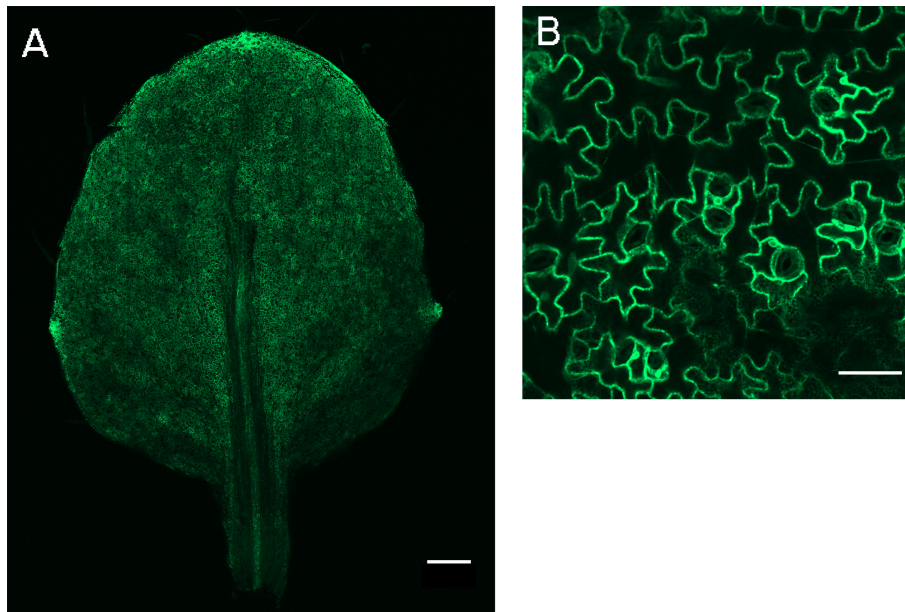


**Figure 2.53** Expression of *DR5rev::GFP* in leaves 9 days after initiation showing **A**, whole leaf and **B**, close-up on a central lamina region. Scale bars **A**, 200  $\mu\text{m}$  and **B**, 40  $\mu\text{m}$ .

### 2.3.3 Growth Factors to Genes

An integrated model with simple interactions could account for the spatiotemporal patterns of leaf growth. The model is based on a small number of growth and polarity factors, which are likely to combine the function of many genes known to be involved in these processes (Efroni et al., 2008). It is possible that each model factor, applied throughout the developmental period, represents the function of a number of temporally coordinated genes. Below some of these genes have been discussed in relation to the factor expression patterns and functions predicted by the model. The leaf model provides a basis for leaf growth, which can be extended in further studies to include more specific interactions of known genes.

#### 2.3.3.1 PROX and LAMINA (LAM)

In the leaf models, growth parallel and perpendicular to the polarity gradient is controlled by two different factors,  $i_{PROX}$  and  $i_{LAM}$ . Several studies suggest that leaf length and width are controlled differentially. For instance, mutants in the gene *ANGUSTIFOLIA* (*AN*) have a reduced cell number and overall size in the leaf width direction, whilst maintaining a roughly wild-type length (Bai et al., 2010; Hülskamp et al., 1994; Tsuge et al., 1996). The *AN*

phenotype is thought to be a result of reorientations of microtubules parallel to the epidermal plane, thereby increasing leaf thickness instead of width (Kim et al., 2002). Leaves of other mutants, such as *rotundifolia3* (*rot3*), have a width similar to wild-type but are shorter (Kim et al., 1998, 1999; Tsuge et al., 1996). *ROT3* has a high similarity to genes involved in biosynthesis of brassinosteroids (BRs; Goda et al. 2002). In BR mutants, plants are dwarfed, primarily due to a reduction in cell expansion (Kauschmann et al., 1996; Nakaya et al., 2002; Szekeres et al., 1996). BR-signalling mutants are often more affected along their proximodistal axis (Savaldi-Goldstein et al., 2007), similar to the phenotype of *rot3* mutant leaves (Kim et al., 1998, 1999). In mutants of *big brother*, leaves are wider but shorter, therefore preserving overall leaf area (Disch et al., 2006).

In the models presented here,  $\mathbf{i}_{PROX}$  and  $\mathbf{i}_{LAM}$  are the key model components, which directly determine the growth rates. In their absence, growth rates are zero irrespective of the presence of other growth factors. Therefore,  $\mathbf{i}_{PROX}$  and  $\mathbf{i}_{LAM}$  represent genes essential for growth along the two main axes, and in whose absence growth is limited to the remaining axes.

### 2.3.3.1.1 PROX

$\mathbf{i}_{PROX}$  promotes growth along  $K_{par}$  and has a linear proximodistal gradient across the canvas, which deforms with growth. Since a proximodistal gradient of growth rates has been observed in a wide variety of species (Avery, 1933; Erickson, 1966; Koehl et al., 2008; Schmudt et al., 1998; Wolf et al., 1986),  $\mathbf{i}_{PROX}$  presents one of the most interesting factors to unravel. Unfortunately, currently there are no good candidates that fulfill the function of  $\mathbf{i}_{PROX}$ . Since the progression of the cell division front follows a proximodistal gradient (Donnelly et al., 1999), many genes show a proximodistal expression pattern. However, generally this expression is confined to the onset of division arrest (Dhondt et al., 2010; Disch et al., 2006; Hu et al., 2006; Rodriguez et al., 2010).

### 2.3.3.1.2 LAMINA (LAM)

In the models,  $i_{LAM}$  drives lateral growth and a needle-like leaf is generated in the absence of  $i_{LAM}$ .  $i_{LAM}$  has a non-uniform distribution in the leaf blade and is present at a low concentration in the petiole.

Mutants with severe ad/abaxial polarity defects have needle-like leaves (Eshed et al., 2001, 2004; McConnell and Barton, 1998). The abaxially expressed *YABBY* (*YAB*) genes present very good candidates for  $i_{LAM}$ , as they are only found in evolutionary clades of plants with lamina-forming leaves (Sarojam et al., 2010). In *Arabidopsis*, 5 members of the *YAB* family are expressed on the abaxial side of leaves (Siegfried et al., 1999). *FILAMENTOUS FLOWER* (*FIL*) and *YAB3* are most highly expressed in lateral leaf regions (Kumaran et al., 2002; Sarojam et al., 2010; Sawa et al., 1999; Watanabe and Okada, 2003), while *YAB2* and *YAB5* expression is higher in the midvein and petiole regions (Sarojam et al., 2010). Despite their different expression patterns there seems to be functional redundancy between the *YAB* family members, as single knock-outs of *fil*, *yab2* or *yab3* are not phenotypically different from wild-type (Nole-Wilson and Krizek, 2006; Stahle et al., 2009).

$i_{LAM}$  levels are low in the petiole. Ectopic or overexpression of the genes *LEAFY PETIOLE* (*LEP*; Graaff et al. 2003; van der Graaff et al. 2000), *JAGGED* (*JAG*; Dinneny et al. 2004) and *BLADE-ON-PETIOLE* (*BOP*; Ha et al. 2003; Norberg et al. 2005) give rise to laminar outgrowth along the petiole. *LEP* and *JAG* are expressed in the blade regions of young leaves and their expression decreases with age (Ohno et al., 2004; van der Graaff et al., 2000). *LEP* concentration is proportional to the extent of blade outgrowth along the petiole. *BOP1*, in contrast, is expressed in the petiole and at early stages of development in the midvein (Norberg et al., 2005). However, in *BOP 1* and *2* mutants, blade outgrowth along the petiole is patchy (rather than a smooth continuation of the lamina as observed for *LEP* overexpression), due to the expression of *class I KNOTTED-1 homeobox* (*KNOX*) genes in the petiole (Ha et al., 2003; Norberg et al., 2005).

### 2.3.3.2 LATE

The decrease in growth rates over time has been modelled by the uniformly increasing immobile inhibitor  $\mathbf{i}_{LATE}$ . However, the mode of growth deceleration could not be clearly resolved during the period analysed by time lapse imaging. Assuming that growth deceleration is uniform throughout the leaf, there are several ways in which  $\mathbf{i}_{LATE}$  could act. For instance, as modelled here,  $\mathbf{i}_{LATE}$  could act as an inhibitor and increase over time, by being produced throughout the tissue. Alternatively,  $\mathbf{i}_{LATE}$  could be produced in a particular region and propagate rapidly through the rest of the tissue. Concentration increases of growth inhibitors with time are known in the leaf. For instance, concentrations of the leaf senescence promoting gene *ORESARA-1* increase with age (Kim et al., 2009), while the gaseous hormone ethylene diffuses rapidly through the leaf and inhibits cell elongation and promotes leaf senescence (Kieber, 1997).

Alternatively, instead of inhibiting growth,  $\mathbf{i}_{LATE}$  could be a growth promoting factor that decreases with age. The low-motility BRs, for example, promote both cell division and expansion (Kauschmann et al., 1996; Nakaya et al., 2002; Szekeres et al., 1996) and in the absence of BRs plants are dwarfed (Reinhardt et al., 2007). BRs are most highly expressed in actively growing tissues and their concentration decreases over time (Reinhardt et al., 2007; Symons and Reid, 2004).

### 2.3.3.3 MIDVEIN (MID)

$\mathbf{i}_{MID}$  inhibits lateral growth in the midline regions of the leaf. The distinction of the midvein region from the rest of the tissue occurs at an early stage as seen from the vasculature marker AtHB8 (Scarpella et al., 2006) and may be correlated with the leaf vasculature development. How vasculature development in the mesophyll layers affects epidermal growth rates is, however, unclear.

#### 2.3.3.4 RIM

$i_{RIM}$  inhibits lateral growth in the margin regions of the canvas lamina. In *Arabidopsis*, the gene *PETAL LOSS* (*PTL*) is expressed around the margins of young leaves and is restricted to the proximal region, including the petiole, at later stages (Brewer et al., 2004). *PTL* restricts growth. For example, in flowers, *PTL* is thought to maintain the separation between adjacent newly forming petals and sepals (Griffith et al., 1999). Ectopic expression of *PTL* results in reduced growth with dwarfed, curly leaves (Brewer et al., 2004).

#### 2.3.4 Morphospace

In the past, several studies have quantified differences in leaf shape between different ecotypes or mutants of the same species or between related species (Bensmihen et al., 2008; Feng et al., 2009; Langlade et al., 2005). Changing the values of two parameters of the leaf model generated a range of observed leaf shapes. This flexibility of the model suggests that different leaf shapes may be readily brought about by small genetic changes, while maintaining the same underlying growth and polarity networks. The ease with which different leaf shapes could be generated suggests a large amount of evolutionary conservation in the processes underlying leaf growth, which was also evident in the clonal patterns of leaves of *Antirrhinum* and *Arabidopsis*. The clones of both species were large in proximal regions and small in distal regions and followed the geometry of the leaf. Comparable clonal patterns have also been observed for the tobacco and cotton leaf (Dolan and Poethig, 1998; Poethig and Sussex, 1985). In addition, similar trends in leaf growth rate distributions are observed for several, also more distantly, related plant species (Avery, 1933; Erickson, 1966; Schmundt et al., 1998; Wolf et al., 1986). The large variety in generated model shapes might account for why leaf shape is of limited use for plant classification above the species level (Vanderpoorten and Zartman, 2002).

#### 2.3.5 Future

The study of growth and polarity in the generation of leaf shapes has given insights into the type of polarity system that is likely to underly leaf

development. All types of modelled excision experiments showed differences in the predicted principal orientations of growth between different systems. Therefore, it would be interesting to continue the excision experiments and time lapse imaging of excised leaves to determine whether the polarity field is dynamic and is potentially reorganised post cutting, as suggested by changes in the distributions of auxin. Exploring the effect of excision on the polarity field might therefore also uncover the role of auxin in polarity specification.

Another interesting aspect of leaf growth is the deceleration of growth with time to generate a determinate leaf size. During the period analysed here, it was not possible to explore the mechanism of growth arrest. However, time lapse imaging of later stages of leaf growth would allow the leaf model to be extended further in time and growth arrest to be studied fully. In particular, it would be interesting to investigate whether growth deceleration is uniform throughout the leaf or has spatial patterns, which should result in changes in leaf shape.

## Chapter 3

# Leaf Serrations

### 3.1 Introduction

In the previous chapter, a deforming polarity field was used to specify the anisotropic leaf growth dynamics. Based on normal growth of the wild-type leaf, it was not possible to distinguish between an organising system, in which the polarity field is fixed early and only deforms with the geometry of the tissue, or an organising system, which remains responsive to changes in a morphogen gradient. Leaf excision experiments suggested that the polarity field remains dynamic throughout the period analysed. Here, the importance of growth and polarity in leaf serration formation was explored to provide further insights into the organising systems of the leaf.

Prior to leaf initiation the auxin efflux carriers PIN1 reorientate towards the site of the incipient primordium at the shoot apical meristem (SAM; Reinhardt et al. 2003). Polar auxin transport is thought to be necessary for primordium outgrowth (Benková et al., 2003; Okada et al., 1991; Sauer et al., 2006) and may be necessary to determine leaf polarity. In addition, for correct development, the boundary of the new primordium needs to be specified. In the absence of the boundary genes *CUP-SHAPED COTYLEDONS* (*CUCs*) emerging cotyledons are fused, forming a cup, and the plant struggles to establish the SAM (Aida et al., 1997; Blein et al., 2008; Hibara et al., 2006).

Interestingly, the same factors (auxin and *CUCs*) are necessary to drive

other forms of outgrowth. During the development of simple leaves such as those of *Arabidopsis*, serrations form along the proximal leaf margins. In complex leaves, such as those of tomato, these outgrowths develop into leaflets.

This raises the question whether serration outgrowth is guided by a polarity field or is simply a result of local modulations in growth rates. Here, the leaf model was employed to investigate the role of polarity and growth in driving serration outgrowth.

### 3.1.1 Serration Genetics

At the early stages of leaf development an auxin maximum is visible at the distal tip of the primordium. Slightly later in development similar auxin maxima arise at the tips of incipient serrations and leaflets (Barkoulas et al., 2008; Kawamura et al., 2010). In the absence of auxin maxima the leaf margins remain smooth (Hay and Tsiantis, 2006).

In addition to auxin, the boundary gene *CUC2* and to a lesser extent *CUC3* are required for outgrowth (Blein et al., 2008; Hasson et al., 2011; Nikovics et al., 2006; Taoka et al., 2004). *CUC2* is initially expressed all along the proximal margins of the leaf and is then downregulated at the site of the auxin maxima, most likely by auxin itself. Auxin is thought to activate CUC degradation through miR164 (Bilsborough et al., 2011; Hasson et al., 2011; Nikovics et al., 2006). *CUC2* continues to be expressed at one or both flanks of the serration.

In simple leaves, the correct localisation of *CUC2* and an auxin maximum are required for serration formation (Bharathan and Sinha, 2001; Bilsborough et al., 2011; Hay and Tsiantis, 2006). In complex leaves, leaflet formation also requires the expression of *KNOX* genes at the margins, which delay differentiation of margin cells and most likely maintain cells in a fast growing state (Bharathan and Sinha, 2001; Blein et al., 2009; Hay and Tsiantis, 2006). In plants with simple leaves, *KNOX* expression is confined to the organ boundary (Byrne et al., 2000).

Clonal analysis in *Cardamine hirsuta* has shown that only a small number of founder cells along the margins contribute to the formation of lateral leaflets (Barkoulas et al., 2008). In most leaves serrations and leaflets de-

velop symmetrically on both sides of the proximal leaf blade. Serration pairs appear sequentially proximal to the youngest pair (Bilsborough et al., 2011; Pyke et al., 1991; Tsuge et al., 1996; Tsukaya and Uchimiya, 1997). Leaf 1 of *Arabidopsis* only develops a single pair of serrations.

### 3.1.2 Proposed Serration Mechanisms

Above, the genetic interactions necessary for outgrowths have been outlined. To date, it is not clear how these components interact to determine the shape, size, number and site of new outgrowths.

It has long been observed that margins have somewhat different growth dynamics from the leaf blade and were thought to retain meristematic growth potential for longer (Avery, 1933; Reinhardt et al., 2007). It has been proposed that CUC2 might restrict lateral growth in the indentations flanking the serrations, while the remaining part of the margins continues growing and dividing (Bilsborough et al., 2011; Nikovics et al., 2006). This is supported by evidence that CUCs repress cell division at the organ boundary of the floral meristem (Breuil-Broyer et al., 2004). According to this theory serrations do not represent sites of outgrowth, but are the result of normal unrestricted growth. Alternatively, growth could be promoted at the serration sites by auxin (Larue et al., 2009). CUC2 may restrict the auxin maxima by promoting the generation of PIN1 convergence points (Bilsborough et al., 2011). These two hypotheses are not mutually exclusive and it has been proposed that CUCs may downregulate growth at the indentations and non-autonomously promote growth in the serrations (Blein et al., 2008). A combination of these two hypotheses has also been explored in a recent computational study, where it has been assumed that auxin increases growth rates at the margins while CUC2 reduces them (Bilsborough et al., 2011).

Recently, Kawamura et al. (2010) observed that cell files near the leaf margins curve towards the serrations. This suggests that there is a change in the leaf polarity field near the serrations, which might contribute to their formation.

Equally elusive is the mechanism that controls the site of new serrations

and their spacing. Bilsborough et al. (2011) suggested that new auxin maxima can only develop a minimum distance away from existing ones. Thus, once the proximal margins grow out of reach of the auxin maxima at the tip, new maxima form in the basal regions.

Another question is how serrations are maintained during development. A quantitative analysis of serration size in *Arabidopsis* leaf 6 has revealed that serration size increases throughout development (Hasson et al., 2011). Serrations seem to have similar cell division and expansion periods to the rest of the leaf. However, it is possible that these events are not directly linked to cell division and expansion transitions of the leaf lamina, since the expression of *ARGOS-LIKE*, which coincides with expanding regions, is visible earlier in the serrations than in the main part of the leaf (Hu et al., 2006).

### 3.1.3 Generating Serrations

Apart from the recent study by Bilsborough et al. (2011), the question of serration and leaflet outgrowth has not been explored computationally. Bilsborough et al. (2011) studied the role of auxin and *CUC2* in serration spacing and leaf outline generation. In their model, which was based on overall leaf growth trends, the authors assumed that auxin and *CUC2* modulate growth rates normal to the margins, thus assuming polarised growth.

Here, the role of growth and polarity in serration formation was explored, separately and in combination, using the leaf model generated in the previous chapter, which is based on accurate growth information. The different serration mechanisms proposed have been assessed based on the generated leaf and serration shapes as well as the ability to correctly maintain and position serrations during development. Since leaf 1 of *Arabidopsis* only forms one pair of serrations, the question of serration spacing and initial positioning was not explored.

## 3.2 Results

### 3.2.1 Serration Development

To accurately model the development of serrations in leaf 1, serration growth dynamics were first quantified using a similar approach to Hasson et al. (2011). Leaves were removed from the plant at various stages, flattened and imaged. Serration width was measured as the distance between the boundaries of the serrations and the lamina (Fig. 3.1A). Serration length was measured as the distance between the line describing serration width and the serration tip, where the length line was always orthogonal to the width line. This method provided a loose description of serration size, but did not take into account the curvature of the leaf margins and asymmetries in the length of the serration arms. As the leaf model only captures leaf growth up to day 9 after leaf initiation, leaf dimensions were quantified based on a number of leaves for this early part of leaf development only. Together with this quantification the spatiotemporal patterns of auxin-associated genes were investigated using *GFP* fusion constructs of *PIN1* (*PIN1::PIN1-GFP*) and the auxin response marker, *DR5* (*DR5rev::GFP*).

Serrations of leaf 1 were first visible about 5 days after leaf initiation, at a leaf width of about 250  $\mu\text{m}$  (Fig. 3.1B and C). Prior to a visible outgrowth, *PIN1* expression in the proximal margins became polarised towards the loci of the incipient serrations (Fig. 3.1D; Scarpella et al., 2006). This resulted in the accumulation of auxin at the serration tips, shown by the expression of the auxin response marker *DR5* (Fig. 3.1E, arrows). Serrations initiated as small broad protrusions at the margins close to the petiole (Fig. 3.1F). After an initial period of growth in which serration size increased roughly exponentially with time (up to day 7), serration growth decelerated and serration size only increased slowly for the remainder of the period analysed (Fig. 3.1B and C). During growth, serrations became more pointy and the distance between the serrations and the petiole increased (Fig. 3.1G-I). *DR5* was visible at high levels at the serration tips throughout development (Fig. 3.1H). However, the concentration of *DR5* does not necessarily reflect the actual auxin concen-

trations present (Barbier de Reuille et al., 2006; Stoma et al., 2008; Vernoux et al., 2011).

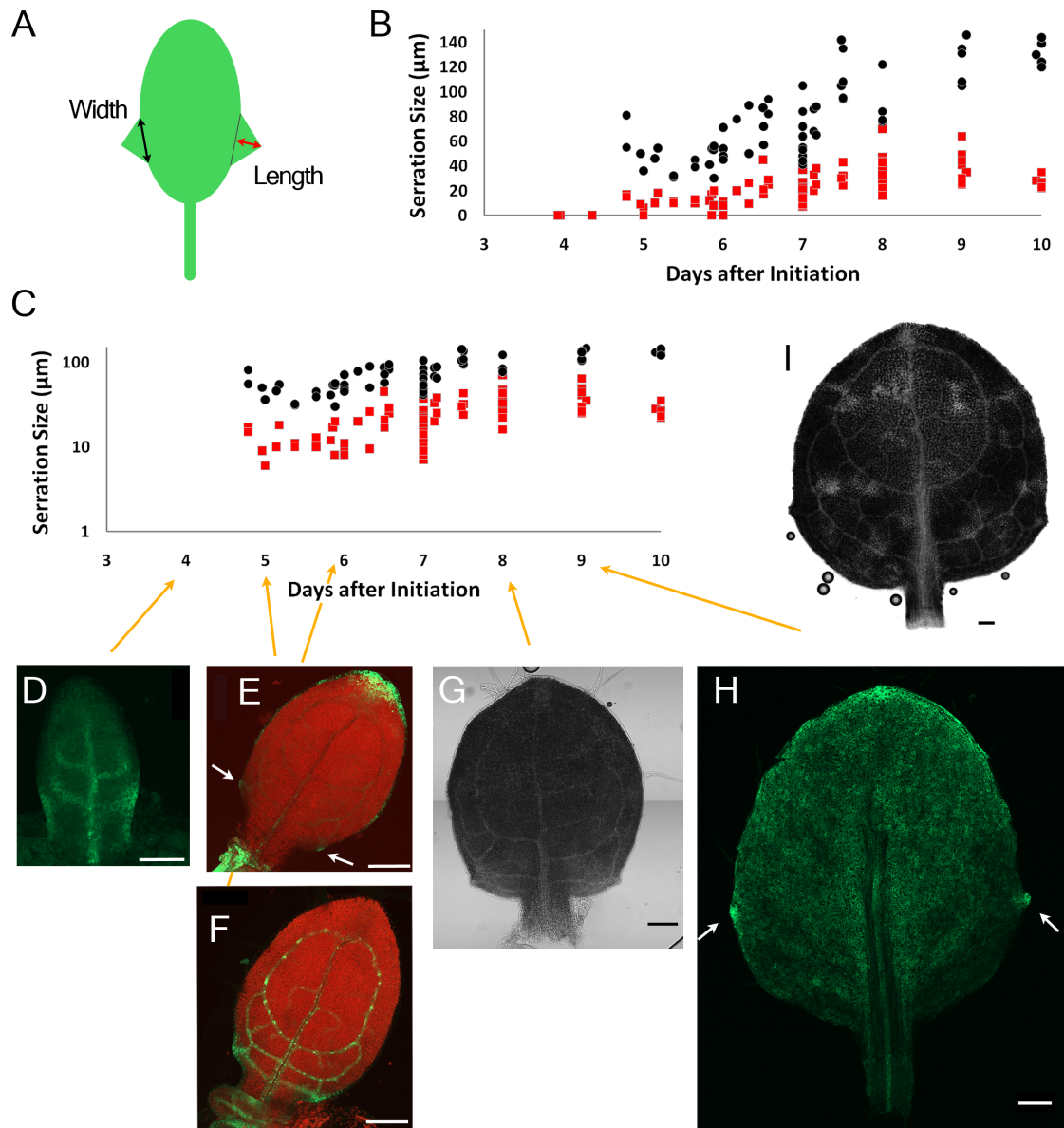


**Figure 3.1** Time course analysis of leaf 1 serration development. **A**, leaf diagram showing the axes along which serration size was measured. **B-C**, measurements of serration dimensions of flattened leaves over time from day 4-10 showing serration length (red squares) and serration width (black circles). **B**, changes in serration size over time. **C**, serration size over time shown on a log scale. **D-I**, example images of leaf shapes at different developmental stages. **D** and **F**, *PIN1::PIN1-GFP* expression in leaves 4 and 6 days after initiation, respectively. **E** and **H**, *DR5rev::GFP* expression in leaves 5 and 9 days after initiation, respectively. White arrows indicate serrations. **G** and **I**, brightfield images of leaves 8 and 9 days after initiation, respectively. Scale bars **D**, 50  $\mu\text{m}$ , **E-G**, **I**, 100  $\mu\text{m}$  and **H**, 200  $\mu\text{m}$ .

### 3.2.2 Organiser-Based Polarity Fields

Based on the more detailed description of the spatiotemporal patterns of serration development, different hypotheses regarding the role of auxin and CUC2 in serration formation were tested using the leaf model generated in the previous chapter.

#### 3.2.2.1 Polarity Field Examples

In the previous chapter, models with a curvilinear proximodistal polarity field provided the best match to the observed growth orientations. Such polarity fields were established by the propagating polarity factor  $\mathbf{s}_{POL}$ , whose gradient determined the two axes of growth in the 2D plane, growth parallel to the gradient ( $K_{par}$ ) and growth perpendicular to the gradient ( $K_{per}$ ). In these models  $\mathbf{s}_{POL}$  was produced at the base of the leaf canvas by the polarity organiser  $\mathbf{i}_{PROXORG}$  and a proximodistal gradient of  $\mathbf{s}_{POL}$  was established by  $\mathbf{s}_{POL}$  decay throughout the canvas.

However, alternatively an  $\mathbf{s}_{POL}$  gradient could be established by  $\mathbf{s}_{POL}$  decay at another polarity organiser, which would act as an  $\mathbf{s}_{POL}$  sink. Depending on how this sink organiser is positioned, the polarity field may look indistinguishable from the one-organiser model. This can be demonstrated by returning to the square example introduced in the previous chapter (2.2.11 Organiser-Based Polarity Systems). In that example, a linear gradient of growth rates was specified across the canvas to promote  $K_{per}$ , while  $K_{par} = 0\% h^{-1}$  (Fig. 3.2A).

$\mathbf{i}_{PROXORG}$  was expressed at the base of the canvas (Fig. 3.2B) and  $\mathbf{s}_{POL}$  levels were allowed to establish before growth commenced. This created a polarity field that followed the geometry of the canvas.

A visually indistinguishable polarity field can be generated by positioning a sink, here called  $\mathbf{i}_{DISTRORG}$ , at the distal end of the canvas in addition to a source organiser ( $\mathbf{i}_{PROXORG}$ ) at the base (Fig 3.2C).  $\mathbf{i}_{DISTRORG}$  completely absorbed  $\mathbf{s}_{POL}$  levels, setting  $\mathbf{s}_{POL}$  levels to zero. In addition,  $\mathbf{s}_{POL}$  levels were determined by:

$$\frac{\partial \mathbf{s}_{POL}}{\partial t} = D_{pol} \nabla^2 \mathbf{s}_{POL} + p_{pol} \mathbf{i}_{PROXORG}, \quad (3.1)$$

where  $D_{pol}$  is the diffusion rate of  $s_{POL}$  and  $p_{pol}$  is the production rate of  $s_{POL}$  by  $i_{PROXORG}$ .

While a polarity field, which is solely based on  $s_{POL}$  production from one organiser (with  $s_{POL}$  decay), is highly limited by the geometry of the canvas, considerably more flexibility in polarity field specification can be gained by using the two types of organisers. For instance, instead of expressing  $i_{DISTORG}$  all along the distal end of the canvas,  $i_{DISTORG}$  expression could be limited to local regions at the distal end. Expressing  $i_{DISTORG}$  at the two distal corners reorientated the polarity field towards the distal corners, which resulted in an overall rounder canvas shape (Fig. 3.2D). In another example,  $i_{DISTORG}$  was expressed in the centre of the distal end (Fig. 3.2E). This resulted in a pillow-like canvas shape with the polarity field orienting towards the distal centre.

These examples demonstrate the importance of polarity in shape development, since in all cases the underlying specified growth rate distributions were identical.

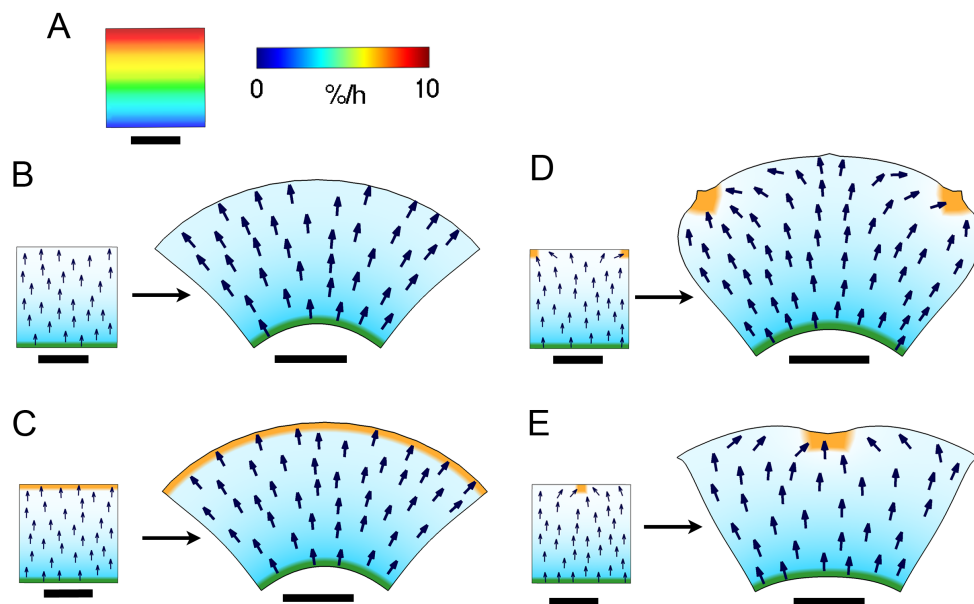


**Figure 3.2** A, linear gradient of growth rates specified across the initial square canvas. B-E, different organiser-based models showing the polarity field (arrow),  $s_{POL}$  (blue),  $i_{PROXORG}$  (green) and  $i_{DISTORG}$  (orange) on the initial and the resultant canvas shapes. B, one-organiser model. C-E, two-organiser models. Scale bars 1 *mm*.

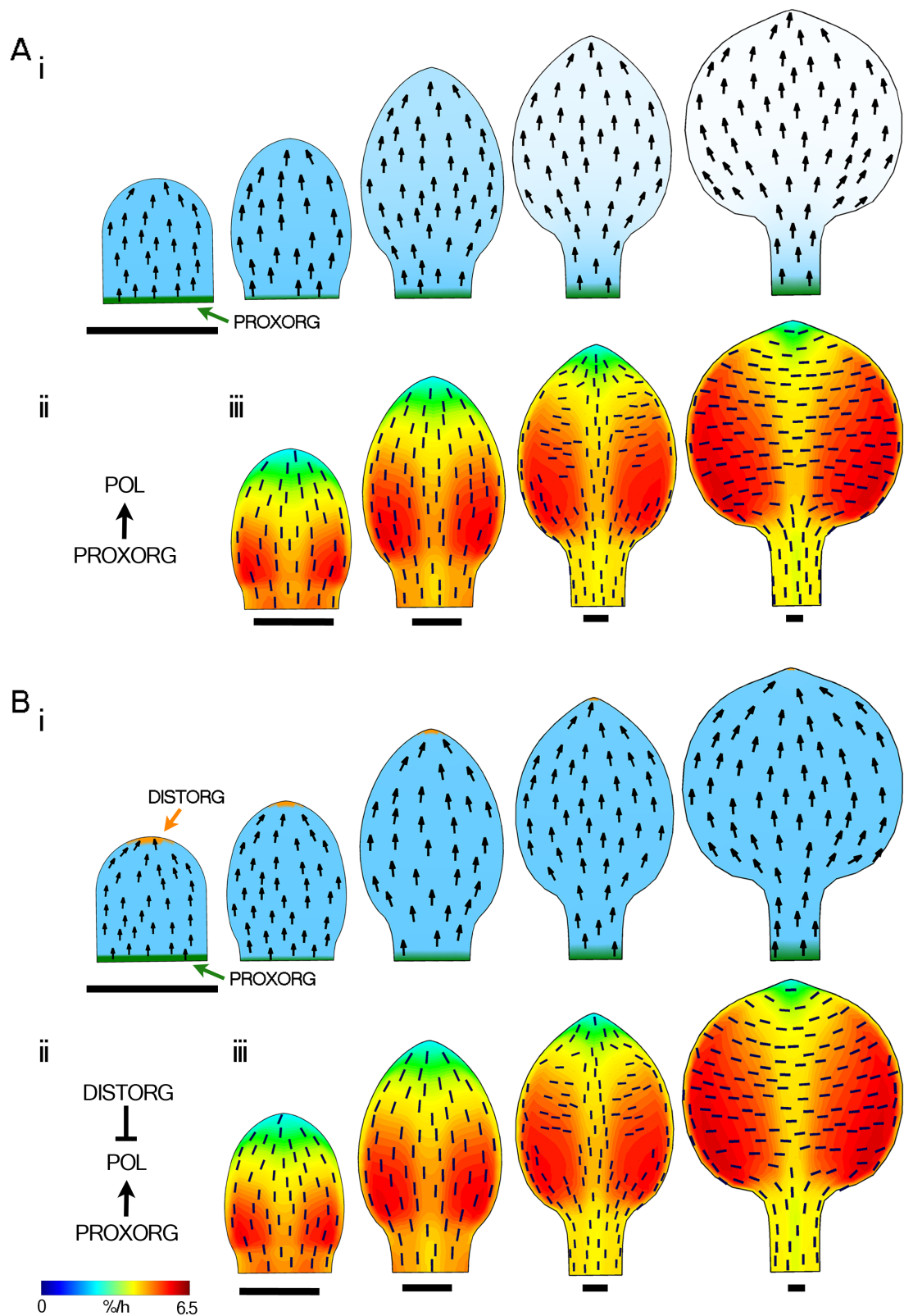


**Figure 3.3** **A**, one-organiser model with dynamic polarity field and  $s_{POL}$  decay throughout the canvas. **B**, two-organiser model with dynamic polarity field and  $s_{POL}$  decay at  $i_{DISTORG}$  only. (i) polarity field (arrows) with  $s_{POL}$  (blue),  $i_{PROXORG}$  (green) and  $i_{DISTORG}$  (orange). (ii) polarity interaction network. (iii) resultant growth rates and principal orientations of growth calculated over 24 h intervals. Orientations shown at an anisotropy > 5 %. Canvas shapes are shown at times corresponding to leaves 4-8 days after initiation. Scale bars 100  $\mu m$ .

### 3.2.2.2 Organiser-Based Leaf Models

The aim of this chapter is to test the effects of changes in the polarity field on serration development. As the two-organiser polarity models provide more control over the polarity field, another organiser ( $\mathbf{i}_{DISTORG}$ ) was added to the leaf model (Fig. 3.3B).  $\mathbf{s}_{POL}$  was subject to decay at  $\mathbf{i}_{DISTORG}$ :

$$\frac{\partial \mathbf{s}_{POL}}{\partial t} = D_{pol} \nabla^2 \mathbf{s}_{POL} - a_{pol} \mathbf{s}_{POL} \mathbf{i}_{DISTORG}, \quad (3.2)$$

where  $a_{pol}$  is the decay of  $\mathbf{s}_{POL}$  at  $\mathbf{i}_{DISTORG}$ .  $\mathbf{s}_{POL}$  propagated according to this equation throughout the simulation and the polarity field remained responsive to  $\mathbf{s}_{POL}$  levels. As before,  $\mathbf{s}_{POL}$  levels were maintained at levels defined by  $b_{pol}$  in regions expressing  $\mathbf{i}_{PROXORG}$  throughout the simulation.

When  $\mathbf{i}_{DISTORG}$  was expressed at the distal end of the canvas, the resulting canvas shapes, polarity fields and growth parameters were visually very similar to those of the dynamic one-organiser model (Fig. 3.3A).

## 3.2.3 Mechanisms of Serration Development

A variety of serration mechanisms were tested computationally by modifying the interactions of the dynamic two-organiser model. To generate serrations on the leaf canvas, new factors were added to the model. For simplicity the distribution of these new factors was established manually through the *GFtbox* interface. To increase modelling accuracy the finite element mesh was subdivided locally in the margins of the proximal half of the canvas at early stages.

For clarity, the model names used in the text and the general mechanism of each model are summarised (see Tab. 3.1 under 3.4 Overview of Serration Models).

### 3.2.3.1 Higher Growth Rates at the Serrations

One way to generate local outgrowths is through higher growth rates at the serration sites compared to the rest of the margins. These higher growth rates can either arise by increasing growth locally or by inhibiting growth of

the adjacent margins.

### 3.2.3.1.1 Inhibition Release Model

In the leaf models generated in the previous chapter,  $K_{per}$  was restricted at the margins. Therefore, an easy way to increase growth rates locally at the margins is to remove the inhibition of  $K_{per}$  at these sites. This was achieved by introducing a new identity factor  $\mathbf{i}_{SER}$  during model setup, whose expression is restricted to two small regions in the proximal margins (Fig. 3.4A).  $\mathbf{i}_{SER}$  negatively affects the inhibitory effect of  $\mathbf{i}_{RIM}$  at the margins (Fig. 3.4B, red). Together with the growth interactions established in the previous chapter (Eqn. 2.15 and Eqn. 2.23) this gives:

$$\begin{aligned}
 K_{par} &= p_{prox} \mathbf{i}_{PROX} \cdot \text{inh}(h_{late}, \mathbf{i}_{LATE}) \\
 K_{per} &= p_{lam} \mathbf{i}_{LAM} \cdot \text{pro}(p_{late}, \mathbf{i}_{LATE}) \cdot \text{inh}(h_{mid}, \mathbf{i}_{MID}) \\
 &\quad \cdot \text{inh}(h_{rim} \cdot \text{inh}(h_{ser}, \mathbf{i}_{SER}), \mathbf{i}_{RIM}), \tag{3.3}
 \end{aligned}$$

where, as previously,  $p_{prox}$  is the promotion of  $K_{par}$  by  $\mathbf{i}_{PROX}$ , which has a linear gradient across the proximodistal axis of the canvas with highest levels at the base.  $h_{late}$  is the inhibition of  $K_{par}$  by  $\mathbf{i}_{LATE}$ , which is expressed uniformly throughout the canvas after day 6 and increases linearly thereafter.  $p_{lam}$  and  $p_{late}$  are the promotion of  $K_{per}$  by  $\mathbf{i}_{LAM}$  and  $\mathbf{i}_{LATE}$ , respectively.  $h_{mid}$  and  $h_{rim}$  are the inhibition of  $K_{per}$  by  $\mathbf{i}_{MID}$  and  $\mathbf{i}_{RIM}$ , respectively. The levels of  $\mathbf{i}_{LAM}$  are high in the proximal lamina regions and low in the very proximal regions of the canvas.  $\mathbf{i}_{MID}$  is expressed along the midline of the canvas.  $\mathbf{i}_{RIM}$  is expressed in the margins of the lamina region of the canvas. In addition in this model, the inhibition of  $K_{per}$  by  $\mathbf{i}_{RIM}$  is reduced by  $\mathbf{i}_{SER}$  at a magnitude of  $h_{ser}$ .

Reducing the inhibition by  $\mathbf{i}_{RIM}$  at the serration sites resulted in higher growth rates at these sites, which formed very small but broad protrusions (Fig. 3.4C). These protrusions were smaller than the observed leaf outgrowths and not pointy. The initial position of outgrowth, as specified by the position of  $\mathbf{i}_{SER}$ , had been determined according to the location of serration initiation

in the real leaves (Fig. 3.4A). The position of the modelled protrusions over time compared well to those observed (Fig. 3.4C). This suggests that leaf growth rates, in the proximal region at least, have been captured well by the leaf model.

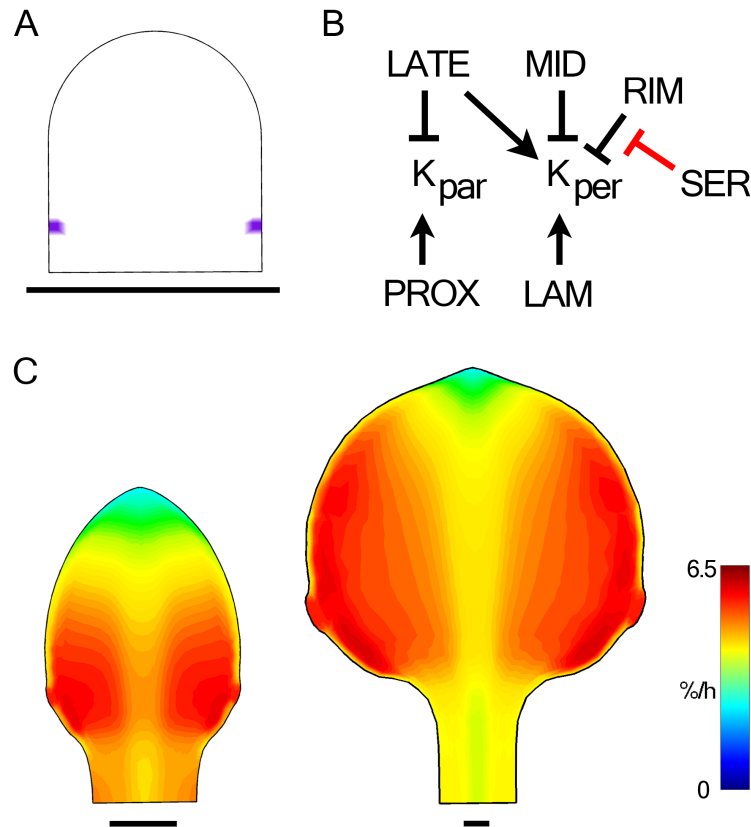


**Figure 3.4** Inhibition release model. **A**, distribution of  $i_{SER}$  on the initial canvas. **B**, growth interaction network with  $i_{SER}$  repressing the inhibitory effect of  $i_{RIM}$  on  $K_{per}$  (red). **C**, model canvasses grown according to the growth interactions in **B** showing resultant areal growth rates calculated over 24  $h$  intervals (colours) at times corresponding to leaves 6 and 8 days after initiation. Scale bars 100  $\mu m$ .

### 3.2.3.1.2 Increased Growth Models

One way of increasing the size of the serrations is to increase the growth rates at the serration sites through  $i_{SER}$ . This idea was tested while maintaining the interactions of the inhibition release model.

First,  $i_{SER}$  increased areal growth rates at the margins (increased areal

growth model; Fig. 3.5B iii):

$$\begin{aligned}
K_{par} &= p_{prox} \mathbf{i}_{PROX} \cdot \text{inh}(h_{late}, \mathbf{i}_{LATE}) \cdot \text{pro}(p_{ser}, \mathbf{i}_{SER}) \\
K_{per} &= p_{lam} \mathbf{i}_{LAM} \cdot \text{pro}(p_{late}, \mathbf{i}_{LATE}) \cdot \text{inh}(h_{mid}, \mathbf{i}_{MID}) \\
&\quad \cdot \text{inh}(h_{rim} \cdot \text{inh}(h_{ser}, \mathbf{i}_{SER}), \mathbf{i}_{RIM}) \cdot \text{pro}(p_{ser}, \mathbf{i}_{SER}), \quad (3.4)
\end{aligned}$$

where  $K_{par}$  and  $K_{per}$  are promoted by  $\mathbf{i}_{SER}$  at an amount determined by  $p_{ser}$ .  $\mathbf{i}_{SER}$  expression was set up in the initial canvas. However, unlike above,  $\mathbf{i}_{SER}$  only influenced growth rates after 120  $h$ , which corresponds to a leaf 5 days after initiation (Fig. 3.5A), 15 hours prior to the canvas reaching the width of about 250  $\mu m$  at which serration outgrowth had been observed in real leaves (Fig. 3.1E). Factors were activated prior to observed outgrowth, as it took time for specified growth patterns to visibly change the canvas shape. Therefore, prior to 120  $h$  the  $\mathbf{i}_{SER}$  parameter values were  $p_{ser} = 0$  and  $h_{ser} = 0$ , and after 120  $h$   $p_{ser} = 0.5$  and  $h_{ser} = 10$ . Increasing both  $K_{par}$  and  $K_{per}$  locally in the margins resulted in extensive round outgrowths (Fig. 3.5B i and ii).

These growth patterns were investigated further by dividing them into the contribution of increased growth along  $K_{par}$  and  $K_{per}$  separately. In both models the settings of the inhibition release model were maintained. To influence  $K_{par}$  but not  $K_{per}$ , the promotion of  $K_{per}$  by  $\mathbf{i}_{SER}$  was taken out of the equation generating the increased  $K_{par}$  model (Fig. 3.5C ii):

$$\begin{aligned}
K_{par} &= p_{prox} \mathbf{i}_{PROX} \cdot \text{inh}(h_{late}, \mathbf{i}_{LATE}) \cdot \text{pro}(p_{ser}, \mathbf{i}_{SER}) \\
K_{per} &= p_{lam} \mathbf{i}_{LAM} \cdot \text{pro}(p_{late}, \mathbf{i}_{LATE}) \cdot \text{inh}(h_{mid}, \mathbf{i}_{MID}) \\
&\quad \cdot \text{inh}(h_{rim} \cdot \text{inh}(h_{ser}, \mathbf{i}_{SER}), \mathbf{i}_{RIM}) \quad (3.5)
\end{aligned}$$

The outgrowths produced by promoting growth along  $K_{par}$  only were very broad and flat (Fig. 3.5C i). Promoting  $K_{per}$  by  $\mathbf{i}_{SER}$  only, in contrast, generated narrower and deeper outgrowths (increased  $K_{per}$  model; Fig. 3.5D ii). The promotion by  $K_{per}$  only was modelled in a similar way as the increased

$K_{par}$  model, by promoting  $K_{per}$  by  $i_{SER}$  only and not  $K_{par}$  (Fig. 3.5D ii):

$$\begin{aligned}
 K_{par} &= p_{prox} \mathbf{i}_{PROX} \cdot \text{inh}(h_{late}, \mathbf{i}_{LATE}) \\
 K_{per} &= p_{lam} \mathbf{i}_{LAM} \cdot \text{pro}(p_{late}, \mathbf{i}_{LATE}) \cdot \text{inh}(h_{mid}, \mathbf{i}_{MID}) \\
 &\quad \cdot \text{inh}(h_{rim} \cdot \text{inh}(h_{ser}, \mathbf{i}_{SER}), \mathbf{i}_{RIM}) \cdot \text{pro}(p_{ser}, \mathbf{i}_{SER}) \quad (3.6)
 \end{aligned}$$

The observed shape of the increased  $K_{per}$  model matched best with the shapes of observed serrations. However, observed serrations are more pointy than the ones generated by the model.

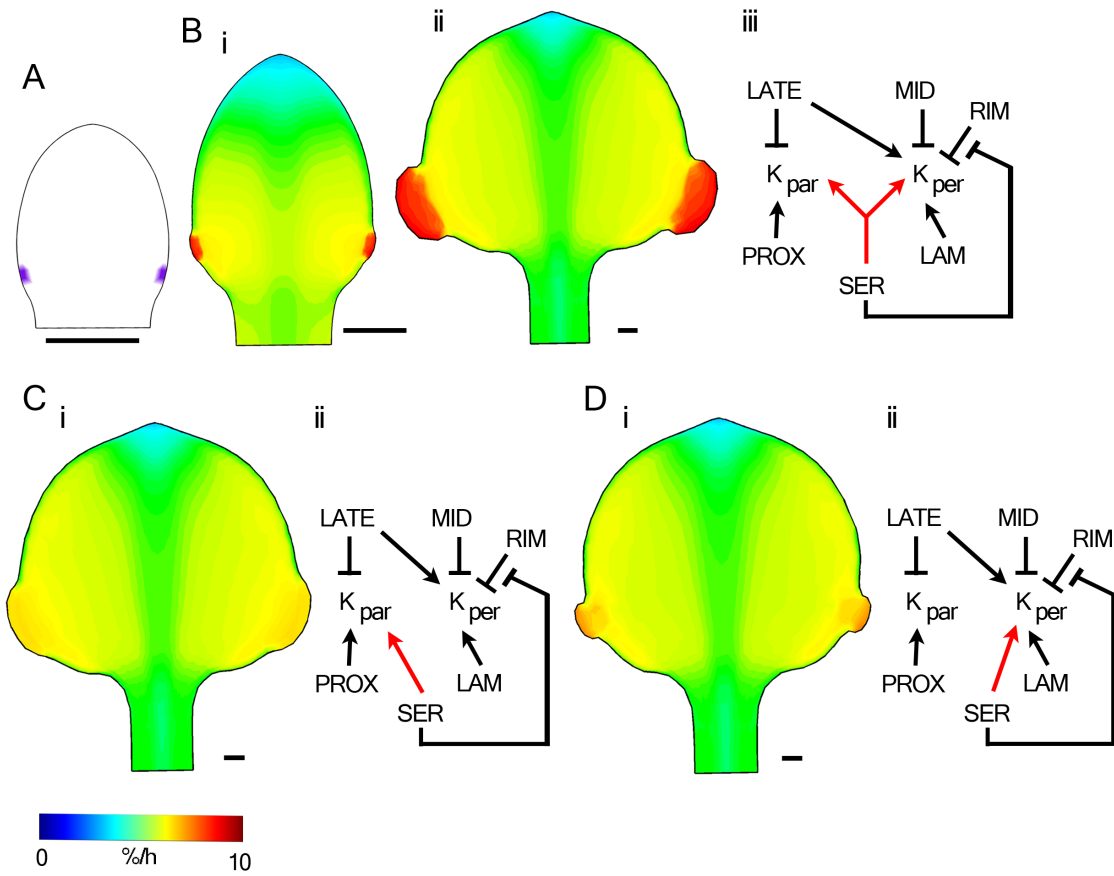


**Figure 3.5** Increased growth models.  $i_{SER}$  increases the growth rates at the serration sites. **A**, distribution of  $i_{SER}$  on the canvas at 120 h, which corresponds to a leaf 5 days after initiation. **B**, increased areal growth model, where  $i_{SER}$  increases both  $K_{par}$  and  $K_{per}$ . Canvas shown at times corresponding to a leaf (i) 6 and (ii) 8 days after initiation. (ii) growth interaction network. **C**, increased  $K_{par}$  model, where  $i_{SER}$  increases  $K_{par}$  only. **D**, increased  $K_{per}$  model, where  $i_{SER}$  increases  $K_{per}$  only. **C-D(i)**, canvas shown at a time corresponding to a leaf 8 days after initiation. (ii) growth interaction network. **B-D**, colours represent resultant areal growth rates calculated over 24 h intervals. Scale bars 100  $\mu m$ .

### 3.2.3.1.3 Reduced Sinus Growth Model

An alternative way to increase the size of the protrusions created by the inhibition release model, is to also increase the inhibition of growth at the sites adjacent to  $\mathbf{i}_{SER}$  (called sinuses or indentations). Therefore, in addition to  $\mathbf{i}_{SER}$ , an identity factor  $\mathbf{i}_{SINUS}$  was added to the model during model setup.  $\mathbf{i}_{SINUS}$  was expressed on both sides adjacent to  $\mathbf{i}_{SER}$  to increase the inhibitory effect of  $\mathbf{i}_{SINUS}$  (Fig. 3.6A). In simple leaves, CUC gene expression is generally limited to the distal side of the serrations (Hasson et al., 2011; Nikovics et al., 2006).  $\mathbf{i}_{SINUS}$  restricted both  $K_{par}$  and  $K_{per}$  (reduced sinus growth model; Fig. 3.6D):

$$\begin{aligned}
 K_{par} &= p_{prox} \mathbf{i}_{PROX} \cdot \text{inh}(h_{late}, \mathbf{i}_{LATE}) \cdot \text{inh}(h_{sinus}, \mathbf{i}_{SINUS}) \\
 K_{per} &= p_{lam} \mathbf{i}_{LAM} \cdot \text{pro}(p_{late}, \mathbf{i}_{LATE}) \cdot \text{inh}(h_{mid}, \mathbf{i}_{MID}) \\
 &\quad \cdot \text{inh}(h_{rim} \cdot \text{inh}(h_{ser}, \mathbf{i}_{SER}), \mathbf{i}_{RIM}) \cdot \text{inh}(h_{sinus}, \mathbf{i}_{SINUS}), \quad (3.7)
 \end{aligned}$$

where  $h_{sinus}$  is the inhibition of growth by  $\mathbf{i}_{SINUS}$ . As in the models above (3.2.3.1.2 Increased Growth Models), both  $\mathbf{i}_{SER}$  and  $\mathbf{i}_{SINUS}$  affected growth after 120  $h$  only (Fig. 3.6A). Restricting growth adjacent to the incipient serrations resulted in indented margins (Fig. 3.6B and C) with similar sized outgrowths as generated by the inhibition release model (Fig. 3.4C). The small amount of observed outgrowths did not become pointy, unlike the serrations in real leaves.

### 3.2.3.2 Serrations through Polarity Field Modifications

Since modifications of the growth rates did not result in pointy serrations, the effect of changes in the polarity field on serration development was tested. This was achieved by expressing a new organiser at the sites of  $\mathbf{i}_{SER}$  expression (Fig. 3.5A). Similar to the models above, the function of  $\mathbf{i}_{SER}$  only took effect after 120  $h$ . The new organiser either promoted the levels of  $\mathbf{s}_{POL}$  (source, specified by  $\mathbf{i}_{PROXORG}$ ) or reduced the levels of  $\mathbf{s}_{POL}$  (sink, specified by  $\mathbf{i}_{DISTORG}$ ). The propagation of  $\mathbf{s}_{POL}$  was defined by the same equation as above (Eqn. 3.2). In the same way as at the base,  $\mathbf{s}_{POL}$  levels were set to levels defined by  $b_{pol}$  at the new sites of  $\mathbf{i}_{PROXORG}$  expression.

Unless indicated otherwise, growth modifications specified by  $i_{SER}$  in the previous models were removed again (Fig. 3.7C).

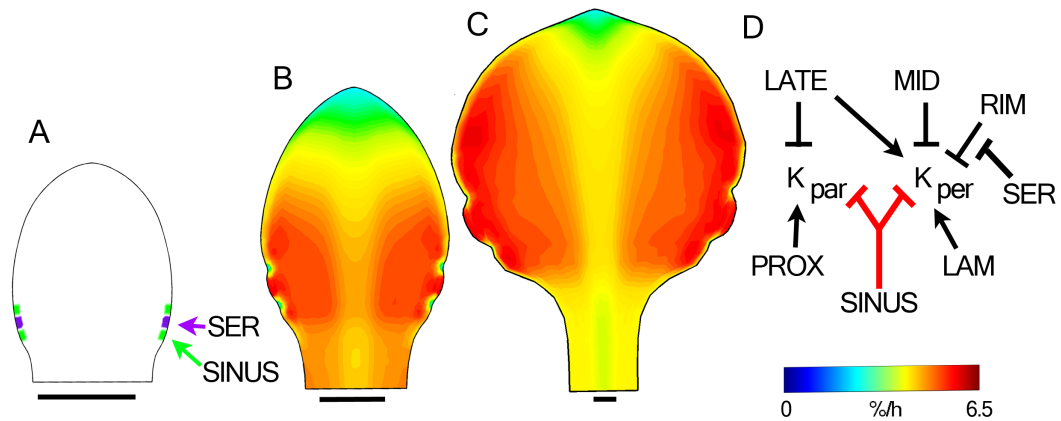


**Figure 3.6** Reduced sinus growth model. **A**, distribution of  $i_{SER}$  (purple) and  $i_{SINUS}$  (green) on the canvas at 120  $h$ , which corresponds to a leaf 5 days after initiation. **B-D**, reduced sinus growth model. Colours represent resultant areal growth rates calculated over 24  $h$  intervals. The canvas is shown at times corresponding to leaves **B**, 6 and **C**, 8 days after initiation. **D**, growth interaction network. Scale bars 100  $\mu m$ .

### 3.2.3.2.1 Source Model

First,  $i_{SER}$  promoted the expression of a new source specified by  $i_{PROXORG}$  (Fig. 3.7D). The introduction of a new  $s_{POL}$  source resulted in slight changes in the polarity field in proximal regions (Fig. 3.7A, black arrows). These changes caused the proximal margins below the outgrowth to become convex, similar to what has been observed in real leaves (Fig. 3.7B, blue arrow). The new polarity field generated small protrusions, which remained small throughout the period analysed. However, the protrusions appeared more pointy than the ones generated by the growth-only models above. The protrusions were also asymmetric with a shorter sharper boundary on the distal side compared to the proximal one. This asymmetry can be observed in real leaves, although it is less clear in leaf 1. The petiole-lamina boundary broadened extensively, whereas in real leaves this boundary remains narrow (Fig. 3.1G-I and Fig. 3.7B).

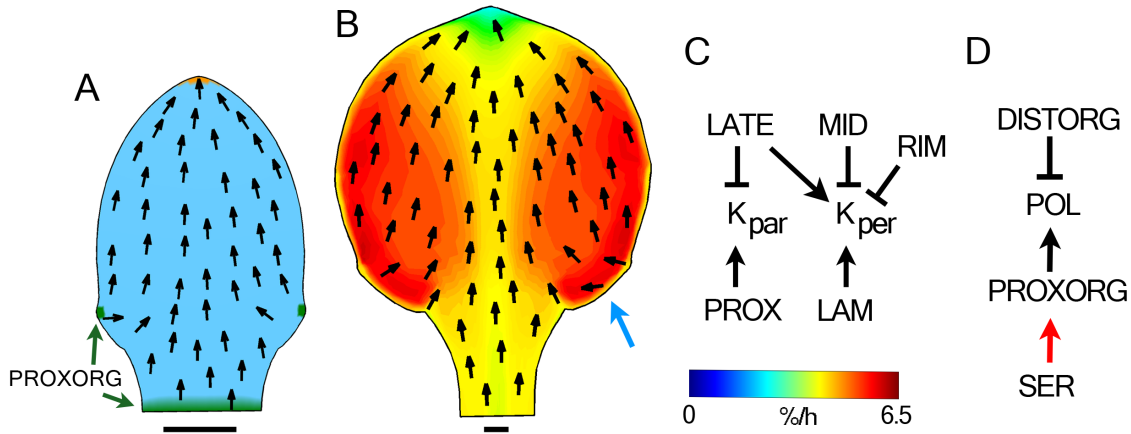


**Figure 3.7** Source model with new  $s_{POL}$  sources (specified by  $i_{PROXORG}$ ) at the sites of  $i_{SER}$  expression. **A**, the canvas at a time corresponding to a leaf 6 days after initiation with  $s_{POL}$  (blue),  $i_{PROXORG}$  (green) and  $i_{DISTORG}$  (orange). Arrows show the polarity field. **B**, canvas at a stage corresponding to a leaf 8 days after initiation showing resultant areal growth rates (colours) calculated over a 24 h interval and the polarity field (arrows). Blue arrow indicates concave proximal margins. **C**, growth interaction network. **D**, polarity interaction network. Scale bars 100  $\mu m$ .

### 3.2.3.2.2 Sink Models

Alternatively to a new source,  $i_{SER}$  may promote the expression of a new sink specified by  $i_{DISTORG}$  (Fig. 3.8B). The new  $i_{DISTORG}$  organisers had a strong effect on the polarity field in the proximal regions of the canvas. The polarity field reoriented towards the new sinks (Fig. 3.8A i). The amount of the divergence of the polarity field increased with simulation time (compare Fig. 3.8A i and ii). The canvas deformed to give rise to small but pointy protrusions at these sites (Fig. 3.8A ii). These protrusions were pointy from the start.

One way to limit repolarisation locally was to assume that a sufficiently steep gradient of  $s_{POL}$  is necessary to determine polarity. During growth the  $s_{POL}$  gradient loses its steepness in particular in regions distant from an organising centre. It is realistic to assume that below a certain gradient steepness, cells are no longer able to determine the direction of the gradient. Therefore, at shallow gradients cells could either lose their polarity or retain the polarity last perceived. Here it was assumed that at shallow gradients

cells retain their last perceived directional information. Therefore, the polarity field was fixed to the canvas in regions where the  $s_{POL}$  gradient dropped below 2 %, the gradient steepness limit eukaryotic cells are able to measure according to previous reports (Hu et al., 2010).

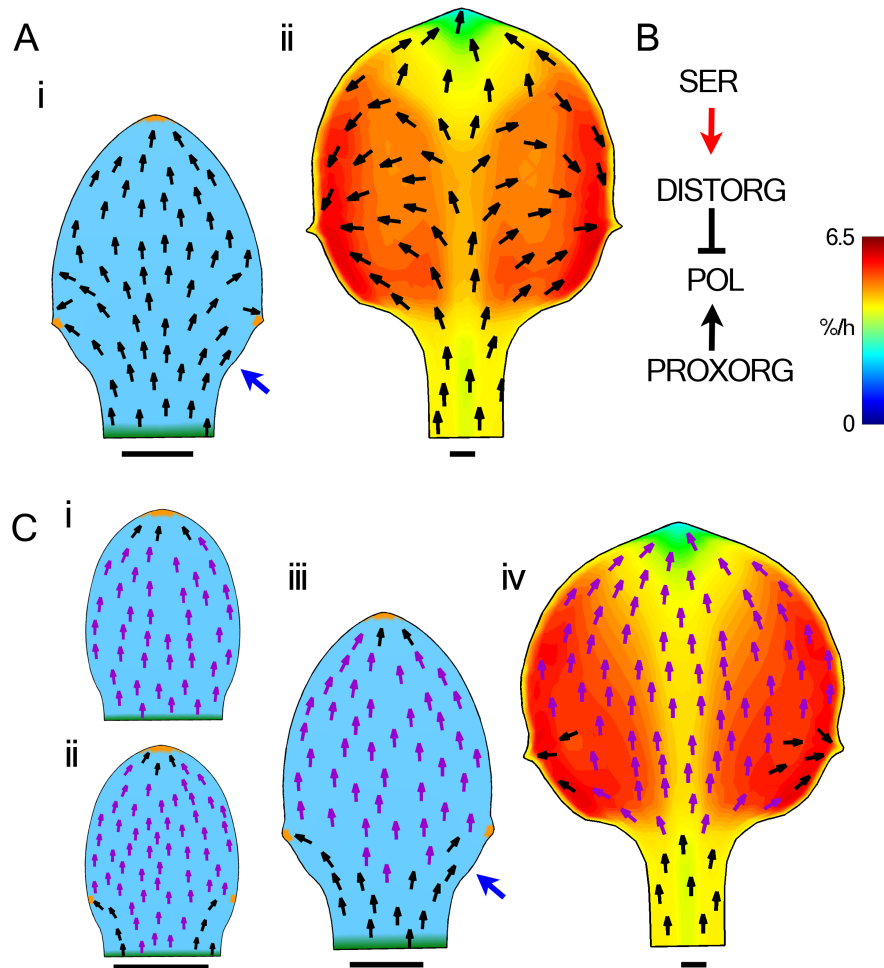


**Figure 3.8** Sink models with new  $s_{POL}$  sinks ( $i_{DISTORG}$ ) at the sites of  $i_{SER}$  expression. **A**, sink model (i) the canvas at a time corresponding to a leaf 6 days after initiation with  $s_{POL}$  (blue),  $i_{PROXORG}$  (green) and  $i_{DISTORG}$  (orange). Arrows show the polarity field. (ii) canvas at a stage corresponding to a leaf 8 days after initiation showing areal growth rates calculated over a 24 h interval (colours) and the polarity field (arrows). **B**, polarity interaction network of the sink models. **C**, sink threshold model with the same model interactions as in **A**, but polarity directions were fixed to the canvas in regions where the  $s_{POL}$  gradient dropped below 2 %. (i - iii) the canvas at a time corresponding to a leaf (i and ii) 5 days and (iii) 6 days after initiation with  $s_{POL}$  (blue),  $i_{PROXORG}$  (green) and  $i_{DISTORG}$  (orange). Arrows show the polarity field. (iv) canvas at a stage corresponding to a leaf 8 days after initiation showing areal growth rates calculated over a 24 h interval (colours) and the polarity field (arrows). In **B** black arrows indicate dynamic polarity orientations and pink arrows indicate regions where the  $s_{POL}$  gradient is below 2 % and polarity orientations were fixed to the canvas. Scale bars 100  $\mu m$ .

Just prior to the induction of  $i_{SER}$ , the  $s_{POL}$  gradient in the main part of the canvas had already dropped below 2 % (sink threshold model, Fig. 3.8C i, purple arrows indicate fixed polarity). However, the initiation of a new sink at the serration points increased the steepness of the gradient again locally and immediately diverted the polarity field (Fig. 3.8C ii, black arrows indicate dynamic polarity). The introduction of a threshold to polarity dynamics reduced the amount of repolarisation of the polarity field due to the new organiser, but still generated similarly shaped protrusions at the margins compared to the sink model without thresholding (Fig. 3.8C iii and iv).

In both of these models the position or orientation of the serrations compared well to those observed (compare Fig. 3.1G-I to Fig. 3.8A ii and C iv). However, the proximal margins of the canvas at early stages were not convex, unlike the margins of real leaves (Fig. 3.8A i and C iii, blue arrows).

### 3.2.3.2.2.1 Principal Orientations of Growth

The pointy serrations generated by the sink models matched well to those observed at later stages of leaf development. However, the polarity field in the sink model was substantially disturbed (Fig. 3.8A ii), which is likely to affect the principal orientations of growth across the canvas. The modelled growth orientations were therefore compared to those measured for the real leaves by time lapse imaging. The principal orientations of growth in the real leaf 8 days after initiation had an overall mediolateral orientation, but pointed slightly upwards towards the distal margins (Fig. 3.9A, blue arrow). In the petiole orientations were strictly oriented along the proximodistal axis. Unfortunately the proximal margin regions, from which serrations develop, were out of focus and could not be tracked.

These observed overall patterns could also be seen in the sink model, where orientations in the distal regions of the canvas aligned mediolaterally and in the distal-lateral regions pointed towards the distal margins (Fig. 3.9B, green arrow). These upward orientations were slightly steeper than those observed in the real leaves. Orientations in the proximal centre regions were oriented towards the midline, unlike observed leaf patterns (Fig. 3.9B, blue arrow).

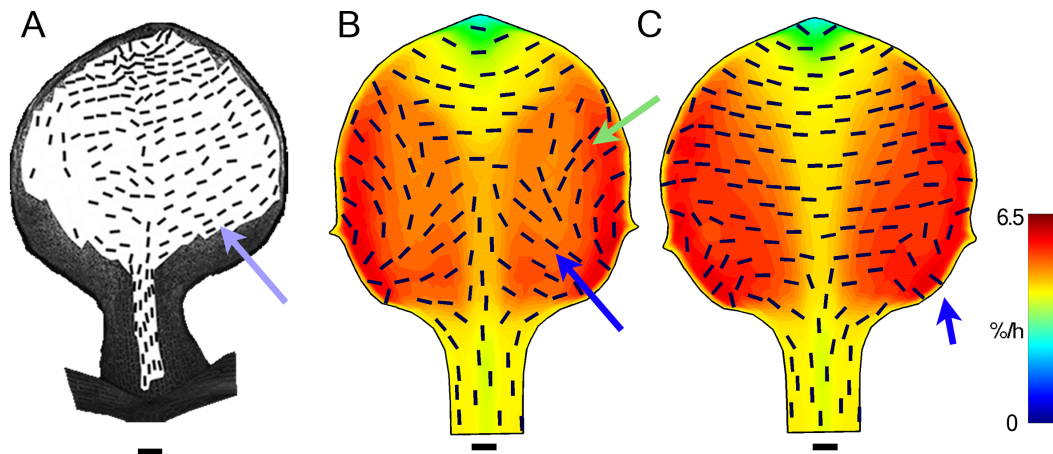


**Figure 3.9** Principal orientations of growth **A**, in a 8 day old tracked leaf, displayed for regions with an anisotropy  $> 10\%$ . Image generated by Samantha Fox. **B**, sink model and **C**, sink threshold model, showing the canvas at a size corresponding to a leaf 8 days after initiation with resultant areal growth rates (colours) and principal orientations of growth, displayed for regions with an anisotropy  $> 5\%$ . All growth rates and orientations were calculated over 24 h intervals. Scale bars 100  $\mu\text{m}$ .

The observed patterns in leaves and the sink model were compared to those of the sink threshold model, in which the polarity field was less affected by the introduction of the new sinks. The milder changes in the polarity field were also reflected in the modelled principal orientations of growth (Fig. 3.9C), which had a mediolateral orientation across most of the canvas. Orientations at the very proximal margins and near the serration sites were orientated largely proximodistally (Fig. 3.9C, blue arrow).

In general, the sink threshold model provided a better match to the observed principal orientations of growth, although growth orientations in the real leaf were more oblique in the lamina regions than those of the sink threshold model.

### 3.2.3.3 Serrations through Growth and Polarity

The serrations generated by the organiser-based models were pointy but small. To increase the serration sizes, combinations of growth and polarity models were explored. As the number of possible growth and polarity combinations is large and in the absence of definite data on serration formation, growth combinations were tested on the sink model only.

First, the inhibition release model interactions were combined with the sink model. In the inhibition release model  $\mathbf{i}_{SER}$  releases the inhibition of  $K_{per}$  by  $\mathbf{i}_{RIM}$  (3.2.3.1.1 Inhibition Release Model; Eqn. 3.3).

The resulting serrations of this sink inhibition release model were slightly bigger than those observed previously with the sink models (compare Fig. 3.8A ii and 3.10A ii). Although this addition made the serrations broader, serrations were still more pointy than those of the growth-only models. This was because the new organising centre in the serrations redirected the polarity patterns. The reduction in the inhibition of  $K_{per}$  now increased growth perpendicular to the length axis of the serration, rather than making the serrations deeper.

Therefore, I tested whether a combination of the sink model and the increased  $K_{par}$  model (instead of increasing  $K_{per}$ ) would generate deeper serrations. The growth equations used for this sink increased  $K_{par}$  model were the same as for the increased  $K_{par}$  model (3.2.3.1.2 Increased Growth Models; Eqn. 3.5). This model resulted in very pointy and large serrations (Fig. 3.10B ii), demonstrating that serration size can be adjusted by a combination of growth and polarity mechanisms. The size of the modelled serrations now exceeded those observed for leaf 1 in *Arabidopsis*. More leaf-like serrations could be produced by reducing the amount of promotion of  $K_{par}$  by  $\mathbf{i}_{SER}$ .

Alternatively, deeper serrations could be generated by combining the sink model with the reduced sinus growth model (sink sinus model). In this case  $\mathbf{i}_{SINUS}$  was expressed just above  $\mathbf{i}_{SER}$  only and inhibited areal growth rates (3.2.3.1.3 Reduced Sinus Growth Model; Eqn. 3.7; Fig. 3.10C a). The second organiser was only expressed above the serration site (unlike in the reduced sinus growth model above), as in *Arabidopsis*, CUC2 is only expressed on the distal side of the serrations (Nikovics et al., 2006).

The resulting canvas shapes showed strong indentations above the serrations, which resulted in bigger and more asymmetric serration shapes (Fig. 3.10C ii).

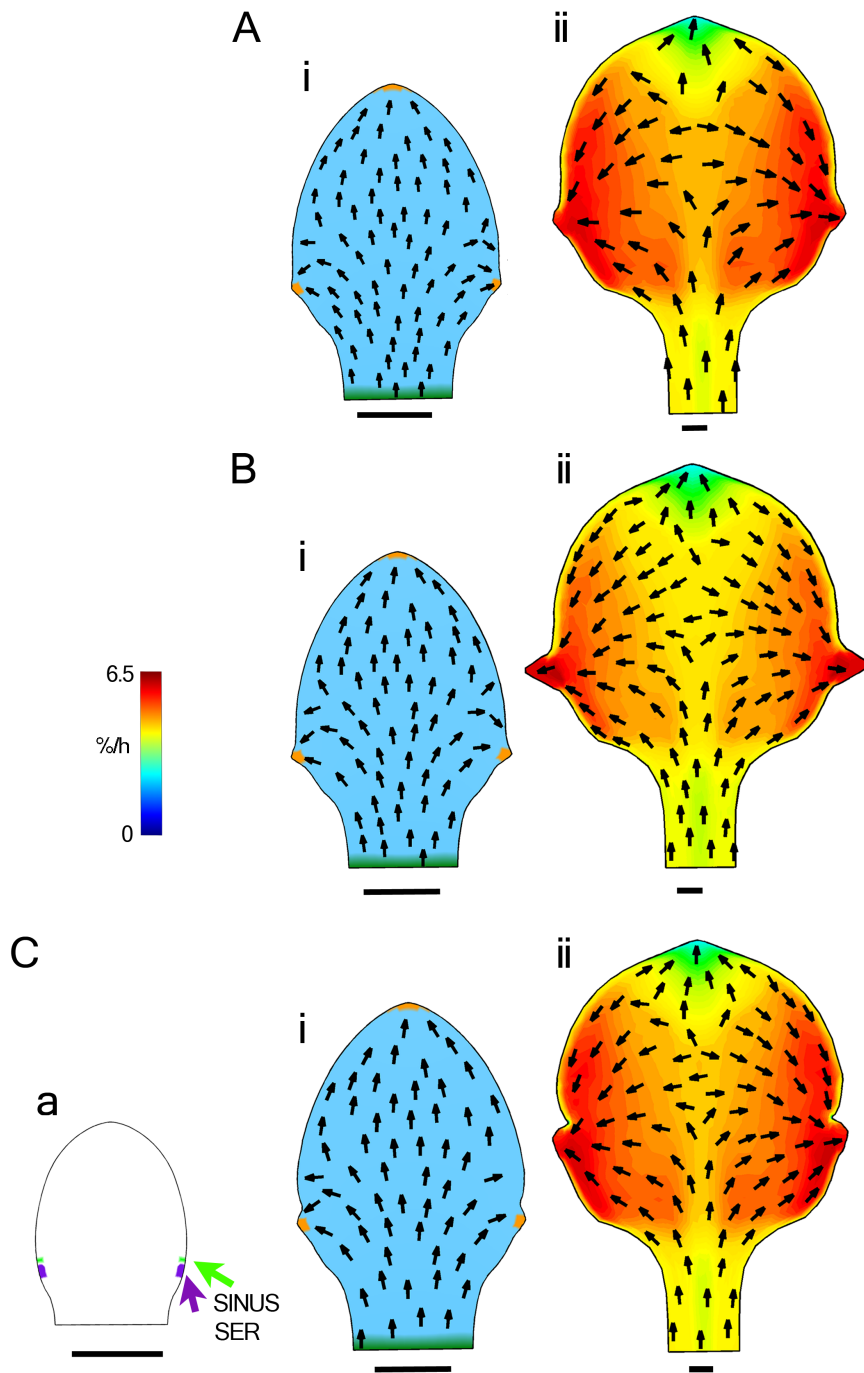


**Figure 3.10** Models with combinations of polarity and growth rate modifications. **A**, the sink inhibition release model, **B**, the sink increased  $K_{par}$  model and **C**, the sink sinus model (**a**) distribution of  $i_{SER}$  and  $i_{SINUS}$  in the sink sinus model. Canvas shown at a time corresponding to a leaf 5 days after initiation. (**i**) the canvas at a time corresponding to a leaf 6 days after initiation with  $s_{POL}$  (blue),  $i_{PROXORG}$  (green) and  $i_{DISTORG}$  (orange). Arrows show the polarity field. (**ii**) canvas at a stage corresponding to a leaf 8 days after initiation showing areal growth rates calculated over a 24 h interval (colours) and the polarity field (arrows). Scale bars 100  $\mu m$ .

### 3.2.3.4 Serrations through Multiple Organisers

None of the models shown above have been able to capture all of the aspects of serration formation observed in leaf 1 of *Arabidopsis*. However, the source model and the sink model each captured a number of the observations. A combination of the two models might therefore describe all observations. The two organisers were combined by expressing one of the organisers at the serration sites and the other organiser just above it (Fig. 3.11A).

First, a model was created where  $\mathbf{i}_{SER}$  determined the initiation of a new sink, defined by  $\mathbf{i}_{DISTORG}$ , and  $\mathbf{i}_{SINUS}$  determined the initiation of a new source, defined by  $\mathbf{i}_{PROXORG}$  (sink-source model).

The combination of the two organisers limited the extent of repolarisation slightly in the central and distal regions compared to the sink model (compare Fig. 3.8A ii and Fig. 3.11B ii). Similar to the sink models sharp pointy outgrowth developed at the sites of  $\mathbf{i}_{SER}$  expression. However, the introduction of a new source above the sink also changed the smoothness of the margins by forming a small protrusion above the pointy serrations. It is therefore questionable if such a system is employed in the leaf.

In the opposite approach the same model setup was used but  $\mathbf{i}_{SER}$  now determined the position of  $\mathbf{i}_{PROXORG}$  and  $\mathbf{i}_{SINUS}$  promoted the expression of  $\mathbf{i}_{DISTORG}$  (source-sink model). Similar to the source model, the proximal margins were convex (Fig. 3.11C ii). Internally, however, the polarity field was disturbed due to the new sink (Fig. 3.11C ii, pink arrow). In addition, small protrusions developed at the sites of the  $\mathbf{i}_{SINUS}$  expression.

Thus, combinations of two organisers do not provide a better match to the data and suggest that leaf serrations are formed by the initiation of one new organiser only, possibly in combination with a modification in growth rates.

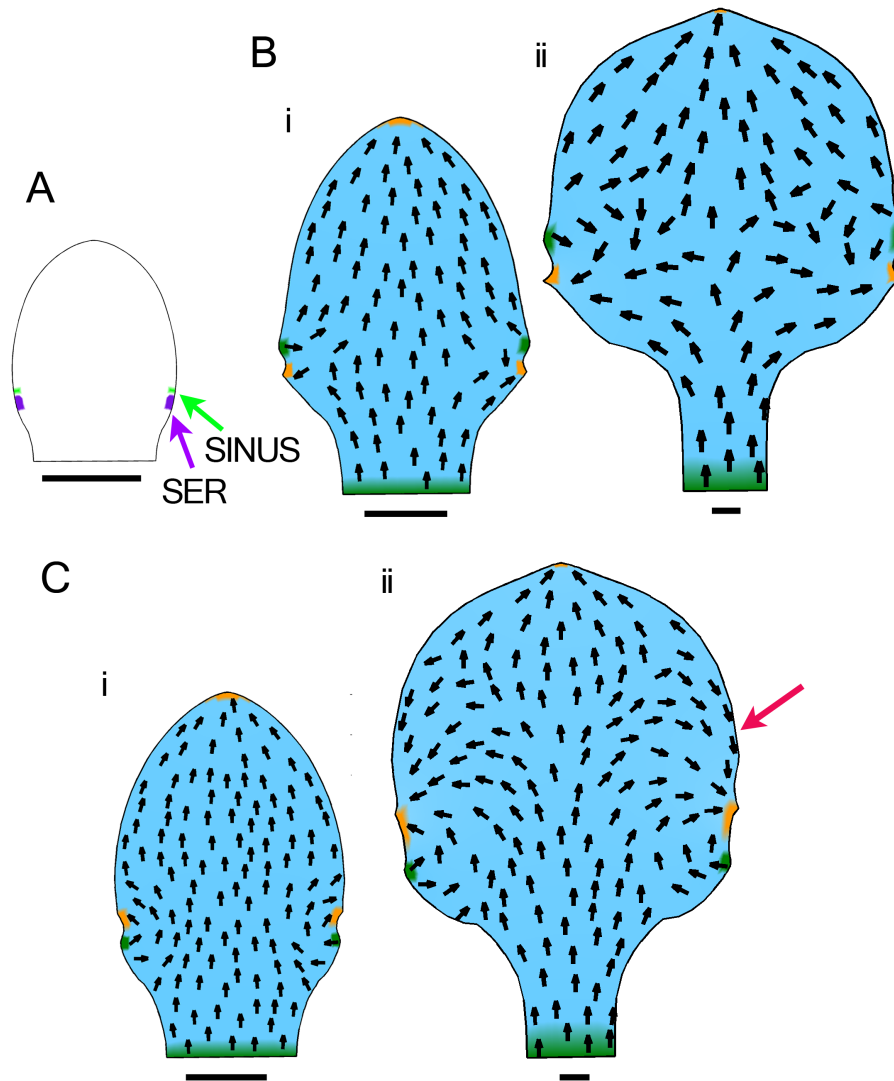


**Figure 3.11** Serration models with combinations of organisers. **A**, canvas corresponding to a leaf 5 days after initiation showing the distribution of  $i_{SER}$  (purple) and  $i_{SINUS}$  (green). **B**, sink-source model, where a new sink is expressed at the sites of  $i_{SER}$  expression and a new source is expressed just above at  $i_{SINUS}$ . **C**, source-sink model, where a new source is expressed at the site of  $i_{SER}$  expression and a new sink is expressed just above at  $i_{SINUS}$ . Canvas corresponding to leaves (i) 6 and (ii) 8 days after initiation showing the distribution of  $s_{POL}$  (blue),  $i_{PROXORG}$  (green),  $i_{DISTORG}$  (orange). Scale bars 100  $\mu m$ .

### 3.2.4 Serration Maintenance

Different mechanisms of serration formation have been explored and qualitatively compared to those observed in real leaves of *Arabidopsis* leaf 1. Models, in which the growth rate properties of the margin regions were modified, generated broad outgrowths. Changes in the polarity field resulted in more pointy outgrowths, which were, however, relatively small. Combinations of

growth and polarity modifications visually generated the best results.

To compare the different models more quantitatively to the leaf data, serrations generated by the models were measured in the same way as the leaf serrations described previously (3.2.1 Serration Development). I compared serrations generated by the increased  $K_{per}$  model, the sink model and the sink inhibition release model to those observed. Serration length was measured as the distance between the line describing serration width and the serration tip, where the length line was always orthogonal to the width line. The proximal end of the serrations generated by the source model was not clearly visible and therefore serration size could not be measured.

Modelled serrations were initially smaller than those observed experimentally (Fig. 3.12, data in red). While sink model serrations (Fig. 3.12, blue) remained small throughout and only increased slowly, increased  $K_{per}$  model serrations (Fig. 3.12, yellow) increased rapidly in size. The serrations of the sink inhibition release model (Fig. 3.12, green) increased the fastest initially and showed the best match to the size of the leaf serrations. However, while growth of real leaf serrations decelerated slightly with time, modelled serrations appeared to continue growing, with the possible exception of the sink inhibition release model. This suggests that a mechanism for serration growth deceleration is needed, which has not been implemented in the models shown here.

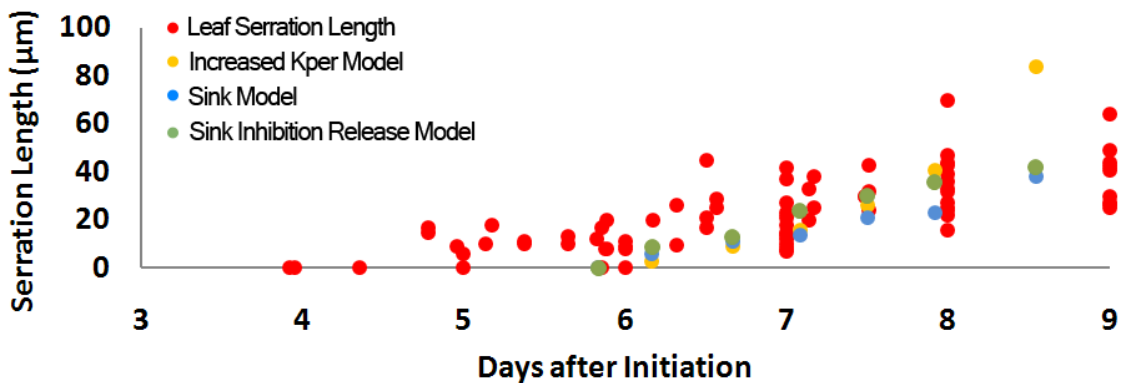


**Figure 3.12** Changes in serration length over time of real leaves and the modelled canvasses.

### 3.2.5 Clonal Analysis of Serrated Leaves

The modelling approach has allowed the evaluation of different mechanisms that may underly serration development. I here showed that these different mechanisms make different predictions regarding the growth and polarity patterns during development, which can be tested experimentally. For instance, time lapse imaging could be employed to determine the principal orientations and rates of growth in the leaf margins. These results could be compared to model outputs. Alternatively, the nature of the serration mechanism might be inferred from clonal analysis, which reveals the underlying growth and polarity patterns (Green et al., 2010; Rolland-Lagan et al., 2005). Since leaves can be removed from the plant and flattened for imaging, clonal analysis provides information for the whole leaf including the margins, which is more difficult to obtain using time lapse imaging. In the past, clonal analysis has been used to identify the number of progenitor cells that give rise to leaflets in complex leaves of *C. hirsuta* (Barkoulas et al., 2008). Therefore, virtual clonal analysis was performed on some of the models presented above to investigate whether clonal patterns are sufficiently different to distinguish between models.

#### 3.2.5.1 Virtual Clonal Analysis

In the previous chapter, virtual clonal analysis was performed by superimposing real cell outlines onto the model. These outlines were obtained from leaves that corresponded to the model canvas size and age. To model clonal patterns near the serration sites, cell outlines have to lie in the proximal margins. However, at early stages of leaf growth the proximal margins are hidden by the cotyledons and real cell outlines for these regions could not be obtained. Therefore, cells were represented by circles at the start of the simulation, which roughly matched the shape and size of early cells (day 3). At the time of  $\mathbf{i}_{SER}$  induction, these circles had grown to ellipses (Fig. 3.13A). Three different model classes were subjected to this virtual clonal analysis. These models included the increased  $K_{per}$  model, the source model, the sink model and the sink threshold model (Fig. 3.13B-E).

Clonal orientations differed slightly between models, in particular at the petiole-lamina boundary and in the proximal lamina regions close to the serrations.

In the increased  $K_{per}$  model, the serrations did not disturb the polarity field, which followed the geometry of the canvas with a proximodistal orientation towards the distal organiser (Fig. 3.13B, small black arrows on canvas). Modelled clones also followed the geometry of the canvas and showed slight tendencies towards the developing serrations due to the increase of growth rates in the serrations (Fig. 3.13B, red arrow).

In the source model, clones in the marginal petiole regions did not follow the geometry of the canvas margins as clearly, but instead remained relatively straight (Fig. 3.13C, blue arrow). This difference is likely to be a result of the difference in the underlying polarity field, which in case of the source model pointed away from the serrations and resulted in clones growing more towards the lamina centre.

Clones generated by the sink model and sink threshold model were visually very similar in the proximal regions (Fig. 3.13D and E). They also looked very similar to those of the increased  $K_{per}$  model, with marginal sectors that followed the geometry of the canvas (compare Fig. 3.13B, D and E, blue arrows). In the sink models, sectors near the serrations also showed a tendency to grow towards the serrations (Fig. 3.13D and E, red arrows).

Thus, the clonal patterns generated using these different methods were very similar. Patterns of the source model were the most distinct, whereas the patterns of the increased  $K_{per}$  model and the sink models looked almost identical despite the differences in the polarity field. The polarity field of the source model oriented sectors away from the serrations, while the polarity fields of the sink models guided clones towards the new serrations.

### 3.2.5.2 Experimental Clonal Analysis

The clonal patterns generated by the different models were compared to clones induced in real leaves using the Cre-Lox heat-shock inducible system

to generate GFP-expressing clonally related cells (Gallois et al., 2002). Clones were induced in leaves 3 days after initiation and imaged 9 days after initiation, which corresponded to similar leaf sizes as the model outputs. The experimental clones were segmented and warped to a mean shape using the *Sector Analysis Toolbox* with the same method as described in the previous chapter (2.2.13.1 Clonal Analysis). This work was carried out by Samantha Fox. Due to the small size of the serrations in leaf 1, serrations did not contribute significantly to the mean shape of the leaf (Fig. 3.13F). Therefore, a brightfield image of an example leaf is shown as a reference of serration position at this age (Fig. 3.13G, black arrows). This example also demonstrates that serration size and position is not always symmetrical in leaf 1, but can be quite variable along the two opposing margins of the leaf. Similar observations have been made for leaf 11 to 15 of *Arabidopsis* (Nikovics et al., 2006).

Leaf clones in the petiole appeared to follow the geometry of the margins (Fig. 3.13F, blue arrows). In general, clones also seemed to be constricted near the lamina base and became wider further away (Fig. 3.13F, red arrow), similar to the modelled clonal patterns. Since the position of the serrations could not be determined from the mean shape, clones of one individual leaf are shown (Fig. 3.13H), which contributed to the warped figure (Fig. 3.13F, red arrow). This showed clonal growth towards the serration (Fig. 3.13H, red arrow).

### 3.2.5.3 Comparison

Based on the clonal patterns, it was not possible to reliably distinguish between the different serration mechanisms. Taken together with the shape of the serrations, the sink threshold model provides the best match to observed patterns.

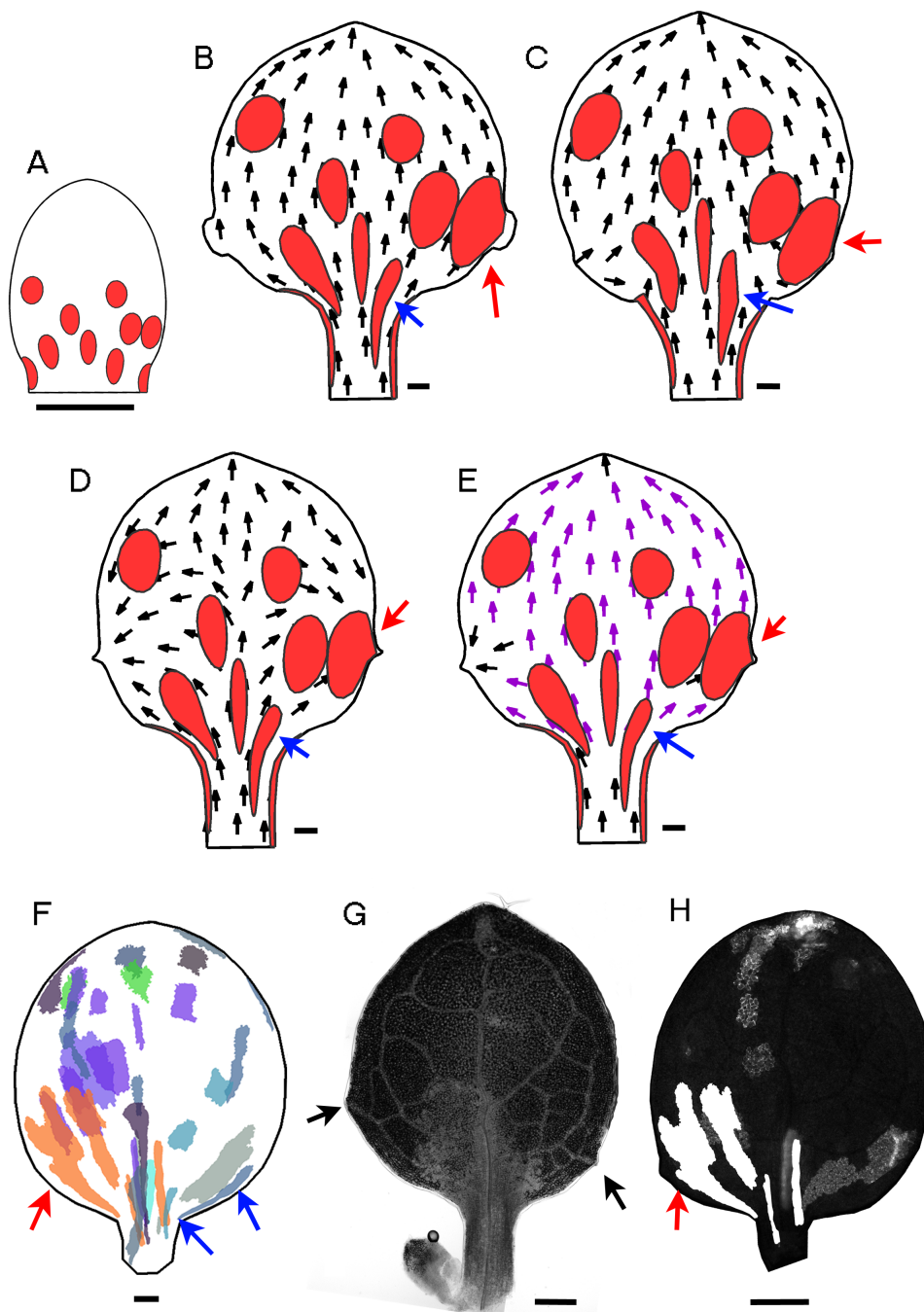


**Figure 3.13** **A**, canvas corresponding to a leaf 5 days after initiation showing virtual clones (red shapes) just prior to the introduction of a serration mechanism. **B-E**, serration models showing virtual clones (red shapes) and the polarity field (small black arrows on the canvas). Clones of interest are highlighted by arrows outside the canvas, where blue arrows point towards proximal clones and red arrows point towards clones close to the serrations. **B**, increased  $K_{per}$  model. **C**, source model. **D**, sink model and **E**, sink threshold model. **F**, clonal analysis of leaf clones induced on day 3 and imaged on day 9. Clones were segmented and warped to a mean shape (black leaf outline). Clones from the same leaf are represented by the same colour. Blue arrows indicate clones that follow the proximal geometry of the leaf. Red arrow indicates clone that grew towards the serration. **G**, example leaf showing serration shapes, sizes and positions (black arrows) on a leaf 9 days after initiation. **H**, one leaf used for the clonal analysis described in **F**. The highlighted sector (red arrow) is the sector highlighted in **F** (red arrow). Scale bars **A-F**, 100  $\mu\text{m}$ , **G**, 200  $\mu\text{m}$  and **H**, 250  $\mu\text{m}$ .

Clones in the proximity of the serrations are expected to look similar to those predicted here. However, a major problem with inferring serration mechanisms from modelled clones is the need for the correct serration positioning during the model simulations. For instance, the serrations in the source model are closer to the petiole-lamina boundary than those observed in real leaves at that age. This means that clonal patterns in the proximal regions are likely to look different when source model serrations are repositioned. Therefore, unless the positions of the modelled serrations are correct, real leaf clonal analysis results are very difficult to interpret against model results.

### 3.3 Discussion

#### 3.3.1 Serrations in Leaf 1

Serration development in *Arabidopsis* leaf 1 has been visualised using expression marker constructs of *PIN1* and the auxin response marker *DR5* as well as brightfield microscopy. The expression of *PIN1* and *DR5* agreed with earlier reports (Nikovics et al., 2006; Scarpella et al., 2006).

Leaf 1 has one pair of sharp serrations, which initiate when the leaf is about 250  $\mu\text{m}$  in width. In leaf 11 to 15, serrations emerge slightly earlier, at a leaf length of about 250  $\mu\text{m}$  (Nikovics et al., 2006). In leaf 1, serrations mostly grow during the early stages of development. An initial rapid increase in serration size has also been measured for leaf 6 in *Arabidopsis* (Hasson et al., 2011). Growth in serration length in leaf 6 also slowed down, but not as much as that of leaf 1. The different dynamics of serration width and length over time might be due to growth. Higher growth rates in the lamina compared to the serrations could stretch the boundary between the serrations and the lamina, thus increasing serration width. The expansion marker *ARGOS-LIKE* accumulates earlier in the serrations compared to the lamina (Hu et al., 2006), suggesting that laminar growth continues for longer.

### 3.3.2 Model Evaluations

The small size of *Arabidopsis* leaf 1 serrations makes leaf 1 a less ideal system to study the generation of serrations. Leaf 1 was chosen, however, as data on other *Arabidopsis* leaves was lacking and more importantly, the model is fitted to leaf 1 growth. Despite the small serration size, it was possible to identify underlying properties of different serration formation hypotheses.

Out of the different hypotheses tested, pointy serrations could only be generated by modulating the polarity field of the leaf. This is in agreement with previous experimental data, which showed that cell files reorient towards the serrations (Kawamura et al., 2010). The requirement for polarity reorganisation provides further support for a leaf organising system, which continuously readjusts according to a morphogen gradient rather than a system, which becomes unresponsive to changes in polarity organising signals from an early leaf age. However, repolarisation is likely to be a localised event in the proximal margins only, given that the real principal orientations of growth in the central lamina did not seem to be affected by the morphogenetic events at the margins.

However, it is unclear whether local repolarisations are organised by a new source or a new sink, since both model classes captured parts of the leaf features observed. The source model generated small serrations, which remained closer to the petiole-lamina boundary than expected, and failed to replicate observed clonal patterns. In addition, the modelled petiole became very broad near the lamina boundary. The observed leaf petiole, in contrast, remains narrow. However, the source model was the only model tested, which generated the observed convex proximal margins. The source model also generated asymmetric serrations, which were slightly shorter on the distal side compared to the proximal side. This difference has been observed in higher metamers of *Arabidopsis* (Bilsborough et al., 2011; Kawamura et al., 2010). Here, serration asymmetry could be generated by the asymmetric inhibition of growth above the serration site only.

In the sink model proximal margins were straight at early stages and recovered some curvature at later stages. However, clonal patterns and serration shapes

matched well to those of real leaves.

Different combinations of organisers generated either the convex margins or the pointy serrations and outgrowths were observed at both the new serration source and sink. It therefore seems unlikely that two polarity organisers are expressed adjacently in the leaf. However, it is possible that one organiser acts non-autonomously, redirecting the polarity field at the serration sites, or that growth inhibition in the sinus prevents a second outgrowth from forming.

Local modification in the margin growth rates in the growth-only models resulted in local rounded outgrowths, which were less sharp than those observed. The best results were obtained for increasing  $K_{per}$  only at the margins. A polar increase in local growth has been employed in a previous modelling approach and generated rounded margin outgrowths (Bilsborough et al., 2011). In their model the authors attributed the increase in growth rate to the action of auxin.

Reductions in growth rates at the sinuses only resulted in indented sinuses rather than clear outgrowths. These results are in agreement with experimental results, which showed by superimposing wild-type and *cuc2* mutant leaves that wild-type leaves grow more at the proximal margins compared to *cuc2* mutants (Kawamura et al., 2010). If the role of CUC2 was to restrict growth, *cuc2* mutants would be expected to have wider leaves than wild-type. However, it is possible that some growth restriction conferred by CUC2 facilitates the formation of asymmetric serrations.

The failure of these growth-only models to generate pointy serrations agrees with the observations that cell cycling activity at the margins is uniform in simple leaves like *Arabidopsis* (Barkoulas et al., 2008; Kawamura et al., 2010). Although in complex leaves, cells initiating leaflets are reported to have higher cell cycling rates (Barkoulas et al., 2008; Blein et al., 2008). However, cell division patterns may not reflect underlying growth patterns.

In the increased growth models presented here, growth rates were uniform throughout the serrations. However, it is possible that a gradient of growth rates exists in the serrations similar to that observed in the lamina, which might result in more pointy serrations.

The best match to real leaf dynamics could be achieved by a combination of growth and polarity mechanisms. These results demonstrate the importance of the interaction of growth and polarity in shape development.

In the models, serrations were initiated at the same loci at which serrations were observed to emerge in the real leaves. Apart from the source model, all models correctly predicted the change in position of the serrations during development. This provides support for the accuracy of the leaf model in general, as the model captures the high growth rates in the proximal regions, which makes up most of the area of the later leaf, as evident from the temporal changes in serration positions.

### 3.3.3 Maintenance

The different models were also assessed based on their ability to reflect the changes in serration length over time. The serration length of the models tested compared relatively well with those of the real leaves. The increased  $K_{per}$  model overestimated serration length at later stages, suggesting that a growth deceleration mechanism is required during serration development. The fact that CUC2 expression above the serration diminishes with time (Nikovics et al., 2006) suggests that the process driving serration outgrowth might not be active throughout leaf development.

A combination of growth and polarity generated serrations, whose sizes compared well to the real leaf serrations, even without a growth deceleration mechanism. This provides further support for an interaction of growth and polarity in shape development.

### 3.3.4 Clones and Future Work

The different models were tested by virtual clonal analysis and compared to real leaf clones. In this comparison, the increased  $K_{per}$  model and the sink model performed best in matching observed clonal patterns. However, the failure of the source model to position the serrations correctly over time

also affected modelled clonal patterns. Therefore, this model should not be dismissed prematurely.

Based on the virtual clones generated by the different models it would be difficult to distinguish between a growth or polarity-based mechanism, since clones might be attracted by a new polarity organiser or simply grow according to an underlying polarity field, which deforms with the geometry of the tissue. Therefore, clonal analysis might not be a very suitable method to verify the different hypotheses. Although it is likely that better results would be generated for more serrated leaves.

Thus, although it is difficult to get accurate time lapse imaging data on leaf margin regions, it appears necessary to resolve how serration development is controlled in the leaf. Time lapse imaging provides growth rate and directional information more readily than clonal analysis.

Leaf 1 was used in this analysis due to the availability of tracking and clonal data. However, the small size and number of leaf 1 serrations limit their usefulness in understanding serration morphogenesis. A better understanding of serrations would be gained by studying higher metamers of *Arabidopsis* with a larger number of more pronounced serrations. However, these are more difficult to track using time lapse imaging.

### 3.3.5 Auxin, CUC2 and Future Work

The predicted position of a sink or source at the serration site correlates with the observed localisation of auxin. The directional transport of auxin is thought to provide polarity to a tissue and is important for primordium outgrowth (Benková et al., 2003; Okada et al., 1991; Reinhardt et al., 2003; Sauer et al., 2006). Thus, changes in local auxin concentrations could reflect local repolarisation. Here,  $s_{POL}$  propagation has been mediated by diffusion, while auxin is largely transported actively (Gälweiler et al., 1998; Kramer and Bennett, 2006; Sauer et al., 2006). Currently, active transport cannot be modelled with the *GFtbox* implementation used here.

Regardless of the method of auxin transport, auxin, together with PIN1, should be sufficient to repolarise the leaf locally to generate serrations. Therefore, theoretically serrations should develop even in the absence of CUC2. The

smooth leaf margins of *cuc2* mutants, however, suggest otherwise (Nikovics et al., 2006). Bilsborough et al. (2011) proposed in their model that CUC2 is necessary to stabilise the auxin maxima. Since, in my work, auxin and CUC2 were represented by abstract factors that did not diffuse or decay, this theory was not tested here. Further experiments have to be conducted to resolve whether CUC2 acts autonomously or has a non-autonomous function. CUC2 might stabilise auxin patterns or even act as a polarity organiser itself. It has been suggested that CUC3 has an autonomous as well as non-autonomous function in leaf serration formation (Blein et al., 2008).

A way to test the role of CUC2 would be to express *CUC2* ectopically but locally and measure the changes in the orientations of growth and growth rates. This work is currently under way by Susana Sauret-Güeto, who induces *CUC2* locally by coupling it to a heat-shock promoter. This work is also carried out in the petal, where CUC2 is normally limited to the organ boundary (Baker et al., 2005). Thus, changes in growth patterns can be attributed to CUC2 only. Using this approach a difference in CUC2 activity in the margins compared to the rest of the tissue can also be tested.

### 3.4 Overview of Serration Models

A summary of the different models used giving their names together with a short description is shown in Table 3.1.

Model Name	Model Description
<b>Modifications of Growth Rates (growth-only models)</b>	
inhibition release model	Inhibition of $K_{per}$ by $i_{RIM}$ is released at the serration sites.
increased areal growth model	In addition to the inhibition release model, $K_{par}$ and $K_{per}$ are both increased at the serration sites.
increased $K_{par}$ model	In addition to the inhibition release model, $K_{par}$ is increased at the serration sites.
increased $K_{per}$ model	In addition to the inhibition release model, $K_{per}$ is increased at the serration sites.
reduced sinus growth model	In addition to the inhibition release model, areal growth rates at the sites adjacent to the serrations are inhibited.
<b>Modifications of the Polarity Field</b>	
source model	New source at the serration sites.
sink model	New sink at the serration sites.
sink threshold model	The sink model with the polarity field fixed to the canvas in regions, where the $s_{POL}$ gradient drops below 2 %.
sink-source model	The sink model with a new source expressed just above the serration sites.
source-sink model	The source model with a new sink expressed just above the serration sites.
<b>Modifications of Growth and Polarity</b>	
sink inhibition release model	Combination of the inhibition release model and the sink model.
sink increased $K_{par}$ model	Combination of the increased $K_{par}$ model and the sink model.
sink sinus model	Combination of the reduced sinus growth model and the sink model.

**Table 3.1** Two-organiser models with a dynamic polarity field used to explore the different hypotheses of leaf serration formation.

# Chapter 4

## 3D Leaf Growth

### 4.1 Introduction

#### 4.1.1 3D Leaf Shapes

In the previous chapters, models of leaf 1 development were generated and used to make predictions regarding the coordination of growth and polarity during development. These two-dimensional models accounted for the planar leaf surface with the two main axes of growth, length and width. Since there is little growth in thickness or rearrangement of cells between layers, the 2D models gave good representations of the overall development of flattened leaf shapes. However, the relatively flat leaf structure bends out of the plane. This 3D curvature has been captured by Karen Lee using optical projection tomography (OPT; Fig. 4.1). OPT images show that the comparatively thick, young leaf grows primarily in width and length (Fig. 4.1A and B). The leaf becomes doubly curved in orthogonal directions with negative Gaussian curvature in the proximodistal direction and positive Gaussian curvature in the mediolateral direction (Fig. 4.1B). The proximodistal curvature increases until the lamina is roughly perpendicular to the petiole with the adaxial side on top (Fig. 4.1C). The lamina then becomes convex on the adaxial and concave on the abaxial side, resembling a cup (Fig. 4.1D). At later stages proximal regions of the leaf straighten and the petiole and proximal midvein regions become aligned, while the curvature remains high at the distal tip (Fig. 4.1E and F).



**Figure 4.1** **A**, confocal image of a 4 day old leaf stained with propidium iodide by Sascha Duttke. **B-F**, leaves imaged by optical projection tomography by Karen Lee on **B**, day 7, **C**, day 8, **D**, day 12, **E**, day 13 and **F**, day 18 after initiation. Scale bars **A**, 20  $\mu m$ , **B-C**, 200  $\mu m$ , **D-F**, 1  $mm$ .

Bending allows cells under compression to release stress (Dumais, 2007; Liang and Mahadevan, 2009; Shraiman, 2005), which can build up as a result of differential growth rates. In the 2D leaf models, growth interactions specify non-uniform anisotropic growth. Here, it was investigated whether these growth interactions are sufficient to explain the 3D leaf shape.

#### 4.1.2 Leaf Buckling

While relatively little research has been conducted on the mechanisms that cause leaves to adopt their 3D shapes, more research has focused on the mechanics underlying material and tissue buckling (Green, 1996; Liang and Mahadevan, 2009, 2011; Sharon et al., 2002). Irreversible buckling can be generated by stretching and then releasing many non-biological materials, such as plastic sheets (Klein et al., 2007; Sharon et al., 2002, 2004). Stretching increases the length of a material locally, which may be accommodated by buckling. Many biological tissues are buckled, such as flower and leaf margins, most likely as a result of differential growth rates or spatial constraints (Dervaux et al., 2009; Dumais, 2007; Liang and Mahadevan, 2009, 2011; Nelson et al., 2005; Shraiman, 2005). Higher growth rates at the margins compared to central regions can induce buckling in leaves and flowers (Koehl et al., 2008; Liang and Mahadevan, 2011).

Previous studies on tissue buckling mainly considered overall tissue shapes without taking specific growth data into account (Liang and Mahadevan, 2009;

Marder, 2003). The leaf model generated here, in contrast, is based on accurate descriptions of leaf growth. Therefore, it was possible to investigate what effect an increase in margin growth rates has on the the margins and the rest of the leaf shape.

Models with modified margin growth properties were compared to the phenotype of the *Arabidopsis* mutant *jaw-D*, which has buckled edges (Palatnik et al., 2003). It is possible that this phenotype is due to an increase in growth rates (Palatnik et al., 2003), a delay in growth arrest (Nath et al., 2003) or a complete failure to arrest growth at the margins. Leaves of this mutant were studied experimentally and computationally. In addition, comparing the model outputs to the shapes of mutant leaves provided another way to verify the leaf model.

#### 4.1.2.1 TCP Genes

In *jaw-D* mutants members of the *TCP* family of transcription factors (named after three members of the family: *TEOSINTE BRANCHED 1*, *CYLOIDEA* and *PROLIFERATING CELL FACTORS*; Cubas et al. 1999) are downregulated resulting in uneven leaf shapes that are difficult to flatten (Aggarwal et al., 2010; Crawford et al., 2004; Nath et al., 2003; Palatnik et al., 2003). *TCP* genes influence leaf growth through a number of developmental pathways. They can be classified into two classes according to differences in their *TCP* domain (Martín-Trillo and Cubas, 2009). In most cases this classification correlates with their function as either a promoter (class I) or inhibitor (class II) of growth.

There are 24 *TCP* genes in *Arabidopsis* (Cubas et al., 1999; Koyama et al., 2007). Due to functional redundancies between *TCP* genes, single loss-of-function mutants do not have a visible phenotype (Efroni et al., 2008; Li et al., 2005). In *Arabidopsis jaw-D* mutants, miR319a is highly upregulated in the leaves and strongly downregulates five of the *Arabidopsis* class II *TCP* genes (*TCP2*, *TCP3*, *TCP4*, *TCP10* and *TCP24*; Palatnik et al. 2003). Most of the class II *TCP* genes can therefore be conveniently downregulated using *35S::miR319* constructs, as in the *jaw-D* mutants (Palatnik et al., 2003).

*TCP* class II genes are expressed in proliferating regions, such as *TCP4*

in *Arabidopsis* (Palatnik et al., 2007), *LANCEOLATE* (*LA*) in tomato (Ori et al., 2007) and *CINCINNATA* (*CIN*) in *Antirrhinum* (Nath et al., 2003). All of these class II *TCP* genes inhibit cell division and their downregulation prolongs the longevity of leaves. Downregulation of *LA* in tomato, for example, extends leaf growth by 2 months (Ori et al., 2007). Class II *TCP* genes in *Arabidopsis* promote leaf senescence by directly regulating the jasmonic acid biosynthesis gene *LIPOXYGENASE2* (Schommer et al., 2008).

#### 4.1.2.2 Mechanisms Underlying the *jaw*-D Phenotype

The pronounced shape differences in *jaw*-D leaves compared to wild-type leaves are particularly evident at the margins. Therefore, it has been suggested that delayed growth arrest at the margins may account for the observed phenotype. Nath et al. (2003) proposed that *CIN* makes cells more responsive to a cell cycle arrest signal. In the absence of class II *TCP* genes in *Arabidopsis*, cells remain in a young, undifferentiated state for longer (Efroni et al., 2008; Koyama et al., 2007; Sarojam et al., 2010).

Alternatively, margin growth rates may be promoted in *jaw*-D mutants compared to wild-type. This theory is supported by observations that in wild-type leaves, *LA* levels are higher in the margins compared to the remaining part of the lamina during the cell proliferation-expansion transition (Shleizer-Burko et al., 2011). Since *LA* acts as a growth inhibitor, it is possible that the downregulation of *LA* might have a stronger effect in the margin regions, resulting in higher margin growth rates.

To investigate the processes that drive leaf curvature in three-dimensions, the 2D leaf model was extended to 3D. In addition to wild-type leaf shapes, the model was used to study the phenotype of *jaw*-D mutant leaves.

## 4.2 Results

To extend the model to 3D, additional parameters need to be taken into account.

### 4.2.1 3D Growth Tensor

As discussed in an earlier chapter (2.2.2.2 Growth Tensors), the deformation of small regions over time can be described by a growth tensor (Hejnowicz and Romberger, 1984). This growth tensor,  $T_{growth}$ , can be computed as the gradients of velocities of points within the small region with respect to the two external axes (Feynman et al., 1965; Hejnowicz and Romberger, 1984) and has the form:

$$T_{growth} = \begin{bmatrix} V_{xx} & V_{yx} \\ V_{xy} & V_{yy} \end{bmatrix},$$

where  $V$  is the gradient of the velocity component (first subscript) in the direction of either the  $x$  or  $y$ -axis (second subscript).

Thus, in 2D the growth tensor has 4 components. Extending the growth analysis to 3D involves the addition of another axis, the  $z$ -axis. It follows that in addition to velocities along the  $x$  and  $y$ -axes, each point has a component of velocity along the  $z$ -axis as well. The growth tensor now consists of 9 components:

$$T_{growth} = \begin{bmatrix} V_{xx} & V_{yx} & V_{zx} \\ V_{xy} & V_{yy} & V_{zy} \\ V_{xz} & V_{yz} & V_{zz} \end{bmatrix}$$

This growth tensor fully describes the deformations of an infinitesimally small region in 3D. As before, particular growth parameters can be extracted from this tensor. For instance, three growth rates ( $K_{max}$ ,  $K_{mid}$  and  $K_{min}$ ) can now be computed, where  $K_{max}$  is the growth rate along the major axis of growth and  $K_{min}$  is the rate along the minor axis of growth, orthogonal to  $K_{max}$ .  $K_{mid}$  is the rate along the third axis of growth, orthogonal to both  $K_{max}$  and  $K_{min}$ . The growth rate along  $K_{mid}$  is in between  $K_{max}$  and  $K_{min}$  (Fig. 4.2).

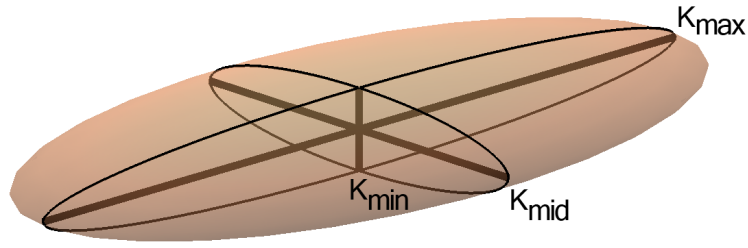


**Figure 4.2** The three orthogonal axes of growth, where  $K_{max}$  is the growth rate along major axis of growth and  $K_{min}$  is the rate along the minor axis, perpendicular to  $K_{max}$ .  $K_{mid}$  is growth in the direction perpendicular to both  $K_{max}$  and  $K_{min}$  and growth rate along  $K_{mid}$  is in between  $K_{max}$  and  $K_{min}$ .

#### 4.2.2 3D Growth in the *GFTbox*

In the *GFTbox*, the canvas consists of a sheet with a thickness. So far in all 2D models, it has been assumed that the two surfaces of the sheet have equal growth rates. However, within the *GFTbox* it is possible to specify differential growth rates on the two surfaces. This means that the specified growth rate  $K_{par}$  can be divided into  $K_{a_{par}}$  and  $K_{b_{par}}$ , which specify growth on the A and B surface, respectively (Fig. 4.3). In terms of leaf growth these two surfaces present the adaxial and abaxial surfaces of the leaf. There is only one rate for growth in thickness,  $K_{nor}$  (growth normal to the plane; Fig. 4.3).

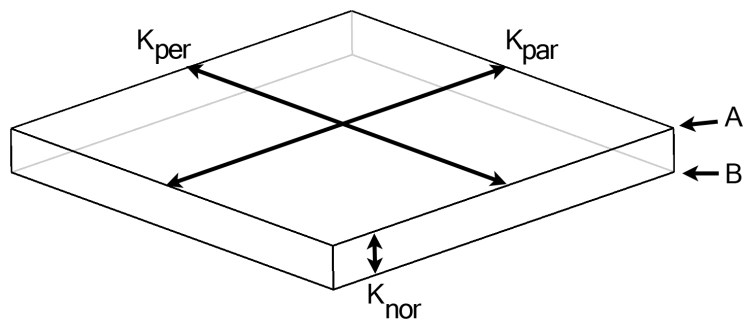


**Figure 4.3** In the *GFTbox*, the canvas consists of two surfaces A and B. Each surface can have a growth rate parallel ( $K_{par}$ ) and perpendicular ( $K_{per}$ ) to a polarity gradient, termed  $K_{a_{par}}$  and  $K_{a_{per}}$  for the A surface and  $K_{b_{par}}$  and  $K_{b_{per}}$  for the B surface.  $K_{nor}$  is the growth rate in thickness.

#### 4.2.3 Bending

To allow the 2D canvas sheet to bend in 3D, a break in symmetry of the canvas is required. Computationally the canvas may not bend out of the plane

if the two surfaces are completely flat. In the models shown previously, the two surfaces of the canvas plane were constrained to remain flat (Fig. 4.4A). Therefore canvas deformations were limited to the 2D plane. In this chapter, a small amount of surface asymmetry along the  $z$ -axis has been introduced (Fig. 4.4B) to allow the canvas to bend according to the growth interactions specified. In the leaf model, this introduced noise was negligible compared to the overall shape and was smaller than the noise shown in Figure 4.4C.

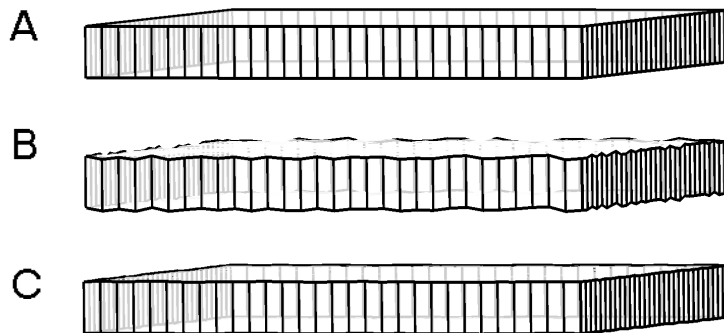


**Figure 4.4** Canvas bending requires the prior breakage of symmetry, which computationally can be achieved by introducing a small amount of initial noise along the  $z$ -axis. Canvas surfaces can either **A**, be completely smooth with a  $z$ -noise of 0 %, **B**, have a relatively large amount of  $z$ -noise, here noise in  $z = 10\%$  of the thickness of the canvas or **C**, have a small amount of  $z$ -noise, here noise in  $z = 2\%$ .

#### 4.2.4 Canvas Thickness

The readiness of a tissue to bend is strongly influenced by the tissue properties and its thickness (Dupuy et al., 2010; Hufnagel et al., 2007). Here it has been assumed that the mechanical properties are homogeneous throughout the tissue and constant over time, while the canvas thickness can vary. The importance of thickness for bending can be demonstrated by a canvas that grows anisotropically along one axis only and with higher rates on one surface compared to the other. This canvas bends more when it is thin (Fig. 4.5). Therefore, to extend the leaf model to 3D, it was important to get a good estimate of growth in thickness of the real leaf.

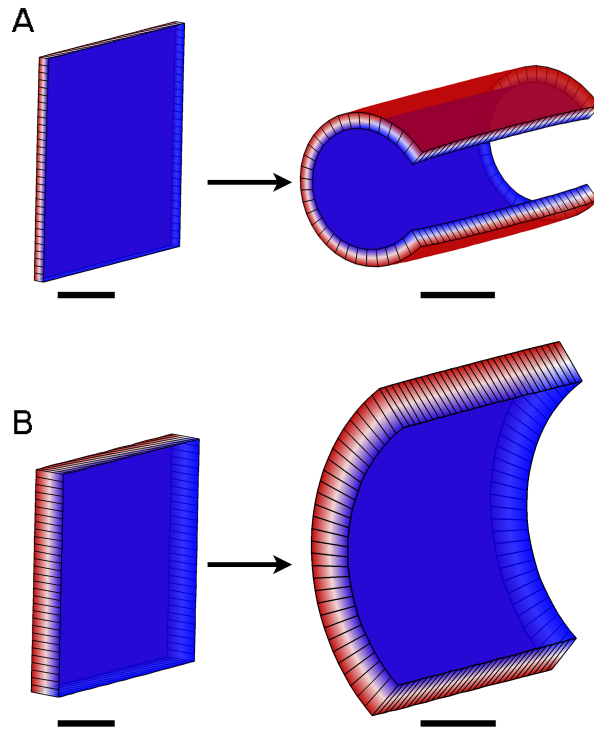


**Figure 4.5** Canvas thickness. Two canvasses, identical apart from their thickness, were grown anisotropically along one axis only with more growth on one surface (red) than the other (blue) for the same period of time. **A**, the thinner canvas bent significantly more than the **B**, 3x thicker canvas. Scale bars 0.5 *mm*.

#### 4.2.5 Leaf Thickness

The 2D leaf models were based on measurements of  $K_{max}$  and  $K_{min}$  across the leaf, where previously  $K_{min}$  was the axis of minimum growth parallel to the leaf surface. Since, in three-dimensions growth in thickness constitutes the axis of minimum growth,  $K_{min}$  now defines growth in thickness, whereas the minimum axis of growth parallel to the plane of the leaf is now called  $K_{mid}$ .

An estimate of  $K_{min}$  was obtained from the 3D leaf images generated using OPT. Leaf thickness was measured by Karen Lee using the image visualisation software *VolViewer*. For each leaf, thickness was measured at the proximal lamina, at the proximal midvein, at the central midvein and at the distal tip. Since the leaf model is limited to the first half of leaf development, an exponential curve was fitted to the average leaf thickness data at these young

leaf stages using least squares minimisation (Fig. 4.6):

$$K_{min} = y e^k, \quad (4.1)$$

where  $y$  is the initial thickness and equals  $0.028 \text{ mm}$ .  $k$  is the exponential growth rate and equals  $0.6 \% h^{-1}$ . This exponential growth rate, was used to drive growth in thickness,  $K_{nor}$ , in the model.

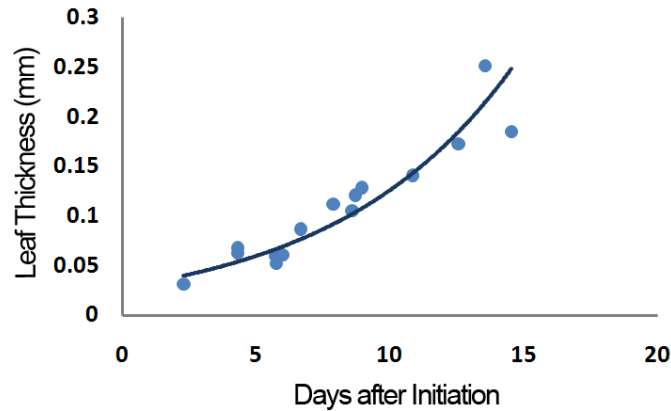


**Figure 4.6** Average leaf thickness measured from OPT images by Karen Lee (data points). An exponential function was fitted to the data (line).

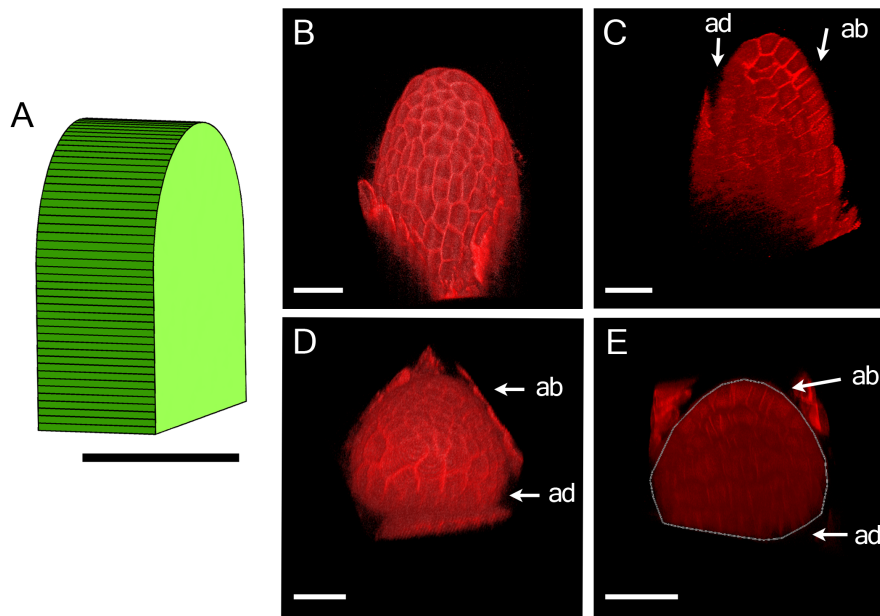


**Figure 4.7** Initial 3D Leaf and Canvas Shape. **A**, initial 3D canvas shape. **B-E**, confocal images of leaf 1 three days after initiation displayed in *VolViewer* by Samantha Fox. **A**, front abaxial view. **B**, side view of virtually dissected leaf. **C**, top view down on the leaf tip. **D**, bottom view of leaf virtually excised from the stem. adaxial (ad), abaxial (ab). Scale bars **A**,  $50 \mu\text{m}$ , **B-D**,  $10 \mu\text{m}$  and **E**,  $25 \mu\text{m}$ .

#### 4.2.5.1 Initial Leaf and Canvas Shape

The initial canvas of the 2D leaf models consisted of a flat sheet. The thickness of the canvas could now be adjusted to the leaf thickness on day 3 after initiation, which was about 40  $\mu\text{m}$  (Fig. 4.6; Fig. 4.7A), while the canvas length and width dimensions were as before 95  $\mu\text{m}$  and 85  $\mu\text{m}$ , respectively. This canvas thickness is a simplification of the leaf thickness, as demonstrated by a 3 day old leaf imaged under the confocal microscope and visualised using *VolViewer* by Samantha Fox (Fig. 4.7B-E). In the real leaves the leaf base is thicker than the tip (Fig. 4.7B and C). Moreover, the adaxial side is flatter than the abaxial one (Fig. 4.7C-E).

#### 4.2.6 3D Leaf Model

To assess the extent to which the 2D leaf model interactions are able to explain leaf growth in 3D, growth of the 3D starting canvas was specified according to the previous growth equations for growth in the plane. The addition of growth in thickness,  $K_{nor}$ , determined growth along the third leaf axis:

$$\begin{aligned}
 K_{par} &= p_{prox} \mathbf{i}_{PROX} \cdot \text{inh}(h_{late}, \mathbf{i}_{LATE}) \\
 K_{per} &= p_{lam} \mathbf{i}_{LAM} \cdot \text{inh}(h_{mid}, \mathbf{i}_{MID}) \cdot \text{pro}(p_{late}, \mathbf{i}_{LATE}) \cdot \text{inh}(h_{rim}, \mathbf{i}_{RIM}) \\
 K_{nor} &= p_{nor},
 \end{aligned}
 \tag{4.2}$$

where, as before,  $p_{prox}$  is the promotion of  $K_{par}$  by  $\mathbf{i}_{PROX}$ , which has a linear gradient with highest levels at the base, and  $h_{late}$  is the inhibition of  $K_{par}$  by  $\mathbf{i}_{LATE}$ , which is expressed uniformly throughout the canvas after day 6 and increases linearly thereafter.  $p_{lam}$  and  $p_{late}$  are the promotion of  $K_{per}$  by  $\mathbf{i}_{LAM}$  and  $\mathbf{i}_{LATE}$ , respectively.  $h_{mid}$  and  $h_{rim}$  are the inhibition of  $K_{per}$  by  $\mathbf{i}_{MID}$  and  $\mathbf{i}_{RIM}$ , respectively. The levels of  $\mathbf{i}_{LAM}$  are high in the proximal lamina regions and low in the very proximal regions of the canvas.  $\mathbf{i}_{MID}$  is expressed in the midline region of the canvas.  $\mathbf{i}_{RIM}$  is expressed at the canvas margins apart from the very proximal regions.  $p_{nor}$  defines the growth in thickness,  $K_{nor}$ , and is equal to the calculated exponential growth rate of the leaf  $k = 0.6\% h^{-1}$ .

To allow the canvas to rotate out of the 2D plane, random surface noise of 1 % relative to the thickness of the canvas was introduced (similar to Fig. 4.4C). The 2D leaf model explained shape and growth patterns during the early stages of leaf development (up to day 8-9) only. Therefore, 3D shape investigations were limited to the first half of leaf development.

Growing the canvas generated a resultant shape that remained approximately flat throughout the simulation time (Fig. 4.8A), unlike the real leaves (Fig. 4.8B).

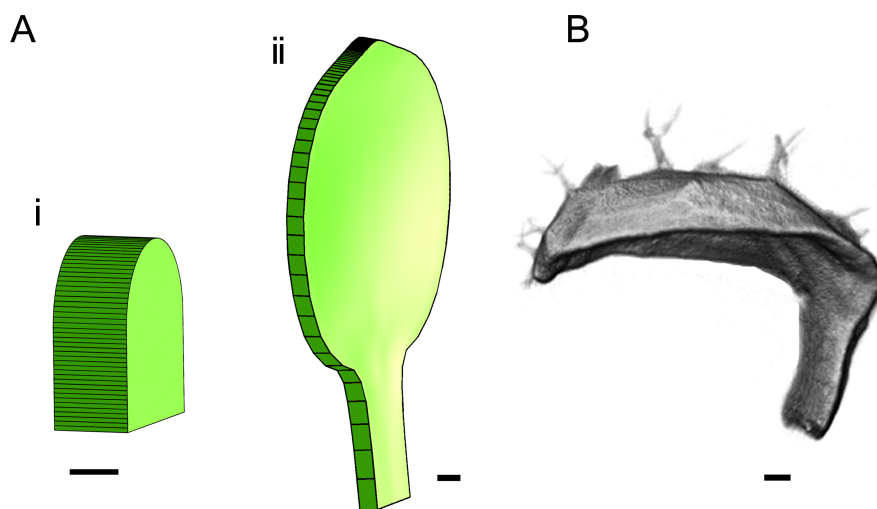


**Figure 4.8** Model in 3D. **A(i)**, 3D model starting canvas and **(ii)** resultant canvas corresponding to a leaf 9 days after initiation. **B**, OPT image by Karen Lee of leaf 9 days after initiation. Scale bars **A(i)** 25  $\mu m$ , **A(ii)** and **B** 100  $\mu m$ .

#### 4.2.6.1 Reducing Canvas Thickness

Since thickness plays an important part in the bending properties of a tissue, it was tested whether a thinner canvas may yield rotations out of the plane based on the model growth interactions (Eqn. 4.2). The thickness of the canvas was reduced to 5  $\mu m$  (compared to 40  $\mu m$  measured for the leaf thickness; Fig. 4.9A i).

With such a starting canvas, the lamina part not only formed a cup-shape, but the main axis of the canvas also bent so that the petiole region was perpendicular to the lamina part, similar to the real leaf shapes (Fig. 4.8B ii and Fig. 4.9A ii).

This shows that the model growth interactions are sufficient to explain the overall three-dimensional shape of the leaf. However, the initial leaf thickness prevents the out-of-plane curvature. To allow bending as specified by the growth interactions, the initial canvas thickness had to be reduced considerably compared to the measured initial leaf thickness. Although it is possible that the initial leaf thickness was overestimated, the young leaf is clearly thicker than the thin canvas generated here. The direction of bending (either over the A or B surface) is determined by the initial random asymmetries across the  $z$ -axis. This means that in the leaf, there would have to be similar asymmetries to force the leaf to bend in the right direction, which may be conferred by the initial asymmetry in primordium shape.

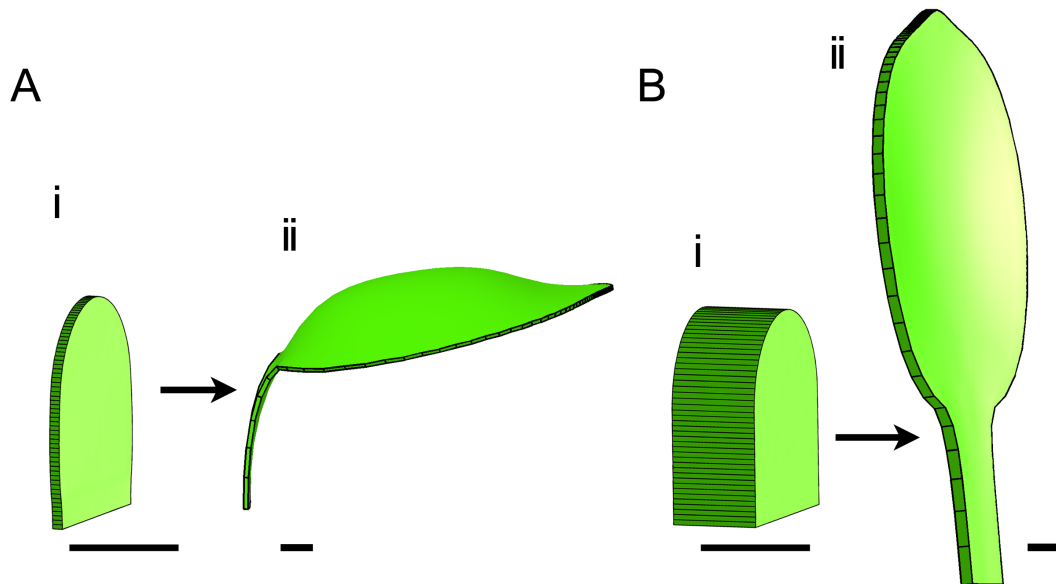


**Figure 4.9** **A**, 3D model starting canvas with a thickness of  $5 \mu m$ . **B**, 3D model with  $K_{nor} = 0\% h^{-1}$  and a starting canvas with an initial thickness of  $40 \mu m$ . Canvas shapes shown on at times corresponding to leaves (i) 3 days and (ii) 9 days after initiation. Scale bars (i)  $50 \mu m$  and (ii)  $100 \mu m$ .

It is also possible that the growth rate in thickness,  $K_{min}$ , was overestimated, as it exceeded the  $K_{min}$  measured previously (Pyke et al., 1991). To test the impact of growth in thickness on the 3D leaf shape, a uniformly thick starting canvas, with a thickness of  $40 \mu m$ , was grown with  $K_{nor} = 0\% h^{-1}$  (Fig. 4.9B i). Although the canvas was relatively thin at the end of the simulation, it remained largely flat (Fig. 4.9B ii).

These results suggest that there are additional factors involved in leaf bending.

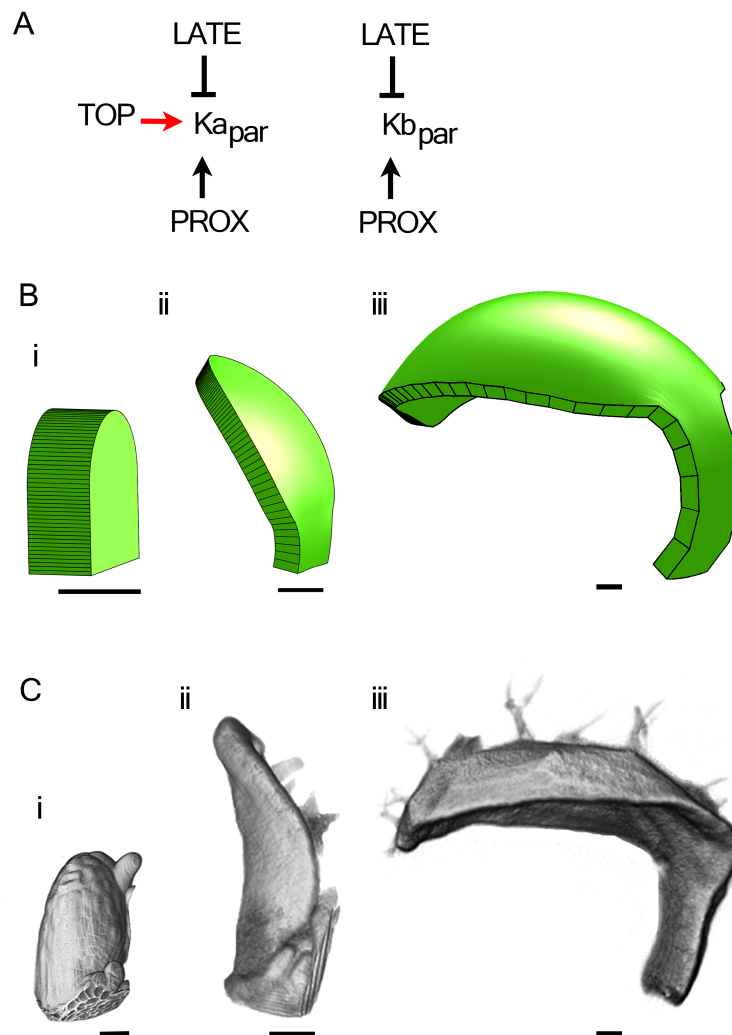


**Figure 4.10** A-B, 3D model with slightly higher  $Ka_{par}$  than  $Kb_{par}$  showing A, the growth interaction network for  $K_{par}$  and B, the model canvas. C, OPT images of leaves at comparable stages as the model at (i) 3 days, (ii) 6 days and (iii) 9 days after initiation. Scale bars B(i)  $50 \mu m$ , C(i)  $20 \mu m$ , (ii-iii)  $100 \mu m$ .

#### 4.2.6.2 Differential Surface Growth

Since the leaf model was unable to account for the observed 3D leaf shapes, it is possible that there are small asymmetries in the material properties or growth rates that help to increase the rotations specified by the underlying growth interactions. Alternatively, there might be small differences in growth rates on the two surfaces of the canvas. This idea was tested by introducing

an additional factor,  $\mathbf{i}_{TOP}$ , which is expressed at a level of 1 throughout the canvas and promotes  $K_{par}$  on the A surface only (Fig. 4.10A):

$$\begin{aligned} K_{a_{par}} &= p_{prox} \mathbf{i}_{PROX} \cdot \text{inh}(h_{late}, \mathbf{i}_{LATE}) \cdot \text{pro}(p_{top}, \mathbf{i}_{TOP}) \\ K_{b_{par}} &= p_{prox} \mathbf{i}_{PROX} \cdot \text{inh}(h_{late}, \mathbf{i}_{LATE}), \end{aligned} \quad (4.3)$$

where  $p_{top}$  is the amount of promotion by  $\mathbf{i}_{TOP}$ . It is assumed that the A surface corresponds to the adaxial (top) surface of the leaf and the B surface corresponds to the abaxial (bottom) surface.

With the addition of  $\mathbf{i}_{TOP}$  on the A surface, the canvas adopted curvatures similar to those observed (Fig. 4.10B and C). At intermediate stages, the canvas became doubly curved in orthogonal directions with the B surface being concave along the proximodistal axis and convex along the mediolateral axis (Fig. 4.10B ii). At later stages, the B surface became strongly concave along both axes (Fig. 4.10B iii). Thus, with a slight modification to the model, the 3D curvature during early stages of leaf development could be captured.

#### 4.2.7 Modelling Mutants

With slight modifications to the 2D leaf models, the same growth interactions could explain development of the 3D leaf shape. This 3D extension was tested by also trying to account for the 3D shape of mutant leaves, using the model. An *Arabidopsis* mutant, whose leaves show extensive bending out of the plane, is the *jaw-D* mutant, in which the expression of several class II *TCP* genes is suppressed. This mutation increases the growth rates and longevity of the leaves, amongst other phenotypes (Nath et al., 2003; Ori et al., 2007; Palatnik et al., 2003; Schommer et al., 2008). The 3D model was used to investigate the development of the *jaw-D* mutant leaf 1.

To get a better idea of the mutant leaf phenotype, *jaw-D* leaves were imaged in 3D using OPT by Karen Lee (Fig. 4.12B). For this purpose mutant plants were grown *in vitro*. Although when grown *in vitro* the mutant phenotype was less severe than that of plants grown on soil (Fig. 4.11), it was easier to distinguish developmental defects with this milder phenotype. Moreover,

**Figure 4.11** Abaxial view on mature *jaw-D* leaf grown on soil. Scale bar 1 *mm*.



mutant leaves grown on plates are more comparable with the leaf model and wild-type data, which are both specific to *in vitro* growth conditions.

#### 4.2.7.1 *jaw-D* Leaf Shapes

The shape of leaf 1 of mutants and wild-type could not be distinguished initially, although the *jaw-D* leaves developed more slowly with about 1-2 days delay (compare Fig. 4.12A i and ii and Fig. 4.12B i). Previously a delay of 3 days has been reported (Efroni et al., 2008). As there was no growth curve available to estimate the initiation time of *jaw-D* leaf 1, leaf ages are given in days after stratification. Wild-type leaves initiate about 1 day after stratification.

During development the downward curvature along the proximodistal axis observed in wild-type became more pronounced in the *jaw-D* mutants with an inward rolled distal tip (Fig. 4.12B ii-iv). At the same time serrations formed at the proximal margins of the lamina. The lamina margins pointed upwards from the midvein. At late stages similar to wild-type, the proximal regions straightened along the proximodistal axis to flatten the leaf spine, while the margins buckled (Fig. 4.12A iv and v; Fig. 4.12B iv and v). An increase in divergence from the wild-type phenotype with age has also been observed in tomato when miR319 was overexpressed (Shleizer-Burko et al., 2011).

Thus, the uneven buckled margins characteristic for *jaw-D* leaves only appear late in development. Other characteristic phenotypic differences to wild-type include the curled up leaf tips and the larger number and more pronounced serrations.

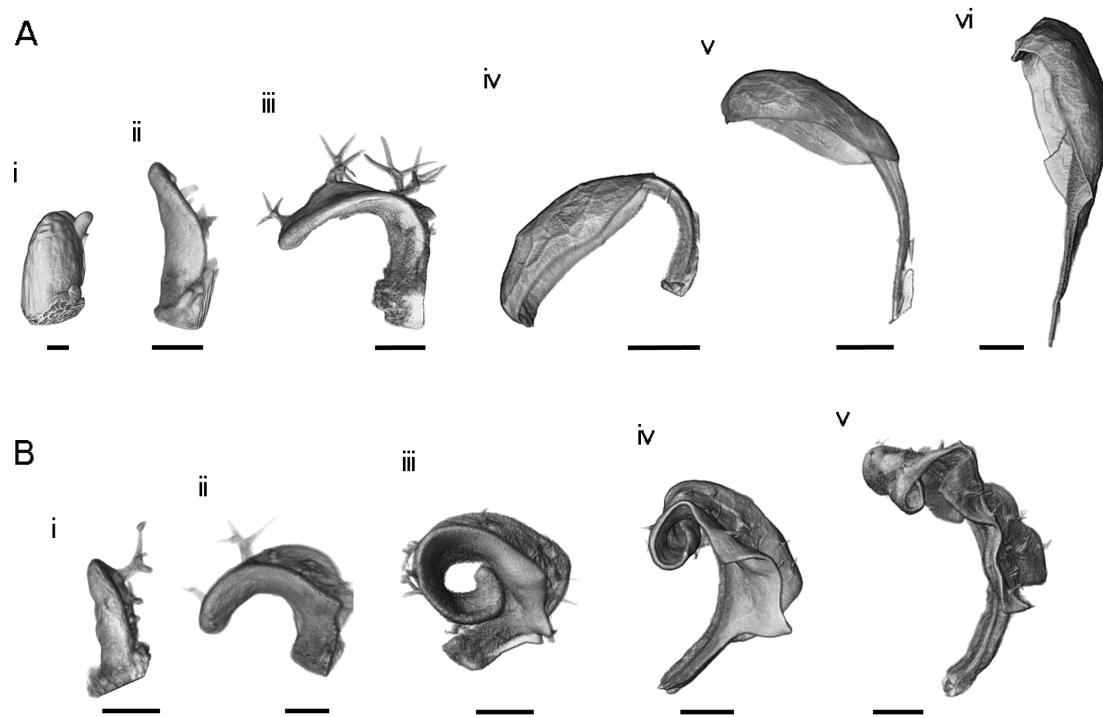


**Figure 4.12** Wild-type and *jaw-D* leaves grown *in vitro*. **A**, wild-type leaves at different days after stratification. **(i)** 5 day old leaf stained with propidium iodide by Sascha Duttke. **(ii-vi)** OPT images by Karen Lee of leaves on **(ii)** day 8, **(iii)** day 9, **(iv)** day 13, **(v)** day 14 and **(vi)** day 19. **B**, OPT images of *jaw-D* mutant leaves by Karen Lee shown at different days after stratification on **(i)** day 6, **(ii)** day 8, **(iii)** day 10, **(iv)** day 14, **(v)** day 16. Since there was no standard growth curve available for the mutant leaves, the time of leaf initiation could not be calculated. In general *jaw-D* leaf development was 1-2 days behind wild-type leaf development. Scale bars **A**: **(i)** 20  $\mu\text{m}$ , **(ii-iii)** 200  $\mu\text{m}$ , **(iv-vi)** 1 mm. **B**: **(i-ii)** 130  $\mu\text{m}$ , **(iii)** 260  $\mu\text{m}$ , **(iv-v)** 520  $\mu\text{m}$

#### 4.2.7.2 Measuring *jaw-D* Leaf Growth

To investigate the mechanisms behind the *jaw-D* mutant leaf phenotypes, first the local growth rate profiles were analysed. Due to the uneven leaf shapes it was difficult to generate high resolution images of the leaf margin regions using time lapse imaging. Moreover, growth of the mutant leaves was affected by the conditions in the tracking chamber. Therefore, it was not possible to get reliable tracking data for the mutant leaves.

An alternative method for generating growth data is clonal analysis (Rolland-Lagan et al., 2005). In the previous chapters, wild-type clonal patterns have been warped to mean leaf shapes. However, variability in mutant leaf shape and developmental timing made it difficult to derive a mean representative *jaw-D* leaf shape. In addition, this variability made it difficult to reliably

compare mutant and wild-type leaves of the same age.

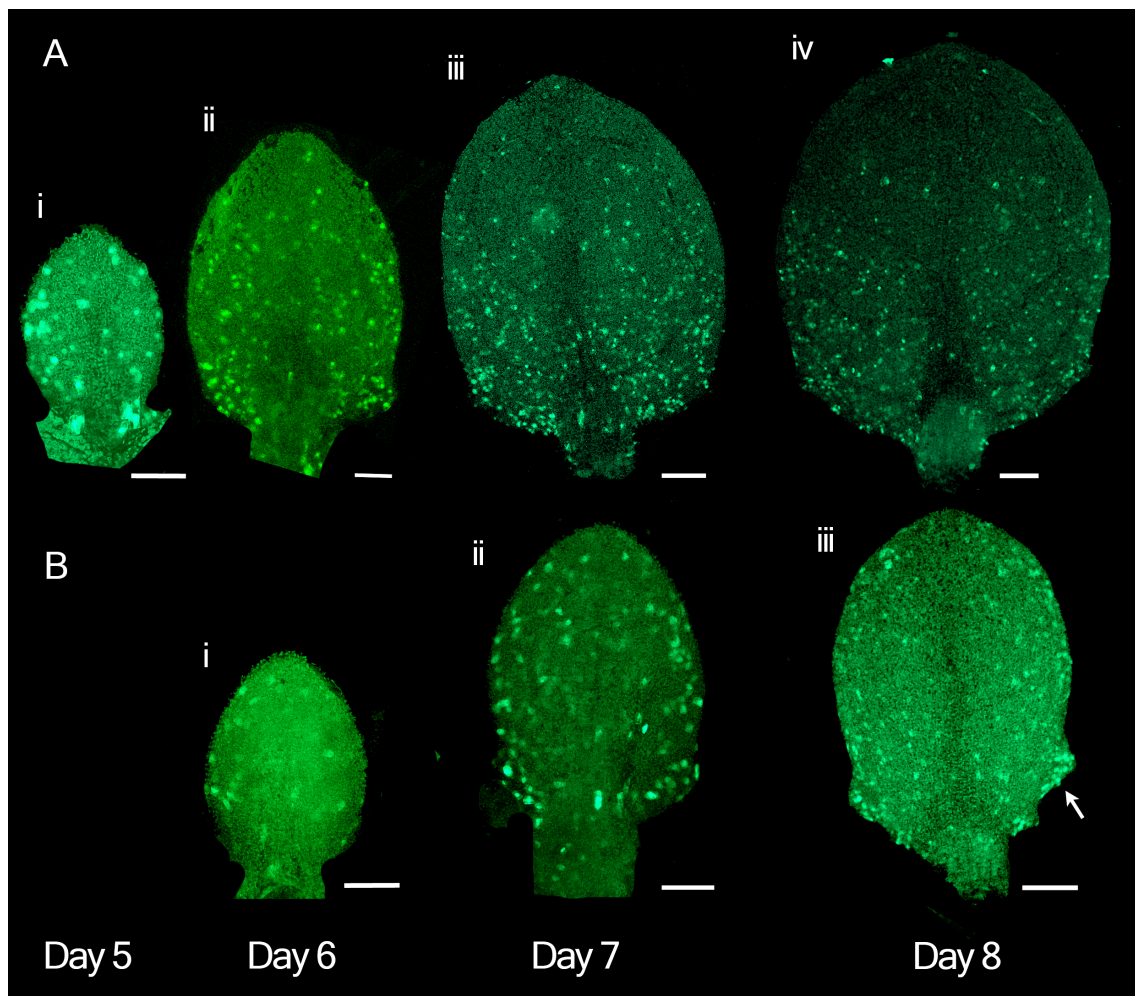


**Figure 4.13** *CyclinB1;1:GFP* expression in **A**, wild-type and **B**, *jaw-D* leaves at different days after stratification. Scale bars **A(i-ii)** and **B(i-ii)**, 50  $\mu\text{m}$ ; **A(iii-iv)** and **B(iii)**, 100  $\mu\text{m}$

Therefore the cell division marker construct *cyclinB1;1:GFP* was used to get some idea of the *jaw-D* growth dynamics, although cell division patterns may not be representative of the underlying growth dynamics. Wild-type and *jaw-D* leaves expressing *cyclinB1;1:GFP* were compared based in their age and size. However, due to the variability in mutant leaf growth, these staging methods may not be accurate.

The expression of *cyclinB1;1:GFP* in wild-type and *jaw-D* leaves was similar when taking the slower growth rates of *jaw-D* leaves into account. In both cases, cell divisions were initially observed throughout the organs (Fig. 4.13A i and B i-ii). Cells ceased to divide first at the tip (Fig. 4.13A ii and

B iii) and then progressively in more proximal regions (Fig. 4.13A iv; Fig. 4.14B) until cells in the whole leaf stopped dividing (Fig. 4.14A and C). For wild-type, these observations are in agreement with earlier studies (Donnelly et al., 1999).

However, there were some discrepancies between wild-type and mutant leaves. For instance, in the mutant leaves the division rates in the serrated regions were clearly higher, potentially explaining the large serrations (Fig. 4.13B iii, white arrow; Fig. 4.14B, white arrow). When grown on soil *jaw-D* leaves are thought to significantly delay or even lack growth arrest (Efroni et al., 2008; Nath et al., 2003). Under *in vitro* conditions cell division and most likely growth do arrest or decelerate in leaf 1. Cell divisions arrest not long after wild-type leaves arrest (Fig. 4.14C). At this stage it was not possible to completely flatten the mutant leaves.

Thus, based on the cell division dynamics, it appears that growth rates are slightly higher in the margin regions of *jaw-D* leaves compared to wild-type.

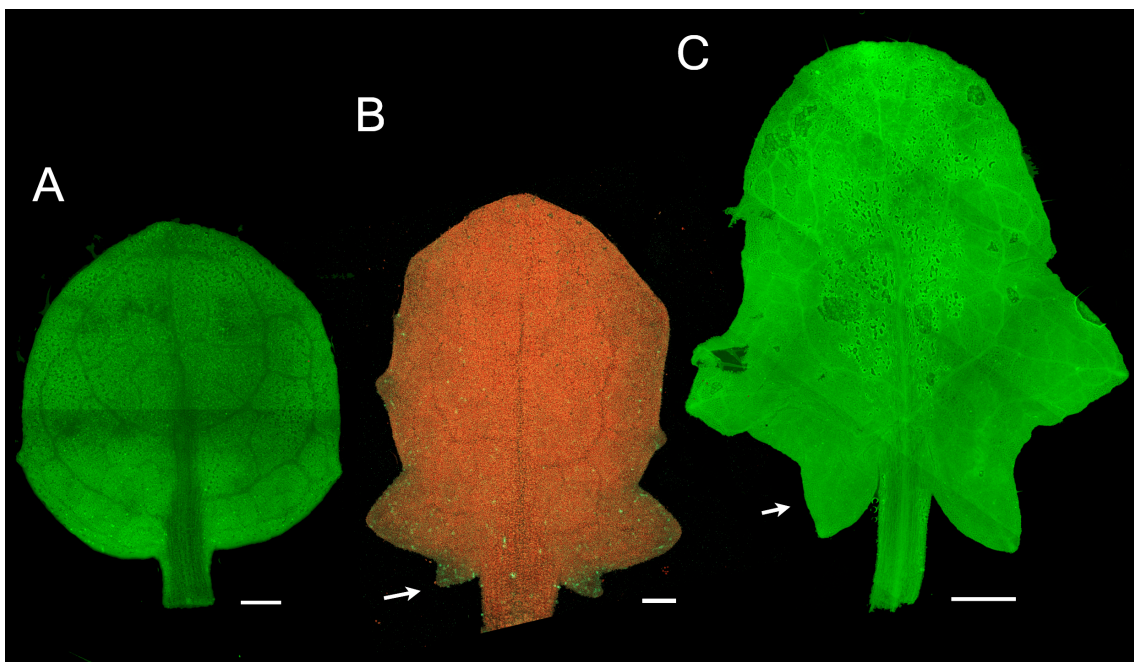


**Figure 4.14** *CyclinB1;1:GFP* expression in **A**, wild-type leaf 10 days after stratification. **B-C**, *jaw-D* leaves **B**, 12 days and **C**, 14 days after stratification. Scale bars **A-B**, 200  $\mu\text{m}$  and **C**, 500  $\mu\text{m}$ .

Flattening the early mutant leaves also revealed clear differences in the shapes of mutant and wild-type leaves. Interestingly, mutant leaves were more

elongated than wild-type suggesting that growth rates parallel to the midline are higher or lateral growth is inhibited. This higher amount of longitudinal growth might be connected to the curling of the leaves along the midline axis.

#### 4.2.7.3 *jaw*-D Models

*CyclinB1;1:GFP* expression suggests that growth rates, in the proximal margins at least, are higher in *jaw*-D compared to wild-type leaves. This was tested computationally. Growth rates in the leaf model margins were modified compared to those of the wild-type model. Since, the model is restricted to early phases, only the early stages of *jaw*-D leaf development were modelled (up to Fig. 4.15B).

##### 4.2.7.3.1 Increased Marginal Growth Rates

First, growth at the margins was increased by the growth factor  $\mathbf{i}_{RIM}$ .  $\mathbf{i}_{RIM}$  is expressed along the lamina margins and was so far used to restrict  $K_{per}$  to match the observed clonal patterns in *Arabidopsis* (2.2.13.1 Clonal Analysis, Eqn. 4.2). The restriction of  $K_{per}$  by  $\mathbf{i}_{RIM}$  was modified so that  $\mathbf{i}_{RIM}$  promoted growth along both  $K_{par}$  and  $K_{per}$  (Fig. 4.15C ii):

$$\begin{aligned}
 K_{a_{par}} &= p_{prox} \mathbf{i}_{PROX} \cdot \text{inh}(h_{late}, \mathbf{i}_{LATE}) \cdot \text{pro}(p_{top}, \mathbf{i}_{TOP}) \cdot \text{pro}(p_{rim}, \mathbf{i}_{RIM}) \\
 K_{b_{par}} &= p_{prox} \mathbf{i}_{PROX} \cdot \text{inh}(h_{late}, \mathbf{i}_{LATE}) \cdot \text{pro}(p_{rim}, \mathbf{i}_{RIM}) \\
 K_{a_{per}} &= p_{lam} \mathbf{i}_{LAM} \cdot \text{inh}(h_{mid}, \mathbf{i}_{MID}) \cdot \text{pro}(p_{late}, \mathbf{i}_{LATE}) \cdot \text{pro}(p_{rim}, \mathbf{i}_{RIM}) \\
 K_{b_{per}} &= K_{a_{per}} \\
 K_{nor} &= p_{nor},
 \end{aligned} \tag{4.4}$$

where  $p_{rim}$  is the promotion of both  $K_{par}$  and  $K_{per}$  by  $\mathbf{i}_{RIM}$  and was set to 0.3 in both cases. To ensure accurate growth calculations, the finite element mesh was subdivided in regions expressing  $\mathbf{i}_{RIM}$ .

With the promotion of areal growth by  $\mathbf{i}_{RIM}$  the leaf margins expanded extensively (Fig. 4.15C i) and the resultant canvas shape differed from that of the wild-type model (Fig. 4.10B iii) or wild-type real leaf shape (Fig. 4.15A).

The canvas margins curved strongly upward, while the leaf midline axis bent downward. Qualitatively, this canvas shape was similar to that observed

at early stages of development for the *jaw*-D mutant (Fig. 4.15B).

It was further investigated whether an increase in areal growth rates is necessary to generate this canvas shape or if it is sufficient to promote growth along  $K_{par}$  or  $K_{per}$  only. First the individual effects of  $K_{per}$  were investigated. For this purpose, in Equation 4.4, the  $p_{rim}$  of  $K_{par}$  was set to 0, but remained 0.3 for  $K_{per}$  (Fig. 4.15D ii). With the marginal promotion of  $K_{per}$  only, the canvas developed a broad cup-shaped lamina, more similar to the wild-type leaf than the mutant (compare Fig. 4.15A, B and D i). This suggested that the observed canvas shape, with high areal margin growth rates, might mainly be attributed to extra growth along  $K_{par}$ . This was tested by setting  $p_{rim}$  of  $K_{par}$  to 0.3 and inhibiting growth in the margins again along  $K_{per}$  as had been the case in previous models (Fig. 4.15E ii):

$$\begin{aligned}
Ka_{par} &= p_{prox} \mathbf{i}_{PROX} \cdot \text{inh}(h_{late}, \mathbf{i}_{LATE}) \cdot \text{pro}(p_{top}, \mathbf{i}_{TOP}) \cdot \text{pro}(p_{rim}, \mathbf{i}_{RIM}) \\
Kb_{par} &= p_{prox} \mathbf{i}_{PROX} \cdot \text{inh}(h_{late}, \mathbf{i}_{LATE}) \cdot \text{pro}(p_{rim}, \mathbf{i}_{RIM}) \\
Ka_{per} &= p_{lam} \mathbf{i}_{LAM} \cdot \text{inh}(h_{mid}, \mathbf{i}_{MID}) \cdot \text{pro}(p_{late}, \mathbf{i}_{LATE}) \cdot \text{inh}(h_{rim}, \mathbf{i}_{RIM}) \\
Kb_{per} &= Ka_{per} \\
K_{nor} &= p_{nor},
\end{aligned} \tag{4.5}$$

The resultant final canvas shape was similar to that of high areal margin growth rates (compare Fig 4.15C i and E i). However, the margin in the  $K_{par}$  only model curved upward more strongly. Thus, by increasing growth at the margins along  $K_{par}$  or  $K_{per}$  only, it was evident that the out of plane rotation can be attributed to an elevation in  $K_{par}$ . However, it is unclear whether the *jaw*-D leaf shape is a result of increased areal growth rates or if growth is increased anisotropically along  $K_{par}$  only.

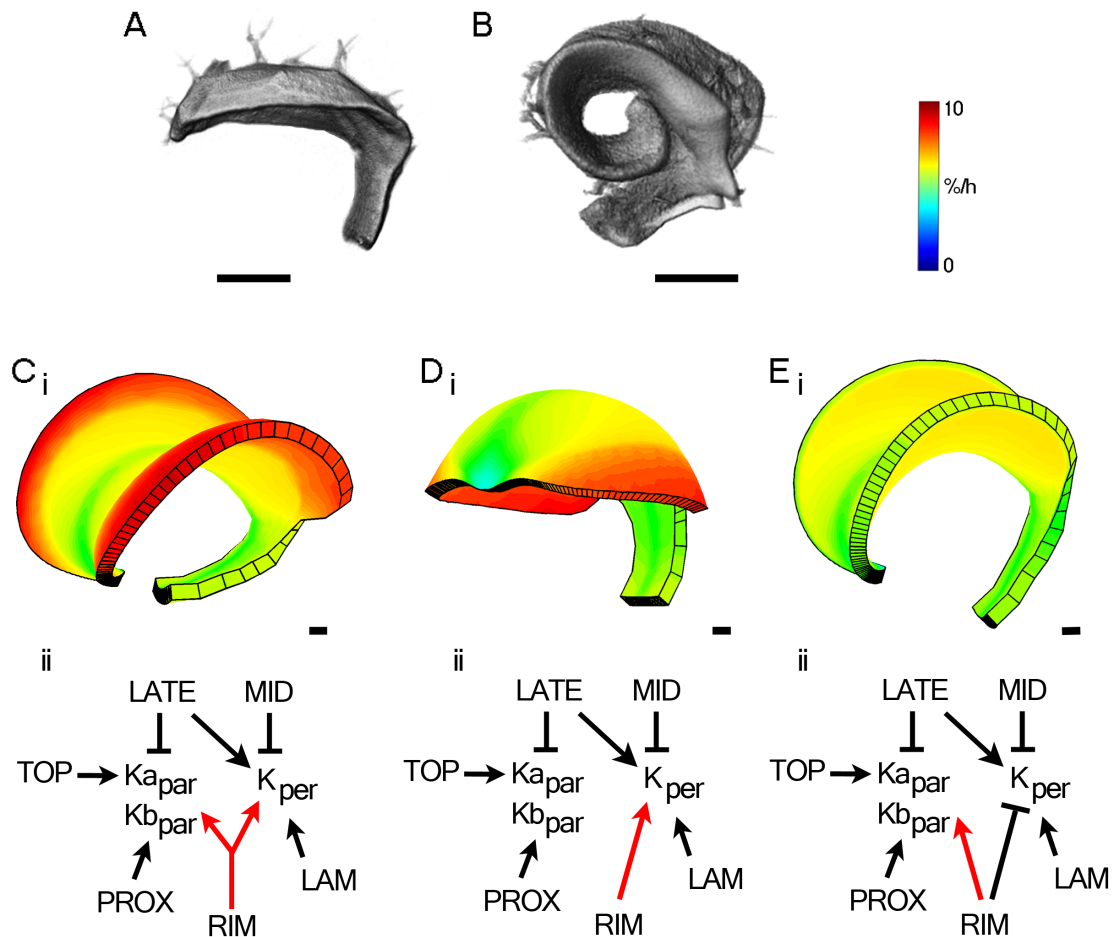


**Figure 4.15** A-B, OPT images by Karen Lee of **A**, wild-type leaf and **B**, *jaw-D* leaf 10 days after stratification. **C-E**, 3D models with increased growth at the margins through  $i_{RIM}$  showing (i) canvas at a time that corresponds to day 10 after wild-type leaf stratification and (ii) growth interaction network. **C**,  $i_{RIM}$  increases both  $K_{par}$  and  $K_{per}$  at the margins. **D**,  $i_{RIM}$  increases  $K_{per}$  only at the margins. **E**,  $i_{RIM}$  increases  $K_{par}$  only at the margins, while  $i_{RIM}$  inhibits  $K_{per}$ . Colours represent resultant areal growth rates calculated over 24 h intervals. Scale bars **A**, 400  $\mu m$ , **B**, 520  $\mu m$  and **C-E**, 100  $\mu m$ .

#### 4.2.7.3.2 Failed Arrest Perception

Major phenotypic differences between wild-type and *jaw-D* leaves are not evident at very early stages. This suggests that instead of increased growth rates at the margins, mutant leaf margins might not be able to perceive a growth arrest signal or have a delayed response. A delay in arrest perception may account for the *cin* mutant leaf phenotypes of *Antirrhinum* (Nath et al., 2003).

In the leaf models presented here, growth slows down along  $K_{par}$  only (through the action of  $i_{LATE}$ ; Fig. 4.16A i). Above, it was shown that in-

creases in marginal growth rates along  $K_{par}$  are sufficient to account for the *jaw-D* phenotype. Therefore, it was tested whether inhibiting the negative action of  $\mathbf{i}_{LATE}$  on  $K_{par}$  in the margins would generate canvas shapes comparable to the *jaw-D* leaves:

$$\begin{aligned}
 K_{a_{par}} &= p_{prox} \mathbf{i}_{PROX} \cdot \text{inh}(h_{late} \cdot \text{inh}(h_{rim \rightarrow late}, \mathbf{i}_{RIM}), \mathbf{i}_{LATE}) \cdot \text{pro}(p_{top}, \mathbf{i}_{TOP}) \\
 K_{b_{par}} &= p_{prox} \mathbf{i}_{PROX} \cdot \text{inh}(h_{late} \cdot \text{inh}(h_{rim \rightarrow late}, \mathbf{i}_{RIM}), \mathbf{i}_{LATE}) \\
 K_{a_{per}} &= p_{lam} \mathbf{i}_{LAM} \cdot \text{inh}(h_{mid}, \mathbf{i}_{MID}) \cdot \text{pro}(p_{late}, \mathbf{i}_{LATE}) \cdot \text{inh}(h_{rim}, \mathbf{i}_{RIM}) \\
 K_{b_{per}} &= K_{a_{per}} \\
 K_{nor} &= p_{nor},
 \end{aligned} \tag{4.6}$$

where  $h_{rim \rightarrow late}$  is the inhibition of the action of  $\mathbf{i}_{LATE}$  by  $\mathbf{i}_{RIM}$ .

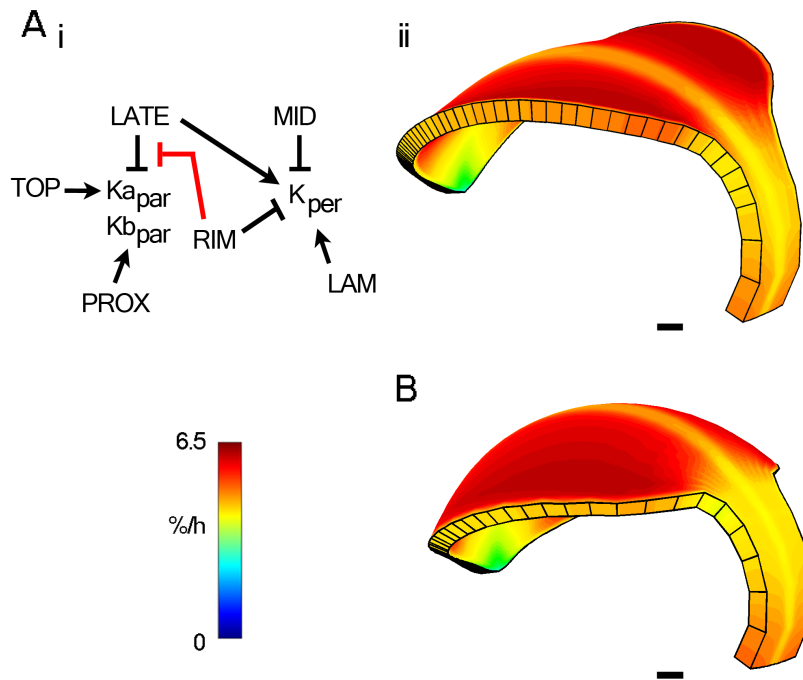


**Figure 4.16** **A**, 3D leaf model without arrest perception at the margins showing **(i)** growth interaction network and **(ii)** the canvas at a time corresponding to day 10 after wild-type leaf stratification. **B**, 3D wild-type leaf model at the same time as in **A(ii)**. Colours represent resultant areal growth rates calculated over 24 *h* intervals. Scale bars 100  $\mu m$ .

The absence of growth rate deceleration in the margins did not have a strong effect on the canvas shape compared to the wild-type model canvas shape (Fig. 4.16A ii and B). Thus, under the current model growth inter-

actions, a simple delay in growth deceleration perception is insufficient to account for the *jaw-D* phenotypes. It therefore appears that marginal growth rates have to exceed those of the lamina from an early age.

#### 4.2.7.4 Buckling

Increased marginal growth rate models captured the upward folded margins and proximodistal curvature of the *jaw-D* mutant leaves. It has previously been shown computationally, that high marginal growth rates can lead to tissue buckling (Liang and Mahadevan, 2009, 2011). A phenotype, which has also been observed for *jaw-D* leaves at later stages (Fig. 4.12B iv and v). In general, differential growth rates within a tissue can lead to buckling or out of plane rotations. This was demonstrated by growing a simple model consisting of a square canvas with a linear distribution of isotropic growth rates for a certain period of time (Fig. 4.17A). The resulting canvas remained flat in areas with low growth rates, whereas areas with high growth rates buckled to release the tension created by the tissue connectedness (Fig. 4.17B).

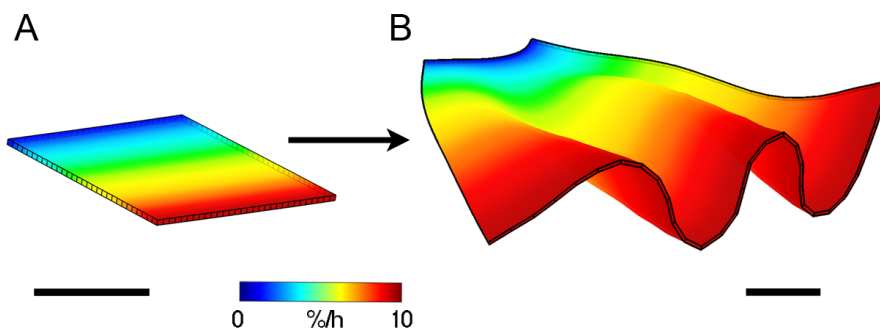


**Figure 4.17** Isotropically growing canvas with a linear distribution of growth rates **A**, initial canvas and **B**, resultant canvas buckles in fast growing regions. Colours represent specified areal growth rates. Scale bars 1 *mm*.

It is therefore likely that the same interactions, which induce the saddle-shaped lamina at early stages can account for margin buckling at later stages. Liang and Mahadevan (2009) showed that the shape adopted by a rectangular sheet depends on the dimensions of the rectangle as well as the amount of growth rates at the margins compared to the rest of the sheet. When the sheet was closer to a square and margin growth rates lower, the sheet adopted a saddle shape. With a more elongated sheet and higher margin growth rates,

the sheet buckled to minimise its elastic energy. The difference between a saddle and a buckled shape is the wavelength, where the saddle shape has a long-wavelength, whereas buckles have a shorter wavelength.

Linking these results back to the *jaw-D* mutant suggests that buckling may be a result of the more elongated leaf shape at later stages. In addition, *jaw-D* leaves are more elongated compared to wild-type, which may facilitate buckling further. Given that on plates leaves reach a final size relatively shortly after wild-type leaves stop growing, it is unlikely that margin growth rates increase with time. In addition, it has been shown previously that *TCP* genes act early in development (Efroni et al., 2008).

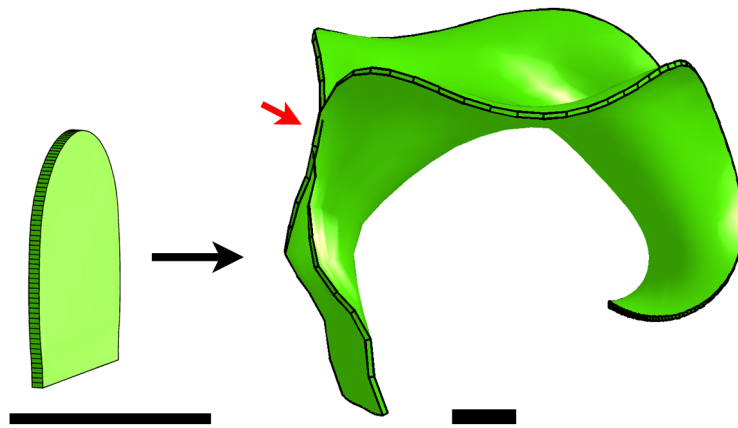


**Figure 4.18** The tendency of the margin regions of a canvas to buckle was tested at different amounts of canvas thickness. Areal growth rates are increased in the margins where  $i_{RIM}$  is expressed. Canvas is shown at times corresponding to leaves 3 and 9 days after initiation. The initial canvas has a thickness of  $5 \mu m$ . Scale bars  $100 \mu m$ .

Apart from the in-plane dimensions, a tissues readiness to bend depends on its thickness (Hufnagel et al., 2007; Sharon et al., 2002). Thickness has not directly been considered by Liang and Mahadevan (2009). Based on measured leaf thickness, the model starting canvas is thick relative to its area and compared to the relative thickness at later stages. To test the impact of the thickness of the starting canvas on buckling, the model with high areal margin growth rates (4.2.7.3.1 Increased Marginal Growth Rates) was simulated under the same parameters as above but with a thin starting canvas,  $5 \mu m$  in thickness. This canvas buckled more compared to models with a thick starting canvas (Fig. 4.18).

Thus, when leaf thickness is small relative to leaf area, buckling is observed, whereas at larger leaf thickness relative to leaf area, stresses are dissipated by the formation of a saddle-shape. This suggests that leaf buckling is a result of an increase in the leaf surface area and the associated decrease in relative thickness.

#### 4.2.7.5 Serrations

The *jaw-D* model with a thin starting canvas shows that the upward curved margins are in danger of colliding if growth continues as specified at early stages (Fig. 4.18, red arrow). However, such collision has not been observed for the real leaves. This would indicate that high marginal growth rates are not maintained throughout development, which is supported by the observed arrest in cell division in *jaw-D* leaves at later stages (Fig. 4.14B and C). However, buckling of the *jaw-D* mutant leaves late in development suggests that marginal growth rates continue to be high until leaf maturity (Liang and Mahadevan, 2009, 2011).

A possible explanation for this discrepancy might be found by considering other developmental abnormalities of *jaw-D* leaves. For instance, serrations are very pronounced in the *jaw-D* leaves. In the previous chapter, it was shown that serrations are likely to result from an interaction of growth and polarity. The pointed shape of the *jaw-D* serrations suggests that this is also the case here. It is, therefore, possible that a change in the polarity field might redirect growth patterns and prevent the opposite margins from colliding. In addition, serrations might facilitate the transition from the long-wavelength saddle shape to short-wavelength buckling by breaking the smooth margin integrity. However, serrations cannot be the sole reason for margin buckling as in *jaw-D* and *cuc2* double mutants, serrations are suppressed, while the wavy margin phenotype is maintained (Hasson et al., 2011).

Visualising the expression of the auxin response marker DR5 (*DR5rev::GFP*) shows that serrations in the *jaw-D* leaves are likely to be formed by similar mechanisms as serrations in wild-type. In both mutant and wild-type leaves,

DR5 expression is visible at the tip only at early stages (Fig. 4.19A i-ii and B i). DR5 levels then increase at the tip and spread towards more proximal regions along the leaf margins (Fig. 4.19A iii and B ii). In addition strong localised DR5 expression is visible in the proximal regions at sites of serration emergence (Fig. 4.19A iii and B ii, white arrows). At later stages DR5 also penetrates into the lamina of wild-type leaves (Fig. 4.19A iv-v). This was observed less clearly in the mutant leaves as well (Fig. 4.19B iv). The size of the serrations is also substantially larger than those of wild-type.

*Arabidopsis* leaf 1 only develops one pair of serrations. In leaf 1 of the *jaw-D* mutant, however, another pair of serrations develops proximally to the initial pair (Fig. 4.14B and C, white arrows). Moreover, in some cases another pair or a single serration develop along the distal half of the lamina (Fig. 4.19B iv, orange arrow). In wild-type, serrations only initiate proximal to the most recent pair.

The larger size of serrations in the mutant might be a result of higher growth rates in the margins. The higher number of serrations in the mutant may simply be a result of a larger perimeter allowing more auxin maxima to form (Bilsborough et al., 2011). The formation of new DR5 maxima and serrations off existing ones in higher metamers agrees with this hypothesis (Fig. 4.20, white arrows).

Thus, serrations also represent a major phenotypic difference between wild-type and *jaw-D* leaves, which would be interesting to explore further. The importance of serrations in shaping the *jaw-D* leaf suggests that polarity plays an important part in accounting for the mutant phenotype; thus again underlining the importance of the interaction between growth and polarity in development.

**Figure 4.20** *DR5rev::GFP* expression in *jaw-D* leaf 3. White arrows indicate new *DR5rev::GFP* maxima on and in between serrations.

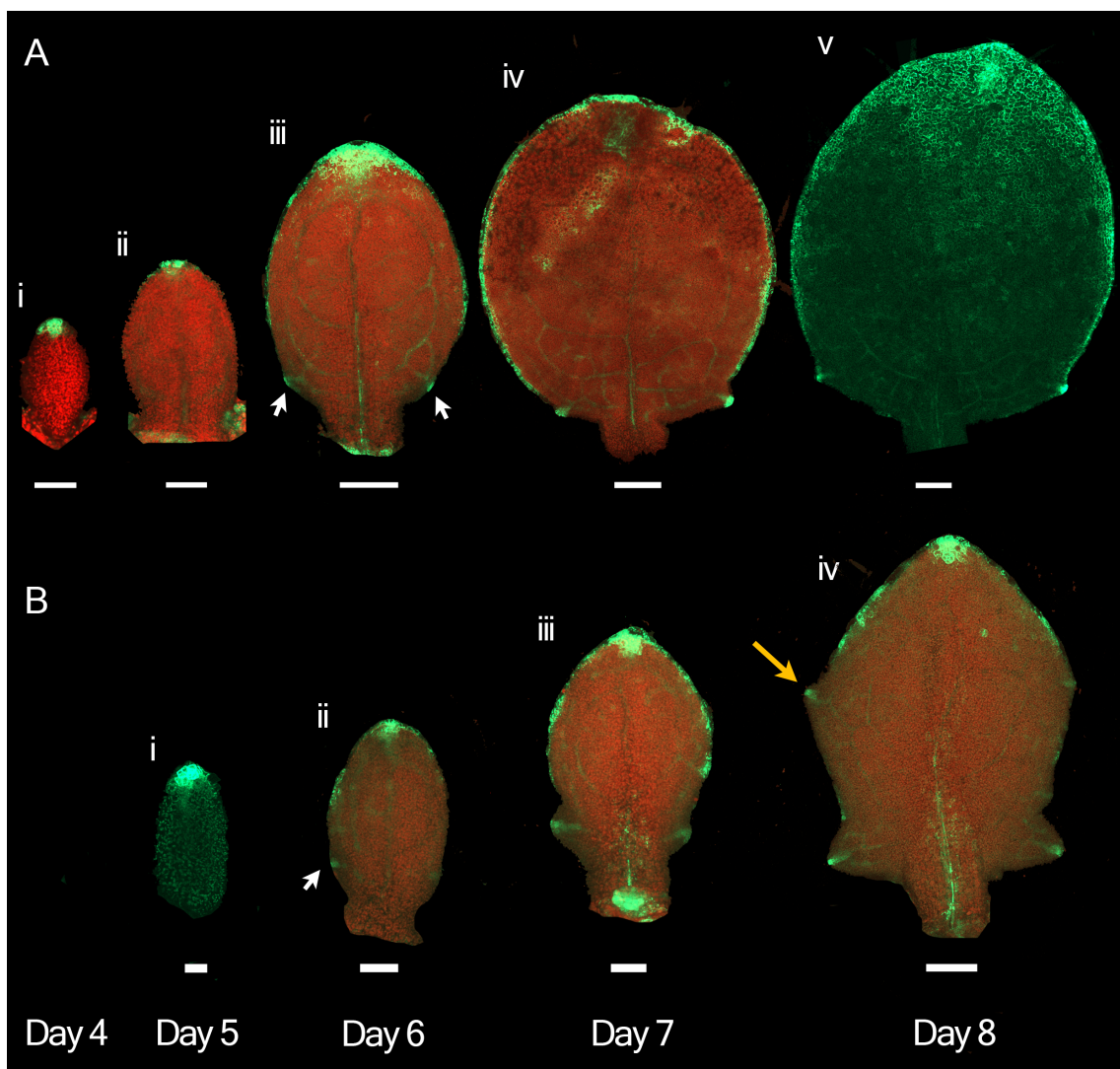
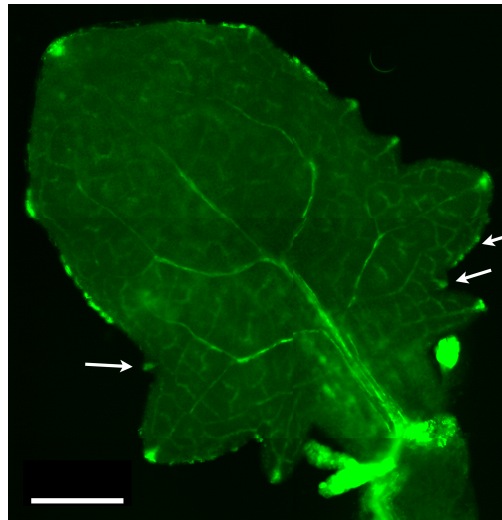


**Figure 4.19** *DR5rev::GFP* expression (green) in **A**, wild-type and **B**, *jaw-D* leaves at different days after stratification. Scale bars **B i**, 20  $\mu\text{m}$ ; **A(i-ii)** and **B(i-iii)**, 50  $\mu\text{m}$ ; **A(iii-v)** and **B(iv)**, 100  $\mu\text{m}$ .

## 4.3 Discussion

### 4.3.1 3D Wild-type Model

Modelling the 3D leaf curvature has shown that the early leaf shapes can be explained by growth interactions that are established at early stages and are maintained during development. However, the thickness of the early leaf prevented the leaf from bending out of the plane (Hufnagel et al., 2007; Sharon et al., 2002). Here, out of plane rotations were induced by differential growth rates on the two canvas surfaces.

There is some evidence that growth rates of the two surfaces differ. For instance, Siegfried et al. (1999) observed that the central abaxial domain of the primordium becomes vacuolated. This is thought to cause the primordium to arch over the shoot apical meristem and the adaxial surface. Shortly after this, the curvature reverses and the leaf begins to arch over its abaxial side. Donnelly et al. (1999) found that more cells expressed the division marker *cyc1At* on the adaxial epidermis compared to the abaxial epidermis, potentially indicating higher growth rates, which could account for the reversal in curvature. In addition, the expression of many genes, including those involved with auxin transport and synthesis, is specific to either the abaxial or adaxial side of the leaf (Kidner and Timmermans, 2007). Therefore, it is possible that growth rates of the two surfaces differ.

In the *GFtbox*, residual stresses are discarded and therefore do not build up. However, it cannot be excluded that observed 3D shapes are a way to dissipate stress, which would otherwise build up in the organ (Dumais, 2007; Shraiman, 2005). Alternatively, it is possible that differential physical properties across the leaf induce bending. Thus, the mechanism explored here is sufficient to account for the majority of the observed leaf shape at early stages, but may not be the only explanation. Growth data for both surfaces is necessary to resolve this issue.

#### 4.3.1.1 Future

Since leaf thickness was shown to play a major part in determining the shape of the leaf, a model based on more detailed leaf thickness data might

give more information on the extent to which growth rates on the two surfaces are expected to differ. For instance, the leaf midvein is substantially thicker than the lamina regions, in particular at later stages (Avery, 1933; Pyke et al., 1991). More accurate analysis of OPT images is needed to incorporate more realistic thickness parameters.

To resolve what developmental changes take place in the leaf at later stages and if there are indeed differences in growth rates on the two leaf surfaces, better growth data is needed. For instance, it would be interesting to explore the straightening out of the leaf spine at later stages. The high resolution images necessary to calculate growth rates for tracked leaf cells and the duration of imaging make it difficult to track larger leaves under the confocal microscope. In addition, for accurate growth calculations from tracking data the leaf has to be flat, which is not the case at later stages.

Alternatively, it is possible to track leaves using OPT. OPT has the advantage over confocal time lapse imaging, that the two leaf surfaces can be imaged simultaneously and leaf flattening is not required. This allows difference in growth of the two surfaces to be detected. Unfortunately, since the leaf cannot be removed from the plant, the image quality is usually not sufficient to faithfully identify natural landmarks, such as veins, trichomes and stomata, on the surfaces. A solution to this problem is to use *GFP*-constructs, which help to visualise landmarks. Karen Lee has tracked leaves expressing *GFP* in their trichomes. This data has not been analysed, yet, but will undoubtedly help to extend the leaf model to account for later stages of development.

### 4.3.2 *jaw-D* Leaves

Previous experimental analysis of *jaw-D* leaves has shown that the down-regulation of several class II *TCP* genes in *Arabidopsis* results in a change in transcription levels of hundreds of genes (Efroni et al., 2008). Thus, understanding mutant shape development based on the expression of specific genes would be very difficult. Here, the leaf model adapted to the first half of wild-type leaf development was used to explain how leaf growth might be altered

in the mutants. The *TCP* genes downregulated in *jaw-D* mutants are mainly active early in development (Efroni et al., 2008), during a period covered by the leaf model.

I have shown that the mutant phenotype can be explained by an increase in margin growth rates from an early age, while, under the growth interactions of the model, a simple failure to perceive an arrest signal is not sufficient. Margin buckling is only observed at later stages of mutant leaf development, which could not be taken into account by the model. The analyses performed here and in previous studies (Liang and Mahadevan, 2009, 2011) suggest, however, that buckling is a result of an increase in leaf surface area and the associated decrease in relative thickness.

A better idea of the importance in changes in leaf thickness could be gained by making accurate measurements of mutant leaf thickness over time, using OPT images. These measurements could be incorporated into the leaf model. In addition, margin growth data could be generated by time lapse imaging using OPT. OPT is especially useful for the *jaw-D* mutant leaves, which are difficult to flatten at later stages and cannot easily be grown in a chamber under the microscope. To investigate leaf buckling properly, however, the leaf model has to be extended to capture the late stages of leaf development, as well.

#### 4.3.2.1 *jaw-D* Serrations

Another striking feature of the *jaw-D* leaves is the large size and high number of serrations. Changes in *TCP* gene expression are known to affect the expression of *CUC* boundary gene family members essential for serration development. For instance, overexpression of *TCP3* or *TCP4* result in reduced *CUC* expression (Koyama et al., 2007; Palatnik et al., 2003). Similarly, the dominant negative expression of *TCP3* results in ectopic expression of *CUC1* and *CUC3* in the leaf (Koyama et al., 2007). In tomato, overexpression of *LA* converts the tomato compound leaf into a small simple leaf (Ori et al., 2007). Shleizer-Burko et al. (2011) proposed that the timing and localisation

of *LA* expression underlies the different leaf complexities observed in tomato, aubergine and potato.

Thus, serrations are a fundamental part of the *jaw-D* phenotype, which has not been explored here computationally. It would, however, be interesting to test if changes in the polarity field can generate the observed serrations and associated leaf shape changes, which might prevent problems of margin collision encountered in this work. This can be achieved by combining serration models discussed in the previous chapter with the 3D models generated here. Thus, the *jaw-D* leaf shape is likely to underly changes in growth patterns as well as in the polarity field.

Finally, the *jaw-D* leaves provide an interesting system to study the patterning of serrations, since mutant leaves have been shown to frequently initiate small serrations in the distal part of the leaf at later stages.

## Chapter 5

# General Discussion

In this work, different aspects of shape development have been investigated by studying the interplay between growth and polarity during the early stages of leaf development, when the characteristic leaf shape is largely established. The fundamental processes of leaf development have been captured by a model based on leaf time lapse imaging data. Small modifications of this model explained observed clonal patterns, leaf excision experiments, serration growth and positioning, and the 3D shapes of wild-type and mutant leaves. In addition, changes in the model parameter values could generate a versatile array of leaf shapes, many of which have been observed in nature.

### 5.1 Validity of Computational Methods

The two- and three-dimensional structure of the leaf was modelled as a continuous sheet using the finite element method. In this method, the tissue is considered as a continuum, but is divided into smaller elements for computational purposes. Treating the leaf as a continuous sheet allows growth to be captured on the tissue scale without having to account for the large number of cells at later stages, thus saving computational time.

The validity of this generalisation is supported by that fact that cellular growth parameters, calculated by time lapse imaging, were relatively uniform within regions of the tissue rather than different for each individual cell. Similar observations have been made by other studies that looked at the spatial distribution of growth rates (Kwiatkowska and Dumais, 2003; Schmundt et al., 1998) or cell division dynamics (Baena-Lopez et al., 2005; Milan et al., 1996;

Reddy et al., 2004). The tight junction between cells, in the absence of cell rearrangements, makes individual cell dynamics mechanically dependent on those of their neighbours. Together these observations suggest that the *Arabidopsis* leaf could be regarded as behaving like a continuum (Silk and Erickson, 1979).

### 5.1.1 Factors

Apart from the tissue abstraction, which ignores individual cells, the factors that control growth and polarity are also a generalisation of genetic interactions and pathways. This simplification allowed core functional interactions in leaf development to be determined. Although, it would have been possible to incorporate specific known genetic interactions, given the large number of genes and genetic redundancies (Gonzalez et al., 2010; Horiguchi et al., 2006a), such incorporations might have been misleading as to the importance of particular genes and would have distracted from the core mechanisms controlling leaf shape development. In addition, the model would have been highly limited by the availability of genetic data.

The benefit of such simplification has been demonstrated by the ABC model of flower development (Coen and Meyerowitz, 1991). In the ABC model, the abstract view of the system has allowed the identification the core interactions that are necessary for flower organ identity. Although many genetic components of this system are now known, the system is still often simplified to these three abstract components.

## 5.2 Growth Coordination

### 5.2.1 Proximodistal Gradient of Growth

In this and previous studies, leaf tracking of a variety of species revealed a clear proximodistal gradient of growth rates in the leaf (Avery, 1933; Erickson, 1966; Schmundt et al., 1998; Wolf et al., 1986). Previous studies, however, have concentrated on later stages of leaf development, whereas here it was shown that growth rates are non-uniform from a very early stage. In

addition, the nature of this gradient has not been studied before. By visualising the growth rate gradient along the midline only, it was demonstrated that the gradient is initially approximately linear and that the shape of the gradient changes with growth. These changes in gradient shape could be explained purely by growth itself, where low growth rates in the distal regions maintain a steeper decline than high growth rates in the proximal regions. This results in largely uniform growth rates in the proximal regions. Thus, gradients are not static entities that are imposed onto the system, but are themselves shaped by growth (Jaeger et al., 2008). The importance of growth and cell division in determining growth factor distributions has been demonstrated in the *Drosophila* embryo, where the morphogen Wingless (Wg) was tethered to the membrane of cells that normally secrete Wg (Pfeiffer et al., 2000). The resulting embryos could not easily be distinguished from wild-type embryos, in which Wg diffuses freely.

In the leaf, the distribution of growth rates has a large impact on the fate of individual regions at later stages. The high proximal growth rates mean that initially proximal regions make up a large area of the leaf at later stages. These results agree with a previous study of the *Arabidopsis* sepal, which also showed that distal regions make up very little of the final organ (Roeder et al., 2010). Incorporating these observations into a 2D model showed that the contribution of proximal regions to the leaf shape is so extensive that it may be mistaken for leaf regeneration after distal leaf excision, which had been the case previously (Sena et al., 2009).

## 5.2.2 Establishment of Growth Patterns: Early or Re-patterning

Another question discussed in this work is whether the underlying growth patterns are established early or if growth patterns change at the different developmental stages.

The observed proximodistal gradient in growth rates could be explained by a model, where patterns are established very early in development and are maintained locally during growth, which was also assumed for most other growth factors. This assumption was verified by leaf surgery. Time lapse imaging of excised leaves showed that distal leaf excision has no major effect

on the distribution of growth rates across the remaining leaf, suggesting that patterns are largely controlled locally by the time of leaf excision.

The models presented here did not deal with the question of how this initial coordination is set up, as it appears to be established prior to the period analysed by time lapse imaging. In developmental patterning, there are many examples where morphogen gradients are only active early on in development, but induce the permanent expression of downstream genes (Schwank and Basler, 2010; Wolpert, 1996). It is therefore possible that in the leaf patterns are established early on in development and permanently alter the cellular growth machinery through activation of downstream processes.

In addition to the early-established overall growth rate patterns, the models assume that there are changes in the temporal patterns. While growth in leaf length appeared to decrease with time, growth in width is likely to increase at least temporally. In the models, these patterns were described by a factor that increases uniformly throughout the canvas after day 6 and inhibits growth in leaf length and promotes growth in leaf width. These interactions generated the switch in the orientation of principal growth observed in the leaf at later stages. Thus, it appears that temporal re-patterning is required to generate observed growth dynamics and leaf shapes.

However, it is possible, that the observed changes in growth rates are not mediated by growth rate re-patterning, but instead due to a reorientation of the polarity field. Reorientation during development would require more stringent control of the polarity field and is likely to involve several polarity organisers. Thus, the model generated here presents a simpler way to account for the changes in principal orientations of growth, given that rates become more isotropic in the lamina.

Apart from the tissue wide re-patterning with age, growth rates appear to be modified locally during leaf morphogenesis. For instance, it is possible that during serration formation growth rates are modified locally at the proximal margins. In addition, tissue excision resulted in local changes in growth rates at the cut edge.

### 5.2.2.1 Growth Deceleration

Since time lapse imaging was restricted to the early stages of leaf development, growth deceleration with time, to yield a leaf of determinate size, has only been captured partially and the mode of deceleration could not be determined.

I assumed that growth rates decrease uniformly through the accumulation of an immobile growth inhibitor. In this implementation, growth deceleration was controlled individually by each region. This mechanism was a simple way to introduce uniform deceleration. However, it not only requires the tissue to have a notion of time, but also that the cell internal clocks are synchronised across the whole tissue. Given genetic variability and stochastic differences in gene expression (Jaeger et al., 2008) such synchronisation might be better generated by a fast-propagating morphogen, which could coordinate deceleration globally across the tissue.

Alternatively, instead of a growth inhibitor, growth deceleration might be controlled by a growth promoter, whose levels decrease over time. Such a decrease could be mediated by dilution due to an increase in size (Day and Lawrence, 2000). However, as has been shown for the proximodistal growth rates, dilution with size reduces growth rates too quickly in the absence of further growth factor production. In addition, the rate of dilution would vary with the rate of growth, which is spatially non-uniform.

It would be very interesting to shed light on the spatiotemporal patterns of growth deceleration, which might not be uniform throughout the leaf, and their contribution to the final organ size and shape. This, however, requires an extension of the model and the available time lapse imaging data to later developmental stages. Thus, based on the current data, it is difficult to determine whether growth deceleration involves further spatial patterning mechanisms late in development, or whether deceleration is spatially uniform and only has a temporal component.

## 5.3 Organising Systems

The regional alignment of orientations of growth observed in the leaf indicates that growth patterns are coordinated throughout the period analysed. It was explored whether tissue orientations specified by the polarity field are likely to be retained during development, irrespective of changes in tissue geometry, or whether orientations change according to the tissue geometry or other polarity re-organisation events. Interestingly, with the underlying growth dynamics used, all polarity-based models generated relatively well matching leaf shapes.

### 5.3.1 Maintenance

By comparing the tracked principal orientations of growth to those generated by models with different underlying polarity fields, it was shown that the polarity field of the leaf most likely deforms with the leaf's geometry, rather than being maintained according to the initial conformations.

It therefore appears that the leaf polarity system differs from that of the dorsal petal of *Antirrhinum*, where clonal patterns are maintained perpendicular to the base throughout development in spite of tissue rotations (Rolland-Lagan et al., 2003). The patterns in the petal were explained by a combination of source and sink polarity organisers (Coen et al., 2004; Green et al., 2010).

However, it is possible that the leaf model with a different non-deforming initial polarity field, based on, for instance, oblique orientations in the proximal canvas regions, would generate patterns more similar to those observed in the leaf. This idea could not be tested due to *GFtbox* implementation limitations. It is also important to note that for an organiser-based mechanism, polarity does not need to be organised from a source region. It is equally possible that all regions within a tissue produce a polarity factor, which is captured at a particular site that thereby acts as an organiser.

### 5.3.2 Deformation or Re-orientation

Although observed leaf patterns could be generated by a model, in which the polarity field was fixed to the tissue at early stages, equally good matches were generated with a polarity field that is controlled by a continuously prop-

agating polarity factor. When the polarity field is fixed to the canvas, the polarity field deforms locally with the canvas. Similarly, the propagation of a polarity factor is restricted by the canvas geometry. While these two polarity versions performed equally well to simulate growth of the intact leaf, the principal orientations of growth, generated by time lapse imaging of leaves subjected to distal excision, were better represented by models with a dynamic polarity field. Excision changed the geometry of the canvas, which the dynamic model was able to adjust to. However, it is possible that in addition excision triggers repolarisation signals, as indicated by the accumulation of auxin at the cut edge.

Dynamic polarity systems also seem to underlie insect appendage development (Aigouy et al., 2010). For instance, experiments, in which the proximal part of a cockroach leg was grafted onto a distal stump, showed that firmly established PCP orientations reorientate at the grafting site (reviewed in Meinhardt, 2007). This suggests that polarity patterns are able to readjust to new signals. Models that best explained the generation of leaf serrations all predicted local polarity re-organisations at the serration sites.

If the polarity field was fixed at early stages, similar to the initial gradient of growth rates, the polarity field might be initially coordinated by a propagating factor, which induces local downstream changes. Such a system has the advantage that tissue polarity has to be coordinated over a small field of cells only, since computational analyses have shown that known mechanisms of coordination fail to globally align the polarity field of larger tissue (Axelrod and Tomlin, 2011; Goodrich and Strutt, 2011; Weiner, 2002). However, if polarity is fixed at early stages, it has to be passed on to both daughter cells upon division. It is unclear how such a mechanism of polarity inheritance would function. Thus, based on the results obtained here, it might be more likely that the polarity field is able to dynamically adjust to the levels of a polarity factor, the distribution of which changes with the leaf geometry. In addition, the polarity field is likely to be repolarised locally to initiate serrations. As this study concentrated on the early stages of leaf development, polarity factor propagation was sufficient to align the polarity field throughout the whole

simulation period. Given the largely isotropic growth rates in the leaf blade at later stages, it would be interesting to investigate whether polarity field alignment is necessary at later stages.

## 5.4 Rotation, Polarity and Growth

Although growth and polarity were specified independently, it is clear that both feedback on each other. In models where the polarity was fixed to the canvas at early stages, polarity orientations rotated locally with the canvas. In models where the polarity field was dynamic, propagation directions were limited by the geometry of the locally rotating canvas. The geometry and amount of rotation of the canvas was controlled by the non-uniform growth rates acting upon the connected canvas. Thus, while the orientation of growth is determined by the polarity field, growth rates cause canvas regions to rotate, which changes the local orientations of the polarity field (Jaeger et al., 2008). This interaction might explain why several morphogens have been reported to function in both growth and polarity control (Baena-Lopez et al., 2005; Lawrence and Struhl, 1996; Widmann and Dahmann, 2009). In three-dimensions, the specified growth and polarity interactions together with tissue connectedness resulted in rotations out of the plane to generate the 3D shapes of wild-type and mutant leaves.

## 5.5 Modelling Loop

The leaf models were based on time lapse imaging data. Additional modifications to the models were also inspired by experimental observations. Recreating observations by computational modelling, reveals many issues associated with a particular problem. Often these issues only become apparent when trying to replicate the system. Therefore, modelling can verify if the basic components of a mechanism are likely to be known or show what components might be missing. However, for a model to be truly useful, it should be able to make further predictions about the system, which can then be tested experimentally. In this way modelling results lead to experiments performed to

test computational results. This creates a loop leading from experimental observations to computational models, which raise new ideas that can be tested experimentally and the results re-implemented computationally.

In case of the leaf model, which was based on time lapse imaging data, it was assumed that growth and polarity patterns are established early on and are maintained during development. These assumptions were in contrast to results obtained in leaf regeneration experiments by Sena et al. (2009). Repeating these experiments computationally inspired actual experimental repetition, which led to a more accurate model. In addition, together the experimental and computational results not only disprove earlier regeneration claims, but also provide an explanation for why the observations may be mistaken for regeneration.

Other questions in this work have not fully undergone the experiment-modelling-experiment loop. For instance, young *jaw-D* mutant leaves are extremely curved along their proximodistal axis, whereas at later stages leaf margins buckle. It has been shown previously that these shape difference may be a result of differences in tissue dimensions and in the amount of excess growth at the margins (Liang and Mahadevan, 2009, 2011). In agreement with these results, in this study, an increase in growth rates at the margins was necessary to generate shapes similar to those observed for *jaw-D* leaves at early stages. In addition, differences in canvas thickness were sufficient to generate either saddle-like canvas shapes or induce margin buckling. To investigate that these phenotypic differences are due mechanical differences in leaf thickness in proportion to leaf area, rather than continuous increases in margin growth rates during leaf development, accurate measurements of leaf thickness and margin growth rates are necessary.

The leaf morphospace, generated by changing some of the model parameter values, has demonstrated that the model can account for a variety of observed leaf shapes. To complete the loop, growth analysis of leaves, with shapes predicted by the morphospace, could verify if these simple changes are the only differences in growth between the leaf under analysis and the *Arabidopsis* leaf. In addition, this would provide strong support for the leaf model.

In case of serration development, the models have allowed potential functions of auxin and CUC2 to be defined. The best fitting models proposed a role for auxin or CUC2 as polarity factors. This could be tested by ectopically expressing auxin or *CUC2* in a small region and measuring changes in the orientation or rate of growth at this site. It is likely that if auxin or CUC2 are able to divert the polarity field near the serrations, they are also responsible for establishing polarity throughout the leaf. Thus, models can provide a means of identifying the key components and remaining questions of a system and thereby allow for more focused experiments.

Another important aspect of modelling is to guide the experimental work necessary to distinguish between different hypotheses. For instance, during virtual clonal analysis, clones generated by the different hypotheses of serration formation looked very similar. Therefore, time lapse imaging, although difficult, might be a more suitable method for testing the model predictions for the different serration hypotheses.

## 5.6 Outlook

Together with minor modifications, the fundamental leaf model generated in this work was able to explain a variety of morphogenetic events, suggesting that it accurately reflects leaf development at early stages. However, it would be useful to expose the model to further developmental processes, which can either be explained using the model, or which help to break and improve the model.

The largest shortcoming of the current model is that it is limited to the first half of leaf development due to the promotion of mediolateral growth at later stages of the model. To investigate morphogenetic questions at late stages of leaf development, such as growth deceleration and the 3D leaf shape of wild-type and mutant leaves, growth data of later stages is needed to extend the model further in time. In addition, growth data of the margin regions is needed to explore potential changes in rates and orientations of growth upon serration formation.

Comparison of model predictions and tracking results post leaf excision suggested that polarity is controlled dynamically. Further time lapse imaging of different leaf excision experiments may clarify to what extent the polarity field is affected by the cut. It is possible, that the polarity field is dynamic and 1) reorients with changes in the tissue geometry post excision or 2) is also affected by new polarity organising signals post excision. Since auxin accumulates at the cut edge as shown here and previously (Sauer et al., 2006; Wabnik et al., 2010), it is possible that the polarity is reorganised post cutting.

Another follow-up from this work would be to look at the growth patterns of leaves with shapes similar to those predicted by the model morphospace. This work could be conducted with *Arabidopsis* leaf shape mutants or on leaves of a variety of plant species. Evidence of a proximodistal gradient in growth rates has already been provided in a number of leaf species (Avery, 1933; Erickson, 1966; Koehl et al., 2008; Schmundt et al., 1998; Wolf et al., 1986). Thus, from an evolutionary point of view, it would be fascinating to demonstrate that simple changes are sufficient to generate versatile shapes in closely and more distantly related species.

Finally, in the process of generating a comprehensive leaf model, the actions of individual genes have largely been ignored. It is unlikely that each factor in the model represents one gene or even one pathway. However, some of the factors utilised in the model seem to show a closer match to observed gene functions and expression patterns. For instance, the  $\mathbf{i}_{LAM}$  factor, which controls lateral lamina outgrowth, might represent the action of genes, such as *JAGGED*, *LEAFY PETIOLE* or *YABBY* family members. Mutations in all of these candidates either result in a disturbance of mediolateral outgrowth or a change in the petiole-lamina boundary (Dinneny et al., 2004; Eshed et al., 2001, 2004; McConnell and Barton, 1998; Ohno et al., 2004; van der Graaff et al., 2000). Thus, the underlying interactions of the leaf model generated here allow more specific genetic interactions and expression patterns to be introduced, to test the role of specific genes in development. For instance,

further analysis could involve generating more accurate spatiotemporal expression data for prospective candidate genes. In addition, genes could be ectopically expressed in real leaves and the leaf model to explore their effects on tissue shape, growth and polarity.

# Chapter 6

## Materials and Methods

### 6.1 General Methods

#### 6.1.1 Standard Growth Conditions

*Arabidopsis* plants were grown on plates under standard growth conditions. Seeds were sterlised using 0.05 % sodium dodecyl sulfate and 70 % ethanol for 10 *min*. Seeds were then rinsed with 100 % ethanol and sown on plates, 12 per dish, containing 25  $\mu$ l MS agar medium [0.8 % (w/v) agar, 1x Murashige and Skoog salt mixture, 1 % (w/v) sucrose, 100  $\mu$ g  $ml^{-1}$  inositol, 1  $\mu$ g  $ml^{-1}$  thiamine, 0.5  $\mu$ g  $ml^{-1}$  pyridoxin, 0.5  $\mu$ g  $ml^{-1}$  nicotinic acid, 0.5  $\mu$ g  $ml^{-1}$  MES, pH 5.7]. The seeds were stratified in the dark at 4 °C for 3 nights. They were then transfered to the growth room (20 °C, 16 *h* light).

### 6.2 Data Acquisition and Processing

#### 6.2.1 Arabidopsis Leaf Growth Curves

##### 6.2.1.1 Ecotype Landsberg *erecta*

This work has been carried out by Samantha Fox. Wild-type plants of ecotype Landsberg *erecta* were grown on plates under standard growth conditions up to 20 days after stratification (DAS). Leaf 1 was imaged at various days after stratification over this period. Seedlings 2-6 DAS were stained with propidium iodide (Truernit et al., 2008) and imaged under the confocal microscope [Zeiss EXCITER Laser Confocal Microscope]. At later DAS, leaf 1 was removed from multiple seedlings, flattened and imaged. Leaf length and width

was measured along the longest axis of the leaf (petiole base to leaf tip) and across the widest point of the lamina. For very curved young leaves (2-6 DAS) measurements were taken in 3D using *VolViewer* by Jerome Avondo (<http://cmpdartsvr1.cmp.uea.ac.uk/wiki/BanghamLab/index.php/VolViewer>). Older leaves were flattened, photographed and measured from the 2D images using Fiji (<http://fiji.sc>).

### 6.2.1.2 Ecotype Columbia

This work has been carried out by Samantha Fox and myself. *Arabidopsis* plants of ecotype Columbia-0 were grown on plates under standard growth conditions up to 20 days after stratification. On various days after stratification leaf 1 was removed from multiple seedlings, flattened and imaged under brightfield. Young leaves, 4-7 DAS, were imaged under the confocal microscope [Zeiss EXCITER Laser Confocal Microscope]. Older leaves were imaged on a compound microscope [Leica DM6000]. The width of leaves imaged with either of these microscopes was measured using ImageJ (<http://rsbweb.nih.gov/ij/>). As above, leaf width was measured across the widest point of the leaf lamina. Mature leaves and those close to maturity were imaged using a stereo microscope [Zeiss Lumar v12 Stereo-Fluorescence microscope] and measured using the microscope associated software [AxioVision Rel. 4.7].

### 6.2.1.3 Curve Fitting

The dynamics of the leaf length and width over time were described by fitting individual logistic curves to the datasets:

$$y = \frac{-A}{1 + e^{(t-t_m)k}} + A, \quad (6.1)$$

where  $A$  is final leaf size,  $t$  is time,  $t_m$  the time of inflection where half of the growth has occurred and  $k$  is the early exponential growth rate. This function was fitted to the datasets using least-squares minimisation (MATLAB tool written by Pierre Barbier de Reuille) and then manually adjusted to generate a better fit for the younger stages studied in this work. The mean leaf shapes were generated as described under clonal analysis (6.2.3.3 Analysing Clonal

Data).

#### 6.2.1.4 Calculating Leaf Initiation

The initiation time of Landsberg *erecta* leaf 1 was estimated by interpolating the fitted logistic function back to a leaf size of 0.02 *mm*, which corresponds to the size of about two cells and is assumed to be the leaf size at initiation. Since, the fitted parameter values differed slightly for leaf length and width, the width parameters were used to calculate the time of leaf initiation only. According to this method leaf initiation was 21 *h*, about 1 day after stratification.

### 6.2.2 Time Lapse Imaging

#### 6.2.2.1 Tracking

*Arabidopsis* seedlings of ecotype Landsberg *erecta* were grown on plates up to 5 or 7 days after stratification under standard growth conditions. In these seedlings the plasma membrane was fluorescently labelled by either *pAR169* (*pATML1::mCitrine-RCI2A*; Roeder et al. 2010), or *Lti6b* (*p35S::GFP-LTI6b*; Kurup et al. 2005). Plants, with leaf 1 of comparable width, were then transferred to the tracking chamber (Sauret-Güeto et al., 2011), which was placed under the Zeiss EXCITER Laser Confocal Microscope. Plants were grown in the tracking chamber for 2 or 3 days under constant flow of liquid media [1/4 strength Murashige and Skoog, 0.75 % sucrose, 1.1  $\mu\text{g ml}^{-1}$  MES, pH 5.8] at 1  $\mu\text{l s}^{-1}$ . The abaxial epidermis of leaves was imaged every 6 to 12 *h* using the 488-*nm* line of an argon ion laser. Emitted light was filtered through a 500-550-*nm* band-pass filter. Leaves were imaged with either a 10x dry or 20x dry objective lens. The mounted chamber was externally illuminated by a cold light source set to a long-day photoperiod of 16 *h*. The room temperature was maintained at 20 °C.

#### 6.2.2.2 Tracking Image Analysis

This work was carried out by Samatha Fox. Microscope image *z*-stacks were converted into individual *png* slices using a script by Jerome Avondo, *Bioformats Converter*. The *png*-stacks of the leaf abaxial epidermis were con-

verted to flat 2D image projections to using *Merryproj* (Barbier de Reuille et al., 2005).

### 6.2.2.3 Tracking Growth Calculations

This work was carried out by Samantha Fox. Using these time series 2D image projections the growth tensor field was calculated by tracking cell vertices using software called *Point Tracker* by Pierre Barbier de Reuille. *Point Tracker* is written in Python and uses the NumPy and SciPy packages (Jones et al., 2001) for the data analysis and PyQt4 (<http://www.riverbankcomputing.co.uk/software/pyqt>) for the user interface.

Points were placed on corresponding cell vertices in consecutive images. Placed points were linked to form polygonal regions. Regions mostly corresponded to individual cells, but in particular at later stages were made up of a small number of cells. For each region the growth tensor was estimated from the linear transformation that best approximated the deformation. The square error of each vertex position between the transformation and observed final position was minimised.

Form the transformation the scaling was extracted by singular value decomposition. Due to the large time steps (24 h) the scaling had to be further corrected. For this correction, it was assumed that the tissue grows at a constant growth rate during the time step, according to the Lagrangian reference system. The strain tensor was then calculated from the scaling. Areal growth rates were calculated as the sum of growth in the major,  $K_{max}$ , and minor,  $K_{min}$  orientation of growth.

#### 6.2.2.3.1 Midline Growth

Growth rates along the leaf midline were extracted and displayed on a 1D graph. From the tracked regions, cells along the leaf midline were selected manually by Samantha Fox and myself. The tracked cell vertices, as saved by *Point Tracker*, were used to calculate the growth tensor for each region, as described above, using a script written by Pierre Barbier de Reuille and Sarah Robinson. I modified this script to align the manually defined leaf midline with

the  $y$ -axis of the image (showing the final leaf of each growth interval). The midline axis was defined by manually selecting two points that lie on it. Since more than one cell file along the midline was tracked, the position of aligned cells along the  $x$ -axis differed slightly. This variation along the  $x$ -axis was small and ignored. The position of each cell centroid along the leaf axis was determined by its distance along this midline axis, where the petiole-lamina boundary base was always defined as the origin. When the leaf midline did not grow straight, the leaf midline was divided into segments and defined for each segment separately, as above. Each segment was aligned independently and the length of each segment added to calculate the whole leaf length.

Areal growth rates were extracted from the growth tensor fields. Growth rates parallel and perpendicular to the midline axis were calculated by projecting the unit vector of the midline axis onto the unit vector of the major and minor axis of growth.

### 6.2.3 Clonal Analysis

#### 6.2.3.1 Generating *Arabidopsis* Clones

This work was carried out by Samantha Fox. *Arabidopsis* plants in ecotype Landsberg *erecta* expressing *35S::lox-uidA-loxGFP* and *hsp18.2::Cre* (Gallois et al., 2002) were grown on plates under standard growth conditions. Plants were heat shocked 4 or 7 days after stratification by placing the sealed plates into a water bath at 38.5 °C for 2.5 *min*. This induced *35S::GFP* expression in few random cells across the leaf. Plates were then returned to standard growth conditions for another 3 or 6 days. After this period leaves with a width within +/- 10 % from the expected size at their age, as calculated from the growth curve (340  $\mu\text{m}$  for leaves 7 DAS and 1.2 *mm* for leaves 10 DAS), were removed from the plant, flattened and their abaxial surface was imaged under a confocal microscope [Zeiss EXCITER Laser Scanning Confocal Microscope] or a compound microscope [Leica DM6000], depending on their size. Images were taken under different magnifications and rescaled to the scale of the image with the lowest resolution (largest  $\mu\text{m}/\text{pixel}$ ).

### 6.2.3.2 Generating *Antirrhinum* Clones

This work was carried out by Sandra Bensmihen. The unstable *Antirrhinum* line pal-244 (Harrison and Fincham, 1964) was grown on soil under continuous light at 25 °C. When metamer 2 was between 4 and 6 mm in width, corresponding to a metamer 4 width of 50-100  $\mu\text{m}$ , plants were transferred to 15 °C for 24 h to induce transposon excision. Plants were then returned to 25 °C and grown until metamer 4 was mature. Metamer 4 leaves were then flattened and photographed using a Kodak DCS Pro 14N camera. The distance of the camera and the specimens was maintained constant.

### 6.2.3.3 Analysing Clonal Data

This work was carried out by Samantha Fox (*Arabidopsis* analysis), Sandra Bensmihen and myself (*Antirrhinum* analysis), Paul Southam and Andrew Hanna (toolbox development).

Clones on *Arabidopsis* and *Antirrhinum* leaves were analysed using *Sector Analysis Toolbox* implemented in MATLAB (<http://www.uea.ac.uk/cmp/research/cmpbio/SectorAnalysisToolbox>). First the leaf and sector shapes were segmented. *Arabidopsis* leaves and clones were segmented manually using Photoshop. *Antirrhinum* leaves and clones were segmented semi-automatically using a segmentation algorithm with further manual adjustment in the *Sector Analysis Toolbox*. For each leaf project, leaves were warped to a mean leaf shape by placing 50 points around the segmented leaf outlines with several reference points. For *Arabidopsis* there were 5 reference points, two at each side of the petiole base, two at each side of the petiole-lamina boundary and one at the tip. For *Antirrhinum* there were only 2 reference points, as the petiole had been removed before imaging. These reference points were located in the middle of the petiole-lamina boundary (now the base of the leaf) and the leaf tip. These placed points were subjected to Procrustes Alignment (Gower, 1975) and normalised for scale. Each clone was warped to the corresponding mean shape using a Piecewise Linear Warp (Goshtasby, 1986). For completion a petiole was added to the warped *Antirrhinum* leaf, by photographing a corresponding leaf and extracting the petiole in Photoshop.

#### 6.2.3.4 Cell Outline Extraction

To simulate clonal analysis with the model, cell outlines were extracted from leaves 3 and 6 days after initiation. Outlines were superimposed onto the canvas at the appropriate stages. Outlines of the 6 day old leaf were extracted from one of the tracked leaves. Samantha Fox placed points around random cells in the leaf image using *Point Tracker*. The cell positions generated by *Point Tracker* were loaded into the modelling toolbox, *GFtbox*, and superimposed onto the canvas.

For the 3 day old leaf, the high abaxial leaf surface curvature precluded the use of 2D projections for obtaining cell outlines. Cells on the leaf surface were therefore approximated using a flattening algorithm in *VolViewer* (<http://cmpdartsvr1.cmp.uea.ac.uk/wiki/BanghamLab/index.php/VolViewer>). This was carried out by Jerome Avondo. The curved abaxial surface of the leaf primordium was first approximated by a 2D plane, placed onto the confocal image. The 2D plane was discretised into a regular grid with 64 x 64 vertices with connected diagonals to form 8192 triangles. The  $x$  and  $y$ -axis of the grid were curved independently to intersect the middle of the epidermal surface using two manually specified parameters. These parameters define the grid displacement along the  $z$ -axis at each vertex using a sinusoid (sin) function. The grid was then flattened by computing the  $xy$ -distance between vertices, removing the  $z$ -displacement and translating each vertex back to its  $xy$ -position. Samantha Fox extracted the cell outlines from the flattened image by placing points around evenly distributed cells in *Point Tracker*.

#### 6.2.4 Leaf Excisions

Excision experiments were performed by Samantha Fox. *Arabidopsis* plants were grown under standard growth conditions until 7 DAS. Individual seedlings were then placed in a drop of water on a glass slide. Excision of leaf 1 was performed using a Zeiss PALM laser dissecting microscope. Leaves were viewed under a 10x objective and the PALM software was used to direct the laser beam, which cut the leaf. The laser beam at 100 % power travelled at a speed of  $5 \mu\text{m s}^{-1}$ . At the leaf age at which the cuts were performed, the laser cut through all layers.

For the distal excision, the *pAR169* line (*pATML1::mCitrine-RCI2A*, ecotype *Ler*; Roeder et al. 2010) was used, which expresses YFP in the epidermal plasma membranes. The lamina of leaves was cut in half, perpendicular to the midvein. The diagonal cut was performed on the *DR5rev::GFP* line ecotype Col-0 (Friml et al., 2003) by cutting diagonally to the midvein in the distal half of the lamina. In both cases the excised leaf tissue was removed using fine forceps. Leaf incision was performed in the *DR5rev::GFP* line at the distal margins and the leaf was incised laterally about two-thirds up the leaf lamina. Seedlings were then returned to standard growth conditions for a further 6 days. The cut leaf 1 was removed, flattened and imaged under the confocal microscope [Zeiss EXCITER Laser Confocal Microscope].

#### 6.2.4.1 Tracking Straight Cut Leaves

Leaves expressing *pAR169* were excised with a straight cut to remove the distal half of the lamina, as described above. Immediately after excision seedlings were mounted into the tracking chamber. Cut leaves were tracked for 3 days under the Zeiss LSM 5 EXCITER Laser Scanning Microscope (6.2.2 Time Lapse Imaging).

#### 6.2.5 Leaf Serration Measurements

Serrations of wild-type leaves ecotype Col-0 (expressing *DR5rev::GFP* (Friml et al., 2003) or *PIN1::PIN1-GFP* (Benková et al., 2003)) were measured based on a similar method as used by Hasson et al. (2011). Plants were grown on plates under standard growth conditions, removed from the plants at various stages and flattened. Depending on their size leaves were imaged using a confocal microscope [Zeiss EXCITER Laser Confocal Microscope] or a compound microscope [Leica DM6000]. Serrations were measured after imaging using the microscope supplied software, which in case of the Zeiss EXCITER was the LSM Image Browser and in case of the Leica DM6000 was the Leica LAS AF software.

Serration width was measured as the distance between the boundaries of the serrations and the lamina. Serration length was measured as the distance between the line describing serration width and the serration tip, where the

length line was always orthogonal to the width line.

## 6.2.6 Optical Projection Tomography

Wild-type ecotype Landsberg *erecta* leaves and *jaw-D* (*35S::miR-319a*; Efroni et al. 2008) mutant leaves in ecotype Col-0 were imaged by Karen Lee using optical projection tomography (OPT; Lee et al. 2006; Sharpe et al. 2002).

Plants were grown on plates under standard growth conditions and imaged at various stages. Leaf imaging was performed in the same way as in Lee et al. (2006). Leaves were removed from the plants and incubated overnight in 100 % ethanol. Cleared leaves embedded in 1 % low-melting-point agarose and kept in methanol overnight. The agarose was cleared in a 1:2 mixture of benzyl alcohol and benzyl benzoate (Sigma-Aldrich) for 12 *h* until almost transparent.

Embedded leaves were imaged using a prototype OPT device (Lee et al., 2006; Sharpe et al., 2002). Visible light transmission images were collected using a 20-W halogen lamp connected to the OPT device. OPT images were reconstructed into slices and visualised in 3D using *VolViewer*.

### 6.2.6.1 Leaf Thickness Measurements

Leaf thickness at various stages was measured by Karen Lee from the OPT imaged wild-type leaves. Leaf thickness was measured using *Bioptonics Viewer* by Jerome Avondo, which is a previous version of *VolViewer*. Thickness was measured at four different points on the leaf; the lamina centre, the midvein centre, the midvein base and the lamina tip. To get a general estimate of leaf width these measurements were averaged for each plant. I fitted an exponential curve to the average leaf thickness using Excel.

### 6.2.7 *jaw-D* Crosses

The *jaw-D* (*35S::miR319a*; Efroni et al. 2008) plants were crossed to *cyclinB1;1:GFP* (Reddy et al., 2004) and *DR5rev::GFP* (Friml et al., 2003) expressing plants. All plants were of ecotype Col-0, sown on plates and grown under standard growth conditions for about one week. Plants were then trans-

ferred onto soil [John Innes No. 2 with osmocote and exemptor] grown under 16 h of light at 20°C. Crosses were performed using a light microscope. The *jaw-D* mutants were always used as the female plant due to reduced male fertility.

### 6.2.8 Imaging Leaves with Fluorescent Constructs

Florescence images of leaves expressing *DR5rev::GFP* (Friml et al., 2003), *PIN1::PIN1-GFP* (Benková et al., 2003) or *CyclinB1;1::GFP* (Reddy et al., 2004) were taken at various times. In addition, *jaw-D* line crossed with the *DR5rev::GFP* or *CyclinB1;1::GFP* lines were also imaged. All plants were of ecotype Col-0. Plants were grown under standard growth conditions. Leaves were removed and flattened. Up to 9 DAS, leaves were imaged under the confocal microscope [Zeiss EXCITER Laser Confocal Microscope] using the 488-nm line of an argon ion laser. The emitted light was passed through a 500-550-nm band-pass filter. Leaves were imaged using either an oil objective lens with 40x magnification or a dry lens with 20x or 10x magnification. Leaves older than 9 DAS were imaged using a compound microscope [Leica DM6000] with a 10x objective lense. Fluorescence was captured using a 460-540-nm filter. Brightfield images of wild-type leaves were also captured using the Leica DM6000.

## 6.3 Computational Modelling

The details of each model are described in the appropriate chapter sections. Here, general methods are shown together with the parameter values used for each model. Growth along the midline was simulated using a one-dimensional model in MATLAB. Leaf growth in 2D and 3D was modelled using the GPT-framework, which was implemented in the MATLAB application, *GFtbox* (Kennaway et al., 2011).

### 6.3.1 The Canvas

The 1D models are based on a canvas comprising a line made up of 1000 segments of equal length joined at vertices. The line has a length of 100  $\mu m$ ,

corresponding to the part of the leaf that forms the lamina.

The 2D and 3D models are based on an initial canvas, which is oriented with regard to the external  $xy$ -coordinate system such that the canvas base is parallel to the  $x$ -axis and the midline is parallel to the  $y$ -axis. The initial finite element mesh is  $84 \mu m$  in width (parallel to the  $x$ -axis) and  $95 \mu m$  in length (parallel to the  $y$ -axis). In the 3D models the thickness of the canvas was varied as outlined in the 3D chapter. Growth at the baseline is constrained to be parallel to the  $x$ -axis, reflecting the anchoring of the leaf to the stem.

In most 2D models the canvas consists of 2944 elements. In the serration models, the mesh only consists of 2080 elements, but is locally subdivided after  $120 h$ , generating a mesh consisting of 2592 elements. Similarly in the *jaw*-D models, the margins are subdivided to generate a mesh consisting of 3134 elements. Elements are not subdivided during the simulations.

### 6.3.2 Factors

In all models, growth and polarity are controlled by factors, which are distributed over the canvas and have one value for each vertex or segment. Factors can either propagate, designated by  $\mathbf{s}_{FACTORNAME}$  for signalling, or retain fixed values for segments of the tissue, designated by  $\mathbf{i}_{FACTORNAME}$  for identity. It is assumed that factor levels do not dilute with growth. Parameters associated with these factors are subscripted with the factor name in lower case. Factors may promote growth rates through the linear function *pro*, defined as:

$$\text{pro}(p_f, \mathbf{x}_F) = 1 + p_f \mathbf{x}_F, \quad (6.2)$$

where  $\mathbf{x}_F$  is a factor, and  $p_f$  is the promotion coefficient of the factor. Factors may inhibit growth through the function *inh*, defined as:

$$\text{inh}(h_f, \mathbf{x}_F) = 1/(1 + h_f \mathbf{x}_F), \quad (6.3)$$

where  $h_f$  is the inhibition coefficient of  $\mathbf{x}_F$ . All multiplications and divisions are elementwise.

### 6.3.3 Model Output Times

Outputs of the 1D and 2D models were generated at times comparable to the leaf data shown (Tab. 6.1). The initial canvas sizes are slightly smaller than the starting size of the leaves captured by time lapse imaging. Therefore, the models start at a time slightly earlier than the age of the initial tracked leaves. The canvas starting size corresponds to leaves at the end of 3 days after initiation. Growth was simulated up to 205  $h$ , which corresponds to leaves 8-9 days after initiation depending on the growth conditions and natural variation in leaf development. Model output times are given at times that best matched the times and sizes at which the real leaves are shown. Real leaf timings are given in hours after initiation as an average of the three datasets available. The time step of each model was one virtual hour.

Model Name	Initiation	T1	T2	T3	T4
Tracking Data	90	120	141	177	201
1D Models	87	117	148	181	205
2D Models	87	117	148	180	205

**Table 6.1** Data and model output times in hours after leaf initiation.

### 6.3.4 1D Models

The parameter values used in the 1D models to simulate growth along the lamina midline are shown in Table 6.2. In the propagating inhibitor model,  $\mathbf{s}_{DIST}$  levels reached steady state before each growth step.  $\mathbf{s}_{DIST}$  was considered at steady state levels when the relative change in  $\mathbf{s}_{DIST}$  levels was below  $1^{-10}$ . The diffusion equation of  $\mathbf{s}_{DIST}$  was solved using the *ode15* function in MATLAB (Shampine and Reichelt, 1997; Shampine et al., 1999). Growth was calculated at intervals of 1  $h$ .

The parameters values used for the fixed activator model for early stages also applied to the fixed activator models with dilution and with  $\mathbf{i}_{LATE}$ .

Parameter	Description	Value
<b>Propagating Inhibitor</b>		
$D_{dist}$	$s_{DIST}$ diffusion rate	$5 \times 10^{-6} \text{ mm}^2 \text{ h}^{-1}$
$\mu_{dist}$	$s_{DIST}$ decay rate	$0.005 \text{ h}^{-1}$
$p_{max}$	maximum growth rate	$0.032 \text{ h}^{-1}$
$b_{dist}$	$s_{DIST}$ production at source	$2.5 \text{ h}^{-1}$
$h_{dist}$	inhibition of $K$ by $s_{DIST}$	1
<b>Fixed Inhibitor</b>		
$D_{dist}$	$s_{DIST}$ diffusion rate	$2 \times 10^{-6} \text{ mm}^2 \text{ h}^{-1}$
$\mu_{dist}$	$s_{DIST}$ decay rate	$4.5 \times 10^{-3} \text{ h}^{-1}$
$p_{max}$	maximum growth rate	$0.032 \text{ h}^{-1}$
$b_{dist}$	$s_{DIST}$ production at source	$1.9 \text{ h}^{-1}$
$h_{dist}$	inhibition of $K$ by $s_{DIST}$	1
<b>Fixed Activator for early stages</b>		
$b_{prox}$	minimum levels of $\mathbf{i}_{PROX}$	0.195
$p_{prox}$	growth promotion by $\mathbf{i}_{PROX}$	$0.04 \text{ h}^{-1}$
<b>Models with <math>\mathbf{i}_{LATE}</math></b>		
$g_{late}$	increase in $\mathbf{i}_{LATE}$ over time	$0.0048 \text{ h}^{-1}$
$h_{late}$	growth inhibition by $\mathbf{i}_{LATE}$	4.5

**Table 6.2** 1D model parameter values.

### 6.3.5 2D Models

The 2D models were generated using the GPT-framework implemented in a toolbox in MATLAB, the *GFtbox*. The *GFtbox* is available on <http://www.uea.ac.uk/cmp/research/cmpbio/GFtbox>. In the *GFtbox* implementation, each model has two interconnected networks: the Polarity Regulatory Network (PRN) specifies tissue polarity, and the Growth rate Regulatory Network (KRN) determines how factors influence specified growth rates. In total, growth interactions are specified by three equations, one for the PRN and two for the KRN. These networks determine the specified polarity and growth fields across the canvas. The deformation of the canvas is calculated according to linear elasticity theory of small displacements. Due to the connectedness of the canvas this specified growth differs from the resultant growth by which the system is deformed.

### 6.3.5.1 Simulation Details

Models (using about 3000 finite elements) take about 20 *min* to run on a dual core desktop computer for 139 steps (the period simulated), solving the elasticity and diffusion equations with a tolerance of  $10^{-4}$  relative to the magnitude of the numbers.

#### 6.3.5.1.1 Simulation Loop

At each simulation step, actions are carried out in the following order.

- Calculate levels and distribution of growth factors as specified.
- Calculate the extend of diffusion during the time step.
- Calculate the growth tensor field specified by the factors
- Calculate the resulting displacement of each vertex to obtain the computed growth field.
- From the displacement field calculate the region of identity factor expression in the new volume after growth.

#### 6.3.5.1.2 Material Properties

The canvas is considered to be a solid volume. It is assumed that the elasticity is homogeneous across the canvas. The Poisson's ratio is 0.3.

### 6.3.5.2 2D Leaf Model Parameters

#### 6.3.5.2.1 Growth Parameters

In the core 2D models (generated in chapter 2 Leaf Growth and Polarity) the growth is specified as:

$$K_{par} = p_{prox} \mathbf{i}_{PROX} \cdot \text{inh}(h_{late}, \mathbf{i}_{LATE})$$

$$K_{per} = p_{lam} \mathbf{i}_{LAM} \cdot \text{inh}(h_{mid}, \mathbf{i}_{MID}) \cdot \text{pro}(p_{late}, \mathbf{i}_{LATE}) \cdot \text{inh}(h_{rim}, \mathbf{i}_{RIM})$$

The parameters and parameter values for the core 2D model are shown in Table 6.3. Some of the parameter values varied between models. In models

where  $K_{per}$  is reduced by  $\mathbf{i}_{RIM}$ ,  $p_{lam}$  is increased to  $0.024 h^{-1}$ . In the cutting models, growth at the cut edge is inhibited by different levels. In the distal cut model  $h_{inc} = 5$ . In the diagonal cut model  $h_{inc} = 10$ . In the side cut  $h_{inc} = 1$ .

Parameter	Description	Value
<b>Core Model</b>		
$b_{prox}$	minimum levels of $\mathbf{i}_{PROX}$	0.195
$g_{late}$	increase in $\mathbf{i}_{LATE}$ over time	$0.0048 h^{-1}$
$p_{prox}$	growth promotion by $\mathbf{i}_{PROX}$	$0.041 h^{-1}$
$p_{lam}$	growth promotion by $\mathbf{i}_{LAMINA}$	$0.023 h^{-1}$
$p_{late}$	growth promotion by $\mathbf{i}_{LATE}$	2
$h_{late}$	growth inhibition by $\mathbf{i}_{LATE}$	1.8
$h_{mid}$	growth inhibition by $\mathbf{i}_{MID}$	0.5
$h_{rim}$	$K_{per}$ inhibition by $\mathbf{i}_{RIM}$	1
<b>Special Cases, Leaf Growth and Polarity Chapter</b>		
$h_{pet}$	growth inhibition by $\mathbf{i}_{PET}$ in the isotropic growth model	5
$h_{inc}$	growth inhibition by $\mathbf{i}_{INC}$	variable
<b>Leaf Serrations Chapter</b>		
$h_{ser}$	inhibition of $\mathbf{i}_{RIM}$ function by $\mathbf{i}_{SER}$	10
$p_{ser}$	growth promotion by $\mathbf{i}_{SER}$	0.5
$h_{sinus}$	growth inhibition by $\mathbf{i}_{SINUS}$	5
<b>3D Leaf Growth Chapter</b>		
$p_{nor}$	growth in $K_{nor}$ (thickness)	$0.006 h^{-1}$
$p_{top}$	$K_{par}$ promotion by $\mathbf{i}_{TOP}$	0.08
<b>jaw-D Models</b>		
$p_{rim}$	growth promotion by $\mathbf{i}_{RIM}$	0.3
$h_{rim \rightarrow late}$	inhibition of $\mathbf{i}_{LATE}$ function on $K_{par}$ by $\mathbf{i}_{RIM}$	10

**Table 6.3** Growth parameters used in the 2D models.

In addition to the factors and parameters used for the core leaf models, two identity factors,  $\mathbf{i}_{SER}$  and  $\mathbf{i}_{SINUS}$ , were added in the serration models. The distribution of these two factors was specified manually, by selecting the appropriate nodes on the mesh through the GFtbox user interface. Depending on the serration model  $\mathbf{i}_{SER}$  and  $\mathbf{i}_{SINUS}$  controlled different parameter values. In the sink increased  $K_{par}$  model  $p_{ser} = 0.3$  instead of the value given in Table 6.3.

In the 3D models, the thickness of the initial canvas is either set to 40  $\mu m$  (wild-type model) or 5  $\mu m$  (thickness tests).

### 6.3.5.2.2 Polarity Parameters

The polarity field was specified differently, as described in the respective chapters. The parameter values used are given in Table 6.4.

In the midvein and midline models,  $D_{pol} = 2.5 \times 10^{-6}$  and  $\mu_{pol} = 0.01$ .

Parameter	Description	Value
$b_{pol}$	maximum levels of $\mathbf{i}_{POL}$ and $\mathbf{s}_{POL}$	0.1
$D_{pol}$	$\mathbf{s}_{POL}$ diffusion rate	0.01 $mm^2 h^{-1}$
$\mu_{pol}$	$\mathbf{s}_{POL}$ decay rate	0.1 $h^{-1}$
$a_{pol}$	$\mathbf{s}_{POL}$ decay by $\mathbf{i}_{DISTORG}$	1 $h^{-1}$

**Table 6.4** Polarity parameters used in the 2D models.

### 6.3.5.3 2D Example Models

Possible growth and polarity systems were explored using simple example models based on a square canvas. In all these models,  $K_{par} = 0 \% h^{-1}$  and  $K_{per}$  is specified as a linear gradient ranging from 0 to 10  $\% h^{-1}$  distributed over the canvas parallel to the  $y$ -axis. In the initial isotropic growth models, the linear gradient of growth rates promotes both  $K_{par}$  and  $K_{per}$ .

The parameter values used are given in Table 6.5. In the two-organiser models,  $\mathbf{s}_{POL}$  is fixed at  $\mathbf{i}_{DISTORG}$  to 0, but produced freely at  $\mathbf{i}_{PROXORG}$ .

Parameter	Description	Value
<b>Non-Deforming and Deforming Polarity Models</b>		
$b_{pol}$	maximum levels of $i_{POL}$	1
<b>Organiser-Based Models - Leaf Growth and Polarity Chapter</b>		
$b_{pol}$	$s_{POL}$ production by $i_{PROXORG}$	1
$D_{pol}$	diffusion rate of $s_{POL}$	0.1
$\mu_{pol}$	decay rate of $s_{POL}$	1
<b>Organiser-Based Models - Leaf Serrations Chapter</b>		
$b_{pol}$	$s_{POL}$ production by $i_{PROXORG}$	1
$D_{pol}$	diffusion rate of $s_{POL}$	1
$\mu_{pol}$	decay rate of $s_{POL}$	1

**Table 6.5** Example models of polarity systems.

### 6.3.5.3.1 3D Canvas Bending

The importance of canvas thickness was demonstrated by introducing different growth rates on the two surfaces. In this model, instead of a linear gradient of growth rates, on the A surface  $Ka_{par} = 0.5 h^{-1}$  and  $Ka_{per} = 0 h^{-1}$ , while the B surface does not grow. The thickness of the canvas is either 5 % or 15 % of the square canvas width.

To induce canvas buckling, growth is isotropic and non-uniform (as specified by a linear gradient of growth rates). The initial variability along the  $z$ -axis is 1 % relative to the initial thickness of the canvas. The initial thickness is 1 % of the length and width of the canvas.

# List of Abbreviations

Abbreviation	Full Name
AN	ANGUSTIFOLIA
ANT	AINTEGUMENTA
AUX1	AUXIN RESISTANCE 1
BOP	BLADE-ON-PETIOLE
BR	Brassinosteroid
CIN	CINCINNATA
Col-0	<i>Arabidopsis thaliana</i> ecotype Columbia
CUC	CUP-SHAPED COTYLEDON
DAS	days after stratification
Dpp	Decapentaplegic
DR5	auxin response marker
FEM	finite element method
FIL	FILAMENTOUS FLOWER
GFP	green fluorescent protein
GPT framework	Growing Polarised Tissue framework (Kennaway et al., 2011)
HAS	hours after stratification
HD-ZIP III	class III homeodomain leucine zipper
JAG	JAGGED
KAN	KANADI
KLU	KLUH
KNOX	class I KNOTTED-1 homeobox
LA	LANCEOLATE

Abbreviation	Full Name
LEP	LEAFY PETIOLE
Ler	<i>Arabidopsis thaliana</i> ecotype Landsberg <i>erecta</i>
OPT	optical projection tomography
PCP	planar cell polarity
PHB	PHABULOSA
PIN	PINFORMED
PTL	PETAL LOSS
ROT	ROTUNDIFOLIA
SAM	shoot apical meristem
Shh	Sonic Hedgehog
TCP	TEOSINTE BRANCHED 1, CYLOIDEA and PROLIF- ERATING CELL FACTORS
Wg	Wingless
YAB	YABBY
YFP	yellow fluorescent protein

# Bibliography

- M. Affolter and K. Basler. The Decapentaplegic morphogen gradient: from pattern formation to growth regulation. *Nature Review Genetics*, 8(9):663–674, 2007.
- P. Aggarwal, M. Das Gupta, A. P. Joseph, N. Chatterjee, N. Srinivasan, and U. Nath. Identification of specific DNA binding residues in the TCP family of transcription factors in Arabidopsis. *The Plant Cell*, 22(4):1174–89, 2010.
- M. Aida, T. Ishida, H. Fukaki, H. Fujisawa, and M. Tasaka. Genes involved in organ separation in Arabidopsis: An analysis of the cup-shaped cotyledon mutant. *The Plant Cell*, 9(6):841–857, 1997.
- B. Aigouy, R. Farhadifar, D. B. Staple, A. Sagner, J. C. Roper, F. Jülicher, and S. Eaton. Cell flow reorients the axis of planar polarity in the wing epithelium of Drosophila. *Cell*, 142(5):773–786, 2010.
- R. Aloni, K. Schwalm, M. Langhans, and C. I. Ullrich. Gradual shifts in sites of free-auxin production during leaf-primordium development and their role in vascular differentiation and leaf morphogenesis in Arabidopsis. *Planta*, 216(5):841–53, 2003.
- K. Amonlirdviman, N. A. Khare, D. R. P. Tree, W.-S. Chen, J. D. Axelrod, and C. J. Tomlin. Mathematical modeling of planar cell polarity to understand domineering nonautonomy. *Science*, 307(5708):423–426, 2005.
- E. Anastasiou, S. Kenz, M. Gerstung, D. MacLean, J. Timmer, C. Fleck, and M. Lenhard. Control of plant organ size by KLUH/CYP78A5-dependent intercellular signaling. *Developmental Cell*, 13(6):843–856, 2007.
- G. S. Avery. Structure and development of the tobacco leaf. *American Journal of Botany*, 20(9):565–592, 1933.
- J. D. Axelrod and C. J. Tomlin. Modeling the control of planar cell polarity. *Wiley Interdisciplinary Reviews: Systems Biology and Medicine*, 3(5):588–605, 2011.
- L. A. Baena-Lopez, A. Baonza, and A. Garcia-Bellido. The orientation of cell divisions determines the shape of Drosophila organs. *Current Biology*, 15(18):1640–1644, 2005.
- Y. Bai, S. Falk, A. Schnittger, M. J. Jakoby, and M. Hülskamp. Tissue layer specific regulation of leaf length and width in Arabidopsis as revealed by the cell autonomous action of ANGUSTIFOLIA. *The Plant Journal*, 61(2):191–199, 2010.
- C. C. Baker, P. Sieber, F. Wellmer, and E. M. Meyerowitz. The early extra petals1 mutant uncovers a role for microRNA miR164c in regulating petal number in Arabidopsis. *Current Biology*, 15(4):303–315, 2005.
- F. Baluska, J. S. Parker, and P. W. Barlow. A role for gibberellic-acid in orienting microtubules and regulating cell-growth polarity in the maize root cortex. *Planta*, 191(2):149–157, 1993.

- N. Bao, K. W. Lye, and M. K. Barton. MicroRNA binding sites in Arabidopsis class III HD-ZIP mRNAs are required for methylation of the template chromosome. *Developmental Cell*, 7(5):653–662, 2004.
- P. Barbier de Reuille, I. Bohn-Courseau, C. Godin, and J. Traas. A protocol to analyse cellular dynamics during plant development. *The Plant Journal*, 44(6):1045–1053, 2005.
- P. Barbier de Reuille, I. Bohn-Courseau, K. Ljung, H. Morin, N. Carraro, C. Godin, and J. Traas. Computer simulations reveal properties of the cell-cell signaling network at the shoot apex in Arabidopsis. *Proceedings of the National Academy of Sciences of the United States of America*, 103(5):1627–1632, 2006.
- M. Barkoulas, C. Galinha, S. P. Grigg, and M. Tsiantis. From genes to shape: regulatory interactions in leaf development. *Current Opinion in Plant Biology*, 10(6):660–666, 2007.
- M. Barkoulas, A. Hay, E. Kougioumoutzi, and M. Tsiantis. A developmental framework for dissected leaf formation in the Arabidopsis relative *Cardamine hirsuta*. *Current Opinion in Plant Biology*, 40(9):1136–1141, 2008.
- T. I. Baskin. Anisotropic expansion of the plant cell wall. *Annual Review of Cell and Developmental Biology*, 21:203–222, 2005.
- G. T. S. Beemster, F. Fiorani, and D. Inzé. Cell cycle: the key to plant growth control? *Trends in Plant Science*, 8(4):154–158, 2003.
- E. Benková, M. Michniewicz, M. Sauer, T. Teichmann, D. Seifertová, G. Jürgens, and J. Friml. Local, efflux-dependent auxin gradients as a common module for plant organ formation. *Cell*, 115(5):591–602, 2003.
- S. Bensmihen, A. I. Hanna, N. B. Langlade, J. L. Micol, A. Bangham, and E. S. Coen. Mutational spaces for leaf shape and size. *HFSP Journal*, 2(2):110–120, 2008.
- G. Bharathan and N. R. Sinha. The regulation of compound leaf development. *Plant Physiology*, 127(4):1533–1538, 2001. doi: 10.1104/pp.010867.
- G. D. Bilborough, A. Runions, M. Barkoulas, H. W. Jenkins, A. Hasson, C. Galinha, P. Laufs, A. Hay, P. Prusinkiewicz, and M. Tsiantis. Model for the regulation of Arabidopsis thaliana leaf margin development. *Proceedings of the National Academy of Sciences of the United States of America*, 108(8):3424–3429, 2011.
- T. Blein, A. Pulido, A. Vialette-Guiraud, K. Nikovics, H. Morin, A. Hay, I. E. Johansen, M. Tsiantis, and P. Laufs. A conserved molecular framework for compound leaf development. *Science*, 322(5909):1835–1839, 2008.
- T. Blein, A. Hasson, and P. Laufs. Leaf development: what it needs to be complex. *Current Opinion in Plant Biology*, 13(1):75–82, 2009.
- J. Bolduc, L. Lewis, C. Aubin, and A. Geitmann. Finite-element analysis of geometrical factors in micro-indentation of pollen tubes. *Biomechanics and Modeling in Mechanobiology*, 5(4):227–236, 2006.
- J. Bonner. *Why size matters: from bacteria to blue whales*. Princeton University Press, 2006. ISBN 9780691128504.
- L. Borghi, M. Bureau, and R. Simon. Arabidopsis JAGGED LATERAL ORGANS is expressed in boundaries and coordinates KNOX and PIN activity. *The Plant Cell*, 19(6):1795–1808, 2007.
- A. Boudaoud. An introduction to the mechanics of morphogenesis for plant biologists. *Trends in Plant Science*, 15(6):353–360, 2010.

- S. Breuil-Broyer, P. Morel, J. de Almeida-Engler, V. Coustham, I. Negru-tiu, and C. Trehin. High-resolution boundary analysis during *Arabidopsis thaliana* flower development. *The Plant Journal*, 38(1):182–192, 2004.
- P. B. Brewer, P. A. Howles, K. Dorian, M. E. Griffith, T. Ishida, R. N. Kaplan-Levy, A. Kilinc, and D. R. Smyth. PETAL LOSS, a trihelix transcription factor gene, regulates perianth architecture in the *Arabidopsis* flower. *Development*, 131(16):4035–4045, 2004.
- G. W. Brodland. Finite-element methods for developmental biology. *International Review of Cytology*, 150:95–118, 1994.
- M. E. Byrne, R. Barley, M. Curtis, J. M. Arroyo, M. Dunham, A. Hudson, and R. A. Martienssen. Asymmetric leaves1 mediates leaf patterning and stem cell function in *Arabidopsis*. *Nature*, 408(6815):967–971, 2000.
- K. M. Cadigan. Regulating morphogen gradients in the *Drosophila* wing. *Seminars in Cell and Developmental Biology*, 13(2):83–90, 2002.
- Y. Cheng, X. Dai, and Y. Zhao. Auxin synthesized by the YUCCA flavin monooxygenases is essential for embryogenesis and leaf formation in *Arabidopsis*. *The Plant Cell*, 19(8):2430–2439, 2007.
- Y. F. Cheng, X. H. Dai, and Y. D. Zhao. Auxin biosynthesis by the YUCCA flavin monooxygenases controls the formation of floral organs and vascular tissues in *Arabidopsis*. *Genes & Development*, 20(13):1790–1799, 2006.
- E. Coen, A. G. Rolland-Lagan, M. Matthews, J. A. Bangham, and P. Prusinkiewicz. The genetics of geometry. *Proceedings of the National Academy of Sciences of the United States of America*, 101(14):4728–4735, 2004.
- E. S. Coen and E. M. Meyerowitz. The war of the whorls: genetic interactions controlling flower development. *Nature*, 353(6339):31–37, 1991.
- V. Conte, J. J. Muñoz, and M. Miodownik. A 3D finite element model of ventral furrow invagination in the *Drosophila melanogaster* embryo. *Journal of the Mechanical Behavior of Biomedical Materials*, 1(2):188–198, 2008.
- D. J. Cosgrove. Growth of the plant cell wall. *Nature Reviews Molecular Cell Biology*, 6(11):850–861, 2005.
- B. C. W. Crawford, U. Nath, R. Carpenter, and E. S. Coen. CINCINNATA controls both cell differentiation and growth in petal lobes and leaves of *Antirrhinum*. *Plant Physiology*, 135(1):244–253, 2004.
- P. Cubas, N. Lauter, J. Doebley, and E. Coen. The TCP domain: a motif found in proteins regulating plant growth and development. *The Plant Journal*, 18(2):215–222, 1999.
- S. J. Day and P. A. Lawrence. Measuring dimensions: the regulation of size and shape. *Development*, 127(14):2977–2987, 2000.
- M. J. M. De Boer, F. D. Fracchia, and P. Prusinkiewicz. *A model for cellular development in morphogenetic fields. In Lindenmayer Systems: Impacts on Theoretical Computer Science, Computer Graphics, and Developmental Biology.* 1992.
- J. Dervaux, P. Ciarletta, and M. Ben Amar. Morphogenesis of thin hyperelastic plates: A constitutive theory of biological growth in the Föppl-von Kármán limit. *Journal of the Mechanics and Physics of Solids*, 57(3):458–471, 2009.

- E. Dessaud, V. Ribes, N. Balaskas, L. L. Yang, A. Pierani, A. Kicheva, B. G. Novitsch, J. Briscoe, and N. Sasai. Dynamic assignment and maintenance of positional identity in the ventral neural tube by the morphogen Sonic Hedgehog. *PLoS Biology*, 8(6), 2010.
- S. Dhondt, F. Coppens, F. De Winter, K. Swarup, R. M. H. Merks, D. Inzé, M. J. Bennett, and G. T. S. Beemster. SHORT-ROOT and SCARECROW regulate leaf growth in Arabidopsis by stimulating S-phase progression of the cell cycle. *Plant Physiology*, 154(3):1183–1195, 2010.
- J. R. Dinneny, R. Yadegari, R. L. Fischer, M. F. Yanofsky, and D. Weigel. The role of JAGGED in shaping lateral organs. *Development*, 131(5):1101–1110, 2004.
- S. Disch, E. Anastasiou, V. K. Sharma, T. Laux, J. C. Fletcher, and M. Lenhard. The E3 ubiquitin ligase BIG BROTHER controls Arabidopsis organ size in a dosage-dependent manner. *Current Biology*, 16(3):272–9, 2006.
- L. Dolan and R. S. Poethig. Clonal analysis of leaf development in cotton. *American Journal of Botany*, 85(3):315–315, 1998.
- P. M. Donnelly, D. Bonetta, H. Tsukaya, R. E. Dengler, and N. G. Dengler. Cell cycling and cell enlargement in developing leaves of Arabidopsis. *Developmental Biology*, 215(2):407–419, 1999.
- T. Dubatolova and L. Omelyanchuk. Analysis of cell proliferation in Drosophila wing imaginal discs using mosaic clones. *Heredity*, 92(4):299–305, 2004.
- A. T. Dudley, M. A. Ros, and C. J. Tabin. A re-examination of proximodistal patterning during vertebrate limb development. *Nature*, 418(6897):539–544, 2002.
- J. Dumais. Can mechanics control pattern formation in plants? *Current Opinion in Plant Biology*, 10(1):58–62, 2007.
- L. Dupuy, J. Mackenzie, and J. Haseloff. Coordination of plant cell division and expansion in a simple morphogenetic system. *Proceedings of the National Academy of Sciences*, 107(6):2711–2716, 2010.
- I. Efroni, E. Blum, A. Goldshmidt, and Y. Eshed. A protracted and dynamic maturation schedule underlies Arabidopsis leaf development. *The Plant Cell*, 20(9):2293–2306, 2008.
- R. O. Erickson. Relative elemental rates and anisotropy of growth in area: a computer programme. *Journal of Experimental Botany*, 17(51):390–403, 1966.
- S. Eriksson, L. Stransfeld, N. M. Adamski, H. Breuninger, and M. Lenhard. KLUH/CYP78A5-dependent growth signaling coordinates floral organ growth in Arabidopsis. *Current Biology*, 20(6):527–532, 2010.
- K. Esau. *Plant Anatomy*. Wiley, New York, 1965.
- Y. Eshed, S. F. Baum, J. V. Perea, and J. L. Bowman. Establishment of polarity in lateral organs of plants. *Current Biology*, 11(16):1251–1260, 2001.
- Y. Eshed, A. Izhaki, S. F. Baum, S. K. Floyd, and J. L. Bowman. Asymmetric leaf development and blade expansion in Arabidopsis are mediated by KANADI and YABBY activities. *Development*, 131(12):2997–3006, 2004.

- P. Fayant, O. Girlanda, Y. Chebli, C.-E. Aubin, I. Villemure, and A. Geitmann. Finite element model of polar growth in pollen tubes. *The Plant Cell*, 22(8):2579–2593, 2010.
- X. Feng, Y. Wilson, J. Bowers, R. Kennaway, A. Bangham, A. Hannah, E. Coen, and A. Hudson. Evolution of allometry in *Antirrhinum*. *The Plant Cell*, 21(10):2999–3007, 2009.
- R. Feynman, R. Leighton, and M. Sands. *The Feynman lectures on physics*. Addison-Wesley Pub. Co., 1965. v. 2.
- A. J. Fleming. The molecular regulation of leaf form. *Plant Biology*, 5(4):341–349, 2003.
- G. Frankhauser. The effects of changes in chromosome number on amphibian development. *The Quarterly Review of Biology*, 20(1):20–78, 1945.
- J. Friml and K. Palme. Polar auxin transport – old questions and new concepts? *Plant Molecular Biology*, 49(3):273–284, 2002.
- J. Friml, A. Vieten, M. Sauer, D. Weijers, H. Schwarz, T. Hamann, R. Offringa, and G. Jürgens. Efflux-dependent auxin gradients establish the apical-basal axis of *Arabidopsis*. *Nature*, 426(6963):147–153, 2003.
- J.-L. Gallois, C. Woodward, G. V. Reddy, and R. Sablowski. Combined SHOOT MERISTEMLESS and WUSCHEL trigger ectopic organogenesis in *Arabidopsis*. *Development*, 129(13):3207–3217, 2002.
- L. Gälweiler, C. Guan, A. Müller, E. Wisman, K. Mendgen, A. Yephremov, and K. Palme. Regulation of polar auxin transport by AtPIN1 in *Arabidopsis* vascular tissue. *Science*, 282(5397):2226–2230, 1998.
- A. Geitmann and J. K. Ortega. Mechanics and modeling of plant cell growth. *Trends in Plant Science*, 14(9):467–78, 2009.
- H. Goda, Y. Shimada, T. Asami, S. Fujioka, and S. Yoshida. Microarray analysis of brassinosteroid-regulated genes in *Arabidopsis*. *Plant Physiology*, 130(3):1319–1334, 2002.
- A. Goldshmidt, J. P. Alvarez, J. L. Bowman, and Y. Eshed. Signals derived from YABBY gene activities in organ primordia regulate growth and partitioning of *Arabidopsis* shoot apical meristems. *The Plant Cell*, 20(5):1217–1230, 2008.
- N. Gonzalez, S. De Bodt, R. Sulpice, Y. Jikumaru, E. Chae, S. Dhondt, T. Van Daele, L. De Milde, D. Weigel, Y. Kamiya, M. Stitt, G. T. S. Beemster, and D. Inzé. Increased leaf size: Different means to an end. *Plant Physiology*, 153(3):1261–1279, 2010.
- C. R. Goodall and P. B. Green. Quantitative analysis of surface growth. *Botanical Gazette*, 147(1):1–15, 1986.
- K. C. Goodbody and C. W. Lloyd. Actin-filaments line up across *tradescantia* epidermal-cells, anticipating wound-induced division planes. *Protoplasma*, 157(1-3):92–101, 1990.
- L. V. Goodrich and D. Strutt. Principles of planar polarity in animal development. *Development*, 138(10):1877–1892, 2011.
- V. Gor, B. E. Shapiro, H. Jonsson, M. Heisler, G. V. Reddy, E. M. Meyerowitz, and E. Mjolsness. A software architecture for developmental modeling in plants: The computable plant project. pages 345–354, 2006.
- A. Goshtasby. Piecewise linear mapping functions for image registration. *Pattern Recognition*, 19(6):459–466, 1986.

- J. Gower. Generalized procrustes analysis. *Psychometrika*, 40(1):33–51, 1975.
- E. Graaff, C. Nussbaumer, and B. Keller. The Arabidopsis thaliana rlp mutations revert the ectopic leaf blade formation conferred by activation tagging of the LEP gene. *Molecular Genetics and Genomics*, 270:243–252, 2003.
- C. Granier and F. Tardieu. Water deficit and spatial pattern of leaf development. variability in responses can be simulated using a simple model of leaf development. *Plant Physiology*, 119(2):609–620, 1999.
- A. A. Green, J. R. Kennaway, A. I. Hanna, J. A. Bangham, and E. Coen. Genetic control of organ shape and tissue polarity. *PLoS Biology*, 8(11):e1000537, 2010.
- P. B. Green. Growth and cell pattern formation on an axis: Critique of concepts, terminology, and modes of study. *Botanical Gazette*, 137(3):187–202, 1976.
- P. B. Green. Expression of form and pattern in plants – a role for biophysical fields. *Seminars in Cell & Developmental Biology*, 7(6):903–911, 1996.
- J. T. Greenberg. Programmed cell death: a way of life for plants. *Proceedings of the National Academy of Sciences*, 93(22):12094–12097, 1996.
- T. Gregor, W. Bialek, R. R. van Steveninck, D. W. Tank, and E. F. Wieschaus. Diffusion and scaling during early embryonic pattern formation. *Proceedings of the National Academy of Sciences of the United States of America*, 102(51):18403–18407, 2005.
- V. A. Grieneisen, J. Xu, A. F. M. Marée, P. Hogeweg, and B. Scheres. Auxin transport is sufficient to generate a maximum and gradient guiding root growth. *Nature*, 449(7165):1008–1013, 2007.
- M. E. Griffith, A. da Silva Conceicao, and D. R. Smyth. PETAL LOSS gene regulates initiation and orientation of second whorl organs in the Arabidopsis flower. *Development*, 126(24):5635–5644, 1999.
- J. Gros, J. K.-H. Hu, C. Vinegoni, P. F. Feruglio, R. Weissleder, and C. J. Tabin. WNT5A/JNK and FGF/MAPK pathways regulate the cellular events shaping the vertebrate limb bud. *Current Biology*, 20(22):1993–2002, 2010.
- W. Grunewald and J. Friml. The march of the PINs: developmental plasticity by dynamic polar targeting in plant cells. *EMBO Journal*, 29(16):2700–2714, 2010.
- G. E. Gudesblat and E. Russinova. Plants grow on brassinosteroids. *Current Opinion in Plant Biology*, 14(5):530–537, 2011.
- J. B. Gurdon and P. Y. Bourillot. Morphogen gradient interpretation. *Nature*, 413(6858):797–803, 2001.
- J. B. Gurdon, A. Mitchell, and D. Mahony. Direct and continuous assessment by cells of their position in a morphogen gradient. *Nature*, 376(6540):520–521, 1995.
- C. M. Ha, G.-T. Kim, B. C. Kim, J. H. Jun, M. S. Soh, Y. Ueno, Y. Machida, H. Tsukaya, and H. G. Nam. The BLADE-ON-PETIOLE 1 gene controls leaf pattern formation through the modulation of meristematic activity in Arabidopsis. *Development*, 130(1):161–172, 2003.
- G. Haberer and J. J. Kieber. Cytokinins. new insights into a classic phytohormone. *Plant Physiology*, 128(2):354–362, 2002.

- S. Hake and J. L. Micol. The development of plant leaves. *131*(2):389–394, 2003.
- O. Hamant and J. Traas. The mechanics behind plant development. *New Phytologist*, *185*(2):369–385, 2010. Times Cited: 12.
- O. Hamant, M. G. Heisler, H. Jonsson, P. Krupinski, M. Uyttewaal, P. Bokov, F. Corson, P. Sahlin, A. Boudaoud, E. M. Meyerowitz, Y. Couder, and J. Traas. Developmental patterning by mechanical signals in Arabidopsis. *Science*, *322*(5908):1650–1655, 2008.
- O. Hamant, J. Traas, and A. Boudaoud. Regulation of shape and patterning in plant development. *Current Opinion in Genetics & Development*, *20*(4):454–459, 2010.
- N. Harder, F. Mora-Bermudez, W. J. Godinez, A. Wunsche, R. Eils, J. Ellenberg, and K. Rohr. Automatic analysis of dividing cells in live cell movies to detect mitotic delays and correlate phenotypes in time. *Genome Research*, *19*(11):2113–24, 2009.
- A. Hardham. *Regulation of polarity in tissues and organs*. Academic Press, 1982.
- B. J. Harrison and J. R. S. Fincham. Instability at the pal locus in *Antirrhinum majus*. *Heredity*, *19*(2):237–258, 1964.
- A. Hasson, A. Plessis, T. Blein, B. Adroher, S. Grigg, M. Tsiantis, A. Boudaoud, C. Damerval, and P. Laufs. Evolution and diverse roles of the CUP-SHAPED COTYLEDON genes in Arabidopsis leaf development. *The Plant Cell*, *23*(1):54–68, 2011. doi: 10.1105/tpc.110.081448.
- A. Hay and M. Tsiantis. The genetic basis for differences in leaf form between Arabidopsis thaliana and its wild relative Cardamine hirsuta. *Nature Genetics*, *38*(8):942–947, 2006.
- A. Hay, H. Kaur, A. Phillips, P. Hedden, S. Hake, and M. Tsiantis. The gibberellin pathway mediates KNOTTED1-type homeobox function in plants with different body plans. *Current Biology*, *12*(18):1557–1565, 2002.
- M. G. Heisler, C. Ohno, P. Das, P. Sieber, G. V. Reddy, J. A. Long, and E. M. Meyerowitz. Patterns of auxin transport and gene expression during primordium development revealed by live imaging of the Arabidopsis inflorescence meristem. *Current Biology*, *15*(21):1899–1911, 2005.
- Z. Hejnowicz and J. A. Romberger. Growth tensor of plant organs. *Journal of Theoretical Biology*, *110*(1):93–114, 1984.
- A. Hemerly, J. D. Engler, C. Bergounioux, M. Vanmontagu, G. Engler, D. Inzé, and P. Ferreira. Dominant-negative mutants of the Cdc2 kinase uncouple cell-division from iterative plant development. *EMBO Journal*, *14*(16):3925–3936, 1995.
- K.-i. Hibara, M. R. Karim, S. Takada, K.-i. Taoka, M. Furutani, M. Aida, and M. Tasaka. Arabidopsis CUP-SHAPED COTYLEDON3 regulates postembryonic shoot meristem and organ boundary formation. *The Plant Cell*, *18*(11):2946–2957, 2006.
- G. Horiguchi, A. Ferjani, U. Fujikura, and H. Tsukaya. Coordination of cell proliferation and cell expansion in the control of leaf size in Arabidopsis thaliana. *Journal of Plant Research*, *119*(1):37–42, 2006a.
- G. Horiguchi, U. Fujikura, A. Ferjani, N. Ishikawa, and H. Tsukaya. Large-scale histological analysis of leaf mutants using two simple leaf observation methods: identification of novel genetic pathways governing the size and shape of leaves. *The Plant Journal*, *48*(4):638–644, 2006b.

- B. Hu, W. Chen, W.-J. Rappel, and H. Levine. Determining the accuracy of spatial gradient sensing using statistical mechanics. *10060507*, 1:4, 2010.
- Y. Hu, H. M. Poh, and N. H. Chua. The Arabidopsis ARGOS-LIKE gene regulates cell expansion during organ growth. *The Plant Journal*, 47(1): 1–9, 2006.
- Y. X. Hu, O. Xie, and N. H. Chua. The Arabidopsis auxin-inducible gene ARGOS controls lateral organ size. *The Plant Cell*, 15(9):1951–1961, 2003.
- L. Hufnagel, A. A. Teleman, H. Rouault, S. M. Cohen, and B. I. Shraiman. On the mechanism of wing size determination in fly development. *Proceedings of the National Academy of Sciences of the United States of America*, 104(10):3835–3840, 2007.
- M. Hülskamp, S. Miséra, and G. Jürgens. Genetic dissection of trichome cell development in Arabidopsis. *Cell*, 76(3):555 – 566, 1994. doi: DOI: 10.1016/0092-8674(94)90118-X.
- D. E. Ingber. Mechanical control of tissue growth: Function follows form. *Proceedings of the National Academy of Sciences of the United States of America*, 102(33):11571–11572, 2005.
- K. Ishida and M. Katsumi. Effects of gibberellin and abscisic-acid on the cortical microtubule orientation in hypocotyl cells of light-grown cucumber seedlings. *International Journal of Plant Sciences*, 153(2):155–163, 1992.
- J. Jaeger, D. Irons, and N. Monk. Regulative feedback in pattern formation: towards a general relativistic theory of positional information. *Development*, 135(19):3175–3183, 2008.
- K. Johnson and M. Lenhard. Genetic control of plant organ growth. *New Phytologist*, 191(2):319–333, 2011.
- E. Jones, T. Oliphant, P. Peterson, et al. SciPy: Open source scientific tools for Python, 2001. URL <http://www.scipy.org/>.
- H. Jönsson, M. G. Heisler, B. E. Shapiro, E. M. Meyerowitz, and E. Mjolsness. An auxin-driven polarized transport model for phyllotaxis. *Proceedings of the National Academy of Sciences of the United States of America*, 103(5): 1633–1638, 2006.
- A. Kauschmann, A. Jessop, C. Koncz, M. Szekeres, L. Willmitzer, and T. Altmann. Genetic evidence for an essential role of brassinosteroids in plant development. *The Plant Journal*, 9(5):701–713, 1996.
- K. Kawade, G. Horiguchi, and H. Tsukaya. Non-cell-autonomously coordinated organ size regulation in leaf development. *Development*, 137(24): 4221–7, 2010.
- E. Kawamura, G. Horiguchi, and H. Tsukaya. Mechanisms of leaf tooth formation in Arabidopsis. *The Plant Journal*, 62(3):429–441, 2010.
- R. Kennaway, E. Coen, A. Green, and A. Bangham. Generation of diverse biological forms through combinatorial interactions between tissue polarity and growth. *PLoS Computational Biology*, 7(6):e1002071, 2011.
- S. Kessler and N. Sinha. Shaping up: the genetic control of leaf shape. *Current Opinion in Plant Biology*, 7(1):65–72, 2004.
- L. Kheibarshekan Asl, S. Dhondt, V. Boudolf, G. T. S. Beemster, T. Beckman, D. Inzé, W. Govaerts, and L. De Veylder. Model-based analysis of Arabidopsis leaf epidermal cells reveals distinct division and expansion patterns for pavement and guard cells. *Plant Physiology*, 156(4):2172–2183, 2011.

- A. Kicheva, P. Pantazis, T. Bollenbach, Y. Kalaidzidis, T. Bittig, F. Jülicher, and M. González-Gaitán. Kinetics of morphogen gradient formation. *Science*, 315(5811):521–525, 2007. doi: 10.1126/science.1135774.
- C. A. Kidner and M. C. P. Timmermans. Mixing and matching pathways in leaf polarity. *Current Opinion in Plant Biology*, 10(1):13–20, 2007.
- J. J. Kieber. The ethylene response pathway in Arabidopsis. *Annual Review of Plant Physiology and Plant Molecular Biology*, 48:277–296, 1997.
- G.-T. Kim, H. Tsukaya, and H. Uchimiya. The ROTUNDIFOLIA3 gene of Arabidopsis thaliana encodes a new member of the cytochrome P-450 family that is required for the regulated polar elongation of leaf cells. *Genes & Development*, 12(15):2381–2391, 1998.
- G.-T. Kim, H. Tsukaya, Y. Saito, and H. Uchimiya. Changes in the shapes of leaves and flowers upon overexpression of cytochrome P450 in Arabidopsis. *Proceedings of the National Academy of Sciences of the United States of America*, 96(16):9433–9437, 1999.
- G. T. Kim, K. Shoda, T. Tsuge, K. H. Cho, H. Uchimiya, R. Yokoyama, K. Nishitani, and H. Tsukaya. The ANGUSTIFOLIA gene of Arabidopsis, a plant CtBP gene, regulates leaf-cell expansion, the arrangement of cortical microtubules in leaf cells and expression of a gene involved in cell-wall formation. *EMBO Journal*, 21(6):1267–1279, 2002.
- J. H. Kim, H. R. Woo, J. Kim, P. O. Lim, I. C. Lee, S. H. Choi, D. Hwang, and H. G. Nam. Trifurcate feed-forward regulation of age-dependent cell death involving miR164 in Arabidopsis. *Science*, 323(5917):1053–1057, 2009.
- Y. Klein, E. Efrati, and E. Sharon. Shaping of elastic sheets by prescription of non-euclidean metrics. *Science*, 315(5815):1116–1120, 2007.
- M. A. R. Koehl, W. K. Silk, H. Liang, and L. Mahadevan. How kelp produce blade shapes suited to different flow regimes: A new wrinkle. *Integrative and Comparative Biology*, 48(6):834–851, 2008.
- T. B. Kornberg and A. Guha. Understanding morphogen gradients: a problem of dispersion and containment. *Current Opinion in Genetics & Development*, 17(4):264–271, 2007.
- T. Koyama, M. Furutani, M. Tasaka, and M. Ohme-Takagi. TCP transcription factors control the morphology of shoot lateral organs via negative regulation of the expression of boundary-specific genes in Arabidopsis. *The Plant Cell*, 19(2):473–484, 2007.
- E. M. Kramer and M. J. Bennett. Auxin transport: a field in flux. *Trends in Plant Science*, 11(8):382–386, 2006.
- S. Kumar and P. Bentley. *On Growth, Form and Computers*. Elsevier Academic Press, 2003. ISBN 978-0-12-428765-5.
- M. K. Kumaran, J. L. Bowman, and V. Sundaresan. *YABBY Polarity Genes Mediate the Repression of KNOX Homeobox Genes in Arabidopsis*, volume 14. 2002.
- S. Kurup, J. Runions, U. Köhler, L. Laplace, S. Hodge, and J. Haseloff. Marking cell lineages in living tissues. *The Plant Journal*, 42(3):444–453, 2005.
- A. Kuwabara and T. Nagata. Cellular basis of developmental plasticity observed in heterophyllous leaf formation of *Ludwigia arcuata* (Onagraceae). *Planta*, 224(4):761–770, 2006.

- D. Kwiatkowska and J. Dumais. Growth and morphogenesis at the vegetative shoot apex of *Anagallis arvensis* L. *Journal of Experimental Botany*, 54(387):1585–1595, 2003.
- N. B. Langlade, X. Z. Feng, T. Dransfield, L. Copsey, A. I. Hanna, C. Thebaud, A. Bangham, A. Hudson, and E. Coen. Evolution through genetically controlled allometry space. *Proceedings of the National Academy of Sciences of the United States of America*, 102(29):10221–10226, 2005.
- C. T. Larue, J. Wen, and J. C. Walker. A microRNA–transcription factor module regulates lateral organ size and patterning in *Arabidopsis*. *The Plant Journal*, 58(3):450–463, 2009.
- M. Laskowski, V. A. Grieneisen, H. Hofhuis, C. A. t. Hove, P. Hogeweg, A. F. M. Marée, and B. Scheres. Root system architecture from coupling cell shape to auxin transport. *PLoS Biology*, 6(12):e307, 2008.
- P. A. Lawrence and G. Struhl. Morphogens, compartments, and pattern: Lessons from *Drosophila*? *Cell*, 85(7):951–961, 1996.
- T. Lecuit and L. Le Goff. Orchestrating size and shape during morphogenesis. *Nature*, 450(7167):189–192, 2007.
- K. Lee, J. Avondo, H. Morrison, L. Blot, M. Stark, J. Sharpe, A. Bangham, and E. Coen. Visualizing plant development and gene expression in three dimensions using optical projection tomography. *The Plant Cell*, 18(9):2145–2156, 2006.
- C. X. Li, T. Potuschak, A. Colon-Carmona, R. A. Gutierrez, and P. Doerner. *Arabidopsis* TCP20 links regulation of growth and cell division control pathways. *Proceedings of the National Academy of Sciences of the United States of America*, 102(36):12978–12983, 2005.
- Y. Li, L. Zheng, F. Corke, C. Smith, and M. W. Bevan. Control of final seed and organ size by the DA1 gene family in *Arabidopsis thaliana*. *Genes & Development*, 22(10):1331–6, 2008.
- H. Liang and L. Mahadevan. The shape of a long leaf. *Proceedings of the National Academy of Sciences*, 2009.
- H. Liang and L. Mahadevan. Growth, geometry, and mechanics of a blooming lily. *Proceedings of the National Academy of Sciences*, 108(14):5516–5521, 2011.
- C. Lloyd and J. Chan. Microtubules and the shape of plants to come. *Nature Reviews Molecular Cell Biology*, 5(1):13–23, 2004.
- T. Mammoto and D. E. Ingber. Mechanical control of tissue and organ development. *Development*, 137(9):1407–20, 2010.
- M. Marder. The shape of the edge of a leaf. *Foundations of Physics*, 33(12):1743–1768, 2003.
- A. F. M. Marée, A. V. Panfilov, and P. Hogeweg. Phototaxis during the slug stage of *dictyostelium discoideum*: a model study. *Proceedings of the Royal Society of London. Series B*, 266:1351–1360, 1999.
- M. Martín-Trillo and P. Cubas. TCP genes: a family snapshot ten years later. *Trends in Plant Science*, 15(1):31–39, 2009.
- Y. Matsubayashi and Y. Sakagami. Peptide hormones in plants. *Annual Review of Plant Biology*, 57:649–674, 2006.
- J. R. McConnell and M. K. Barton. Leaf polarity and meristem formation in *Arabidopsis*. *Development*, 125(15):2935–2942, 1998.

- J. R. McConnell, J. Emery, Y. Eshed, N. Bao, J. Bowman, and M. K. Barton. Role of PHABULOSA and PHAVOLUTA in determining radial patterning in shoots. *Nature*, 411(6838):709–713, 2001.
- H. Meinhardt. Computational modelling of epithelial patterning. *Current Opinion in Genetics & Development*, 17(4):272–280, 2007.
- E. M. Meyerowitz. Genetic control of cell division patterns in developing plants. *Cell*, 88(3):299–308, 1997.
- J. L. Micol. Leaf development: time to turn over a new leaf? *Current Opinion in Plant Biology*, 12(1):9–16, 2009.
- M. Milan, S. Campuzano, and A. Garcia-Bellido. Cell cycling and patterned cell proliferation in the wing primordium of *Drosophila*. *Proceedings of the National Academy of Sciences*, 93(2):640–645, 1996.
- Y. Mizukami and R. L. Fischer. Plant organ size control: AINTEGUMENTA regulates growth and cell numbers during organogenesis. *Proceedings of the National Academy of Sciences of the United States of America*, 97(2):942–947, 2000.
- E. Moreno, K. Basler, and G. Morata. Cells compete for Decapentaplegic survival factor to prevent apoptosis in *Drosophila* wing development. *Nature*, 416(6882):755–759, 2002.
- M. Nakaya, H. Tsukaya, N. Murakami, and M. Kato. Brassinosteroids control the proliferation of leaf cells of *Arabidopsis thaliana*. *Plant and Cell Physiology*, 43(2):239–244, 2002.
- U. Nath, B. C. W. Crawford, R. Carpenter, and E. Coen. Genetic control of surface curvature. *Science*, 299(5611):1404–1407, 2003.
- D. Nellen, R. Burke, G. Struhl, and K. Basler. Direct and long-range action of a Dpp morphogen gradient. *Cell*, 85(3):357–368, 1996.
- C. M. Nelson, R. P. Jean, J. L. Tan, W. F. Liu, N. J. Sniadecki, A. A. Spector, and C. S. Chen. Emergent patterns of growth controlled by multicellular form and mechanics. *Proceedings of the National Academy of Sciences of the United States of America*, 102(33):11594–11599, 2005.
- T. P. Neufeld, A. F. A. de la Cruz, L. A. Johnston, and B. A. Edgar. Coordination of growth and cell division in the *Drosophila* wing. *Cell*, 93(7):1183–1193, 1998.
- A. C. Newell, P. D. Shipman, and Z. Sun. Phyllotaxis: Cooperation and competition between mechanical and biochemical processes. *Journal of Theoretical Biology*, 251(3):421–439, 2008.
- C. Niehrs. On growth and form: a Cartesian coordinate system of Wnt and BMP signaling specifies bilaterian body axes. *Development*, 137(6):845–857, 2010.
- K. Nikovics, T. Blein, A. Peaucelle, T. Ishida, H. Morin, M. Aida, and P. Laufs. The balance between the MIR164A and CUC2 genes controls leaf margin serration in *Arabidopsis*. *The Plant Cell*, 18(11):2929–2945, 2006.
- S. Nole-Wilson and B. A. Krizek. AINTEGUMENTA contributes to organ polarity and regulates growth of lateral organs in combination with YABBY genes. *Plant Physiology*, 141(3):977–987, 2006.
- M. Norberg, M. Holmlund, and O. Nilsson. The BLADE-ON-PETIOLE genes act redundantly to control the growth and development of lateral organs. *Development*, 132(9):2203–2213, 2005.

- C. K. Ohno, G. V. Reddy, M. G. B. Heisler, and E. M. Meyerowitz. The Arabidopsis JAGGED gene encodes a zinc finger protein that promotes leaf tissue development. *Development*, 131(5):1111–1122, 2004.
- K. Okada, J. Ueda, M. K. Komaki, C. J. Bell, and Y. Shimura. Requirement of the auxin polar transport-system in early stages of Arabidopsis floral bud formation. *The Plant Cell*, 3(7):677–684, 1991.
- N. Ori, A. R. Cohen, A. Etzioni, A. Brand, O. Yanai, S. Shleizer, N. Menda, Z. Amsellem, I. Efroni, I. Pekker, J. P. Alvarez, E. Blum, D. Zamir, and Y. Eshed. Regulation of LANCEOLATE by miR319 is required for compound-leaf development in tomato. *Nature Genetics*, 39(6):787–791, 2007.
- J. F. Palatnik, E. Allen, X. L. Wu, C. Schommer, R. Schwab, J. C. Carrington, and D. Weigel. Control of leaf morphogenesis by microRNAs. *Nature*, 425(6955):257–263, 2003.
- J. F. Palatnik, H. Wollmann, C. Schommer, R. Schwab, J. Boisbouvier, R. Rodriguez, N. Warthmann, E. Allen, T. Dezulian, D. Huson, J. C. Carrington, and D. Weigel. Sequence and expression differences underlie functional specialization of Arabidopsis microRNAs miR159 and miR319. *Developmental Cell*, 13(1):115–125, 2007.
- I. Pekker, J. P. Alvarez, and Y. Eshed. Auxin response factors mediate Arabidopsis organ asymmetry via modulation of KANADI activity. *The Plant Cell*, 17(11):2899–2910, 2005.
- J. M. Pérez-Pérez, J. Serrano-Cartagena, and J. L. Micol. Genetic analysis of natural variations in the architecture of Arabidopsis thaliana vegetative leaves. *Genetics*, 162(2):893–915, 2002.
- J. M. Pérez-Pérez, H. Candela, P. Robles, V. Quesada, M. R. Ponce, and J. L. Micol. Lessons from a search for leaf mutants in Arabidopsis thaliana. *International Journal of Developmental Biology*, 53(8-10):1623–1634, 2009.
- J. M. Pérez-Pérez, S. Rubio-Díaz, S. Dhondt, D. Hernández-Romero, J. Sánchez-Soriano, G. T. S. Beemster, M. R. Ponce, and J. L. Micol. Whole organ, venation and epidermal cell morphological variations are correlated in the leaves of Arabidopsis mutants. *Plant, Cell & Environment*, 34(12):2200–2211, 2011.
- W. S. Peters and N. Bernstein. The determination of relative elemental growth rate profiles from segmental growth rates (a methodological evaluation). *Plant Physiology*, 113(4):1395–1404, 1997.
- S. Pfeiffer, C. Alexandre, M. Calleja, and J. P. Vincent. The progeny of wingless-expressing cells deliver the signal at a distance in Drosophila embryos. *Current Biology*, 10(6):321–324, 2000.
- S. Pien, J. Wyrzykowska, S. McQueen-Mason, C. Smart, and A. Fleming. Local expression of expansin induces the entire process of leaf development and modifies leaf shape. *Proceedings of the National Academy of Sciences*, 98(20):11812–11817, 2001.
- R. S. Poethig and I. M. Sussex. The cellular parameters of leaf development in tobacco: a clonal analysis. *Planta*, 165:170–184, 1985.
- K. D. Poss. Advances in understanding tissue regenerative capacity and mechanisms in animals. *Nature Reviews Genetics*, 11(10):710–722, 2010.
- K. A. Pyke, J. L. Marrison, and A. M. Leech. Temporal and spatial development of the cells of the expanding first leaf of Arabidopsis thaliana (L.) Heynh. *Journal of Experimental Botany*, 42(11):1407–1416, 1991.

- M. C. Raff, B. Durand, and F. B. Gao. Cell number control and timing in animal development: the oligodendrocyte cell lineage. *International Journal of Developmental Biology*, 42(3):263–267, 1998.
- A. M. Rashotte, M. G. Mason, C. E. Hutchison, F. J. Ferreira, G. E. Schaller, and J. J. Kieber. A subset of Arabidopsis AP2 transcription factors mediates cytokinin responses in concert with a two-component pathway. *Proceedings of the National Academy of Sciences*, 103(29):11081–11085, 2006.
- G. V. Reddy, M. G. Heisler, D. W. Ehrhardt, and E. M. Meyerowitz. Real-time lineage analysis reveals oriented cell divisions associated with morphogenesis at the shoot apex of Arabidopsis thaliana. *Development*, 131(17):4225–4237, 2004.
- B. Reinhardt, E. Hanggi, S. Muller, M. Bauch, J. Wyrzykowska, R. Kerstetter, S. Poethig, and A. J. Fleming. Restoration of DWF4 expression to the leaf margin of a dwf4 mutant is sufficient to restore leaf shape but not size: the role of the margin in leaf development. *The Plant Journal*, 52(6):1094–1104, 2007.
- D. Reinhardt, T. Mandel, and C. Kuhlemeier. Auxin regulates the initiation and radial position of plant lateral organs. *The Plant Cell*, 12(4):507–518, 2000.
- D. Reinhardt, E.-R. Pesce, P. Stieger, T. Mandel, K. Baltensperger, M. Bennett, J. Traas, J. Friml, and C. Kuhlemeier. Regulation of phyllotaxis by polar auxin transport. *Nature*, 426(6964):255–260, 2003.
- D. Reinhardt, M. Frenz, T. Mandel, and C. Kuhlemeier. Microsurgical and laser ablation analysis of leaf positioning and dorsoventral patterning in tomato. *Development*, 132(1):15–26, 2005.
- O. Richards and A. Kavanagh. The analysis of the relative growth gradients and changing form of growing organisms: illustrated by the tobacco leaf. *The American Naturalist*, 77:385–399, 1942.
- R. E. Rodriguez, M. A. Mecchia, J. M. Debernardi, C. Schommer, D. Weigel, and J. F. Palatnik. Control of cell proliferation in Arabidopsis thaliana by microRNA miR396. *Development*, 137(1):103–112, 2010. doi: 10.1242/dev.043067.
- A. H. K. Roeder, V. Chickarmane, A. Cunha, B. Obara, B. S. Manjunath, and E. M. Meyerowitz. Variability in the control of cell division underlies sepal epidermal patterning in Arabidopsis thaliana. *PloS Biology*, 8(5), 2010.
- A. G. Rolland-Lagan, J. A. Bangham, and E. Coen. Growth dynamics underlying petal shape and asymmetry. *Nature*, 422(6928):161–163, 2003.
- A. G. Rolland-Lagan, E. Coen, S. J. Impey, and J. A. Bangham. A computational method for inferring growth parameters and shape changes during development based on clonal analysis. *Journal of Theoretical Biology*, 232(2):157–177, 2005.
- T. Rudge and J. Haseloff. A computational model of cellular morphogenesis in plants. *Development*, 8:78–87, 2005.
- F. Sainsbury, D. A. Collings, K. Mackun, J. Gardiner, J. D. Harper, and J. Marc. Developmental reorientation of transverse cortical microtubules to longitudinal directions: a role for actomyosin-based streaming and partial microtubule-membrane detachment. *The Plant Journal*, 56(1):116–31, 2008.
- R. Sarojam, P. G. Sappl, A. Goldshmidt, I. Efroni, S. K. Floyd, Y. Eshed, and J. L. Bowman. Differentiating Arabidopsis shoots from leaves by combined YABBY activities. *The Plant Cell*, 22(7):2113–2130, 2010.

- M. Sauer, J. Balla, C. Luschnig, J. Wisniewska, V. Reinohl, J. Friml, and E. Benková. Canalization of auxin flow by Aux/IAA-ARF-dependent feedback regulation of PIN polarity. *Genes & Development*, 20(20):2902–2911, 2006.
- S. Sauret-Güeto, G. Calder, and N. Harberd. Transient gibberellin application promotes *Arabidopsis thaliana* hypocotyl cell elongation without maintaining transverse orientation of microtubules on the outer tangential wall of epidermal cells. *The Plant Journal*, 69(4):628–639, 2011.
- A. Sauter, W. J. Davies, and W. Hartung. The longdistance abscisic acid signal in the droughted plant: the fate of the hormone on its way from root to shoot. *Journal of Experimental Botany*, 52(363):1991–1997, 2001.
- S. Savaldi-Goldstein, C. Peto, and J. Chory. The epidermis both drives and restricts plant shoot growth. *Nature*, 446(7132):199–202, 2007.
- S. Sawa, K. Watanabe, K. Goto, E. Kanaya, E. H. Morita, and K. Okada. FILAMENTOUS FLOWER, a meristem and organ identity gene of *Arabidopsis*, encodes a protein with a zinc finger and HMG-related domains. *Genes & Development*, 13(9):1079–1088, 1999.
- E. Scarpella, D. Marcos, J. Friml, and T. Berleth. Control of leaf vascular patterning by polar auxin transport. *Genes & Development*, 20(8):1015–1027, 2006.
- D. Schmundt, M. Stitt, B. Jähne, and U. Schurr. Quantitative analysis of the local rates of growth of dicot leaves at a high temporal and spatial resolution, using image sequence analysis. *The Plant Journal*, 16(4):505–514, 1998.
- C. Schommer, J. F. Palatnik, P. Aggarwal, A. Chetelat, P. Cubas, E. E. Farmer, U. Nath, and D. Weigel. Control of jasmonate biosynthesis and senescence by miR319 targets. *PLoS Biology*, 6(9):e230, 2008.
- G. Schwank and K. Basler. Regulation of organ growth by morphogen gradients. *Cold Spring Harbor Perspectives in Biology*, 2(1), 2010.
- G. Schwank, G. Tauriello, R. Yagi, E. Kranz, P. Koumoutsakos, and K. Basler. Antagonistic growth regulation by Dpp and Fat drives uniform cell proliferation. *Developmental Cell*, 20(1):123–130, 2011.
- E. Semiarti, Y. Ueno, H. Tsukaya, H. Iwakawa, C. Machida, and Y. Machida. The asymmetric leaves2 gene of *Arabidopsis thaliana* regulates formation of a symmetric lamina, establishment of venation and repression of meristem-related homeobox genes in leaves. *Development*, 128(10):1771–1783, 2001.
- G. Sena and K. D. Birnbaum. Built to rebuild: in search of organizing principles in plant regeneration. *Current Opinion in Genetics & Development*, 20(4):460–465, 2010.
- G. Sena, X. N. Wang, H. Y. Liu, H. Hofhuis, and K. D. Birnbaum. Organ regeneration does not require a functional stem cell niche in plants. *Nature*, 457(7233):1150–U110, 2009.
- L. F. Shampine and M. W. Reichelt. The MATLAB ODE suite. *SIAM Journal on Scientific Computing*, 18(1):1–22, 1997. URL <http://link.aip.org/link/?SCE/18/1/1>.
- L. F. Shampine, M. W. Reichelt, and J. A. Kierzenka. Solving Index-1 DAEs in MATLAB and Simulink. *SIAM Review*, 18(3):538–552, 1999.
- E. Sharon, B. Roman, M. Marder, G.-S. Shin, and H. L. Swinney. Mechanics: Buckling cascades in free sheets. *Nature*, 419(6907):579–579, 2002.

- E. Sharon, M. Marder, and H. Swinney. Leaves, flowers and garbage bags: Making waves. *American Scientist*, 92(3):254–261, 2004.
- J. Sharpe, U. Ahlgren, P. Perry, B. Hill, A. Ross, J. Hecksher-Sorensen, R. Baldock, and D. Davidson. Optical projection tomography as a tool for 3D microscopy and gene expression studies. *Science*, 296(5567):541–545, 2002.
- S. Shleizer-Burko, Y. Burko, O. Ben-Herzel, and N. Ori. Dynamic growth program regulated by LANCEOLATE enables flexible leaf patterning. *Development*, 2011.
- B. I. Shraiman. Mechanical feedback as a possible regulator of tissue growth. *Proceedings of the National Academy of Sciences of the United States of America*, 102(9):3318–3323, 2005.
- K. R. Siegfried, Y. Eshed, S. F. Baum, D. Otsuga, G. N. Drews, and J. L. Bowman. Members of the YABBY gene family specify abaxial cell fate in Arabidopsis. *Development*, 126(18):4117–4128, 1999.
- W. K. Silk and R. O. Erickson. Kinematics of plant growth. *Journal of Theoretical Biology*, 76(4):481–501, 1979.
- R. S. Smith, S. Guyomarç’h, T. Mandel, D. Reinhardt, C. Kuhlemeier, and P. Prusinkiewicz. A plausible model of phyllotaxis. *Proceedings of the National Academy of Sciences of the United States of America*, 103(5):1301–1306, 2006.
- M. Snow and R. Snow. Regulation of sizes of leaf primordia by older leaves. *Proceedings of the Royal Society of London Series B-Biological Sciences*, 151(942):39–47, 1959.
- M. I. Stahle, J. Kuehlich, L. Staron, A. G. von Arnim, and J. F. Golz. YABBYs and the transcriptional corepressors LEUNIG and LEUNIG HOMOLOG maintain leaf polarity and meristem activity in Arabidopsis. *The Plant Cell*, 21(10):3105–3118, 2009.
- S. Stoma, J. Chopard, C. Godin, and J. Traas. Using mechanics in the modelling of meristem morphogenesis. 2007.
- S. Stoma, M. Lucas, J. Chopard, M. Schaedel, J. Traas, and C. Godin. Transport enhancement as a plausible unifying mechanism for auxin transport in meristem development. *PLoS Computational Biology*, 4(10):e1000207, 2008.
- N. Street, A. Sjodin, M. Bylesjo, P. Gustafsson, J. Trygg, and S. Jansson. A cross-species transcriptomics approach to identify genes involved in leaf development. *BMC Genomics*, 9(1):589, 2008. doi: 10.1186/1471-2164-9-589.
- K. Sugimoto, S. P. Gordon, and E. M. Meyerowitz. Regeneration in plants and animals: dedifferentiation, transdifferentiation, or just differentiation? *Trends in Cell Biology*, 21(4):212–218, 2011.
- F. Swink and G. Wilhelm. *Plants of the Chicago Region*. Indiana Academy of Science, 4th edition edition, 1994.
- A. W. Sylvester, W. Z. Cande, and M. Freeling. Division and differentiation during normal and LIGULELESS-1 maize leaf development. *Development*, 110(3):985–1000, 1990.
- G. M. Symons and J. B. Reid. Brassinosteroids do not undergo long-distance transport in pea. implications for the regulation of endogenous brassinosteroid levels. *Plant Physiology*, 135(4):2196–2206, 2004.

- M. Szekeres, K. Nemeth, Z. KonczKalman, J. Mathur, A. Kauschmann, T. Altmann, G. P. Redei, F. Nagy, J. Schell, and C. Koncz. Brassinosteroids rescue the deficiency of CYP90, a cytochrome P450, controlling cell elongation and de-etiolation in Arabidopsis. *Cell*, 85(2):171–182, 1996.
- K. Taoka, Y. Yanagimoto, Y. Daimon, K. Hibara, M. Aida, and M. Tasaka. The NAC domain mediates functional specificity of CUP-SHAPED COTYLEDON proteins. *The Plant Journal*, 40(4):462–473, 2004.
- W. D. Teale, I. A. Paponov, and K. Palme. Auxin in action: signalling, transport and the control of plant growth and development. *Nature Reviews Molecular Cell Biology*, 7(11):847–859, 2006. 10.1038/nrm2020.
- A. A. Teleman, M. Strigini, and S. M. Cohen. Shaping morphogen gradients. *Cell*, 105(5):559–562, 2001.
- M. Thery, V. Racine, A. Pepin, M. Piel, Y. Chen, J.-B. Sibarita, and M. Bornens. The extracellular matrix guides the orientation of the cell division axis. *Nature Cell Biology*, 7(10):947–953, 2005.
- D. W. Thompson. *On Growth and Form*. Cambridge University Press, Cambridge, 1917.
- J. Traas and O. Hamant. From genes to shape: Understanding the control of morphogenesis at the shoot meristem in higher plants using systems biology. *Comptes Rendus Biologies*, 332(11):974–985, 2009.
- E. Truernit, H. Bauby, B. Dubreucq, O. Grandjean, J. Runions, J. Barthélémy, and J.-C. Palauqui. High-resolution whole-mount imaging of three-dimensional tissue organization and gene expression enables the study of phloem development and structure in Arabidopsis. *The Plant Cell*, 20(6):1494–1503, 2008.
- T. Tsuge, H. Tsukaya, and H. Uchimiya. Two independent and polarized processes of cell elongation regulate leaf blade expansion in Arabidopsis thaliana (L) Heynh. *Development*, 122(5):1589–1600, 1996.
- H. Tsukaya. Leaf shape: genetic controls and environmental factors. *International Journal of Developmental Biology*, 49:547–555, 2005.
- H. Tsukaya. Mechanism of leaf-shape determination. *Annual Review of Plant Biology*, 57:477–496, 2006.
- H. Tsukaya and H. Uchimiya. Genetic analyses of the formation of the serrated margin of leaf blades in Arabidopsis: combination of a mutational analysis of leaf morphogenesis with the characterization of a specific marker gene expressed in hydathodes and stipules. *Molecular & General Genetics*, 256(3):231–238, 1997.
- A. M. Turing. The chemical basis of morphogenesis. *Philosophical Transactions of the Royal Society of London. Series B, Biological Sciences*, 237(641):37–72, 1952.
- M. Ueda, Z. Zhang, and T. Laux. Transcriptional activation of Arabidopsis axis patterning genes WOX8/9 links zygote polarity to embryo development. *Developmental Cell*, 20(2):264–270, 2011.
- D. Umetsu and C. Dahmann. Compartment boundaries: Sorting cells with tension. *Landes Bioscience*, 4(3):241–245, 2010.
- E. van der Graaff, A. Den Dulk-Ras, P. J. J. Hooykaas, and B. Keller. Activation tagging of the LEAFY PETIOLE gene affects leaf petiole development in Arabidopsis thaliana. *Development*, 127(22):4971–4980, 2000.

- A. Vanderpoorten and C. E. Zartman. The bryum bicolor complex in North America. *Bryologist*, 105(1):128–139, 2002.
- N. Vargesson, J. D. Clarke, K. Vincent, C. Coles, L. Wolpert, and C. Tickle. Cell fate in the chick limb bud and relationship to gene expression. *Development*, 124(10):1909–1918, 1997.
- T. Vernoux, G. Brunoud, E. Farcot, V. Morin, H. Van den Daele, J. Legrand, M. Oliva, P. Das, A. Larrieu, D. Wells, Y. Guedon, L. Armitage, F. Picard, S. Guyomarc’h, C. Cellier, G. Parry, R. Koumproglou, J. H. Doonan, M. Estelle, C. Godin, S. Kepinski, M. Bennett, L. De Veylder, and J. Traas. The auxin signalling network translates dynamic input into robust patterning at the shoot apex. *Molecular Systems Biology*, 7(508):1–15, 2011.
- L. d. Veylder, T. Beeckman, G. T. S. Beemster, J. d. A. Engler, S. Ormenese, S. Maes, M. Naudts, E. v. d. Schueren, A. Jacquard, G. Engler, and D. Inzé. Control of proliferation, endoreduplication and differentiation by the Arabidopsis E2Fa-DPa transcription factor. *EMBO Journal*, 21(6):1360–1368, 2002.
- B. A. Veytsman and D. J. Cosgrove. A model of cell wall expansion based on thermodynamics of polymer networks. *Biophysical Journal*, 75(5):2240–2250, 1998.
- K. Wabnik, J. Kleine-Vehn, J. Balla, M. Sauer, S. Naramoto, V. Reinöhl, R. M. H. Merks, W. Govaerts, and J. Friml. Emergence of tissue polarization from synergy of intracellular and extracellular auxin signaling. *Molecular Systems Biology*, 6(447):1–15, 2010.
- R. Waites and A. Hudson. phantastica: a gene required for dorsoventrality of leaves in *Antirrhinum majus*. *Development*, 121(7):2143–2154, 1995.
- R. Waites, H. R. N. Selvadurai, I. R. Oliver, and A. Hudson. The PHANTASTICA gene encodes a MYB transcription factor involved in growth and dorsoventrality of lateral organs in *Antirrhinum*. *Cell*, 93(5):779–789, 1998.
- K. Watanabe and K. Okada. Two discrete cis elements control the abaxial side-specific expression of the FILAMENTOUS FLOWER gene in Arabidopsis. *The Plant Cell*, 15(11):2592–2602, 2003.
- O. D. Weiner. Regulation of cell polarity during eukaryotic chemotaxis: the chemotactic compass. *Current Opinion in Cell Biology*, 14(2):196–202, 2002.
- T. J. Widmann and C. Dahmann. Dpp signaling promotes the cuboidal-to-columnar shape transition of Drosophila wing disc epithelia by regulating Rho1. *Journal of Cell Science*, 122(9):1362–1373, 2009.
- S. D. Wolf, W. K. Silk, and R. E. Plant. Quantitative patterns of leaf expansion - comparison of normal and malformed leaf growth in *Vitis vinifera* cv Ruby Red. *American Journal of Botany*, 73(6):832–846, 1986.
- L. Wolpert. Positional information and spatial pattern of cellular differentiation. *Journal of Theoretical Biology*, 25(1):1–47, 1969.
- L. Wolpert. One hundred years of positional information. *Trends in Genetics*, 12(9):359–364, 1996.
- L. Wolpert. Positional information and patterning revisited. *Journal Theoretical Biology*, 269(1):359–65, 2011.
- H. Wolters and G. Jürgens. Survival of the flexible: hormonal growth control and adaptation in plant development. *Nature Reviews Genetics*, 10(5):305–317, 2009.

- G. Wu, W. C. Lin, T. B. Huang, R. S. Poethig, P. S. Springer, and R. A. Kerstetter. KANADI1 regulates adaxial-abaxial polarity in Arabidopsis by directly repressing the transcription of ASYMMETRIC LEAVES2. *Proceedings of the National Academy of Sciences of the United States of America*, 105(42):16392–16397, 2008.
- H. Yokoyama. Initiation of limb regeneration: The critical steps for regenerative capacity. *Development, Growth & Differentiation*, 50(1):13–22, 2008.
- S. R. Yu, M. Burkhardt, M. Nowak, J. Ries, Z. Petrasek, S. Scholpp, P. Schwille, and M. Brand. Fgf8 morphogen gradient forms by a source-sink mechanism with freely diffusing molecules. *Nature*, 461(7263):533–536, 2009.
- K. Zandomeni and P. Schopfer. Reorientation of microtubules at the outer epidermal wall of maize coleoptiles by phytochrome, blue-light photoreceptor, and auxin. *Protoplasma*, 173(3-4):103–112, 1993.
- Y. Zhao. The role of local biosynthesis of auxin and cytokinin in plant development. *Current Opinion in Plant Biology*, 11(1):16–22, 2008.
- O. Zienkiewicz. *The finite element method*. Tata McGraw-Hill Publishing, 3rd edition, 1983.